1975

The Shock Production And Quantitative Spectroscopy Of The Magnesium-hydride Doublet-a-pi - Doublet-x-sigma-plus Delta(v)=0 Sequence

Andrew Thomas Mcgregor

THE SHOCK PRODUCTION AND QUANTITATIVE SPECTROSCOPY OF THE MgH $A^2\Pi - X^2\Sigma^+$ $\Delta v=0$ SEQUENCE

by

Andrew Thomas Mc Gregor
Department of Physics

Submitted in partial fulfillment
of the requirements for the degree of
Doctor of Philosophy

Faculty of Graduate Studies
The University of Western Ontario
London, Ontario
April, 1975

ABSTRACT

Three metallic powders, Al, Be and Mg, were subjected to shock excitation in Argon-Hydrogen Test gas mixtures. All these samples yielded spectra of their monohydrides in the heated zone behind the reflected shock front. The $A^2\Pi - X^2\Sigma^+$ band system of MgH was studied by photographic absorption spectrophotometric methods via spectra obtained at shock tube temperatures between 2200°K and 2900°K. A constant value for the "sum of squares of the electronic transition moments" applicable to the (0,0), (1,1) and (2,2) bands was determined to be $\Sigma\Sigma|Re(\bar{r}_{v'v''})|^2 = 0.013 \pm 0.03$ atomic units.

A study of incident and reflected shock front speeds in $Ar:H_2$ Test gas mixtures permitted appropriate allowance for the non-uniformity in cross-sectional area at the viewing station and led to acceptance of P_5, T_5 values (calculated from measured incident front speeds) for conditions existing within the equilibrated region behind the reflected front.

Time resolution of the emitted radiation showed that emission from shock-produced hydrides was less intense in the zone behind the incident front than in the region behind the reflected front over the interval $1800 < T_5 < 4200$°K

The results of all these studies are consistent with a

model of the shock wave-powder sample interaction which considers part of the solid to sublime while the remainder liquefies (with subsequent evaporation) to form an atomic vapour that, interacting with the shock-heated Hydrogen, provides the metal's monohydride. This model agrees with the proposal of Parkinson (1959) for inorganic oxide-shock interaction but disagrees with Tyte's (1966) combustion model for Aluminium powders in an Oxygen environment.

ACKNOWLEDGEMENTS

Experimental measurements, which form the basis of this thesis, were performed in the Department of Physics, University of Western Ontario during the period 1962 - 1967. The author expresses his thanks to the chairman and members of the department who, then, extended to him the use of facilities and their full co-operation.

Most of the theoretical calculations were done while the writer was a member of the Mount Allison University teaching faculty. To Dr. D.P. Crawford, Head, Department of Physics, and to Dr. L.H. Cragg, President of the University, as well as to those other members of the Mount Allison Faculty who aided with their counsel and provided the use of computational facilities, the author extends grateful thanks. Some rechecking of earlier results was done on the University of New Brunswick (Fredericton) IBM 370/158 computing system. This facility was especially useful for comparisons of line profiles obtained via programmes written by the author and others published in the open literature.

The experiments could not have been performed successfully without good technical help. Consequently, the author wishes to acknowledge with thanks the aid offered by Messrs. Roy Koehler, Len Maslin and Fred Seltzer who competently improved the gear and helped keep it running.

Thanks are also due to Dr. R.W. Nicholls, Director of Research, and Dr. H.I.S. Ferguson, chairman of the Supervisory Committee, for

their patience and constructive guidance during the prolonged gestation of this document.

The researches reported herein were supported by funds from the National Research Council of Canada. The author appreciates the award of an NRCC Studentship for the period June 1962 - September 1965.

TABLE OF CONTENTS

*****

LIST OF TABLES

LIST OF FIGURES

NOMENCLATURE

[A]	partial pressure of mixture component A, atmos.
A_{ul}	Einstein A-coefficient for spontaneous emission by one particle, sec^{-1}.
$Ar:H_2$	Test gas mixture composed of Argon & Hydrogen.
a	slope of a graph passing through the origin and of type $\Delta t_{24}=a\Delta t^{\circ}_{12}$.
a	$[\ln(2)]w_c/w_d$ = Line Shape Parameter. Determines the central height and spread of the line profile.
a_i	attenuation produced by the i-th step of a step density filter. a_i is a very slowly varying function of wavelength.
a_j	constant in Heimel et al. (1963) seven constant fit to thermodynamic properties.
a(N)	sound speed in shock region N, km/sec or mm/μsec.
a_{NM}	sound speed ratio a(N)/a(M), dimensionless.
B_v	rotational constant for the v-th vibrational state, cm^{-1}.
$B_\lambda(T)$	Planck Black Body Emission Function, $W/(cm^2-\mu-sr)$ (Radiation intensity for unit wavelength range centred about λ.)
$b(\lvert\lambda-\lambda_0\rvert)$	line profile. $k_\lambda=b(\lvert\lambda-\lambda_0\rvert)k^{\circ}$. Determines the distribution of absorption coefficient with wavelength about the line centre λ_0, cm^{-1}.
C	Contact Surface
c	speed of light in vacuo, $2.997929\times10^{+8}$ m/sec.
c_2	second radiation constant, $hc/k = 1.43879$ cm-K°.
$\bar{C}_p(T)$	Molar constant pressure (temperature-dependent) heat capacity, cal/(mole-K°).
$c_p(T)$	specific constant pressure (temperature-dependent heat capacity, cal/(gram-K°).

$\bar{C}_v(T)$ Molar constant volume (temperature-dependent) heat capacity, cal/(mole-K°).

$D(\lambda")$ Density reading at a position on the microdensitometer tracing corresponding to wavelength $\lambda"$.

$D^\circ_\circ$ energy required for the dissociation of a diatomic molecule(into neutral infinitely separated atoms) from the lowest possible level of the electronic ground state, eV.

$(D^\circ_{T_1})_x$ Heat of formation of one mole of gaseous species x at T_1 and 1 atmosphere pressure from its constituent elements in their standard states under the same conditions. Heimel et al.data (1963) -

= +52097.7 cal/mole of H
= +35600.0 cal/mole of Mg
= -46987.5 cal/mole of MgH

D_v centrifugal rotation-vibration correction constant, cm^{-1}.

E energy of a spectroscopic level, state or term, cm^{-1}.

E_λ spontaneous emissive power (spectral intensity) at wavelength λ, $W/(cm^3-\mu-sr)$.

$\int_{\Delta\lambda} E_\lambda d\lambda$ total power radiated per unit solid angle in the wavelength interval $\Delta\lambda$, $W/(cm^3-sr)$.

ea_o product of electronic charge and radius of the first Bohr orbit, 2.54155×10^{-18} esu-cm, unity in atomic units.

$e^2/(m_e c^2)$ classical electron radius, 2.81785×10^{-13} cm.

eV electron-Volt (energy unit)= 1.60207×10^{-19} Joules or 8066.02 cm^{-1}. A Boltzmann distribution of particles with mean energy 1 eV has an effective temperature 11605.4°K.

$F_i(N)$ rotational energy of the i-th spin doublet component with total angular momentum minus spin equal to N, cm^{-1}.

$\bar{F}^\circ_T(N)$ Molar Gibbs Free Energy of gas mixture in shock region N at temperature T, cal/mole.

$f_{el}(\lambda)$ wavelength-dependent electronic oscillator strength for absorption defined by Eq (6-25) after Schadee (1967).

f_{lu}	electronic absorption oscillator strength, dimensionless.
G(v)	excitation energy of the v-th vibrational level, cm^{-1}. $\Delta G(v+1/2) = G(v+1) - G(v)$.
$g(\lvert\lambda - \lambda'\rvert)$	spectrograph slit function - normalized to unity. A triangular slit function was used. See Eq (A-11).
g_j	statistical weight (degeneracy or multiplicity) of level j.
gf	weighted oscillator strength: symmetrical between emission and absorption; additive for lines, multiplets, terms etc...
H(a,x)	Voigt Function - defined by Eq (A-4), dimensionless.
H_2/Ar	Hydrogen driven shock waves into Argon Test gas.
$H^\circ_T(N)$	Molar enthalpy of shocked gas mixture in region N at temperature T, cal/mole.
H_v	second centrifugal stretching rotation-vibration correction constant allowing for an increase in the internuclear separation of a diatomic molecule with rotation, cm^{-1}.
Half-width	one-half the wavenumber interval between the the half-intensity points on a line profile. For a Voigt line profile, the half intensity points occur at x_h defined by $H(a,x_h)=\frac{1}{2} H(a,0)$.
h	Planck's Constant, 6.6252×10^{-34} Joule-sec.
$h(\lvert\lambda' - \lambda''\rvert)$	Microdensitometer slit function - normalized to unity. A rectangular function was employed. See Eq(A-12).
$h_T(N)$	specific enthalpy of the shock heated mixture in region N at temperature T, cal/gram. $=H^\circ_T(N)/WM(N)$
I_λ	specific radiation intensity at wavelength λ, $W/(cm^2-\mu-sr)$.
J	total angular momentum quantum number for a rotational level.
J	conversion factor from calories to Joules , 4,184 Joules/cal.

k	Boltzmann Constant, 1.38046×10^{-16} erg/(K°).
$k°$	integrated absorption coefficient for an entire line. $\int_{\Delta\lambda} k_\lambda d\lambda = k°$, dimensionless.
k^*_{at}	multiplier defined via Eqs (6-6) & (6-7). This is the factor in $k°_{at}$ which is solely temperature dependent. It is independent of concentration and the gf-sum.
k_λ	absorption coefficient at wavelength λ corrected for stimulated emission, cm^{-1}.
$k_\lambda z$	optical depth (at wavelength λ) of the absorbing layer, dimensionless.
K_p	equilibrium dissociation constant expressed as a function of component partial pressure with atomic gas taken as the reference state. $K_{p1} = [H_2]/[H]^2$ for Hydrogen $K_{p2} = [MgH]/([Mg][H])$ for Magnesium Monohydride, dimensionless.
ln(2)	0.69314 71806 (base e)
[ln(2)]	0.83255 4611
ln(10)	2.30258 5093
$Log_{10}(e)$	0.43429 44819
LTE	local thermodynamic equilibrium
M_s	Incident shock front Mach number = U_1/a_1, dimensionless.
N	magnitude of the total angular momentum minus spin quantum number for a rotating diatomic molecule, dimensionless.
N	species concentration (n/V), moles/litre or particles/cm^3.
N_o^{at}	total gas phase concentration of free atoms of species at, particles/cm^3.
N_o^{mol}	total gas phase concentration of diatomic molecular species mol within the shock-heated mixture, molecules/cm^3.
n	number of moles

n_j concentration of type j molecules, molecules/cm^3.

P(J) rotational branch having J'=J"-1

P(N) total pressure in shock region N, atmospheres.

P_{ji} =P(j)/P(i)= pressure ratio, dimensionless.

P_k the k-th shock-detecting probe - a platinum thin film heat transfer gauge.

Q(J) rotational branch having J'=J"

Q_i^{int} internal partition function for a single molecule of species i referred to the lowest energy state attainable by that species as energy zero. Internal partition function for MgH determined from Heimel et al. data (1963) was in very good agreement with the one evaluated using the method of Haar & Friedman(1955) using the same molecular data.

$q_{v'N'v"N"i'}$ Franck-Condon factor of the i-th spin component of the N' $\leftrightarrow$ N", rotational transition in the (v',v") band. Neglecting rotational effects,

$$q_{v'v"} = \left|\int \psi_1'(r) \cdot \psi_2"(r)\,dr\right|^2$$

ψ_1, ψ_2 are wavefunctions for the vibrational levels of electronic states 1 and 2.

R(J) rotational branch having J'=J"+1.

R Universal gas constant, $8.3143 \times 10^{+7}$ ergs/(mole-K°). Conversion of Heimel et al polynomial data into enthalpies and specific heat capacities required the use of 1.98726 cal/(mole-K°) which had been introduced in the fitting process.

R_{at}^{mol} ratio defined via Eq (6-16) and Eq(6-15a) as [coefficient of k^*_{mol} sum] divided by [coefficient of k^*_{at} sum].

ΣRe^2 $\Sigma\Sigma|Re(\bar{r}_{v',v"})/ea_o|^2/(2S'+1)$, defined in Eq (6-14)

$\Sigma\Sigma|Re(\bar{r}_{v',v"})/ea_o|^2$ sum of squares of electronic transition moments defined by Eqs (6-11) & (6-12), in atomic units. The summation includes all electric dipole transitions between non-degenerate states of specified parity and $\Sigma=\pm 1/2$ values.

$\bar{r}_{v'v''}$	r-Centroid for the (v',v") vibrational band, Å $=[\int\psi_1'(r)\,r\,\psi_2''(r)\,dr]/[\int\psi_1'(r)\,\psi_2''(r)\,dr]$ ψ_1' & ψ_2'' are vibrational wavefunctions in the electronic states 1 and 2. (Nicholls & Jarmain 1956)
radian	57.29577 95131 degrees.
rms	root-mean-square; i.e. for a set of values x_i the rms value of the average of the xs is $x_{rms} = \sqrt{\Sigma x_i^2/n}$ $i = 1,2,3...n.$
S	Spin quantum number. S=±1/2 for both doublet states of MgH, dimensionless.
$\bar{S}$	Line Strength - symmetric between emission and absorption, atomic units.
S_I	Incident Shock Front..
S_J	Hönl-London Factor for a rotational line. The normalization used is $\Sigma S_J=(2S+1)(2J+1)$ and applies only to the combinations (S",J") and (S',J'). S_J is a contracted form of $S_{v'N'v''N''}$.
$S_{v'v''}$	Band Strength, atomic units.
S.E. of estimate	rms deviation of the ordinate about a fitted curve whose abscissa values are assumed error free. $S.E._{.} = \sqrt{(\Sigma d_i^2/n)}$ d_i is i-th deviation; n is the total number of data points.
T	thermodynamic temperature, K°.
T(N)	temperature in shock region N, K°
t	time co-ordinate, second
T_e	electronic state energy measured relative to the electronic ground state taken as energy zero, cm^{-1}.
U	velocity of material flowing behind a shock front relative to an axis fixed in the shock front, km/sec or mm/μsec.
V	particle velocity in the shock flow relative to a co-ordinate system fixed in the end wall (in a laboratory fixed co-ordinate system).
v	vibrational quantum number, dimensionless.

$(v', v")$	the vibrational band arising from the spectroscopic transition involving the upper vibrational level, v', and the lower vibrational level, v". In the present work v' and v" belong to different electronic states.
w_c	collision half-width, cm^{-1} or Å .
w_d	doppler half-width, cm^{-1} or Å .
w_v	voigt half-width, cm^{-1} or Å .
WM_k	Molar mass of constituent k, grams/mole. =39.944 for Argon = 1.008 for monatomic Hydrogen = 2.016 for diatomic Hydrogen =24.320 for Magnesium =25.328 for Magnesium monohydride.
WM(N)	Molar mass of the shock-heated mixture in region N of the flow, grams/mole.
x	length co-ordinate, metre.
X_k	Mole Fraction of k-th constituent of a mixture, [K]/P; dimensionless.
z	geometric path length through an absorbing atmosphere, cm.
Z_{at}	single atom internal partition function; equivalent to Q^{int} for one atom, dimensionless.
Z_{mol}	single molecule internal partition function; equal to Q^{int} for one molecule, dimensionless.
α	atomic scaling parameter used to determine the best fit of synthesized to original microdensitometer tracings, dimensionless.
γ	Ratio of principal specific heat capacities = $\bar{C}_p/\bar{C}_v$. Temperature dependent.
γ_v	spin splitting constant giving the magnitude of the effect that interaction of $\bar{S}$ and $\bar{N}$ vectors have on splitting the spin components, cm^{-1}.
ΔE_{Dk}	energy per gram of equilibrated shock-heated mixture required to produce total equilibration of dissociation, chemical reaction and vapourization of the powder sample material in region k, cal/gram.

ΔX_{ij}	separation of locations i and j, cm.
Δa_{if}	$a_f - a_i$. Final state value minus initial state value.
$\delta_{0,\Lambda}$	Kronecker delta function $\delta_{0,\Lambda}=1$ for $\Lambda=0$ $\delta_{0,\Lambda}=0$ otherwise.
Λ	component of resultant electronic angular momentum directed along the internuclear axis; $\Lambda'=1$ and $\Lambda''=0$ for the MgH green system.
λ_0	wavelength at line centre, cm or Å.
μ	molecular scaling parameter used in determining the best fit of synthesized to original microdensitometer tracings, dimensionless.
μ_{MgH}	reduced mass of the MgH molecule, 0.967480 gram.
ν	radiation frequency, sec^{-1}.
$A^2\Pi$	upper electronic state of the MgH green system.
π	3.14159 26536, dimensionless.
$\sqrt{\pi}$	1.77245 38509, dimensionless.
$\rho(N)$	density of mixture in shock region N, gm/cm^3.
$X^2\Sigma^+$	lower electronic state of the MgH green system and the electronic ground state of MgH.
σ_{ij}^2	optical collision cross-section for the partners i and j, $Å^2$.
ϕ_1	ratio of the total number of Argon atoms to the total number of Hydrogen atoms regardless of chemical compound in which each exists within the shock heated mixture. This ratio is used to specify constancy of elemental atoms.
ϕ_2	ratio of total number of Mg atoms present in a given shock region to the number of Hydrogen atoms present there regardless of the compounds in which each occurs.
ω_e	vibrational constant, cm^{-1}.
$\omega_e x_e$, $\omega_e y_e$ & $\omega_e z_e$	anharmonic oscillator vibrational constants, cm^{-1}.

Superscripts

°	observed value.
°	thermodynamic standard state (e.g. for a perfect gas 1 atmosphere pressure).
p	theoretically predicted value.
—	overbar signifying an average value.
'	upper state of a spectroscopic transition.
"	lower state of a spectroscopic transition.

Subscripts

g	gaseous phase.
s	solid phase
u	upper state (term or level) of a spectroscopic transition. (State of higher total energy.)
l	lower state of a spectroscopic transition.
1	spin doublet component for which J=N + 1/2.
2	spin doublet component for which J=N - 1/2.

CHAPTER 1

INTRODUCTION

1.1 Historical

The shock tube provides a thermally excited high temperature environment suitable for the study of many problems in chemical physics. Conditions in the hot gas behind the incident shock wave are uniquely determined by the gas composition, its initial temperature and pressure and by the incident shock front velocity. These controlled initial conditions and the reflected shock velocity (itself a function of them) serve to define the characteristics of the environment between the reflected shock front and the reflecting surface.

Many of the earlier shock tube kinetic studies were performed in the region behind the incident shock front. Here, it was felt, conditions could be predicted and controlled more closely than behind the reflected front because all the required variables were directly measureable. Recently, after the expenditure of great efforts in simultaneous measurement of pressure, density and temperature behind both shock fronts, researchers (Watson, 1963, 1966; Hurle, 1964; Just, 1970) are agreed that the reflected shock region is one in which local thermodynamic equilibrium often does exist.

They have found that values of thermodynamic variables, in this region, can be predicted from quantities controlled by the experimentalist when generating the incident shock and from that shock's speed.

In chemical kinetics and spectroscopy, temperature is the dominant variable. Thus many investigations have been directed to measurement of temperature behind shock fronts. This has been accomplished by using the spectrum line-reversal method for NaI (Clouston, Gaydon & Glass, 1958; Clouston, Gaydon & Hurle, 1959; Charatis, 1961; Lapworth, 1962), InI and CrI (Clouston, Gaydon & Hurle, 1959) and BaI (Faizullov, Sobolev & Kudryavtsev, 1960) to measure temperatures ca. 5000°K. The experimentally determined quantities have been found to agree with those predicted by one-dimensional shock wave theory within an experimental uncertainty of 2%.

Parkinson and Nicholls (1960) used rotational line intensities of CN and later Reeves and Parkinson (1964) employed selected lines of BaI, CaII, and AlI to measure temperatures ca. 7000-9000°K behind reflected shock fronts in Argon that agreed to 10% precision with predictions based upon initial shock conditions - without using a measured value for the incident shock speed. Miyama and Takeyama (1963) used iso-intensity measurements on lines of OH to determine temperatures in the reflected wave region that lie within 2% of values inferred from one dimensional shock theory, the initial conditions and a measured value of the incident wave

speed. Watson (1963, 1966) has measured reflected shock temperatures by comparing simultaneous emissions from different portions of the OH ultraviolet band system. In the temperature interval 3500-4300°K, his results too are within 2% of the predicted values.

An extensive investigation by Bengston et al (1970) revealed reflected wave temperatures ca. 9000°K - in neon with traces of volatile additives - to be 3% greater than those inferred from measured incident shock speeds, at the lowest test gas pressures used. Just (1970) has reported temperatures of 2000-2700°K measured behind reflected shocks in Argon-Hydrogen mixtures that deviate by no more than 0.6% from values estimated using the incident shock speed.

Shock wave studies of gaseous mixtures complement the more classical methods used for investigating rates of chemical reactions. The shock tube has been used to study fast reactions and as a heat bath to initiate reactions too slow to occur at more conventional temperatures. Thermal decomposition of Chlorine (Diesen & Telmke, 1963), Bromine (Lawrence, 1969; Warshay, 1972), Cyanogen (Knight & Rink, 1961; Levitt, 1968), Fluorine (Blauer, 1972), Hydrogen Chloride (Breshears, 1972a) and Hydrogen (Gardiner & Kistiakowsky, 1961; Patch, 1962; Myerson, 1968; Breshears, 1972a) diluted with inert gases have been studied behind the incident shock front and NH (Seal and Gaydon, 1966) in the reflected wave zone. Rates of reaction and some dissociation energies have been determined. Reactions occurring in the Acetylene-Oxygen system

have been investigated extensively by Stubbeman (1964), and Gutman et al (1967a, 1967b, 1968, 1970, 1972). Moreover the oxidation of Methane (Miyama & Takeyama, 1963, 1965), the pyrolysis of Benzene (Barnard, 1972) as well as the decomposition of ammonia (Hidaki & Yamamura, 1971) and Nitrogen difluoride (Modica & Hornig, 1965) have all been subjects of shock tube investigations. Experiments to measure vibrational relaxation times important for the understanding of the CO_2-N_2 laser system have been reported by Taylor (1969). The effects of additives upon the relaxation processes in NO (Wray, 1962), CO (Hooker, 1963; White, 1966; Borrell, 1972), CO_2 (Weihs, 1969; Eckstrom, 1972), H_2 (Kiefer, 1966; Raff, 1968; Boitnott, 1971; Simpson, 1971) and N_2 (Hurle, 1964) have been studied behind the incident shock front. Hurle (1964) has performed similar studies on N_2 in the reflected wave region. Diebold et al (1974) hasestudied the vibrational relaxation of Fluorine. Associative recombination of Hydrogen atoms has been investigated (Hurle, 1967) and electron-molecular ion dissociative recombination rates have been determined for Kr_2^+ (Cunningham & Hobson, 1972a) and N_2^+ (Cunningham & Hobson, 1972b) afterglows behind incident shock fronts.

The shock tube has proved to be a most useful tool for the study of astrophysically important atomic and molecular spectra. Investigations of FeI and FeII (Weeks, 1967; Byard, 1967; Huber, 1968; Grasdalen, 1969; Wolnik, 1971; Von Rosenberg, 1972; Huber, 1974; Gilbert et al, 1974), CrI and CrII (Wilkerson, 1961; Charatis, 1962; Wolnik, 1968, 1969), SiI (Day, 1969;

Miller, 1969) and TiI and TiII (Boni, 1968) spectra have led to evaluations of gf-values and analysis of spectral line shapes. The BaI (Parkinson & Reeves, 1962) and PbI (Garton, 1966) spectra have been examined in the ultraviolet and followed out to their series limits. Auto-ionization of the AlI doublet at 1932Å and 1936Å (Garton, Parkinson, & Reeves, 1964) and the auto-ionization continua of specific CaI (Newsom, 1968), TlI (Marr & Heppinstall, 1966) and InI (Marr, 1966) lines have been other subjects of investigation. These studies have led to assignments of previously unknown energy levels of these atoms and to the identification of additional lines in the appropriate spectral series.

One of the most important uses of the shock tube has been the production under controlled and known conditions of many molecular spectra important in solar and stellar spectroscopy. The emission spectra of TiO, AlO, BO, and ZrO - molecules prominent in M and S type stars - have all been recorded in spectra produced by the shock excitation of finely divided oxide powders (Parkinson & Nicholls, 1957, 1959; Tyte, 1964). O_2, CN and CH - prominent in solar spectra - have been noted in spectra from shock-excited organic powders (Watson, 1960). OH (Watson, 1963, 1966), N_2 (Keck, 1959; Hurle, 1964), O_2 (Treanor & Wurster, 1959; Sharma & Wray, 1970), NO (Glick, 1957; Wray, 1962; Wray & Teare, 1962) and CO_2 (Breeze, 1963) - all present in the earth's upper atmosphere - have been the subjects of shock tube qualitative photometric investigations.

Some qualitative aspects of these spectra have been known for many years but the shock tube with its characteristic thermal mode of excitation allows quantitative studies to be made. For example, lifetimes and absolute oscillator strengths have been measured for AlO (Tyte & Hébert, 1964), BeO (Drake, 1967), C_2 (Arnold, 1968), CN (Arnold & Nicholls, 1972), N_2^+ (Cooper, 1972), NH (Harrington, 1966), NO (Cann, 1968), O_2 (Sobolev & Faizullov, 1963), OH (Lapp, 1961; Watson, 1963, 1966), SiO (Main, 1968) and VO (Harrington, 1969). And so, it is with an extension of these quantitative studies, which employ shock excitation techniques, that this thesis is concerned.

1.2 Scope of Thesis

Diatomic hydrides are amongst the most abundant molecules in stellar envelopes and MgH, in particular, is one of the more plentiful. Yet, in 1962, when these studies were begun, no absolute electronic oscillator strength - f-number - was known for any radiative transition of this molecule. Therefore andattempt was made to perform an experimental measurement of the absolute electronic oscillator strength for the $A^2\Pi$-$X^2\Sigma^+$ system of MgH using shock excitation techniques. This thesis reports the outcome of that work.

The technique used to introduce MgH into the shock heated test gas, although novel at the time, is an extrapolation of methods used previously in this laboratory. Parkinson's (1957, 1959) work on oxides and McGregor's (1962) on sulphides and

ceramics had shown that shock excitation of finely divided, powdered, solid additives to an Argon test gas could lead to the formation of desired diatomic species - particularly in the region behind the reflected shock front. Solid samples were easily handled and specific compounds were chosen because they contained chemical constituents necessary for the production of a desired diatomic molecule. Often these compounds contained additional elements and various combinations of those constituents would lead to the presence of unwanted species within the Test gas mixture. Consequently, preference was given to suitable binary compounds. MgH_2 is the only reasonably 'stable' binary hydride of magnesium under normal conditions. However, it is rather combustible and dangerous to handle. Furthermore, it reacts with water and water vapour quite readily to form a hydroxide which gives rise to an MgO spectrum that overlaps the MgH $A^2\Pi$-$X^2\Sigma^+$ band system when (nominal) MgH_2 is subjected to shock excitation. For these reasons, use of this hydride was rejected. Instead, successful attempts were made to form MgH within the shock tube by combining elemental magnesium, Mg, (introduced as a powdered sample) with Hydrogen, H_2, present as an appreciable fraction of the predominantly Argon Test gas.

Observations of MgH spectra were restricted to the reflected shock region as this resulted in a longer observation time - approximately 800 μsec compared with 250 μsec for the incident shock region - in addition to providing sufficient time for the production of significant amounts of MgH.

The possibility of extending this technique to the formation of other hydrides was studied with the help of Beryllium and Aluminium powders.

Qualitative shock tube studies, such as wave length determinations in spectra emitted by molecules in excited states, require knowledge only of the initial experimental conditions to characterize the investigation. Quantitative studies such as the evaluation of an f-value demand a complete awareness of the properties - temperature, pressure composition and number densities - within the reacting gaseous mixture during the observation period. The following chapters describe the steps taken to determine the MgH $A^2\Pi$-$X^2\Sigma^+$ oscillator strength. Those steps were

a) Calculation of conditions within the reacting mixture from basic shock tube equations and equilibrium state thermodynamics;

b) Production of hydrides by shock excitation techniques;

c) Experimental measurement of

   i) Emission from a self-luminous reacting mixture, or of

   ii) Absorption by the reacting mixture (when an absorption experiment was performed);

d) Reproduction of microdensitometer tracings of recorded spectra by computer-synthesized spectra that made correct allowance for instrumental response during the recording of experimental data.

e) Evaluation of the oscillator strength.

1.3 Outline of Thesis

The theory needed to account for thermodynamic properties of Argon, diatomic Hydrogen and monatomic Hydrogen mixtures behind incident and reflected shock fronts is developed in Chapter 2. There, too, the effect of added powdered samples is considered. The experimental arrangements, special techniques employed and methods used are presented in Chapter 3. Chapter 4 contains a comparison of predicted and measured shock speeds in Argon and Argon-Hydrogen mixtures of variable composition. In addition, the intensity versus time behaviour of several spectral features is examined in this chapter as well as the influence of the observation zone design upon the incident shock speed (and as a consequence upon the temperature existing behind the reflected shock front). The chapter concludes with a list of impurity radiations emitted from the reflected shock region at high temperature. Emission and absorption spectra obtained during these studies are presented in Chapter 5. Within that chapter, the characteristics of those spectra are discussed and the variation of the spectra with calculated shock temperatures is noted. Chapter 6 is devoted to quantitative spectroscopy: theory necessary for an understanding of intensity variations within spectra obtained from optically thick layers is presented; those results are applied to observed MgH absorption spectra and lead to an evaluation of the desired oscillator strength. Conclusions drawn from all investigations and suggestions for future work are listed in Chapter 7. There are four appendices:

Appendix A - A conglomeration of details vital to the computer synthesis of MgH absorption spectra but not necessary for the understanding of Chapter 6.

Appendix B - a list of the conditions pertinent to each spectrum displayed.

Appendix C - Solution of Shock Tube Equations.

Appendix D - Re-analysis of the available rotational wavenumbers for MgH $A^2\Pi$-$X^2\Sigma^+$ to yield band origins and molecular constants of sufficient precision for the reconstruction of rotational line wavenumbers.

Chapter 2

EVALUATION OF SHOCKED GAS PARAMETERS

This chapter treats the question:

When a known mass of powdered sample is subjected to thermal excitation by a shock wave of incident speed U_1, travelling in a shock tube of uniform, circular cross-section through a test gas originally composed of Argon and diatomic Hydrogen under controlled initial conditions, what are the resultant equilibrium values of temperature, pressure and species concentrations behind the incident and reflected shock fronts?

Although the following pages deal specifically with a Magnesium sample, the algebraic results apply directly to Aluminium and Beryllium - other sample materials used in the present studies.

Knowledge of temperatures and species concentrations is vital for the quantitative interpretation of shock-excited molecular spectra in terms of oscillator strengths, band strengths and electronic transition moments. As the main goal of this research was quantitative spectroscopy of the MgH $A^2\Pi$-$X^2\Sigma^+$ band system from shock-generated spectra, the physical conditions within the shock-heated reacting mixture had to be determined for each set of experimental conditions. Those parameters were evaluated as functions of the incident

shock speed and the experimentally controlled pre-shock equilibrium conditions by application of conservation laws for mass, energy, momentum and number of atoms and by imposing constraints specified by equilibrium state thermodynamics.

The algebraic formulation of the problem is straightforward. However, the multitude of numeric calculations needed to account for different sample sizes and variable test gas composition are tedious and susceptible to human error - particularly in cases where sequential iterations are needed. Therefore, the net of equations linking end state properties was programmed first for the IBM 7040, then available at U.W.O., and later for an IBM 1130 computer present at Mount Allison University, where much of this thesis was written.

Following a description of the shock-excitation processes in section 2.1, the algebraic solution is considered under five headings:

2.2 Assumptions, Limitations and Notation

2.3 Incident Shock Parameters

2.4 Dissociative Equilibrium and Species Concentrations

2.5 Parameter Values in the Region of the Reflected Shock

2.6 Summary of Results

2.1 Shock Excitation

A broad understanding of the operation of a shock tube may be gained from a qualitative description based upon Figure 2-1, an x-t diagram. It depicts the one-dimensional flow patterns within a simple, bursting-diaphragm, pressure-driven shock tube. (The notation is standard (Gaydon & Hurle, 1963; Glass, 1958)).

Initially the driver gas (in the Chamber, region (4)) and the test gas (in the Channel, region (1)), are separated by a Mylar diaphragm. Each gas is separately in thermodynamic equilibrium; i.e. temperatures T(1) and T(4), pressures P(1) and P(4) are constant and there is no net flow in the x-direction, $V(1) = V(4) = 0$. (V(I) is the particle flow velocity in region I measured with respect to a laboratory-fixed reference frame with positive velocities directed to the right.) The pressure ratio P_{41} ($\equiv P(4)/P(1) > 1$) and the identities, compositions, temperatures and molecular weights of the driver and test gas mixtures are known, pre-selected variables. The sound speed, a(4), of the driver gas is greater than that of the test gas, a(1). ($a_{41} > 1$)

When the diaphragm ruptures under pressure difference P(4) - P(1), gas in region (4) experiences an isentropic expansion and a rarefaction wave (of velocity -a(4)) travels into region (4) creating region (3). At first the driver gas tries to expand into region (1) at its own sound speed. However, the test gas can adjust to sudden pressure changes

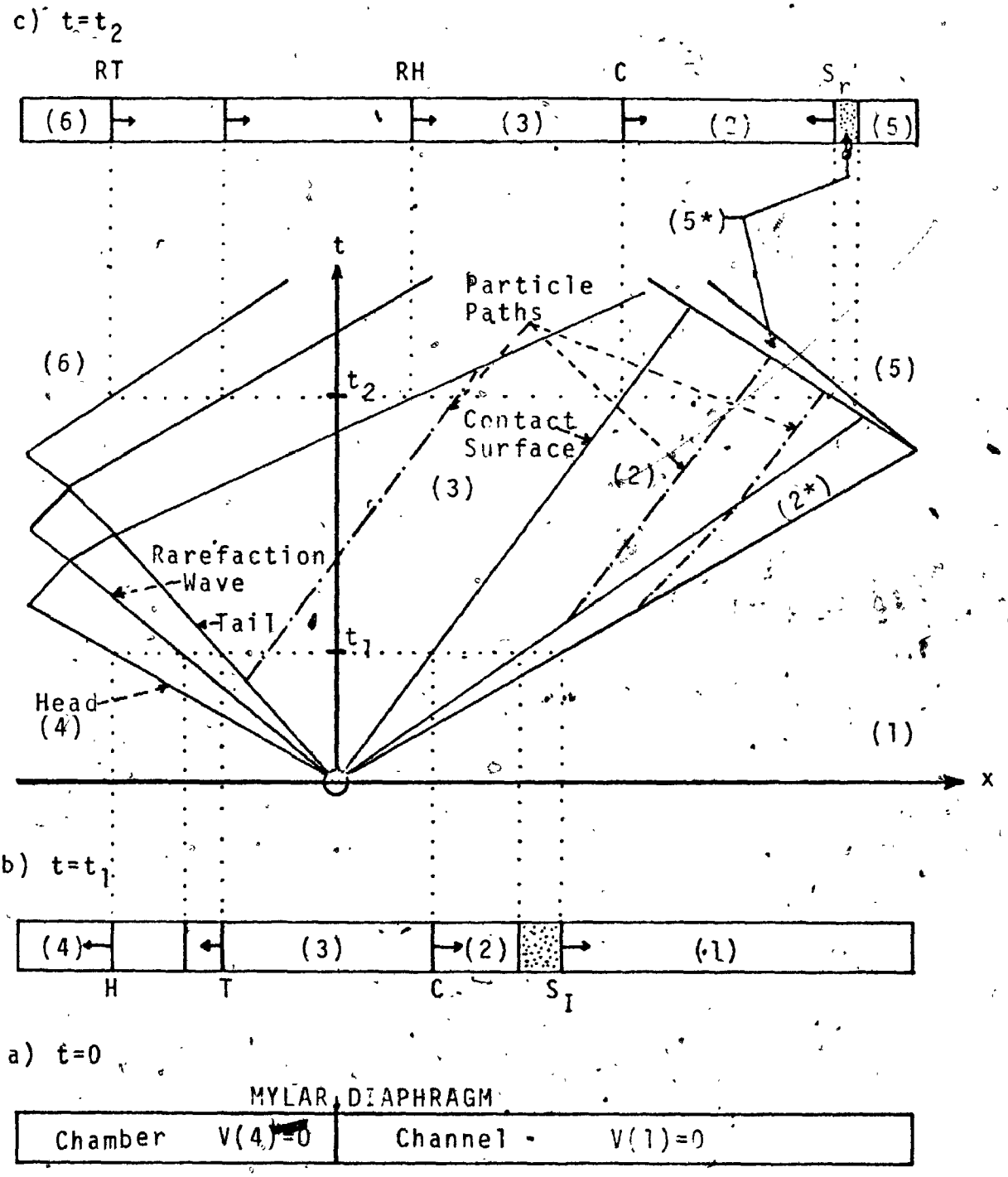

Figure 2-1

x-t Diagram Depicting Shock Tube Flow Regions

a) $t=0$ - Before Diaphragm Rupture
b) $t=t_1$ - Flow Pattern During Incident Shock Generation
c) $t=t_2$ - Flow Pattern After Normal Reflection

at a speed no greater than a(1) (a(1)<a(4)). Thus compression waves which rapidly coalesce into a shock wave travel into the test gas. The boundary between compressed and undisturbed test gas is called the incident shock front, S_I. It moves into region (1) with a velocity greater than +a(1) and the undisturbed particles cannot escape from it.

Compressed test gas is separated from the expanding driver gas by an interface, C, the contact surface. The contact surface moves at the flow velocity (a constant value, less than the shock front velocity) in the x-direction. It separates two regions, (2) and (3), of equal pressure and velocity but different entropy, density and temperature. The contact surface may be envisaged as a piston adiabatically compressing the test gas into a slug moving in the x-direction. At any time instant this slug has a volume defined by the tube cross-section and the relative positions of the incident shock front and the contact surface.

Molecules of the test gas passing through the incident shock front undergo a discontinuous change in temperature, pressure, density and entropy. The sudden reduction in their mean free paths causes an extremely rapid heating of the particles. For Argon-Hydrogen test gas mixtures, the translational and rotational degrees of freedom remain in thermal equilibrium during this transition but vibrational and dissociative modes are not capable of adjusting so rapidly. (Rink (1962) reports that translational and rotational modes

require ca. 10-50 collisions to become thermally equilibrated, whilst vibrational and dissociative modes of Hydrogen may require 100-500 collisions or more. Boitnott (1971) found that about 30 collisions were needed to establish rotational equilibrium behind the shock front at 1200°K. Kiefer & Lutz (1966) determined Hydrogen to be 98% vibrationally equilibrated, at 2000°K and 4 atmospheres pressure, 1 μsec after crossing a shock front.) Consequently, test gas molecules enter region (2*) directly behind the intident shock front in a state of 'frozen' equilibrium at a temperature T(2*). Dissociative relaxation occurs until, in region (2), the shock-heated mixture has achieved complete thermal equilibrium. Temperature T(2) is less than T(2*) for the relaxing system must re-apportion a fixed amount of energy among the available degrees of freedom. If dissociation occurs, pressure P(2) will be greater than P(2*).

The shock and rarefaction fronts travel along the tube until they encounter the end plates. There they experience normal reflection; particles behind the reflected wave fronts are brought to rest relative to the end plates. Thus regions (5) and (6) are formed.

When the incident shock front has reached the end plate, compressed gas in regions (2*) and (2) is still flowing towards that end wall. Therefore, a region of greater compression and more elevated temperature, region (5*), results.

It is another region of frozen equilibrium. However, temperature T(5*) is greater than twice T(2) in simple cases (Gaydon & Hurle, 1963) and P(5*)>P(3) so that complete equilibrium is established much more quickly than in region (2). Region (5), formed by this relaxation, first starts at the shock tube end plate and (like region (5*)) builds out from it. There must still be no net flow within region (5). Consequently, particles in this region have no net velocity in the x-direction (V(5)=0) while region (5) builds out from the end wall with speed U(5) directed to the left.

2.2 Assumptions, Limitations and Notation

Equations linking gas properties (in a shock tube of uniform cross-section) with the incident shock front speed are developed for binary test gas mixtures having a variable amount of diatomic component in a monatomic diluent. Particle flows in regions (1), (2), (2*), (3), (5*) and (5) are treated as isentropic and inviscid. No allowance is made for energy loss via conduction or radiation and ionization of the test gas is considered to be negligible. (The last assumption will be considered separately when species concentrations are derived in section 2.4.)

As the mathematical treatment is developed specifically for Hydrogen-Argon mixtures, chemical symbols are used as subscripts to identify properties of particular components.

A more compact notation results from the use of numeric subscripts to denote flow regions. Thus P(4), used previously, and P_4 are equivalent. Quantities accompanied by double numeric subscripts denote ratios. Thus

$$P_{41} = \frac{P_4}{P_1} = \frac{P(4)}{P(1)} \quad \text{and} \quad a_{52} = \frac{a_5}{a_2} = \frac{a(5)}{a(2)}$$

Parkinson's (1959) work on oxides, the author's (McGregor, 1962) on ceramics and sulphides and other experience in this laboratory have shown that molecular spectra can be excited in the reflected shock zone when its temperature is below 6000°K. At higher reflected wave temperatures only atomic line spectra have been observed. Thus a value of 6000°K was arbitrarily chosen as the upper limit to reflected shock temperature calculations.

In an experimental study of density gradients within $Xe-H_2$, $Ar-H_2$ and $Kr-H_2$ mixtures, Rink (1962) found

$$P_{2*} < P_2$$

for incident shocks with speeds in the 1.033-3.738 km/sec range. That inequality has been employed in this work. Here too, the subscript 2* is used to denote that region directly behind the incident shock front in which: Hydrogen and Argon have the same translational temperature; vibrational and rotational levels are populated according to Boltzmann Distributions at that temperature; and negligible dissociation has occurred. The existence of such a zone was

justified in section 2.1.

Within each flow region, every component of the mixture is assumed to follow the Perfect Gas equation of state (Davidson, 1962, pages 55ff)

$$PV = nRT \qquad (2\text{-}1)$$

- a relation between pressure, P, volume, V, temperature, T, and mole number, n. V will seldom be employed as a symbol for volume. When it is, there should be no confusion with the particle flow velocity. Generally (2-1) will be used in the form -

$$P = NRT \qquad (2\text{-}1a)$$

in which $N = n/V$ = species concentration in moles/litre. R is the molar gas constant.

When several components are present simultaneously, the total pressure is given by Dalton's Law

$$P = \sum_K [K] \qquad (2\text{-}2)$$

where [K] denotes the partial pressure exerted by species K contained within volume V. ([K] is equivalent to P for a single-component system.)

The mass of substance K present in one mole of the reacting mixture is

$$M_K = X_K \cdot WM_K = \frac{[K]}{P} \cdot WM_K \qquad (2\text{-}3)$$

where X_K is the mole fraction of constituent K and WM_K its molar mass. Obviously, (2-2) and (2-3) require

$$\sum_K X_K = 1 \qquad (2\text{-}4)$$

$$WM = \sum_K M_K = \sum_K \left\{ \frac{[K]}{P} \cdot WM_K \right\} \qquad (2\text{-}5)$$

WM is the molar mass of the mixture.

Statement (2-1) is a constraint only upon the translational motion of gas molecules when, as in the present case, the molecular structure and energy levels are independent of the kinetic energy of translation. Allowance for effects due to internal structure - electronic excitation, vibration and rotation - is made by considering the specific enthalpy, h, of each species to be a function of a temperature-dependent, constant-pressure heat capacity, c_p -

$$h_f(T_f) - h_i(T_i) = \int_{T_i}^{T_f} c_p(T)dT \qquad (2\text{-}6)$$

while the principal, molar specific heats are related by

$$\bar{C}_p(T) = \bar{C}_v(T) = R \qquad (2\text{-}7)$$

For computer solution, power series expansions for h and c_p as functions of T are preferable to tabulated values. Therefore, the polynomial expansions listed by Heimel et al (1963) were employed in the present work. They had been obtained from simultaneous least squares fits to extensive tabulations of thermodynamic data derived from spectroscopic and physico-chemical observations on equilibrated systems. Those relations take the form

$$\frac{c_p}{R} = a_1 + a_2T + a_3T^2 + a_4T^3 + a_5T^4$$

$$\frac{h}{RT} = a_1 + a_2\frac{T}{2} + a_3\frac{T^2}{3} + a_4\frac{T^3}{4} + a_5\frac{T^4}{5} + \frac{a_6}{T}$$

where a_1, a_2, a_3, etc. are constant coefficients.

Although measurement of shock parameters is usually performed in a laboratory-fixed reference frame, expressions relating them are customarily referred to an axis system with origin fixed in the shock front. Figure 2-2 depicts the relationship between these two measurement systems. U denotes particle speed relative to a fixed shock front and V with respect to a fixed end wall. The co-ordinate transformations between incident wave flow speeds are (Gaydon & Hurle, 1963)

$$U_1 = W_I - V_1 = W_I - 0 = W_I \qquad (2\text{-}8a)$$

$$U_{2*} = W_I - V_{2*} \qquad (2\text{-}8b)$$

$$U_2 = W_I - V_2 \qquad (2\text{-}8c)$$

They find immediate application in the next paragraph.

2.3 Incident Shock Parameters

The conservation of mass, momentum and energy for unit mass of test gas experiencing adiabatic compression across unit area of an incident shock front is expressible within a shock-fixed co-ordinate system by -

Mass: $$\rho_1 U_1 = \rho_{2*} U_{2*} = \rho_2 U_2 \qquad (2\text{-}9)$$

Momentum: $$P_1 + \rho_1 U_1^2 = P_{2*} + \rho_{2*} U_{2*}^2 = P_2 + \rho_2 U_2^2 \qquad (2\text{-}10)$$

Energy: $$h_1 + \frac{1}{2}\cdot U_1^2 = h_{2*} + \frac{1}{2}\cdot U_{2*}^2 = h_2 + \frac{1}{2}\cdot U_2^2 + \Delta E_{D2} \qquad (2\text{-}11)$$

- for any gas, real or perfect (Gaydon & Hurle, 1963).

a) Measured in Laboratory-fixed Co-ordinates

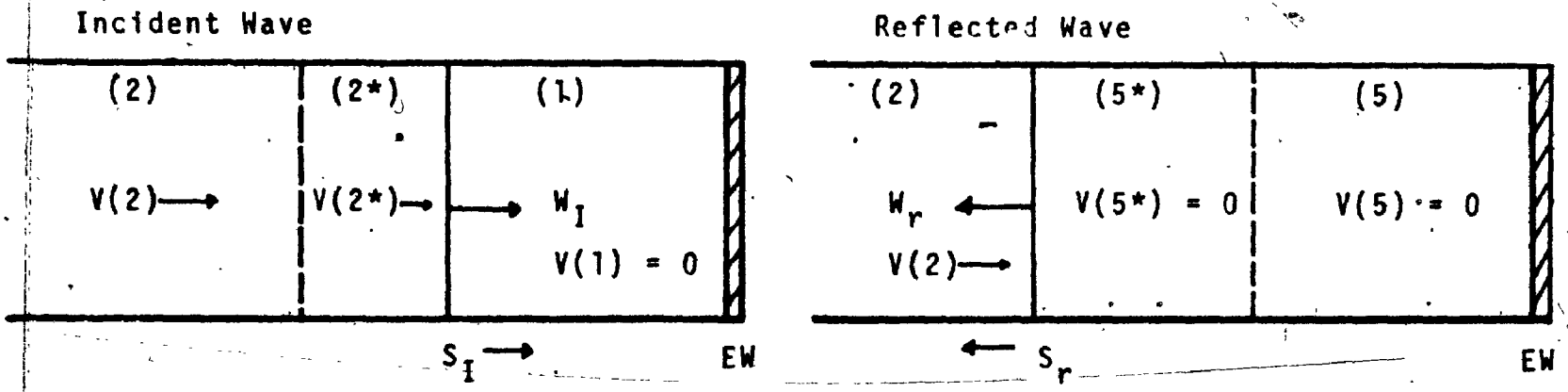

b) Referred to an Axis System Fixed in the Shock Front

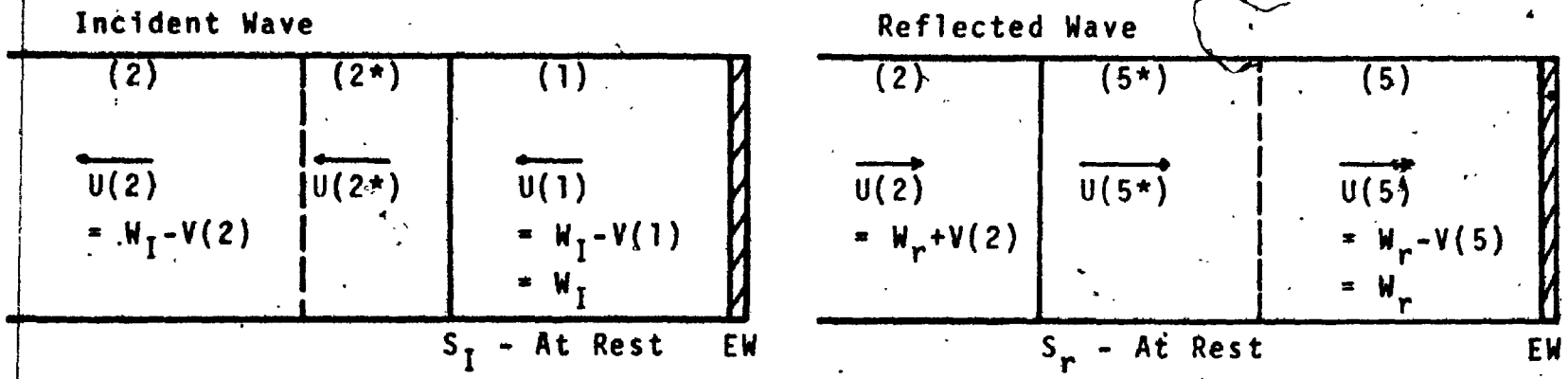

Figure 2-2

Particle Flow Velocities Before and After Normal Shock Reflection From a Rigid End Wall, EW.

(1), (2*) and (2) refer to states of local thermodynamic equilibrium discussed in the previous section. Normally, gas density, ρ, is measured in gm/cc; U in cm/sec; P in atmospheres; and h in cal/gm. Consistency of energy units in (2-11) demands that the kinetic energy terms, in ergs, be divided by the conversion factor $10^7 J$ (J = number of joules per calorie). This factor is included explicitly in later relations. ΔE_{D2} is the energy of the shocked gas that is used to produce equilibrium dissociation of the diatomic component, to vapourize any powdered sample and to produce complete chemical equilibrium in the reacting mixture.

Eq (2-9) requires $U_2 < U_{2*}$ as $\rho_2 > \rho_{2*}$. Consequently, particles in region (2) have less translational kinetic energy than those in (2*) and so $T_2 < T_{2*}$. Pressure ratios across the incident shock front can be obtained as functions of the density ratio for fixed initial parameters and the density ratio by combining Eq (2-9) and Eq (2-10) to yield

$$P_{k1} = 1 + \frac{\rho_1 U_1^2}{P_1} \left\{ 1 - \left(\frac{\rho_1}{\rho_k} \right) \right\} \quad (k=2*,2) \qquad (2\text{-}12)$$

Re-arrangement of (2-11) and substitution for U_k from (2-9) leads to

$$h_k - h_1 = \frac{U_1^2}{2.J.10^7} \cdot \left\{ 1 - \left(\frac{\rho_1}{\rho_k} \right)^2 \right\} - \Delta E_{Dk} \qquad (2\text{-}13)$$

with $\Delta E_{Dk} = 0$ when $k = 2*$.

The right-hand member of Eq (2-13) is a function of ρ_k

for pre-set initial conditions; the left-hand side can be considered predominantly a function of T_k. (h_k is a function only of T for ideal gases; ΔE_{Dk} depends upon values of T, [H], $[H_2]$ plus the sample material and its chemical derivatives). A rapidly convergent iteration scheme may be established if both sides of Eq (2-13) are treated separately as

$$\Delta h(T_k) = (h_k - h_1) \qquad (2\text{-}14)$$

$$\Delta h(\rho_k) = \frac{U_1^2}{2.J.10^7} \cdot \left\{ 1 - \left(\frac{\rho_1}{\rho_k} \right)^2 \right\} - \Delta E_{Dk} \qquad (2\text{-}15)$$

Acceptable values of the evaluated parameters result when

$$|\Delta h(T_k) - \Delta h(\rho_k)| < \xi$$

In this work ξ=0,02 was chosen as a reasonable compromise between suitable precision and computing time. T_k, ρ_k and P_k must satisfy the equation of state. Rewriting (2-1) in the form

$$P = n\left(\frac{RT}{V}\right) = \frac{m}{WM}\left(\frac{RT}{V}\right) = \rho\left(\frac{RT}{WM}\right) \qquad (2\text{-}16)$$

and applying the above simultaneously to regions (1) and (k) yields the expression

$$\rho_{k1} = \frac{P_{k1}}{T_{k1}} \cdot WM_{k1}$$

as the constraint linking density, pressure, temperature and molecular mass ratios. Owing to sample addition and dissociation, the molecular mass varies with region in the shocked gas flow. That variation, the appropriate values for ΔE_{Dk} and the mole fraction of each component were evaluated in a subroutine whose basis is described in section 2.4.

When trial values of ρ_{k1} and species concentrations are

known, Eq (2-13) can be solved iteratively to yield T_k. A new value of ρ_k can be obtained by taking the positive root of the quadratic

$$\rho_{k1}^2 - \left(\frac{WM_{k1}}{T_{k1}}\right)\left\{1 + \frac{\rho_1 U_1^2}{P_1}\right\}\rho_{k1} + \left(\frac{WM_{k1}}{T_{k1}}\right)\left\{\frac{\rho_1 U_1^2}{P_1}\right\} = 0 \qquad (2\text{-}17)$$

- which results from eliminating P_{k1} between Eq (2-12) and (2-16) - after a new set of concentration values, corresponding to temperature T_k, have been calculated.

Thus relations (2-9), (2-12), (2-13), (2-17) and others specifying the mixture composition form a set of coupled equations whose solution yields all the physical quantities of interest, once a reasonable set of starting values is available. The evaluation of those quantities and the iteration scheme used to determine accepted values for the shocked gas parameters is described fully in Appendix C.

2.4 Dissociative Equilibrium and Species Concentrations

The following discussion applies to gas mixtures in shock flow regions (2), (2*), (5*) and (5). Cases in which a powdered sample is present and those in which it is not are treated separately. Requisite input data are the initial conditions (in region (1)), species identity and values for P and T. The subscript k has been dropped as the chemical interactions are assumed to occur under isothermal conditions - i.e. refer to one region at a time.

2.4.1 Concentrations in the Absence of a Powdered Sample

In any region, at any time, the total pressure is given by

$$P = [H] + [H_2] + [Ar] \qquad (2\text{-}18a)$$

and $[H] \neq 0$ in regions (1) and (2*). In regions where equilibrium dissociation does occur, the chemical reaction

$$H + H \rightleftharpoons H_2$$

must conform to the Law of Mass Action (Davidson, 1962, pages 97-101) so that

$$K_{p1} = \frac{[H_2]}{[H]^2} \qquad (2\text{-}19)$$

K_{p1} is the equilibrium dissociation constant for Hydrogen referred to an atomic gas as thermodynamic reference state. K_{p1} has units atm^{-1} and is a function only of temperature for ideal gases.

K_{p1} was evaluated from thermochemical data. (Refer to Appendix C). Although H and H_2 concentrations are related by (2-19), another relation - between Argon and Hydrogen - is needed to allow explicit determination of the three quantities, [H], $[H_2]$ and [Ar]. The relation used comes from Gaydon (1966, page 290). It is a statement of the conservation of atoms across the shock front.

Before shock initiation, the number of Argon atoms relative to Hydrogen atoms in the test gas is (by Eq (2-1a))

$$\phi_1 = \frac{N_{Ar1}}{2N_{H_2 1} + N_{H1}} \equiv \frac{N_{Ar1}}{2N_{H_2 1}} = \frac{n_{Ar1}}{2n_{H_2 1}} = \frac{P_{Ar1}/RT_1}{2P_{H_2 1}/RT_1} = \frac{P_{Ar1}}{2P_{H_2 1}} = \frac{[Ar]_1}{2[H_2]_1}$$

At a later time, in shock flow zone k, this ratio must still have the same numeric value but then

$$\phi_1 = \frac{N_{Ar}}{2N_{H_2}+N_H} = \frac{[Ar]}{2[H_2]+[H]} \qquad (2\text{-}20a)$$

so that

$$[Ar] = \phi_1 \cdot \left\{ 2[H_2]+[H] \right\} .$$

Thus Eq (2-20a) and (2-19) can be combined with (2-18a) to yield a quadratic in [H] -

$$[H]^2 \cdot \left\{ (1+2\phi_1)K_{p1} \right\} + [H] \cdot \left\{ 1+\phi_1 \right\} - P = 0 \qquad (2\text{-}21a)$$

whose positive root yields the partial pressure of monatomic hydrogen. $[H_2]$ is then obtained from (2-19) and [Ar] from (2-20). The concentration of each component follows directly from (2-18).

2.4.2 Concentrations When a Powdered Sample Was Present

In the present work, spectroscopic observations were made near the end wall of the shock tube, transverse to the flow, so that only regions (2) and (5) were of experimental interest. Consequently, the effects of a powdered Magnesium sample upon those observations were treated in the following way.

At the instant the incident shock reached the end wall, the sample material was assumed to be completely vapourized, uniformly distributed throughout the compressed test gas and in thermochemical equilibrium with the other components. The

result of chemical reaction was to cause Mg and MgH to be the only metal-containing substances in the reacting mixture. (MgH_2 - the only other known binary hydride of magnesium - is unstable above 280°-300°C (Hurd, 1952, page 51). Mg_2 was excluded because its concentration, at the temperatures attained in these experiments, is negligible in comparison with that of MgH (Balfour, 1970). Finally, no spectra of other know magnesium compounds was found in the records subjected to quantitative photometry.)

The presence of Mg and MgH in the test gas mixture necessitates modification of equations (2-18a), (2-20a) and (2-21a). For example, the expression for the total pressure becomes

$$P = [H] + [H_2] + [A_r] + [Mg] + [MgH] \qquad (2\text{-}18a)$$

Magnesium and Magnesium Monohydride concentrations, determined by the reaction

$$H + Mg \rightleftarrows MgH \ ,$$

must be related via

$$K_{p2} = \frac{[MgH]}{[Mg][H]} \qquad (2\text{-}22)$$

according to the Law of Mass Action. K_{p2} (the dissociation constant for MgH referred to the 'separated atoms' thermodynamic reference state) is constant at a specified temperature. Consequently,

$$[MgH] = K_{p2} \cdot [Mg][H] \qquad (2\text{-}23)$$

Across the shock fronts, relative numbers of Mg and H must be conserved, Thus

$$\phi_2 = \frac{[Mg] + [MgH]}{2[H_2]+[H]+[MgH]} \qquad (2\text{-}24)$$

must be constant. ϕ_2 has a numeric value, (via Gaydon's relation, noted previously) determined by the pre-shock conditions, as

$$\phi_2 = \frac{n_{Mg1}}{2n_{H_2 1}}$$

An expression for [Mg] as a function only of [H] and temperature is obtained as

$$[Mg] = \phi_2[H] \cdot \left\{ \frac{1 + 2K_{p1}[H]}{1 + K_{p2}[H](1-\phi_2)} \right\} \qquad (2\text{-}25)$$

by elimination of [MgH] between equations (2-23) and (2-24), following some algebraic re-arrangement and substitution for the $[H_2]$ term from (2-19).

ϕ_1 must be modified owing to the presence of sample material for Hydrogen atoms are present in the MgH molecule. The correct expression is

$$\phi_1 = \frac{[Ar]}{2[H_2]+[H]+[MgH]} \qquad (2\text{-}20b)$$

Finally, a quadratic expression for [H] may be reduced to the form

$$[H]^2 K_{p1}^2 \cdot \left\{ 1 + 2\phi_1 + 2\phi_2 \right\} + [H] \left\{ 1 + (\phi_1+\phi_2)(1+K_{p2}[Mg]) \right\} - P=0 \qquad (2\text{-}21b)$$

by manipulation of Eq (2-18a), (2-19), (2-20b) and (2-24). Clearly relations (2-20b) and (2-21b) are identical with (2-20a)

and (2-21a) in the absence of sample material (i.e. ϕ_2=[Mg]=0).

In the experimental work, only a small amount of sample material was used. Consequently the $K_{p2}\cdot$ [Mg] term in relation (2-21a) was considerably less than unity. Thus Eqs (2-21b) and (2-25) were solved iteratively as a coupled pair to yield accepted values for [Mg] and [H]. The remaining partial pressures were determined: [MgH] from (2-22); [H_2] from (2-19); and [Ar] from (2-20b). Once again concentrations were found from Eq (2-1a).

2.4.3 Evaluation of ΔE_{Dk}

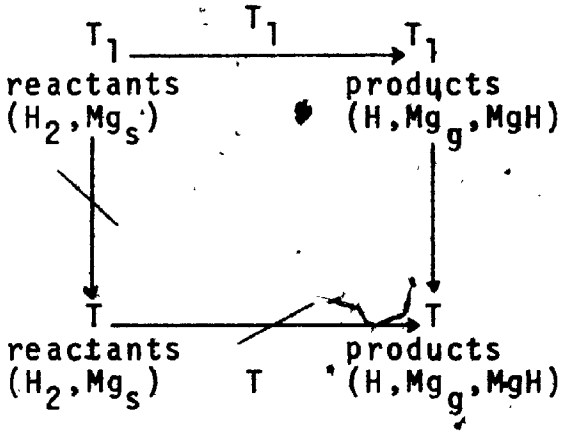

The indicated cycle was used to set up the necessary thermochemical calculations. It purports to show two (of the large number of) paths for taking the initial Channel components to the end state of temperature T. As the present treatment considers only equilibrium end states, the changes in thermodynamic properties of the reacting mixture must be path-independent (Davidson, 1962). Thus, as the diagram indicates, the reactants might be heated to T and then allowed to react isothermally to give the products at the "observed" final conditions; or the reactants could be treated as reacting at the initial temperature, T_1, to give products in the concentrations found in the

final state followed by heating of these products to the final temperature, T. The second alternative was chosen as a basis for computation for it replaces the evaluation of heats of reaction at all T values with one calculation at T_1.

In the absence of sample material, the only reaction of interest is

$$\frac{1}{2}(H_2)_g \xrightarrow{T_1} (H)_g$$

which requires a dissociation energy $(D^\circ_{T_1})_H$ = 52097.7 cal/mole H formed (Heimel et al, 1963). When a magnesium sample is present, two other reactions are important

$$(Mg)_s \xrightarrow{T_1} (Mg)_g$$

with a heat of sublimation $(D^\circ_{T_1})_{Mg}$ = 35,600.0 cal/mole and

$$(Mg)_g + (H)_g \rightarrow (MgH)_g$$

with a heat of reaction $(D^\circ_{T_1})_{MgH}$ = -46,987.5 cal/mole at 25°C (Heimel et al, 1963). Their effects may be summarized with reference to the cycle. In the formation of products from reactants at T_1=298.15°K: ~52 Kcals of energy must be supplied to produce one mole of Hydrogen atoms; ~35.6 Kcals of energy are employed to vapourize one mole of the solid sample; ~47 Kcals of energy are returned per mole of MgH formed by chemical reaction of previously produced atoms. The remaining change in enthalpy is due to heating of products from T_1 to T.

Therefore one gram of the shock-heated mixture (products)

at temperature T has an enthalpy, $h_p(T)$, greater than it has as reactants (before shock excitation) at Temperature T_1, $h_r(T_1)$, by an amount

$$\Delta h = h_p(T) - h_r(T_1) = \frac{\sum X_i \cdot (\bar{H}_i(T) - \bar{H}_i(T_1))}{WM(T)}$$

X_i is the mole fraction and $H_i(T)$ the molar enthalpy of component i at temperature T. They and WM are all temperature dependent.

$$\Delta h = \frac{1}{WM(T)} \left\{ \begin{array}{l} X_{Ar} \cdot (\bar{H}_{Ar}(T) - \bar{H}_{Ar}(T_1)) + X_{H_2} \cdot (\bar{H}_{H_2}(T) - \bar{H}_{H_2}(T_1)) \\ + X_H \cdot (\bar{H}_H(T) - \bar{H}_H(T_1) + (D^o_{T_1})_H) \\ + X_{Mg} \cdot (\bar{H}_{Mg}(T) - \bar{H}_{Mg}(T_1) + (D^o_{T_1})_{Mg}) \\ + X_{MgH} \cdot (\bar{H}_{MgH}(T) - \bar{H}_{MgH}(T_1) + (D^o_{T_1})_{Mg} + (D^o_{T_1})_{MgH} + (D^o_{T_1})_H) \end{array} \right\}$$

$$\Delta h = h_p(T) - h_p(T_1) + \frac{1}{WM(T)} \left\{ (D^o_{T_1})_H \cdot (X_H + X_{Mg}) + (D^o_{T_1})_{Mg} \cdot (X_{Mg} + X_{MgH}) + (D^o_{T_1})_{MgH} \cdot (X_{MgH}) \right\}$$

$$\Delta h = h_p(T) - h_p(T_1) + \Delta E_{Dk} \qquad (2\text{-}26)$$

where, using the definition of mole fraction, X, in terms of partial pressures given in Eq (2-3),

$$\Delta E_{Dk} = \frac{1}{WM(T)} \left\{ \begin{array}{l} (D^o_{T_1})_H \cdot \left(\frac{[H]+[MgH]}{P}\right) + (D^o_{T_1})_{Mg} \cdot \left(\frac{[Mg]+[MgH]}{P}\right) \\ + (D^o_{T_1})_{MgH} \left(\frac{[MgH]}{P}\right) \end{array} \right\} \qquad (2\text{-}27b)$$

The enthalpy change implied in Eq (2-11) is identical with the

definition of (2-26), i.e. h_k refers only to contributions from the species present in the heated mixture.

The first two terms of relation (2-27b) represent kinetic energy decrease caused by the formation of gaseous atoms; the third term corresponds to a kinetic energy increase as some of these atoms undergo exothermal chemical reaction to produce gaseous MgH molecules. Eq (2-27b) simplifies to

$$\Delta E_D = \frac{1}{WM(T)} \cdot (D^o_{T_1})_H \frac{[H]}{P} \qquad (2\text{-}27a)$$

in the absence of an added, powdered sample. In region k, ΔE_D becomes ΔE_{Dk}.

2.5 Parameter Values in the Region of the Reflected Shock

Referred to a co-ordinate system fixed in the reflected shock (see Fig. 2.2), equations expressing the conservation of mass, momentum and energy for unit mass of material adiabatically passing through the reflected shock front take the form given by Lapworth (1969) -

Mass: $$\rho_k U_k = \rho_2 (U_k + V_2) \qquad (2\text{-}28)$$

Momentum: $$P_k + \rho_k U_k^2 = P_2 + \rho_2 (U_k + V_2)^2 \qquad (2\text{-}29)$$

Energy: $$h_k + \frac{1}{2}U_k^2 + \Delta E_{Dk} = h_2 + \frac{1}{2}(U_k + V_2)^2 + \Delta E_{D2} \qquad (2\text{-}30)$$

except for the energy expression, which has been modified (Gaydon & Hurle, 1963) to account for dissociation and chemical reactions. V_2 is the particle speed in the totally

equilibrated region behind the incident shock front referred to a laboratory-fixed reference frame. The subscript k now takes the value 5* or 5. $\Delta E_{D5*} = \Delta E_{D2}$ as dissociation and chemical reaction in region (5) are frozen at their values in region (2). Complete equilibration behind the reflected shock occurs only in region (5).

All parameters of interest behind the reflected shock may be expressed as functions of density and temperature by a treatment similar to that given for the incident shock case. For example, the particle speed relative to the shock front becomes

$$U_k = U_1 \left\{ \frac{\rho_{21}-1}{\rho_{k1}-\rho_{21}} \right\} \qquad (2\text{-}31)$$

after combining Eq (2-8c), (2-9) and (2-28). (From Figure 2-2, it is clear that the reflected shock speed, W_r, equals U_{5*}.) The ratio of test gas pressure behind the reflected shock to its pre-shock value is found to be

$$P_{k1} = 1 + \left(\frac{\rho_1 U_1^2}{P_1}\right)\left\{\frac{\rho_{21}-1}{\rho_{21}}\right\}\left(1 + \rho_{k1}\frac{U_k}{U_1}\right) \qquad (2\text{-}32)$$

- a result of combining the contents of Eq (2-10), (2-28), (2-29) and (2-31). Change in test gas enthalpy from its initial value to the value in region (k) may be written as

$$h_k - h_1 = \frac{U_1^2}{2.Jx10^7}\left\{\left(1-\left(\frac{\rho_1}{\rho_2}\right)^2\right)+\left(1-\frac{\rho_1}{\rho_2}\right)\left(1+\frac{\rho_{k1}}{\rho_{21}}\right)\left(\frac{U_k}{U_1}\right)\right\} - \Delta E_{Dk} \qquad (2\text{-}33)$$

by an algebraic manipulation of Eqs (2-11), (2-28), (2-30) and (2-31). The right hand sides of these last three equalities

(except for the ΔE_{Dk} term) are functions only of the density in region (k) as ρ_{21} has already been evaluated in terms of the initial variables and U_1.

By treating the left hand and right hand members of Eq (2-33) separately as was done for Eq (2-13) - the corresponding expression for the incident shock - a rapidly convergent iteration scheme was set up for the variables T_k and ρ_k. When an improved estimate for T_k was obtained from Eq (2-33), and new values for species concentrations obtained, a revised value for ρ_k was found from

$$\rho_{k1}^2 \left\{\frac{T_{k1}}{WM_{k1}}\right\} - \rho_{k1}\left\{(1-\frac{\rho_1 U_1^2}{P_1})+\rho_{21}(\frac{T_{k1}}{WM_{k1}} + \frac{\rho_1 U_1^2}{P_1})\right\} - \left\{\frac{\rho_1 U_1^2}{P_1}-\rho_{21}(1+\frac{\rho_1 U_1^2}{P_1})\right\}=0 \qquad (2\text{-}34)$$

Eq (2-34) arises from elimination of P_{k1} between relations (2-16) and (2-32). This system of equations was iterated until the difference between left and right sides of Eq (2-33) was less than 0.02 cal/gm in magnitude. As (h_k-h_1) takes values of 100-900 cal/gm in typical cases, such a termination scheme led to no significant error.

Once acceptable values for ρ_k and T_k had been found, values of the other parameters followed from (2-31), (2-32) and the equations governing mixture composition.

2.6 Results

A rather comprehensive computer program has been written and made functional on an IBM 1130, 16K machine. With it,

equilibrium properties behind the incident and reflected shock can be evaluated. The effects of an added powdered sample material upon the temperature, pressure and density in the equilibrated regions behind incident and reflected shock have been investigated. All estimated temperature values, associated with the spectra displayed in later chapters, were obtained from this shock-tube computer programme.

Convergence of this programme is rapid and successive temperature estimates at the end of an iteration scheme agree within 0.5K° of each other over the interval $1000<T<6000°K$. The precision of the computed results is not machine limited. Rather, it must be assessed carefully in terms of: a) the accuracy with which the input thermochemical data is known; and b) the precision associated with incident shock speed measurements.

As the amount of chemical reaction depends greatly upon the dimensions of particular shock tube facilities, initial loading pressures, test gas composition and mole fraction of sample materials, no attempt has been made to produce generalized charts for properties of shock-heated mixtures. Instead, the information illustrated by figures 2-3 to 2-12 refers to conditions actually employed in the present study.

Figure 2-3 shows the values of initial pressure ratio, P_{41}, needed to produce shocks of given speed in Argon-Hydrogen mixtures at constant P_1 with a Hydrogen driver gas. Similar data are depicted in Figure 2-4 for a constant composition

test gas mixture at several initial loading pressures. Figure 2-5 illustrates the effect of added powdered sample materials upon P_{41} for a fixed composition test-gas mixture at one initial loading pressure. The ratio, P_{41}, was evaluated using

$$P_{41} = P_{21}\left\{1 - \frac{(\gamma_4 - 1)}{2}\cdot\left(\frac{V_2}{a_4}\right)\right\}^{\left(\frac{-2\gamma_4}{\gamma_4 - 1}\right)} \qquad (2\text{-}35)$$

(Nagamatsu, 1961) with V_2 the flow speed of the equilibrated, dissociated gas mixture behind the incident shock. Suitable sets of initial loadings, P_1 and P_4, were determined from the desired incident shock speed and Eq (2-35) at several initial test gas pressures and concentrations, but subject to the physical limitations of the available shock tube and diaphragm material. As relation (2-35) presupposes instantaneous diaphragm removal and makes no allowance for the finite distance necessary for shock formation, it was expected that the calculated loadings would yield shocks of lower speed than Eq (2-35) would indicate. This expectation was met as chapter 4 will show.

In the present work, the shock tube has been used as a heat bath of known temperature in the reflected shock zone. Thus the variation of temperature, T_5, is shown as a function of initial $Ar:H_2$ concentrations at fixed initial pressure in Fig. 2-6; and as a function of initial pressure and variable $Ar:H_2$ concentrations in Fig. 2-7.

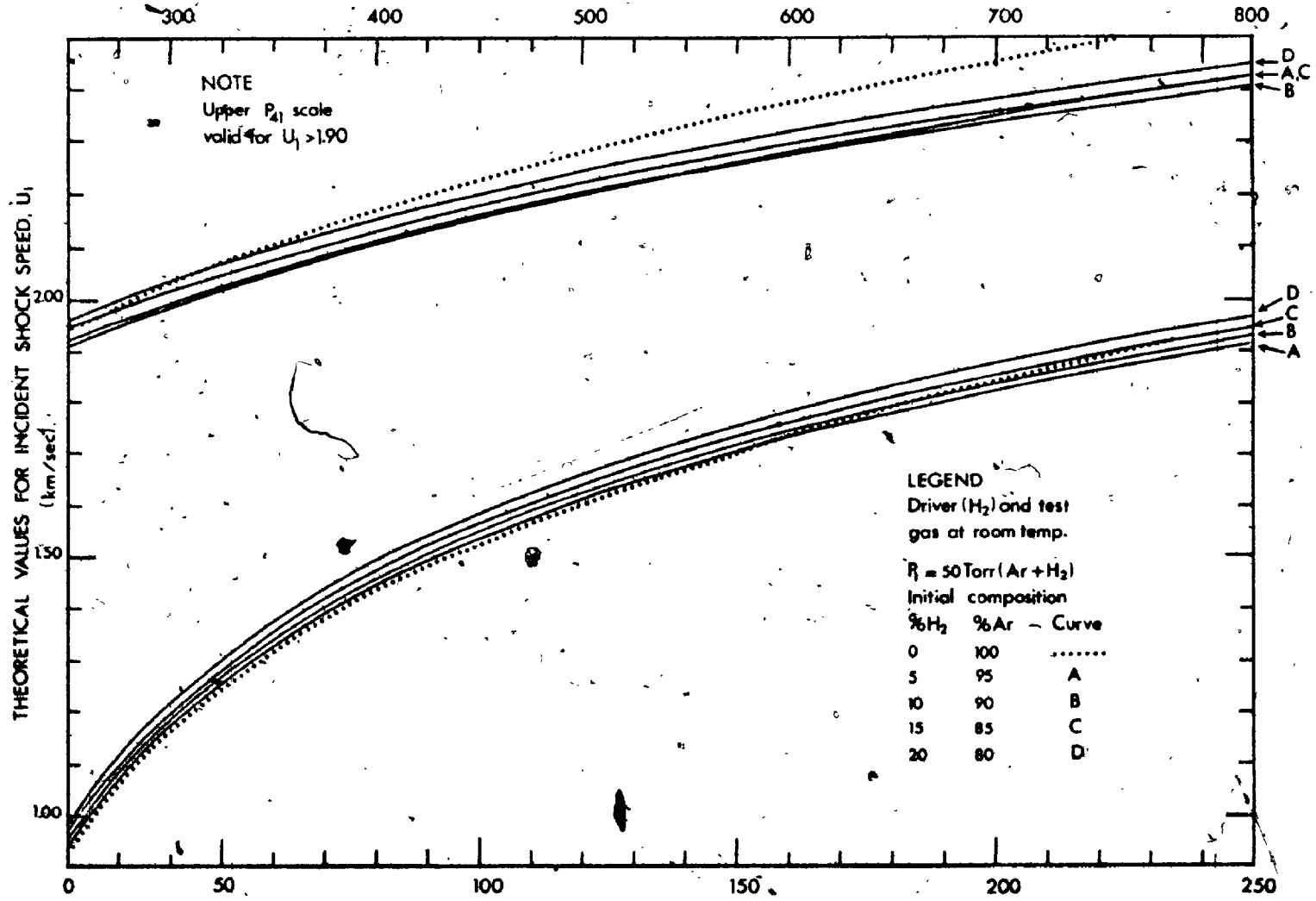

FIGURE 2-3

VALUES OF U_1 AS A FUNCTION OF P_{41} FOR FIVE TEST GAS INITIAL COMPOSITIONS

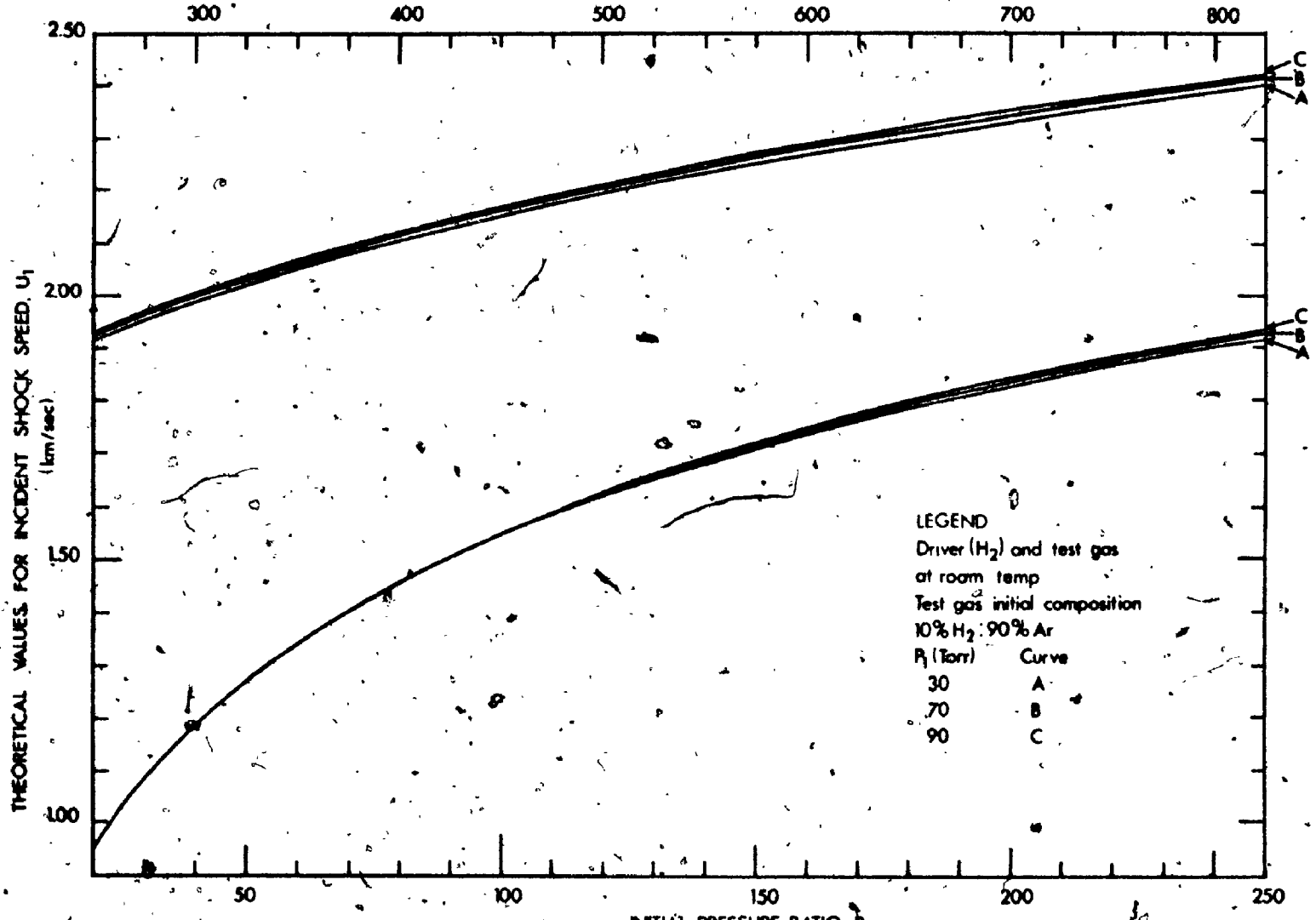

FIGURE 2-4

U_1 AS A FUNCTION OF P_{41} FOR SEVERAL TEST GAS INITIAL PRESSURES AT FIXED COMPOSITION

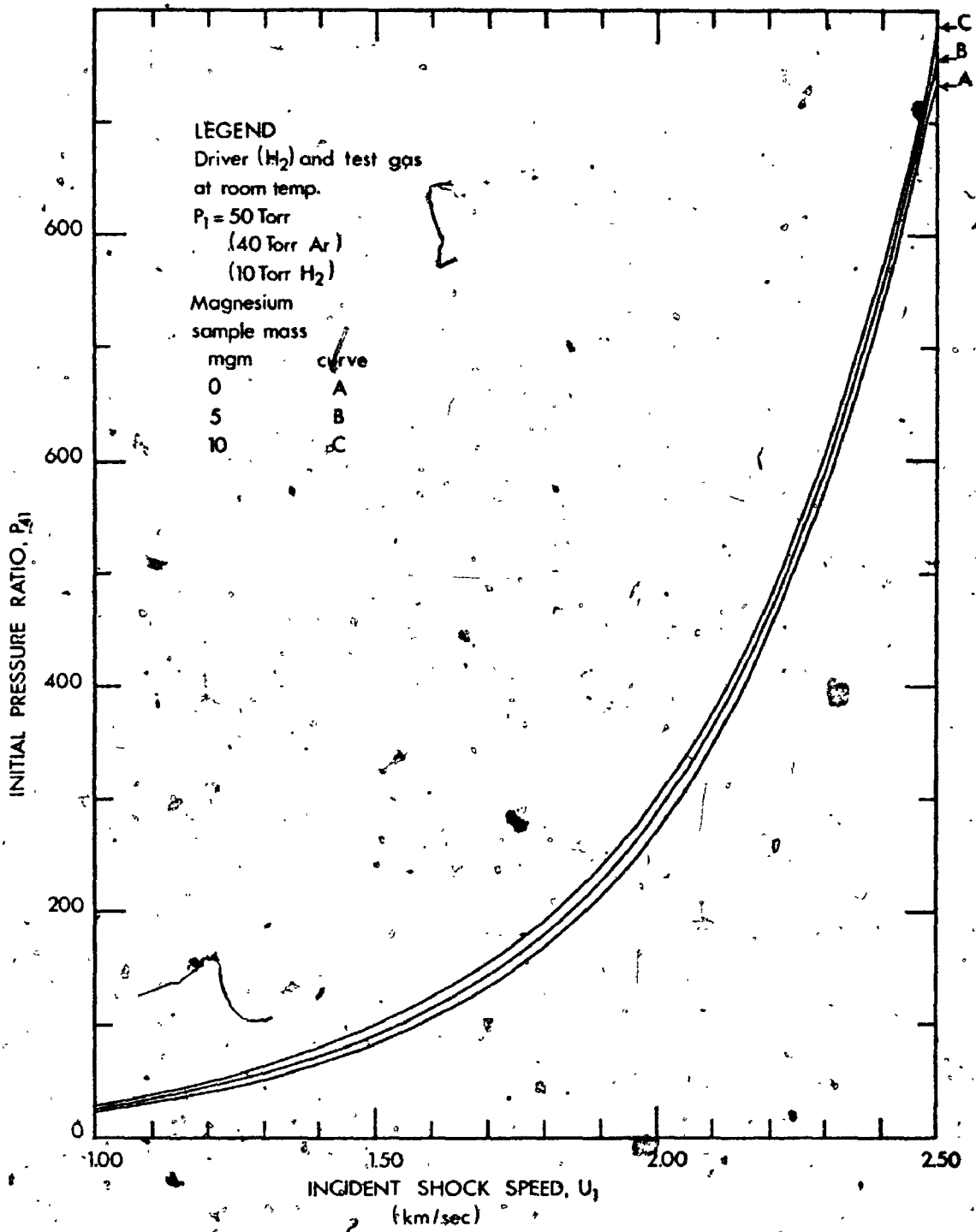

FIGURE 2-5

EFFECT OF POWDERED SAMPLE SIZE UPON THE P_{41} VALUE REQUIRED TO YIELD SHOCKS OF PRE-DETERMINED SPEED

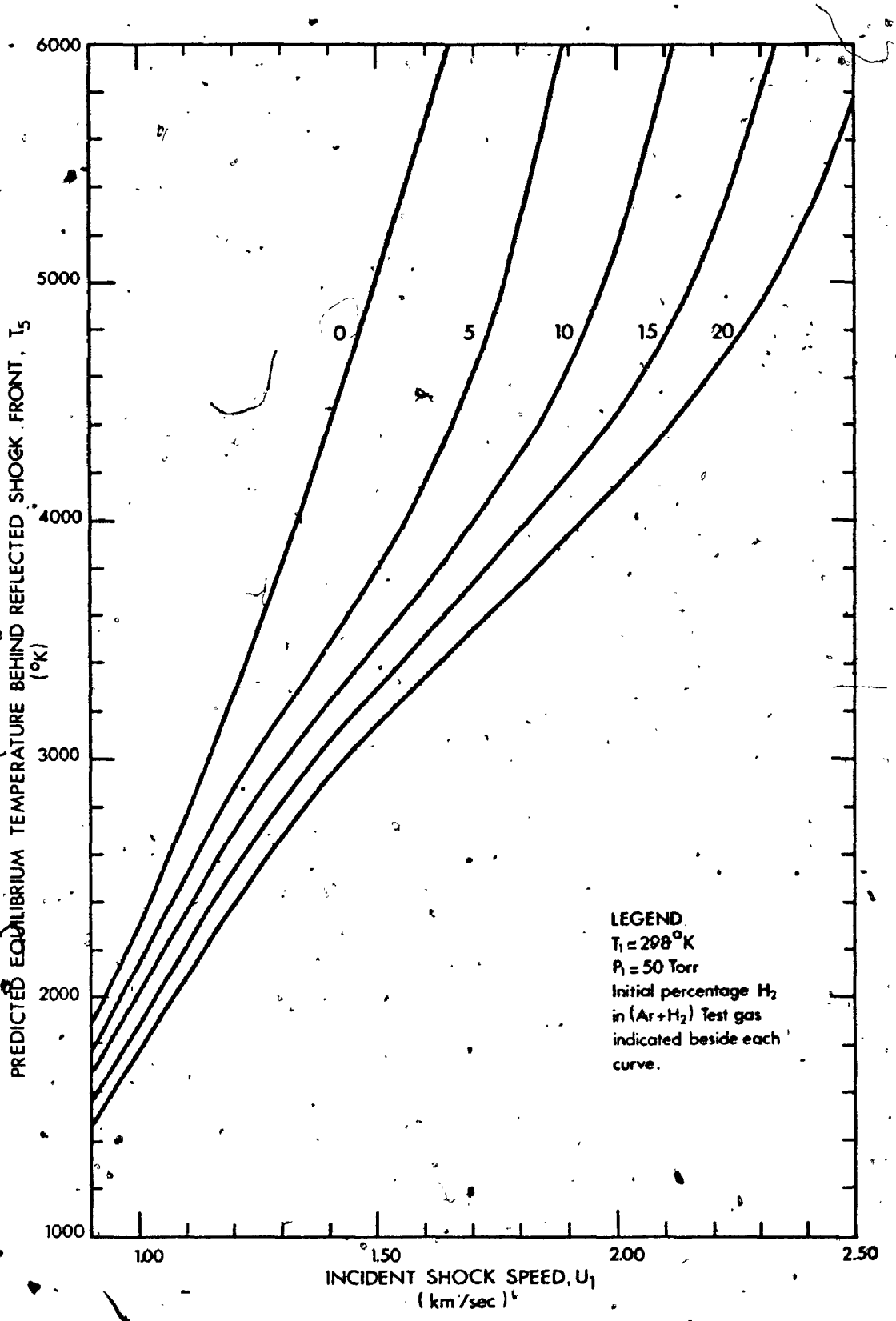

FIGURE 2-6

VARIATION OF T_5 WITH U_1 FOR SEVERAL TEST GAS COMPOSITIONS

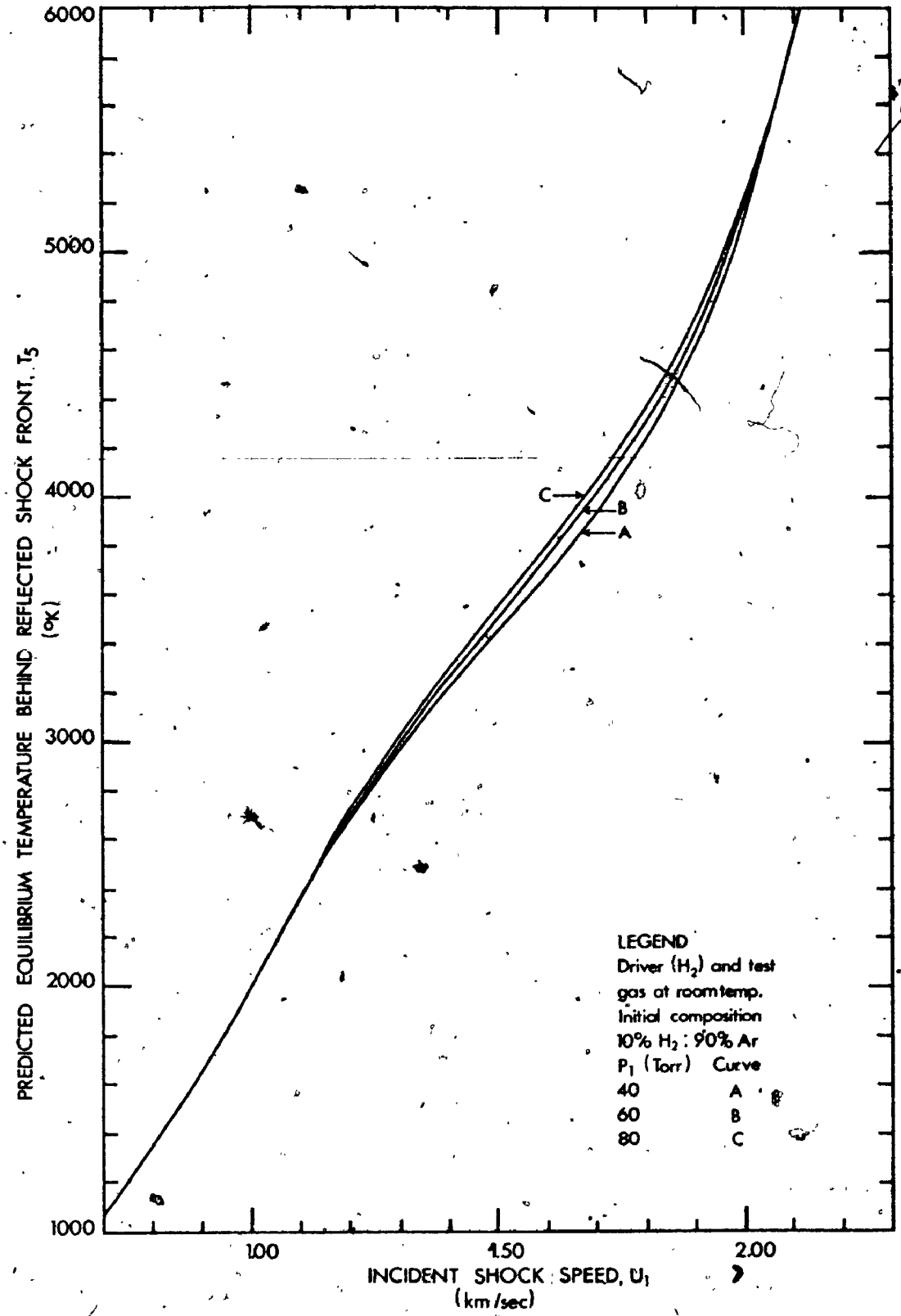

FIGURE 2-7.
T_5 AS A FUNCTION OF U_1, FOR FIXED TEST GAS INITIAL COMPOSITION AT SEVERAL LOADING PRESSURES.

Figure 2-8 shows the calculated reflected shock speed, W_r, as a function of incident shock speed U_1, for various Hydrogen fractions in the test gas mixture at one initial pressure, while Figure 2-9 shows the rate at which region (5) builds out from the end wall. Values of W_r were used to determine appropriate delay-times for absorption flash synchronization when studying material heated by the reflected shock.

Changes in T_5 due to addition of Mg, Al and Be powder samples are shown in Figs. 2-10 to 2-12 for typical shock excitation conditions. The range of sample masses (0-13 mgm) overlaps those used in the present experimental work. For all three sample materials, T_5 is lower than in the no-sample case. This lowering amounts to ~5% for samples as small as 1 mgm of Beryllium, 5 mgm of Aluminium and 10 mgm of Magnesium. There are two principal contributions to the more pronounced temperature lowering by Al and Be: a) Al and Be have heats of sublimation about twice that of Mg at room temperature and greater specific enthalpies in the gaseous state; b) the molar mass of Beryllium is much lower than that of either Al or Mg and so a given Be sample mass requires more energy for its ablation than does Al or Mg.

The effects illustrated in Figure 2-5, as well as the temperature and density variations, are in the same direction as those discussed by Nayfeh (1966) for ablating Teflon spheres. He calculated the time history of the entire ablation process from sample addition to equilibration in the absence of chem-

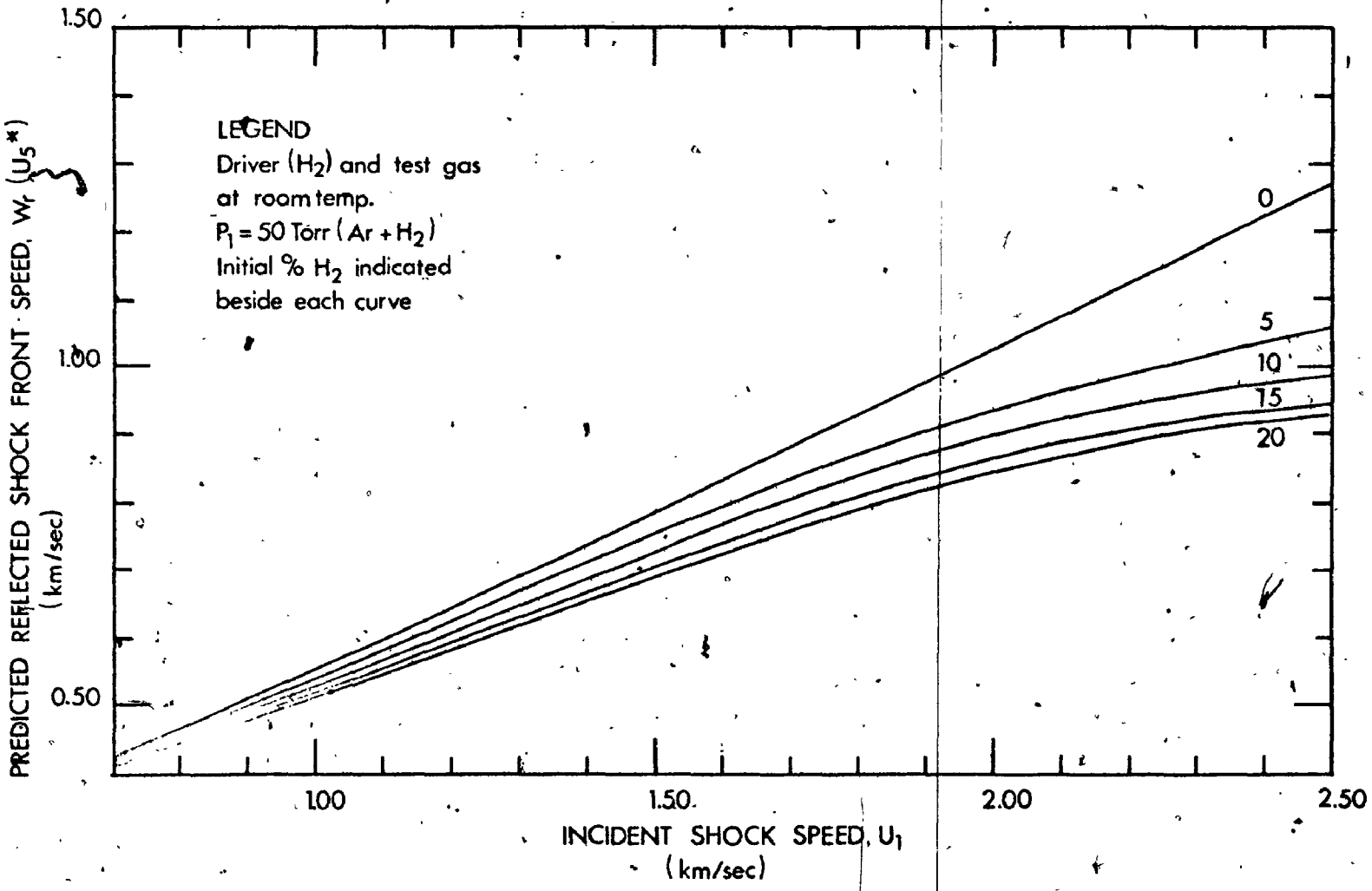

FIGURE 2-8

THEORETICAL DEPENDENCE OF W_r ON INITIAL TEST GAS COMPOSITION FOR INCIDENT SHOCKS OF PRE-DETERMINED SPEED.

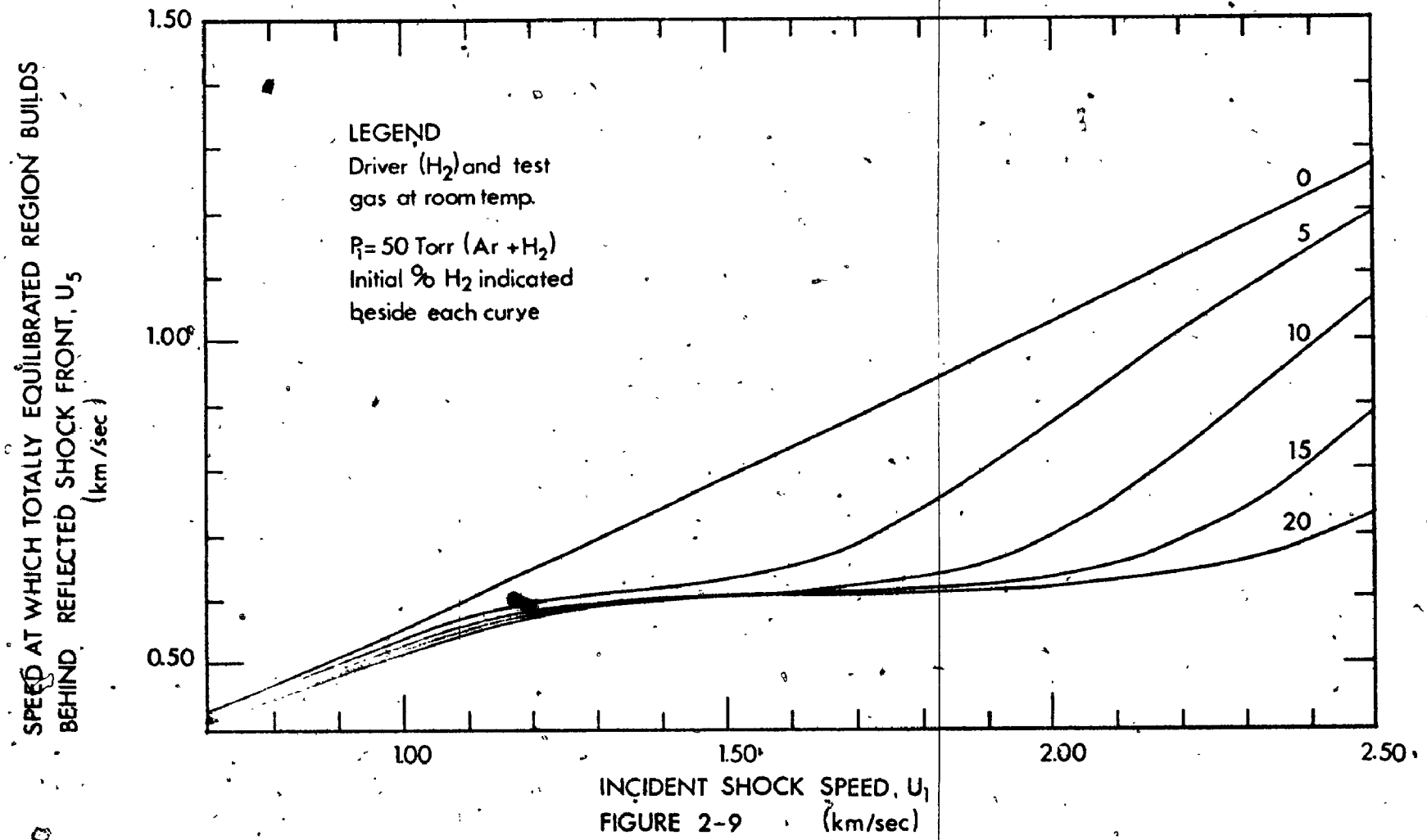

FIGURE 2-9

THEORETICAL VALUES FOR U_5 AS A FUNCTION OF INITIAL TEST GAS COMPOSITION FOR INCIDENT SHOCKS OF GIVEN SPEED.

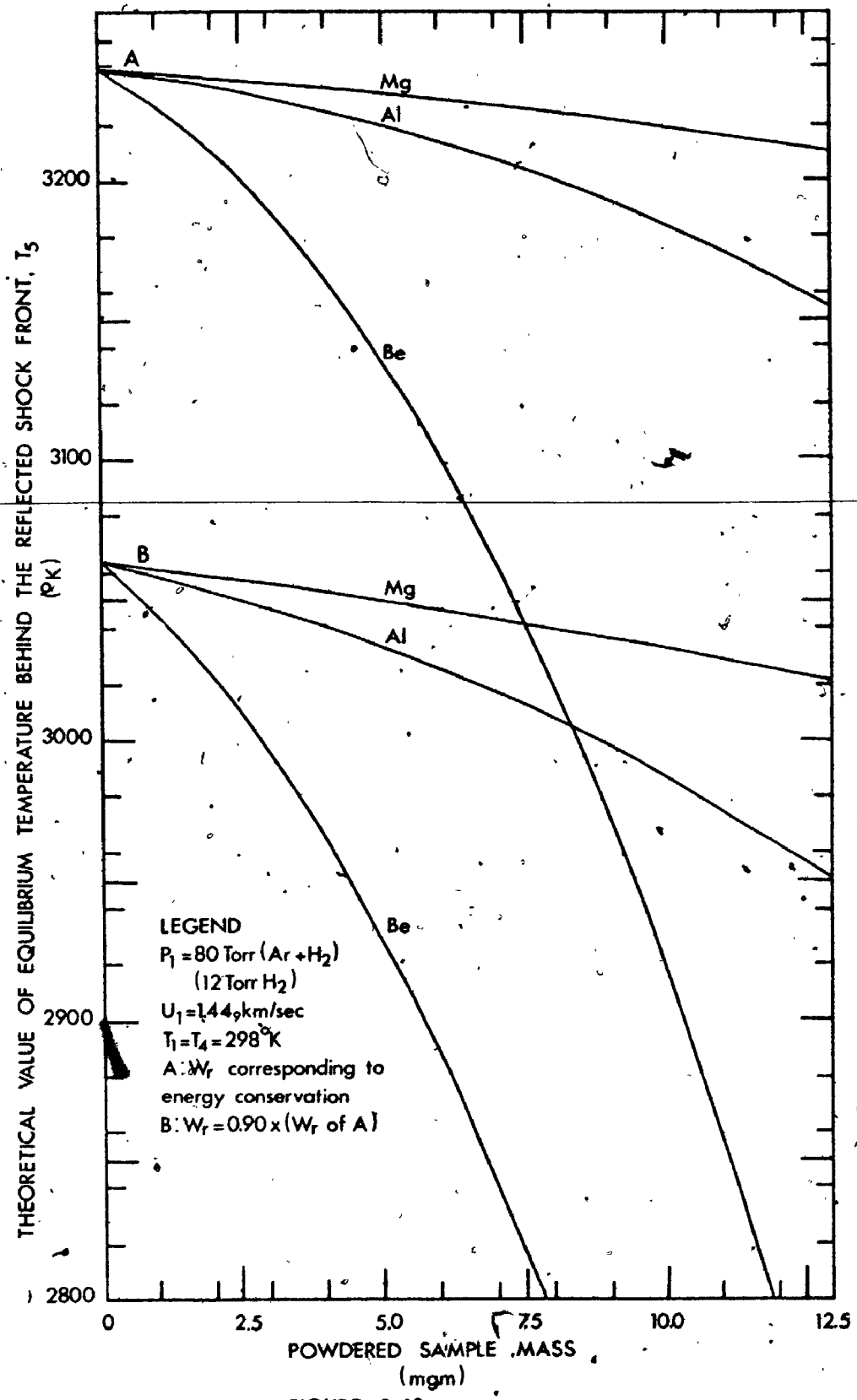

FIGURE 2-10

T_5 VALUES FOR THE SAME SHOCK-EXCITED TEST GAS TO WHICH DIFFERENT POWDERED SAMPLES HAVE BEEN ADDED

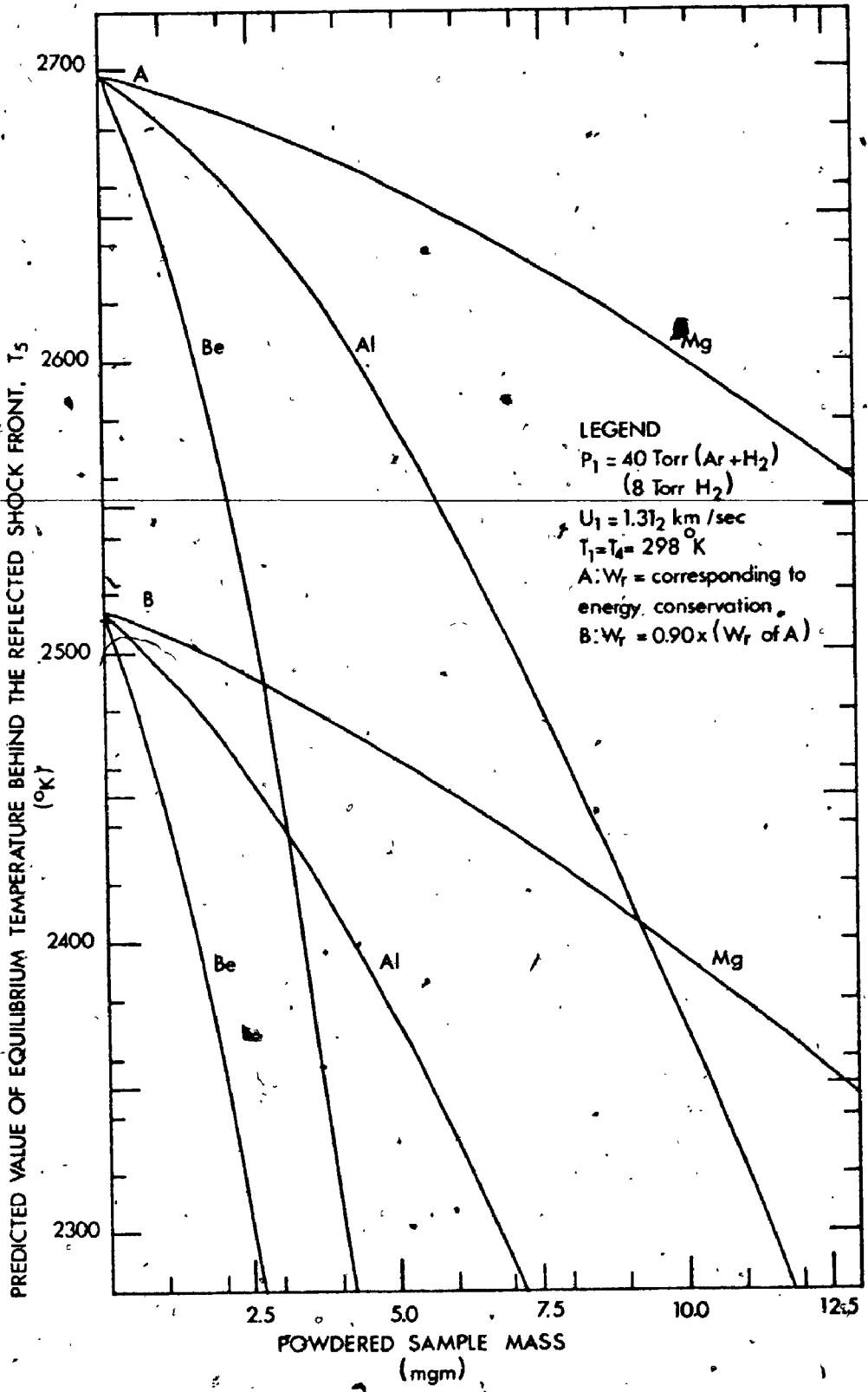

FIGURE 2-11

VARIATION OF T_5 WITH SAMPLE ADDITION FOR THE SAME SHOCK-EXCITED TEST GAS MIXTURE

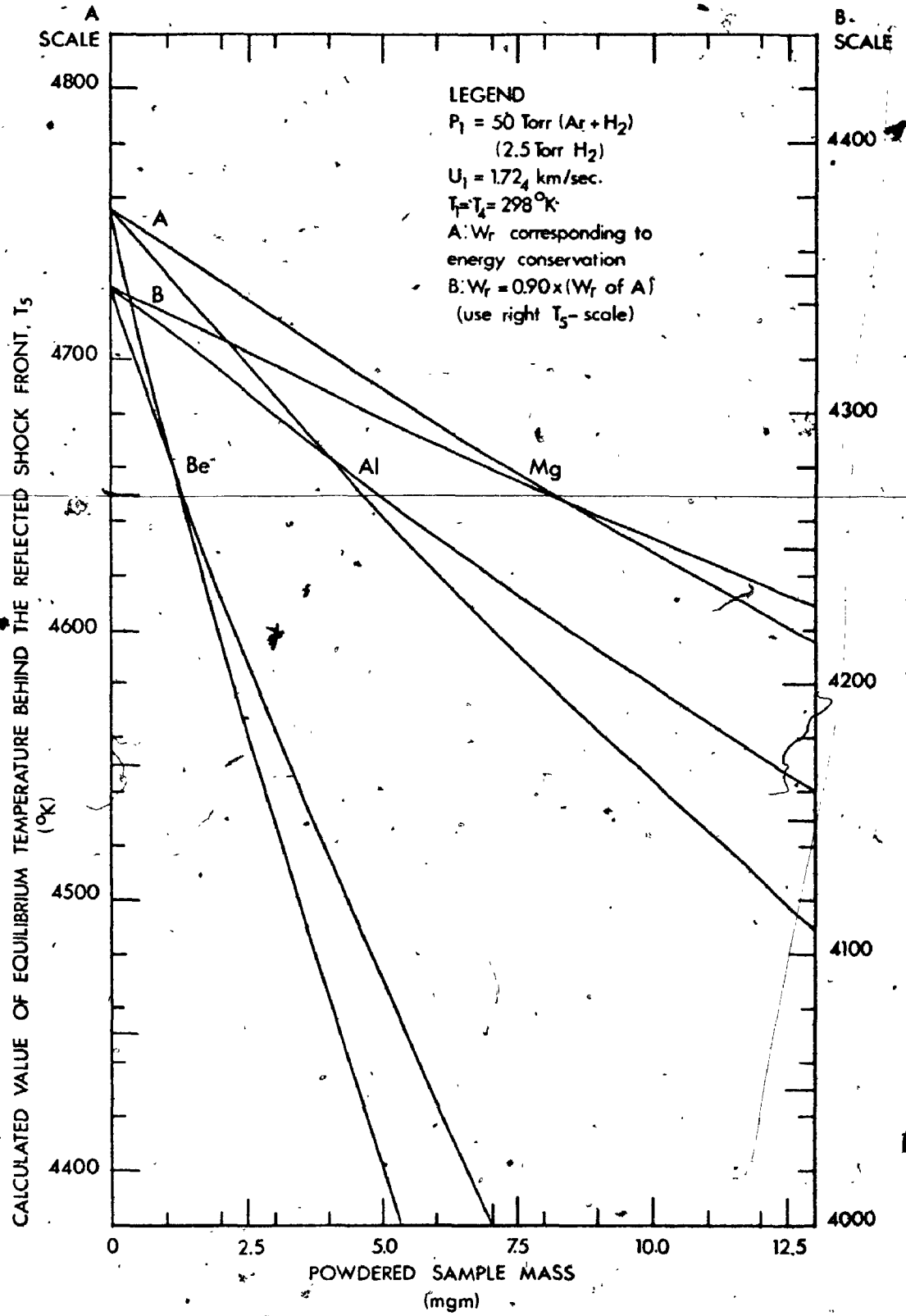

FIGURE 2-12

T_5 AS A FUNCTION OF ADDED SAMPLE FOR THE SAME SHOCK-EXCITED TEST GAS MIXTURE

ical reaction.

Here, only the equilibrated regions are treated, but equilibrium chemistry has been included. Also present in this last group of figures is an estimate of the change to be expected in T_5 when the reflected shock returns with a velocity only 90% of its predicted value, i.e. when energy is no longer conserved.

CHAPTER 3

EXPERIMENTAL

The experimental equipment and techniques employed to generate shock waves, to determine their velocities, to record the resultant shock-excited spectra and to reduce this data quantitatively are described in the appropriate sections below.

3.1 Shock Tube and Accessories

The addition of platinum resistance thermal probes as shock front detectors (described in section 3.1.3) has been the only major alteration to this facility since it was described previously (McGregor, 1962). Therefore, only a brief description of the shock tube, routine operating procedure, and peripheral equipment will be given here.

3.1.1 The Shock Tube

A pressure driven copper shock tube of constant, circular - 2" I.D. (nominal) - cross-section was used. It was made in four sections: one for the chamber (the high pressure section), three for the channel (the low pressure or test section). These sections were interconnected with 2" I.D., 6" face diameter, companion flanges separated by 1/16" rubber gaskets which provided vacuum tight seals. Both ends of the

shock tube were terminated with brass fittings. Mylar polyester film, 0.002" thick, served as the diaphragm material separating high and low pressure sections. One layer of this film ruptured consistently at 63±3 psia of Hydrogen and 55±1 psia Helium in the chamber when the channel pressure was <0.05 Torr. The copper tube safe working pressure rating - 450 psia - was never exceeded. Chamber pressures of 60 to 450 psia were sustained by using multiple Mylar layers.

Hydrogen or Helium gas - depending upon the experiment - was admitted to the chamber through $^1/_4$" copper tubing fitted to the brass end cap. (Refer to Fig. 3-1.) High pressure was measured with a Heise bourdon-type pressure gauge (accuracy ±0.5 psia) equipped with a peak load indicator that recorded the pressure at which the diaphragm ruptured.

One of the three channel sections was mounted permanently on a Dexion framework. (Consult Fig. 3-2.) To this section were attached the vacuum pump outlet, gas inlet, air vent, sample holder, and vacuum gauges. Channel pressure was monitored with a vacustat - for pressures below 10 Torr - and a mercury manometer. The longer of the remaining sections was inserted between the chamber and the permanently mounted portion of the channel. (Fig. 3-1 gives dimensions and Fig. 3-2 a photograph of the test section.) Use of this removable section offered two advantages. The first was an increase in

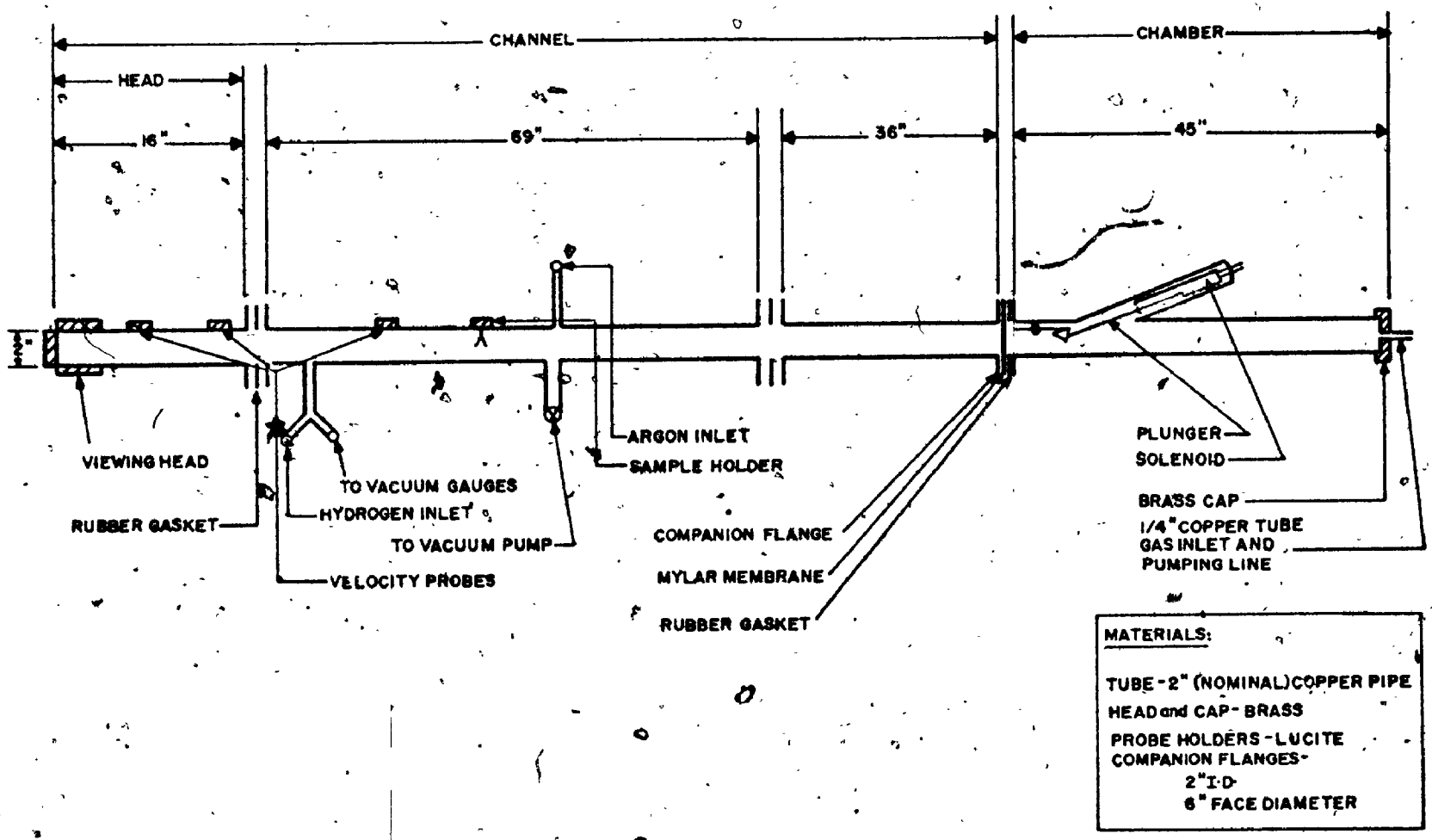

Fig. 3.1 Diagram of Assembled 2" Copper Shocktube Indicating Dimensions

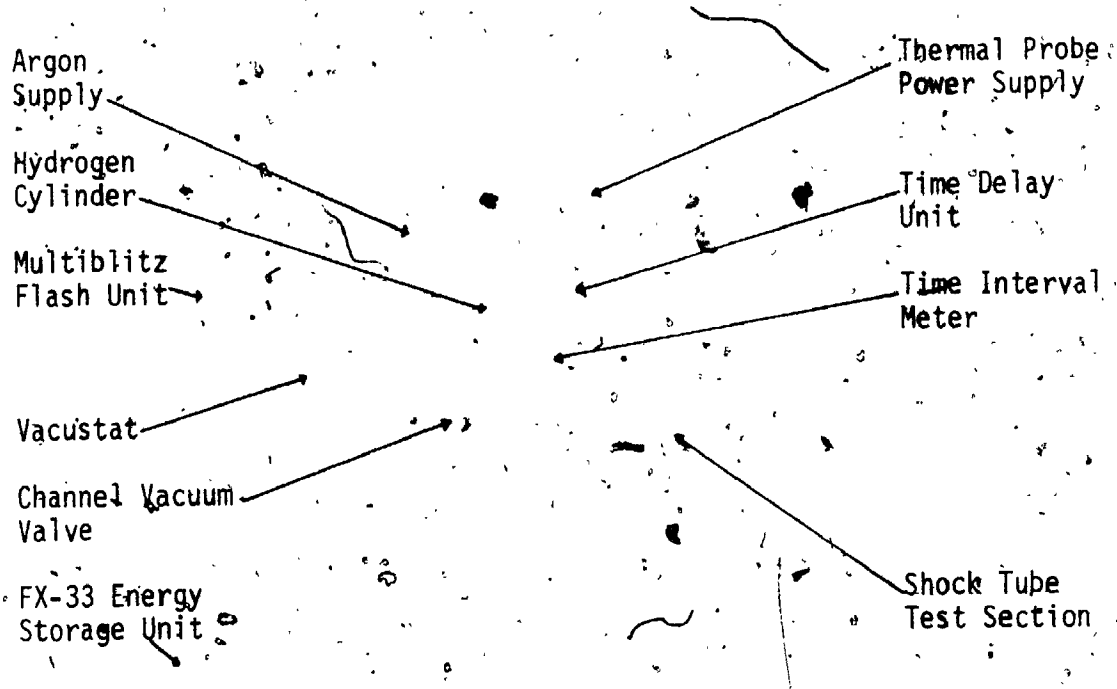
Argon Supply
Hydrogen Cylinder
Multiblitz Flash Unit
Vacustat
Channel Vacuum Valve
FX-33 Energy Storage Unit
Thermal Probe Power Supply
Time Delay Unit
Time Interval Meter
Shock Tube Test Section

Figure 3-2

Shock Tube Test Section and Associated Electronics

total volume of the test section, thereby reducing temperature-lowering effects of added powder samples (as indicated in Chapter 2). The second was better reproducibility of incident shock velocity (refer to Chapter 4) by allowing the shock a longer formation distance before reaching the first shock-detecting thermal probe which was mounted on the permanent section. A second probe was placed on the final section - the 'head' - 50±0.2 cm from the first. A third probe, also attached to the head, was positioned 10 cm further downstream from the second one. The head was designed to afford longitudinal and transverse viewing of the shock-produced luminosity. It was terminated in a brass block with 1 $^{5}/_{8}$" diameter transverse and 2" longitudinal bores. Quartz windows, sealed with rubber O-rings recessed in the brass block, were held in position by brass screw caps. This assembly readily maintained a vacuum of 0.01 Torr, yet could withstand 100 psia pressure following the passage of the reflected shock wave.

3.1.2 Shock Tube Operation

3.1.2.1 Powder Sample Preparation

A Mylar strip, $^{1}/_{4}$" wide and 2 $^{1}/_{2}$" long, was cleaned with acetone and folded over the hook of the sample holder. Then a small quantity (2-10 mgm) of finely powdered metal

(<38 micron diameter and >99.9% purity) was floated over the outer surface with acetone, ethyl alcohol or ether. The sample holder was inserted centrally within the shock tube, 25 cm upstream from the first thermal, shock-detecting probe with the Mylar width transverse to the flow direction.

The latter step was taken to assure maximum possible interaction between sample and shock-heated gas, for luminosity resulting from shock excitation is very strongly dependent upon the amount of that interaction.

3.1.2.2 Preparation and Operation of the Shock Tube

Consideration of measures to minimize contamination of the shock tube and powder samples, as well as safety precautions for handling high pressure gases, led to the following routine operating procedure:

1) The channel was separated into three sections and cleaned at least three times with cloths soaked in acetone. The window-supporting O-rings were greased, windows cleaned and the viewing head reassembled. (The O-rings of the sample holder and velocity probes were re-greased only as necessary.)
2) The rubber gaskets were greased, membranes inserted between channel and chamber and the entire shock tube reassembled.
3) The channel and chamber were evacuated to a

pressure <0.05 Torr.

4) Alignment of the optical system was rechecked by reverse collimation and film placed at the spectrograph focal plane. (In reverse collimation, light originating at the spectrograph focal plane is passed through the entire optical system to be brought to a focus appropriate for a specific experiment.) The optical configurations employed will be discussed later. (A plan view of them may be seen in Fig. 3-13.)

5) When the channel pressure was <0.05 Torr, the chamber was filled with driver gas (H_2 or He) to a pressure of 25 psia and the channel filled with Argon (or an Argon/Hydrogen mixture) to atmospheric pressure.

6) The sample was prepared, inserted and the shock tube evacuated once more.

7) Step 5 was repeated and the tube evacuated once again to minimize contamination of test and driver gases by air.

8) The chamber was pressurized with driver gas to 25 psia.

9) The requisite amount of Hydrogen was admitted to the channel followed by Argon addition to give the desired total pressure, P_1.

10) Driver gas was fed into the chamber until the pressure was 50-70 psia lower than the natural bursting pressure of the diaphragm.

11) Velocity probe circuit, shutter circuit, photocell, photodetectors and associated electronics were set operational and the spectrograph shutter opened.

12) Driver gas was very slowly added to the chamber until the diaphragm burst under pressure P_4. (The solenoid-actuated plunger, shown in Fig. 3-1, was seldom used as the spark produced upon closure of its circuit caused premature triggering of the electronic equipment.)

13) The spectrograph shutter was closed. The shock tube was vented into the room from which an exhaust fan quickly removed the fumes and vapours.

14) The electronic circuitry was deactivated.

15) Either a comparison spectrum (usually of an iron arc) or a sensitometric calibration exposure from a standard lamp was put on the film.

3.1.3 Platinum Resistance Probes for Shock Speed Measurement

An assembled thermal probe is shown in Fig. 3-3a and the unit during various steps in its manufacture is shown in Fig. 3-3b.

a) Assembled Unit

b) Stages in Heat Transfer Gauge Manufacture

Figure 3-3

Platinum Resistance Shock Detecting Probes

A fine strip of Hanovia Liquid Bright Platinum #05-X was painted on a diameter of one end of a fire-polished, clean, $^1/_2$" length of 10 mm pyrex rod and extended along the rod's length. Then the rod was fired in a well-ventilated oven for 15 minutes at a temperature of 650°C-680°C. The resistance of the resultant bright film was measured. This process was repeated until the resistance across the end of the rod was <50Ω. Two fine copper electrodes were soldered to the platinum strip and passed through holes in a machined lucite holder. Next, the rod and electrodes were affixed to the holder with an epoxy resin. When the resin had set, the electrodes were soldered into opposite terminals of a four prong socket to complete the assembly.

The circuit used to power the probe is shown in Fig. 3-5a and a comparison of the available output signals is given in Fig. 3-4. The 1200Ω resistor acts as a load on the battery which the probe "sees" as a constant current power supply. When the shock wave passes the thin platinum film, the high temperature gas raises the film temperature a few degrees in a time<1μsec (Nagamatsu, 1961, p. 118). The associated resistance change, detected as a 5-100 mV voltage pulse across the thin film, was either presented on an oscilloscope display or amplified for use as a triggering pulse to a C.M.C. #756BN digital display time-interval meter. That instrument has a precision of ±1 μsec.

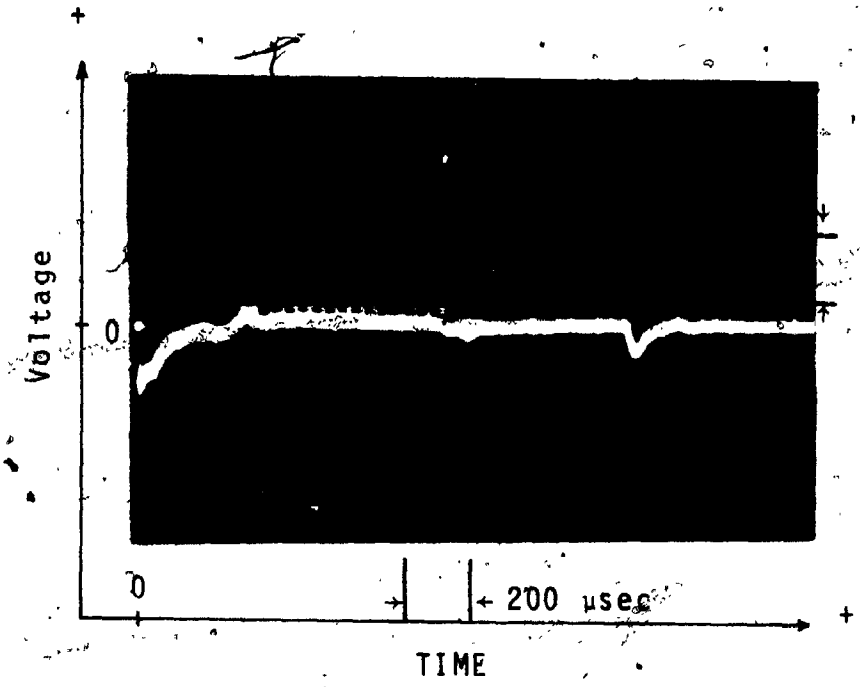

Figure 3-4

Comparison of Thermal Probe Power Supply output pulses

(i) Negative-going pulses-direct probe output following shock front passage.

(ii) Positive peaks-output of pulse amplifier triggered by fast-rising portion of heat transfer gauge output signal.

The thermal probe power supply, two time interval meters, transistorized pulse amplifiers and time delay units were rack-mounted in a cabinet (refer to Fig. 3.2) and the entire assembly referred to as CHARLIE 1.

3.1.4 Electronic Triggering Signals from Shock Luminosity Detectors

During studies of luminosity emitted from the reflected shock region, particularly when triggering signals were needed for photoflash equipment, standard phototubes - RCA 930 and RCA 929 - and photomultipliers - RCA 1P21 - were used. In addition, two Texas Instrument's LS-400 photo-transistors, normally used as auxiliary radiation detectors, could be used to provide triggering information. The simple circuit shown in Fig. 3.5b, was sufficient to allow operation in a regi[illegible] where typical (unsaturated) signal rise and fall times were 1.5 - 2μsec and 17-20μsec as specified by the manufacturer (Texas Instruments, Application Note, 1962).

These luminosity detectors are ideally suited for use with shock tubes. Their small size (0.085" diameter, 0.06" length, nominal), great sensitivity to visible and near I.R. radiation and fast response allow the time history of radiation emanating from positions 1-5 cm apart in the shock tube to be followed without delicate, much-repeated, optical alignment.

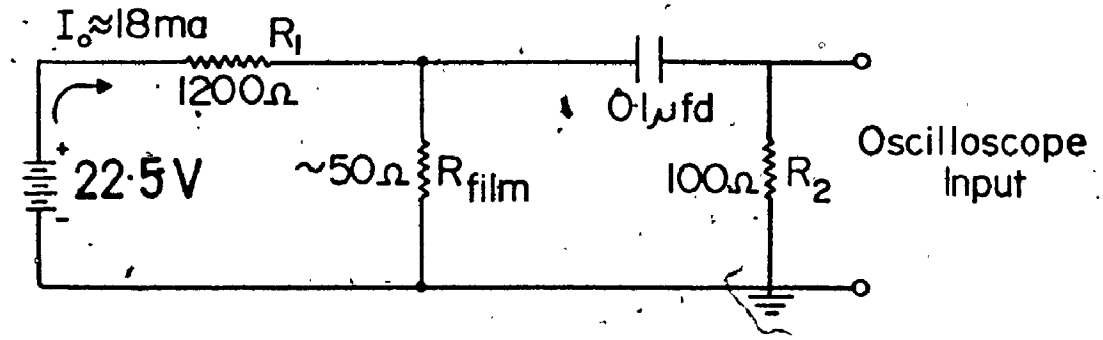

(a) Velocity Probe Power Supply

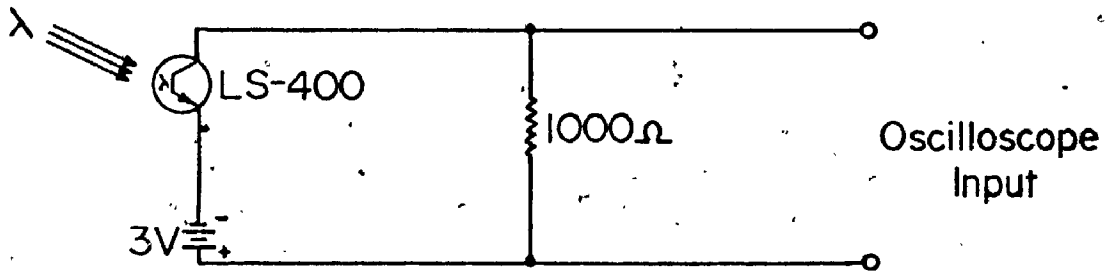

(b) Photodetector Power Supply

Fig 3·5 Probe and Light Detector Power Supplies

In order to protect the LS-400s, to exploit their properties, and to provide a fixed optical configuration, they were mounted in a cylindrical brass holder which could be threaded into the window retaining caps. Consequently, these devices could be used to detect luminosity either longitudinal or transverse to the shocked gas flow. Optical filters - limiting the spectral range detected - and spacers - curtailing each detector's field of view to a cone of angle 2°-6° - could be inserted in the holder. The light sensors could be positioned on either of two mutually perpendicular diameters: on one, they looked out through circular apertures 0.080 cm wide and 3.97 cm apart; on the other, the openings were 0.060 cm in diameter and their separation 3.94 cm. To prevent saturation of the LS-400s, only the latter set of openings was used routinely.

3.2 Spectrograph and Films

Although the shock-excited luminosity was of high intensity, it lasted for only 0.7 to 2.0 msec, depending upon shock strength and the spectral feature. Meaningful, quantitative, intensity measurements of hydride bands required the recording of rotational fine structure of these bands with one shock exposure, using narrow slits (40-70 micron width for emission spectra, 25-50 for absorption spectra). The additional constraints that i) the fine structure be

resolved and ii) film blackening be appreciable, dictated the use of a fast spectrograph and a very fast film-developer combination. The films used are listed in Table 3-1 where a comparison is made of their properties.

As the spectrograph used to record all the reported spectra was built in this laboratory by Mr. James H. Reid - a physics M.Sc. student - and as its features are non-standard, it will be described briefly in the ensuing paragraphs.

The instrument afforded high light-gathering power in the second order from 4200Å to 6500Å as glass Aero-Tessar, f/6, 4" diameter lenses served as collimator and camera. Dispersion of the collimated input light beam was produced by a 6" square, plane grating of 600 lines/mm blazed for first order, 1 micron. The light gathering power corresponding to the maximum f-number of the lenses was never realized because internal reflections from uncoated surfaces caused significant light losses. A baffle (indicated on Fig. 3-6) had to be inserted to prevent unwanted exposure by light reflected from the front surface of the collimator. Interchangeable film holders allowed the use of both 35 mm and 70 mm film. Two slits were cut in the 70 mm film holder: one covering the spectral region 5870Å-5900Å; the other centred on 6000Å. An RCA 1P21 photomultiplier mounted on the back of the film holder could be used to record the course of shock-

TABLE 3-1

Comparison of Films Used to Record Spectra

Emulsion Type	ASA Speed Index*	Available Spectral Range (A)	Spectral Range Employed (Å)	Grain Size
103-F	600	2000 - 7000	4000 - 6700	fine
Tri-X Pan	1200	2000 - 6600	4000 - 6600	moderate
Royal-X Pan Recording	1600	2000 - 6500	4000 - 6500	moderate-coarse

*Speed indices and grain sizes for 8 minute development in Acufine developer.

2 4

OF/DE

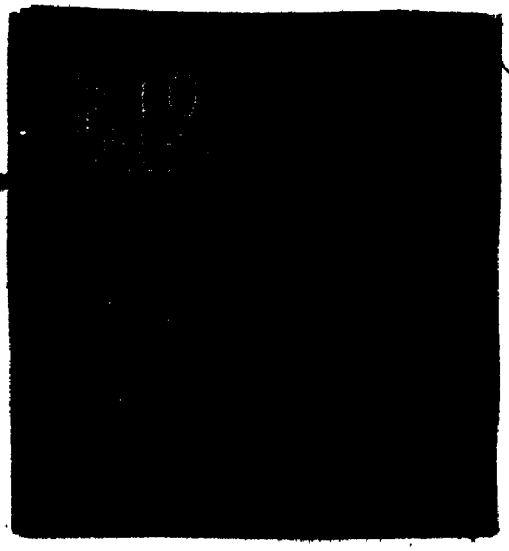

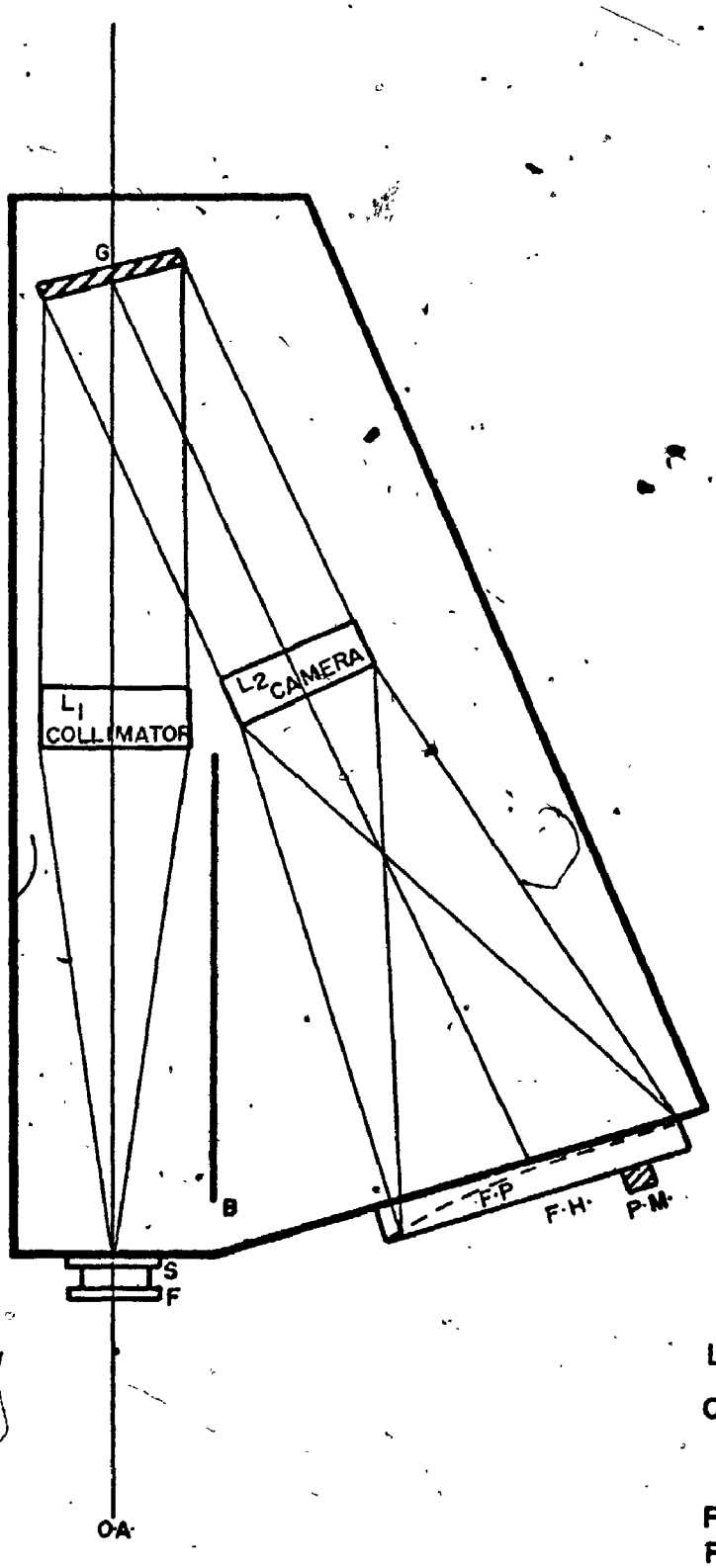

LEGEND:

O·A = Optic Axis
F = Filter Holder
S = Slit Assembly
F·P = Focal Curve
F·H = Film Holder
G = Grating - 600 lines/mm
Blazed for 1 μ
First Order
$L_1 = L_2$ = Aero Tessar Lenses f/6
B = Light Baffle
P·M = 1P21 Photomultiplier

Fig. 3.6 Plan View of Spectrograph

produced or absorption flash luminosity as seen at the spectrograph focal curve through either of these openings.

When the spectrograph entrance slit was aligned parallel to the grating grooves, the spectral line images of the slit were also parallel to those grooves. Tests utilizing a 1P21 photomultiplier confirmed that the amount of light reaching the focal curve was a linear function of slit width for widths >10μ.

The focal curve of the spectrograph was found by trial and error, using spectra excited in an iron arc. Figure 3-7 illustrates the variation of plate factor - reciprocal dispersion - with wavelength for the best focus. The curve was derived from a least squares polynomial fit to a set of 82 FeI lines extending over the spectral interval 3969Å-6495Å.

3.3 High Speed Shutter

A high speed moving shutter was used to control light input to the spectrograph. It fulfilled three distinct functions:

1) When used alone, it limited film exposure to radiation emitted within the reflected shock region by preventing any incident shock luminosity from entering the spectrograph.
2) When synchronized with an absorption flash unit, it prevented exposure to any emission before and

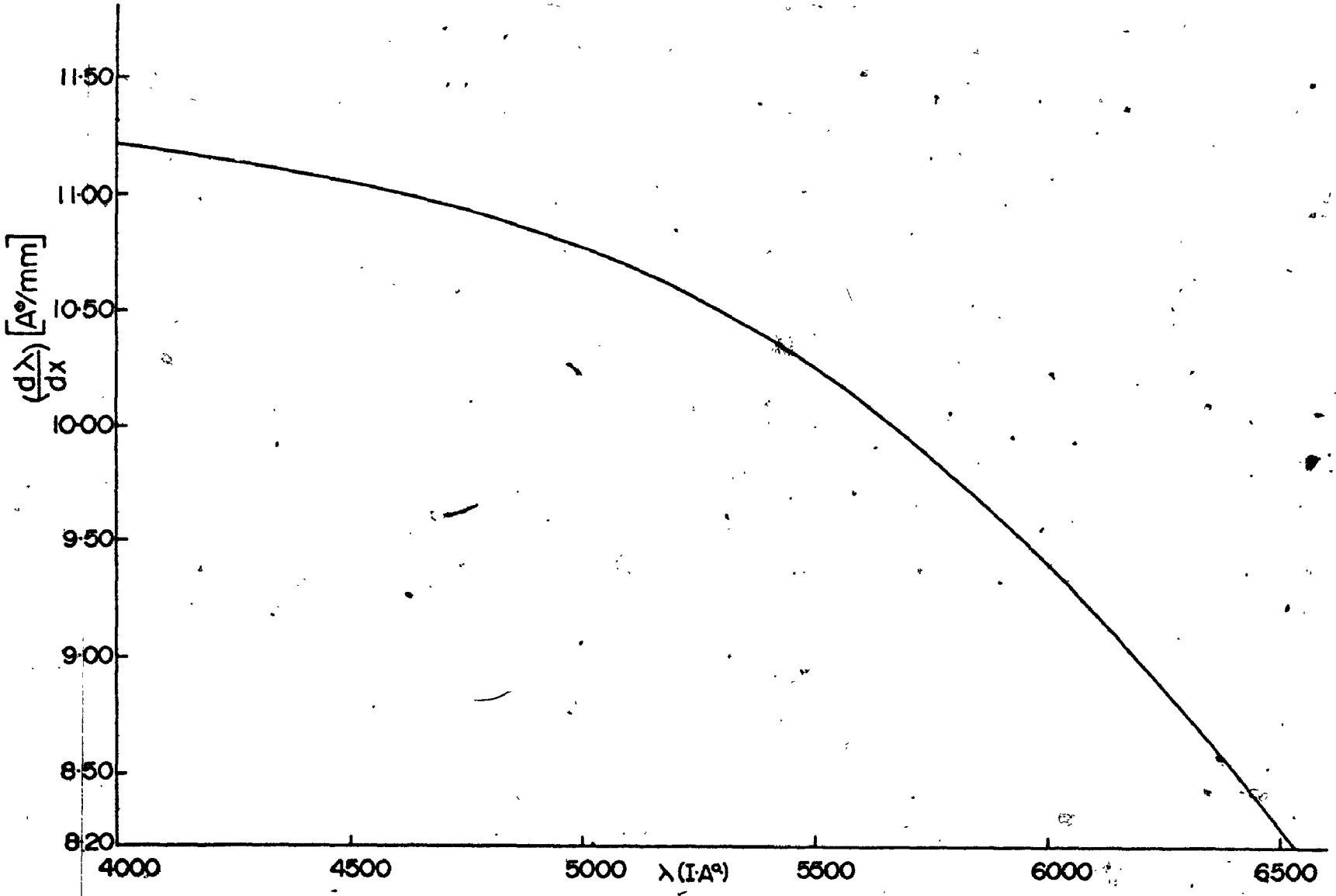

Fig· 3·7 Variation of Plate Factor, $\left(\frac{d\lambda}{dx}\right)$, with Wavelength

after film exposure by an absorption flash. The spectrograph slit was uncovered only during a portion of the absorption flash.

3) When synchronized with an absorption flash unit and triggered by a pulse from a reflected shock radiation detector, it was used to allow recording of an emission and an absorption spectrum from the same test gas sample. A stepped, moving slit was used so that one-half of the open spectrograph slit was uncovered for ~350 μsec immediately following shock reflection, and the remaining portion of the spectrograph slit was uncovered for ~400 μsec thereafter. An absorption flash, synchronized with the change in the spectrograph slit 'open' portion, was fired within ±25 μsec of this change.

A modification of the high-speed shutter described by Camm (1960) was used. Figure 3-8 is a photograph showing the unit attached to the spectrograph. The movable portion - the slider - was a piece of clear plastic (1"x$^3/_4$"x$^1/_{32}$") from which the central portion had been excised and to which carefully aligned strips of black electrical tape were affixed, thus defining a slit. A dovetail groove, cut in the machined aluminium holder, ensured smooth running of the slider. Spectrograph and moving slits were separated about 1 mm by an adapter which allowed the aluminium holder to be

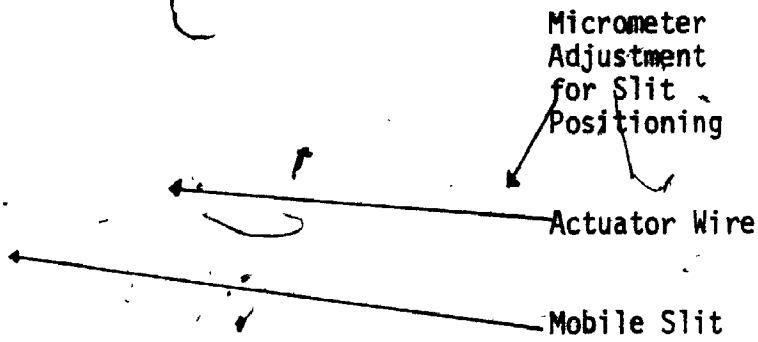
Micrometer
Adjustment
for Slit
Positioning
Actuator Wire
Mobile Slit

Figure 3-8

High-Speed Shutter Assembly Attached to Spectrograph Slit Housing

mounted directly on the spectrograph slit assembly. (The tape side of the slider was adjacent to the spectrograph slit.)

Just before use, the slider was pressed firmly against the actuator wire - #18 chromel - through which a 10 microfarad, rapid-discharge capacitor (charged to 5kV-7.5kV) was discharged. The wire was insulated both from the holder and from the spectrograph slit assembly with mica. When the capacitor was discharged, measurement of the discharge half-cycle gave a value of 17 μsec. The resulting, very rapid thermal expansion of the actuator wire could propel a 3 mm wide mobile slit across a 50 micron spectrograph slit (in a closed-open-closed sequence) within 500 microseconds.

Figure 3-9 records two typical cases of light intensity reaching the spectrograph focal curve when the high speed shutter was used. The circuitry of the capacitor charging unit and the shutter triggering circuit are illustrated by the schematic diagram, Figure 3-10.

3.4 Absorption Equipment

The next three subsections deal with equipment employed in the recording of absorption spectra of shock-heated, chemically reacting gas mixtures.

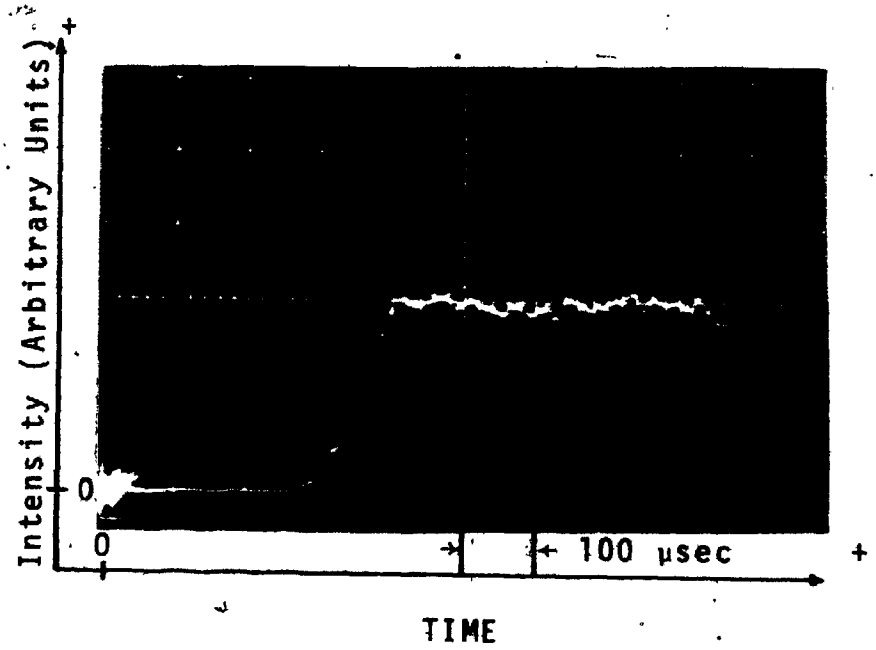

a) Spectrograph slit subjected to constant intensity illumination. Shutter triggered after 275 μsec delay. Rapid-discharge capacitor voltage=5kV. Sliding slit ~3mm wide.

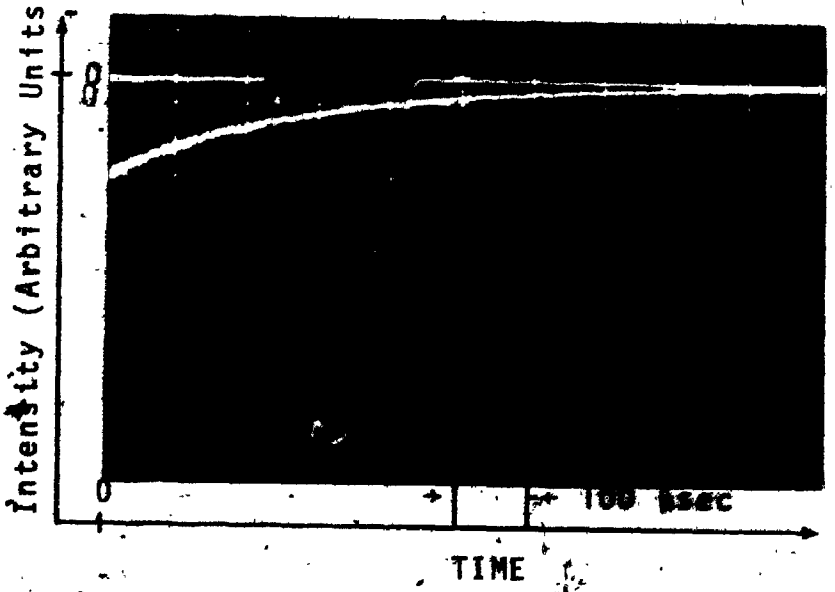

b) Shutter & Multiblitz both triggered after 225 μsec delay. Rapid-discharge capacitor voltage=7.5kV. Sliding slit ~2mm wide.

Figure 3-9

Light Intensity (As Measured By a 1P21 Photomultiplier at the Spectrograph Focal Curve) vs Time for Two Representative Tests of the High-Speed Shutter.

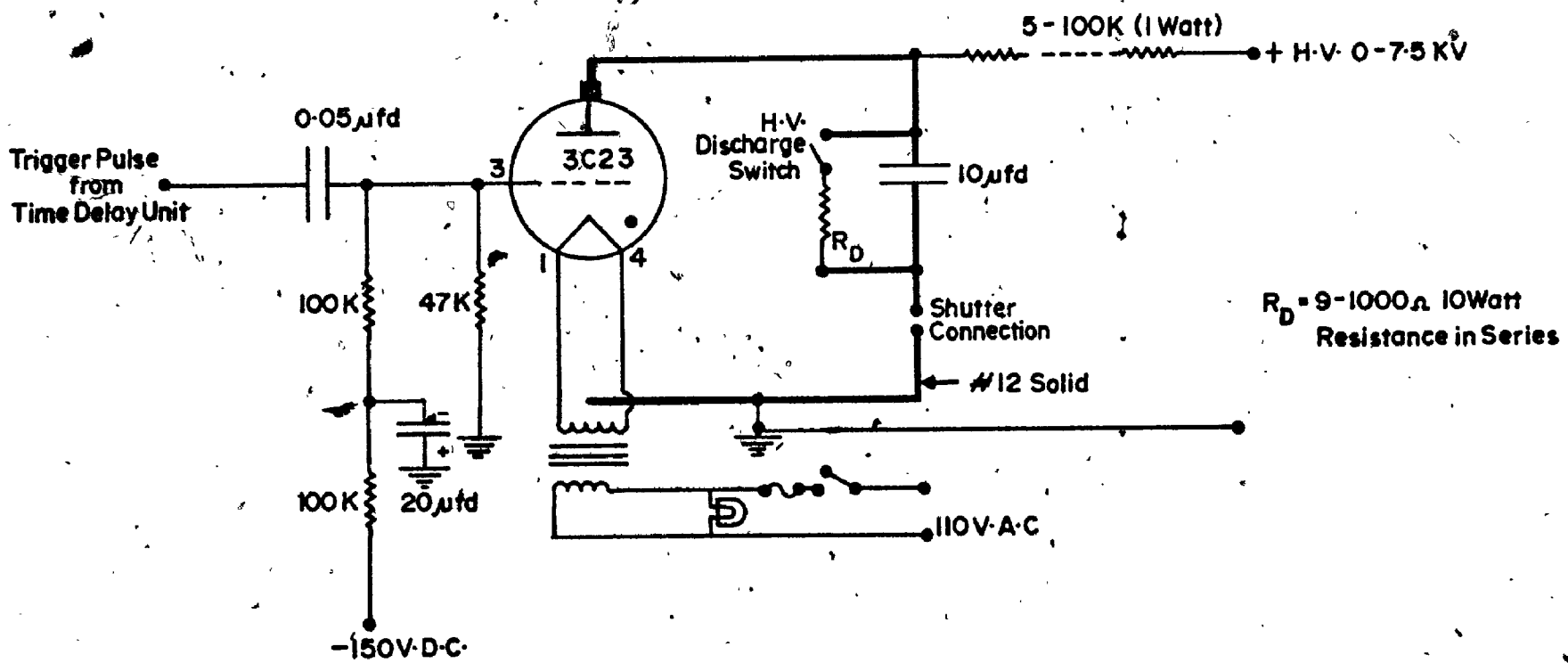

Fig·3·10 Charging and Trigger Circuit for High Speed Shutter

3.4.1 Sources of Absorption Continua

Most of the reported absorption spectra were obtained by use of a Multiblitz Color commercial photoflash unit. Its luminosity was derived from capacitive discharge through a Xenon filled quartz tube and consisted of atomic impurity lines for the first 50 μsec of the discharge period, followed by a 1 msec duration Xenon continuum (color temperature ~5500°K) on which pressure broadened Xenon emission lines were superposed.

The absorption spectra of AlH were recorded using an FX-33 flash tube supplied by Messrs. Edgerton, Germeshausen & Grier, Inc.. An energy storage unit for this device (designed and built in this laboratory by Mr. R. Koehler) consisted of four capacitors - 0.5, 2.0, 38 and 56 μfd - which could be charged separately or in any parallel combination from a continuously variable 0-2kV supply. Luminous pulse duration under these conditions varied from 50 μsec to 100 μsec.

These two flash units were complementary. One was used to observe averages over 'long-times' within the shock-heated gas; the other to record 'short-term' properties. Thus the FX-33 could be used to ensure observation of the heated test gas-powder sample during times short enough that no significant change of conditions within the shock tube occurred. A comparison of light-output versus time for these absorption flash sources is given in Figure 3-11.

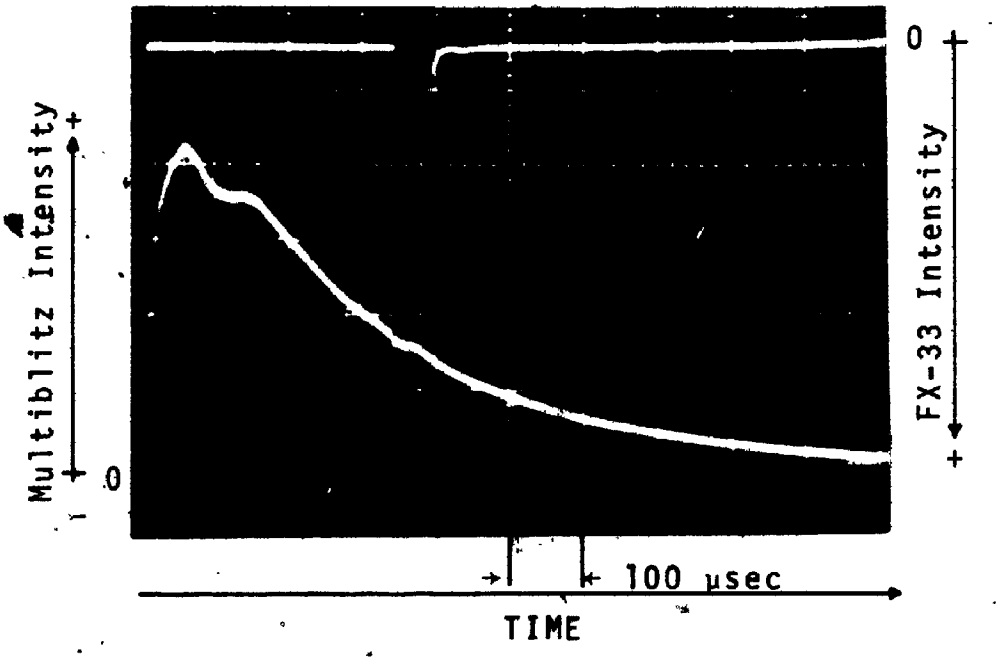

a) Comparison of Intensity Pulse Time Scales for the FX-33 and Multiblitz units. The Intensity units are arbitrary and the two scales are different.

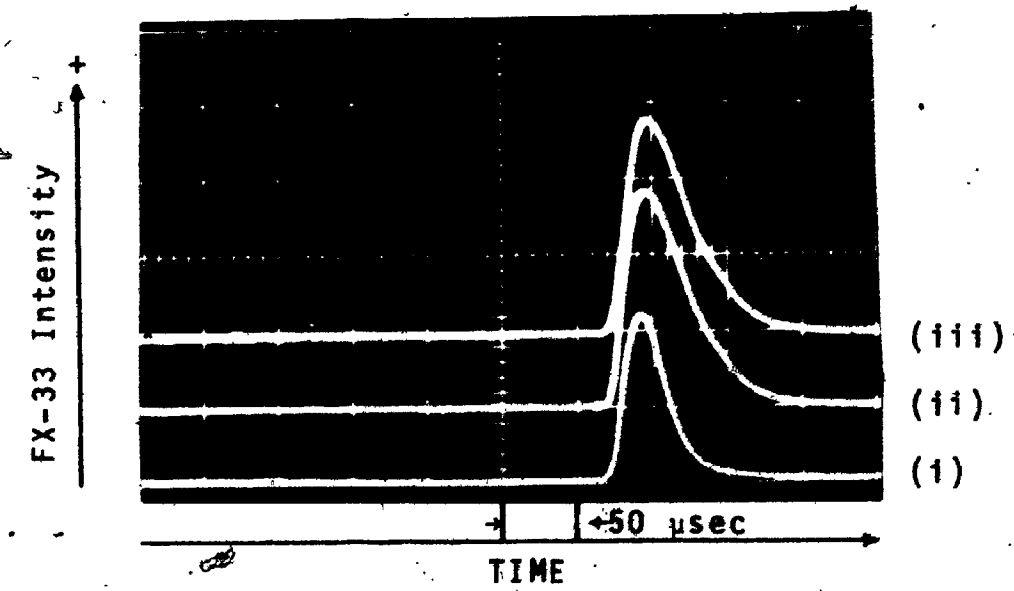

b) Output Light Intensity vs Input Energy for FX-33 (i) 38 µfd, (ii) 56 µfd, (iii) 94 µfd all at 1.3kV and on same intensity scale.

Figure 3-11

Comparison of Light Pulse from Absorption Flash Sources

3.4.2 Time-Delay of Triggering Signals

When heat transfer gauges, detecting shock front passage, or photo-sensitive devices, responding to shock-excited luminosity, were used to provide information on conditions within the shock tube prior to firing absorption flashes or the high speed shutter, some time-lapse had to be provided. This was achieved by means of the time-delay unit shown in the block diagram, Figure 3-12. That unit, too, was built locally (again by Mr. R. Koehler) to control both triggering and synchronization of the moving shutter and electronic flash units.

It has one internal test pulse generator for checking the operation of the device itself and the external units it controls. In addition, there are three switch-selectable inputs which can be used to initiate time-delayed triggering sequences -

1) Pulse Amplifier - which accepts the output signal of the thermal, shock-detector pulse amplifiers.
2) 929 - which powers and receives the output of a 929 photo-cell (a blue and ultraviolet sensitive device).
3) 930 - that powers and accepts the output of a 930 (orange and red sensitive) photo-cell.

The main delay unit provides a delay continuously variable between 4 μsec and 1.5 msec. It affords two output pulses:

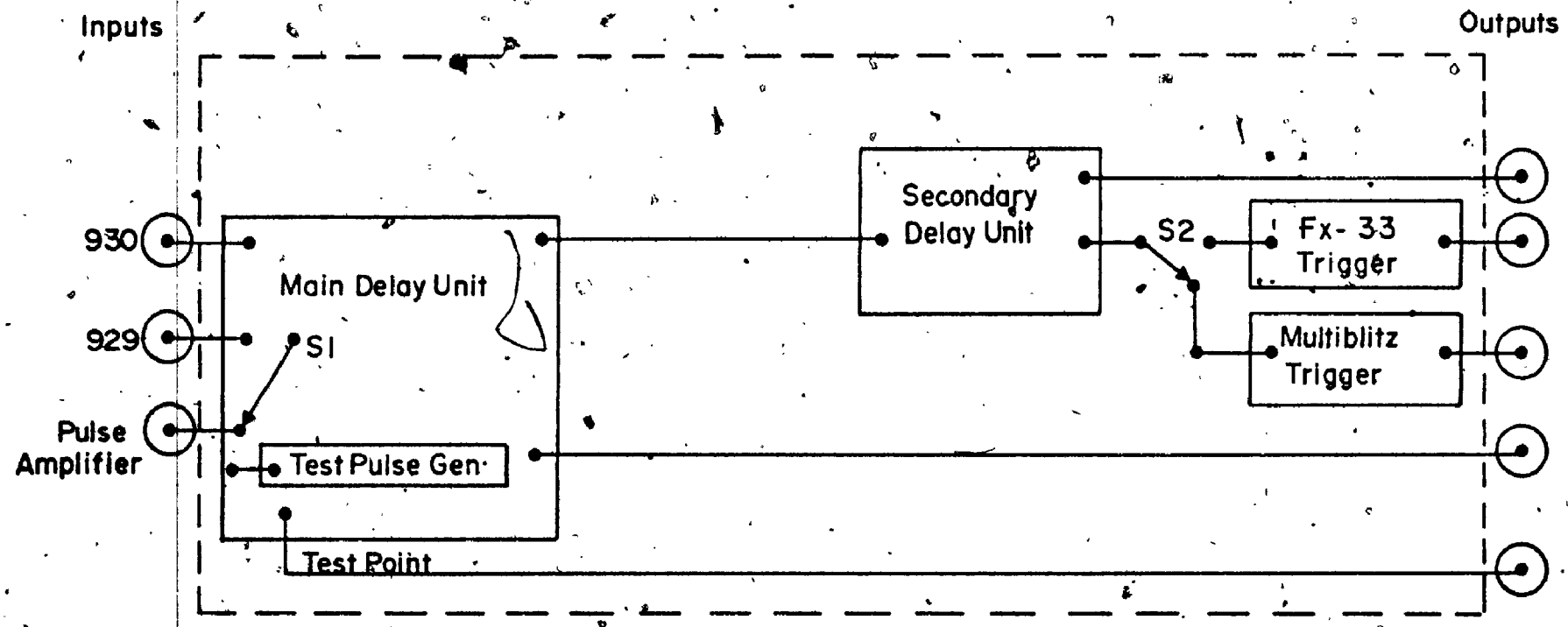

Fig·3·12 Time Delay Block Diagram

one (at 100VDC) for auxiliary use such as triggering of the high-speed shutter supply; the other serving as input to the secondary delay unit. The output of the latter device is used to control two slave units, one of which provides a high voltage pulse for triggering the FX-33, while the other produces a shorting pulse to trigger the Multiblitz.

3.4.3 Arrangement of Optical Components for the Recording of Spectra

In the work reported, four distinct optical configurations - shown schematically in Fig. 3-13 - were used; but only two of them were employed for absorption spectroscopy (Fig. 3-13(iii) and (iv)). In the first arrangement, light from a flash source was focused in the centre of the shock tube near the shock-reflecting end window. Consequently, most of the absorption, recorded using this configuration, was produced in a small volume of material present at the shock tube centre. In the second arrangement, luminosity from the absorption flash was rendered parallel before passage through the shock tube. The resultant beam passed through $^3/_4$" diameter circular stops centrally located on the transverse viewing window retaining caps. (Fig. 3-14b is a photograph of this arrangement when the Multiblitz Color photoflash unit was used. A line drawing of the entire apparatus used in 'parallel light' absorption spectroscopy is

LEGEND

S.S. = SPECTROGRAPH SLIT
S.F. = STEP FILTER (ATTENUATOR)
F = WAVELENGTH-SELECTIVE FILTER
L_1 = TELEVISION CAMERA LENS - f/2.5
L_2 = ACHROMATIC DOUBLET - f/4
L_3 = QUARTZ LENS - f/1.5
$L.S_1$ = LENS STOP
$L.S_2$ = LENS STOP
A.S. = ABSORPTION CONTINUUM SOURCE
O.A. = OPTIC AXIS
S.T. = SHOCK TUBE (VIEW ALONG LONG. AXIS)
H = HIGH SPEED SHUTTER

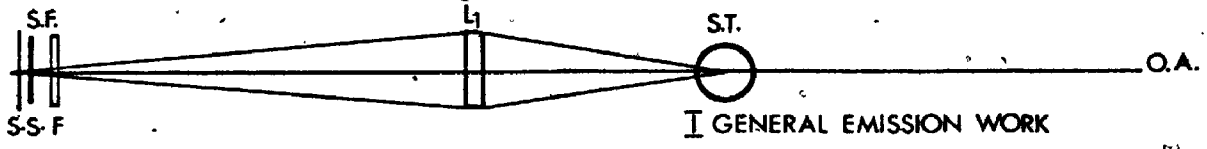

I GENERAL EMISSION WORK

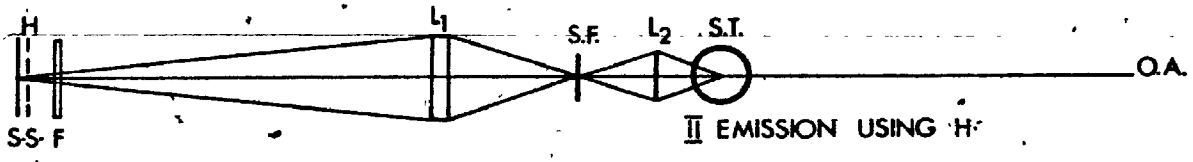

II EMISSION USING H

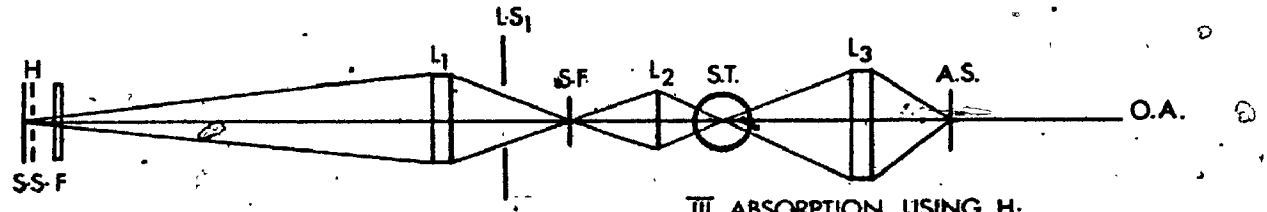

III ABSORPTION USING H
(FOCUS AT CENTRE OF S.T.)

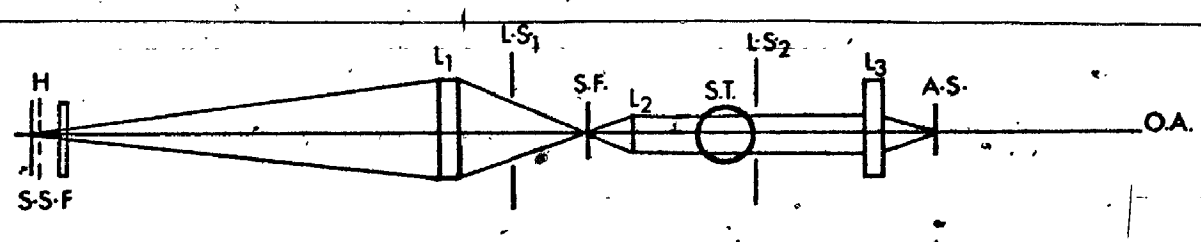

IV 'PARALLEL LIGHT' ABSORPTION
USING H

FIGURE 3-13

PLAN VIEWS OF THE OPTICAL CONFIGURATIONS USED

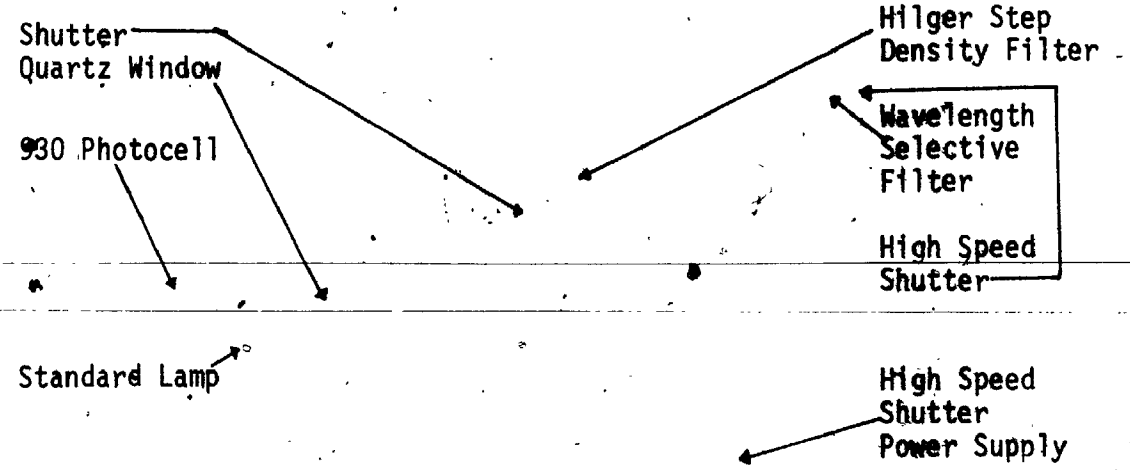
Shutter
Quartz Window
930 Photocell
Standard Lamp
Hilger Step
Density Filter
Wavelength
Selective
Filter
High Speed
Shutter
High Speed
Shutter
Power Supply

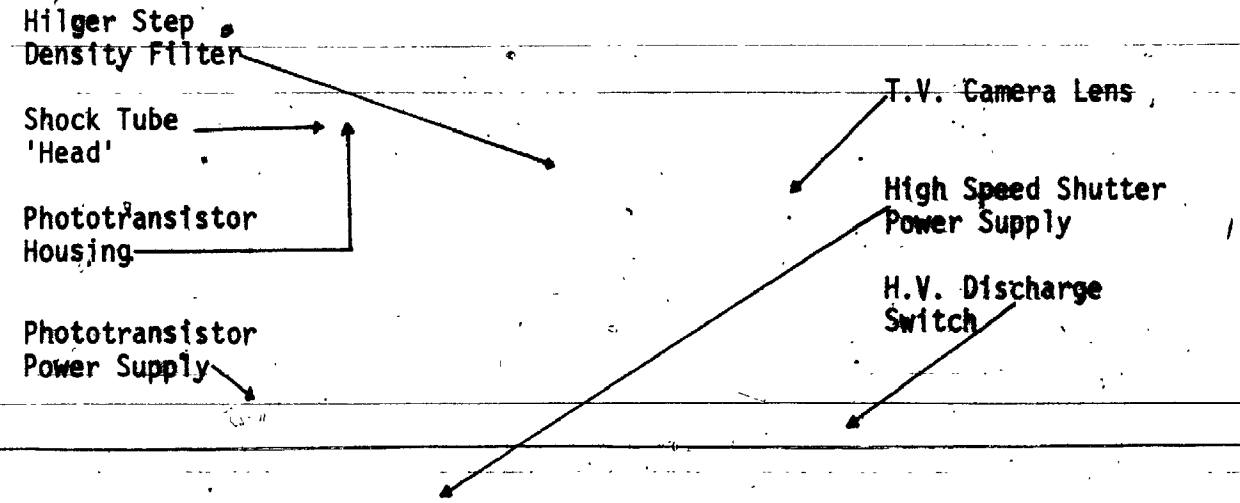
Hilger Step
Density Filter
Shock Tube
'Head'
Phototransistor
Housing
Phototransistor
Power Supply
T.V. Camera Lens
High Speed Shutter
Power Supply
H.V. Discharge
Switch

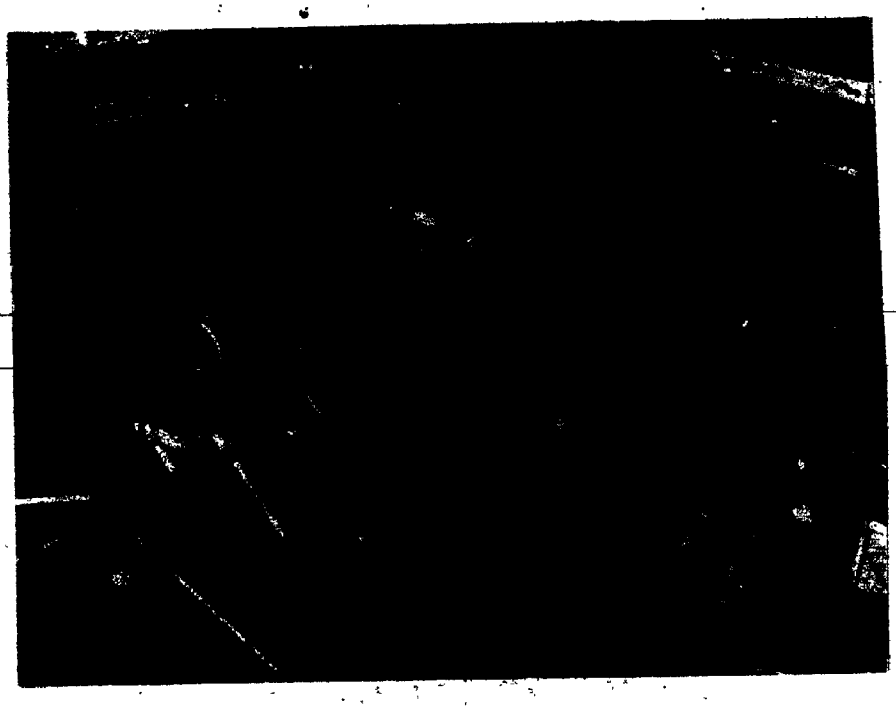

a) Experimental Arrangement for Emission Calibration

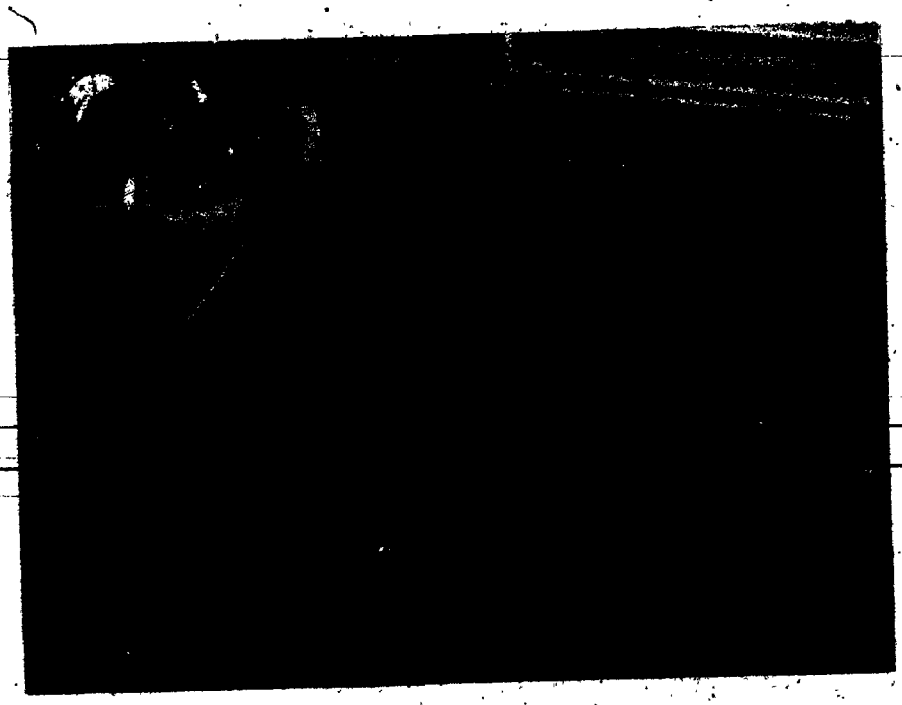

b) Arrangement for Absorption Spectroscopy using Multiblitz Unit

Figure 3-14

Photographs Illustrating two of the Optical Configurations Employed

shown in the plan view of Fig. 3-15.) The 'parallel light' system resulted in a much more pronounced absorption as it afforded a longer optical path - effectively a $^3/_4$" diameter cylinder of length equal to the separation of the transverse viewing windows.

With both absorption systems, the light beam emergent from the shock tube was focused upon a Hilger Step Density Filter and the filter-attenuated beam brought to another focus on the spectrograph slit after passage through wavelength-selective filters. Several workers, in this laboratory, have calibrated the step filter in the spectral range 4000Å-6500Å. An averaged set of their values was adopted.

3.5 Sensitometry

The precision of quantitative photographic spectroscopy is determined to a very great degree by i) the recording of an experimental exposure and a standardizing spectrum from a source of well-defined spectral distribution and intensity on the same film strip and by ii) the subsequent identical treatment of experimental and calibration exposures. Procedure followed to fulfil the above requirements is detailed below.

3.5.1 Standardizing Exposures

Quantitative photometry was restricted to 70 mm film strips which had both experimental and standardizing exposures

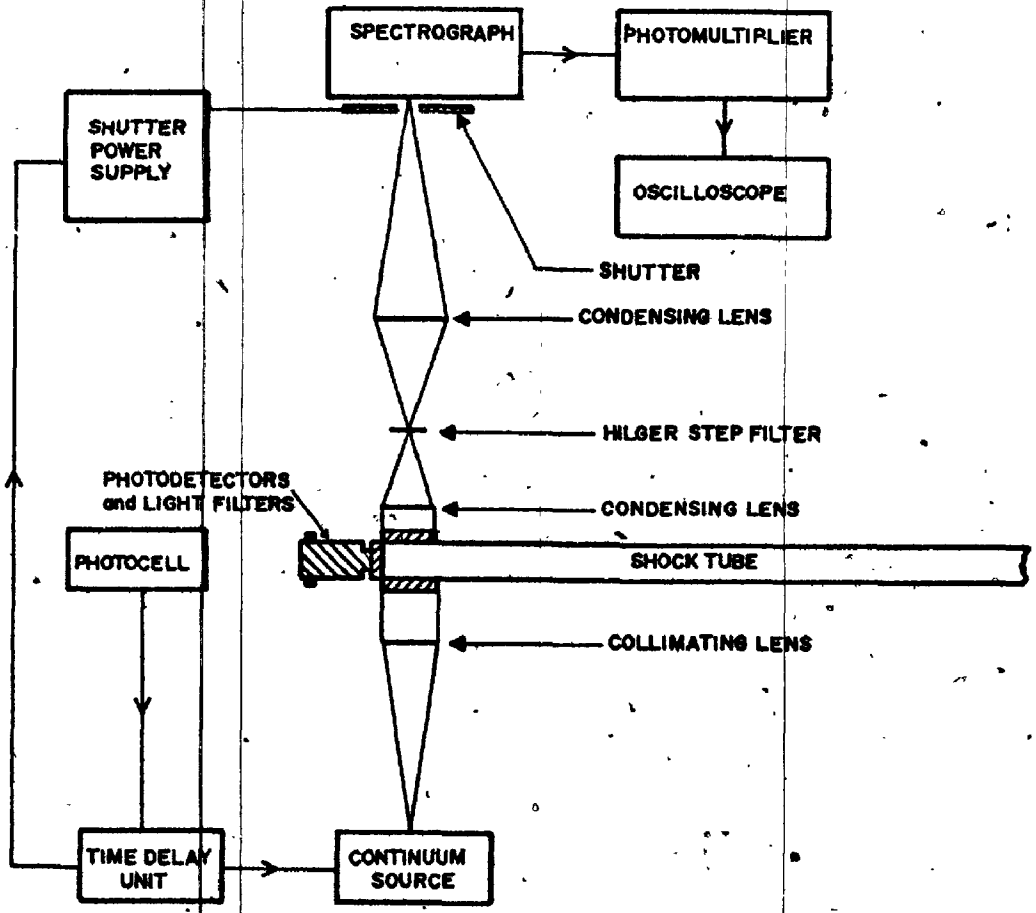

Fig·3·15 Block Diagram of Arrangement for 'Parallel Light' Absorption Spectroscopy

imposed on the same strip. Standard exposures were produced by passing light from a Tungsten strip filament lamp (recently calibrated at the National Research Council of Canada laboratories) through the same optical system as that used in the experiment. Such an arrangement is illustrated by Fig. 3-14a for an emission spectrum calibration.

The lamp current was measured as a voltage drop across two precision 0.1 Ω resistors (in parallel) using a Leeds and Northrup Model K Potentiometer.

A Praktica camera body served as a shutter for the standard lamp exposures. Tests of the $^1/_5$ and $^1/_2$ second exposure time settings - the only ones used - indicated a repeatability better than 1%.

3.5.2 Standard Development Procedure

Every film strip that had been exposed to experimental and standardizing exposures was maintained in a light-tight container for at least twelve hours before processing. This precaution assumed a time interval between film exposure and film development long in comparison with the interval between film exposure to experimental and standardizing spectra. Such a procedure attempts to ensure the same amount of latensification of the pre-developed images.

The film was tank-developed for eight minutes in fresh Acufine developer with ten second agitation at one minute intervals. A thirty second water rinse following development

acted as a stop bath. The negative was hardened and fixed by a ten minute immersion in a Kodak fixing solution during which ten second agitations were provided at one minute intervals. Then the film was washed for thirty to forty minutes in fresh running water, after which it was given a thirty second rinse in distilled water. A final rinse treatment in wetting solution lasted for another thirty seconds. The film, still on its developing reel, was placed in a dust free container to dry in circulating air.

3.5.3 Densitometry

Blackening of the negative as a function of position was converted into a series of pen response versus position graphs using a Joyce-Loebl Mark III C recording densitometer. That instrument uses calibrated, continuous density wedges to indicate density as a linear function of recorder pen deflection - in first approximation. Precise density values were obtained with the aid of correction curves supplied for each wedge by the manufacturer. Usually the corrections were very small and it was sufficient to assume that pen deflection was directly proportional to density change.

CHAPTER 4

CHARACTERISTICS OF THE SHOCK TUBE

The following pages are concerned with properties of the particular shock tube described in Chapter 3. This chapter contains: summary of shock velocity measurements for Hydrogen driven shocks in Ar:H_2 mixtures; the time-dependence of shock-excited luminosity; the identity of spectral impurities detected in light emitted from the reflected shock region; and an indication of the P_5 values attained. All of these results are characteristic of one shock tube.

How does the shock velocity depend on the physical design of this shock tube?

4.1 Shock Velocity Measurements

Measured values of the incident shock velocity have been used in the calculation of T_5 by methods outlined in Chapter 2 and Appendix C. All temperatures quoted in later chapters were determined in this way. Thus it seemed necessary to establish the reliability of the shock speed measures and to determine the effects on the incident shock front speed of

1) Diaphragm rupture, Channel length, sample addition

and ii) Change in Channel cross-sectional area caused by the transverse bore in the 'head'.

The incident shock speed, U_1, was always determined from the time interval, Δt_{12}, between reception of voltage pulses from platinum thin film heat transfer gauges - probes P_1 and P_2 of Fig. 4-1 - signifying passage of the shock front. Observed values of the shock speed calculated from

$$\bar{v}^{o}_{12} = \frac{\Delta x_{12}}{\Delta t_{12}} \qquad \text{with} \quad \Delta x_{12} = 50.0 \pm 0.2 \text{ cm}$$

are mean values over the interval. Consequently, they may not correctly represent gas flow behaviour beyond that interval. In the Mach number range - $3 < M_s < 7$ - employed in these experiments, shocks have been found to accelerate (White, 1958) or decelerate (Bleakney et al, 1949) in different regions of particular shock tubes. Therefore, shock speed measurements were performed on the downstream side of probe P_2 to determine the subsequent behaviour of shocks whose speed had already been found. The following three subsections summarize some of the results obtained for Hydrogen driven shock waves in $Ar:H_2$ Test gas mixtures. The first one deals with the effects of Channel length, diaphragm rupture and sample addition.

4.1.1 Comparison of Observed, $\bar{V}^{o}_{12}$, and Predicted, $\bar{V}^{p}_{12}$, values for the Incident Shock Speed

$\bar{V}^{p}_{12}$, the theoretical value for the incident shock speed, was calculated directly (or found by interpolation in tables

NOTE

Probes P_2 and P_4 have separation distance, Δx_{24}
= 22.9 cm when end insert is used
= 23.5 cm when end insert is removed

Distance between diaphragm and sample holder
= 11.7 cm (~ 2.3 tube diam.) for 'short' channel
= 21.0 cm (~ 4.1 tube diam.) for 'long' channel

LEGEND

V – vacuum pump line
S – sample holder
P_i – velocity probe i
C – companion flange
W – transverse viewing window

Indicated dimensions in cm

Separation precise to ±0.2 cm due to width of Platinum layer on probes

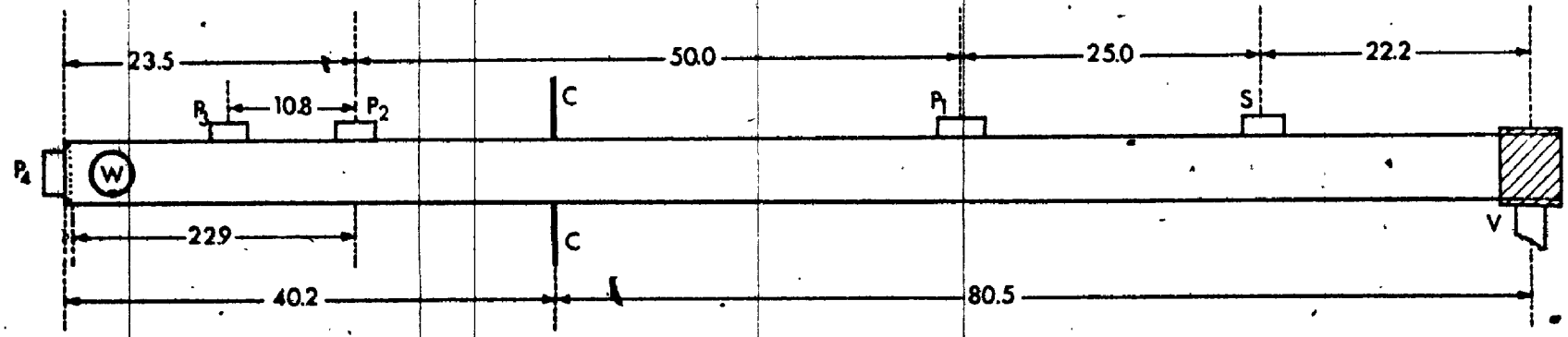

FIGURE 4-1

LINE DRAWING ILLUSTRATING SAMPLE HOLDER AND VELOCITY PROBE LOCATIONS AND SEPARATIONS

of P_{41} vs U_1) for specific initial conditions within the shock tube by the procedures outlined in Chapter 2. Those procedures invoke Eq (2-35)

$$P_{41} = P_{21}\left\{1 - \frac{(\gamma_4-1)}{2}\cdot\frac{V_2}{a_4}\right\}^{\left(\frac{-2\gamma_4}{\gamma_4-1}\right)} \quad \text{with } V_2 = U_1\left\{1 - \frac{\rho(1)}{\rho(2)}\right\}$$

which is based upon the invalid assumption of instantaneous diaphragm removal. White (1958), on the grounds i) that work must be done by the driver gas to break and to push aside the diaphragm and ii) that some driver gas must mix with the Test gas during formation of the shock wave, concluded that the incident shock velocity should be lower for Hydrogen driven shock waves in Argon than a theory invoking (2-35) would predict. Figures 4-2 to 4-4 show that his conclusion is substantiated by the present measurements.

These figures contain data for H_2/Ar shocks. The first two - based on time intervals determined from oscilloscope traces - illustrate the effect of differing Channel length upon the incident shock speed. The data of Fig. 4-2 were obtained when probe P_1 was about 142 cm from the diaphragm. That of Fig. 4-3 was taken with a separation of 235 cm between probe P_1 and the diaphragm. (The 'Short'/'Long' modification of the Channel was produced by removing/inserting a 93.5 cm section adjacent to the diaphragm station.) Both graphs show that the observed shock speed is less than the predicted speed. However, they lead to the further conclusion that weaker shocks are attenuated more in the 'Long' Channel than in the 'Short'

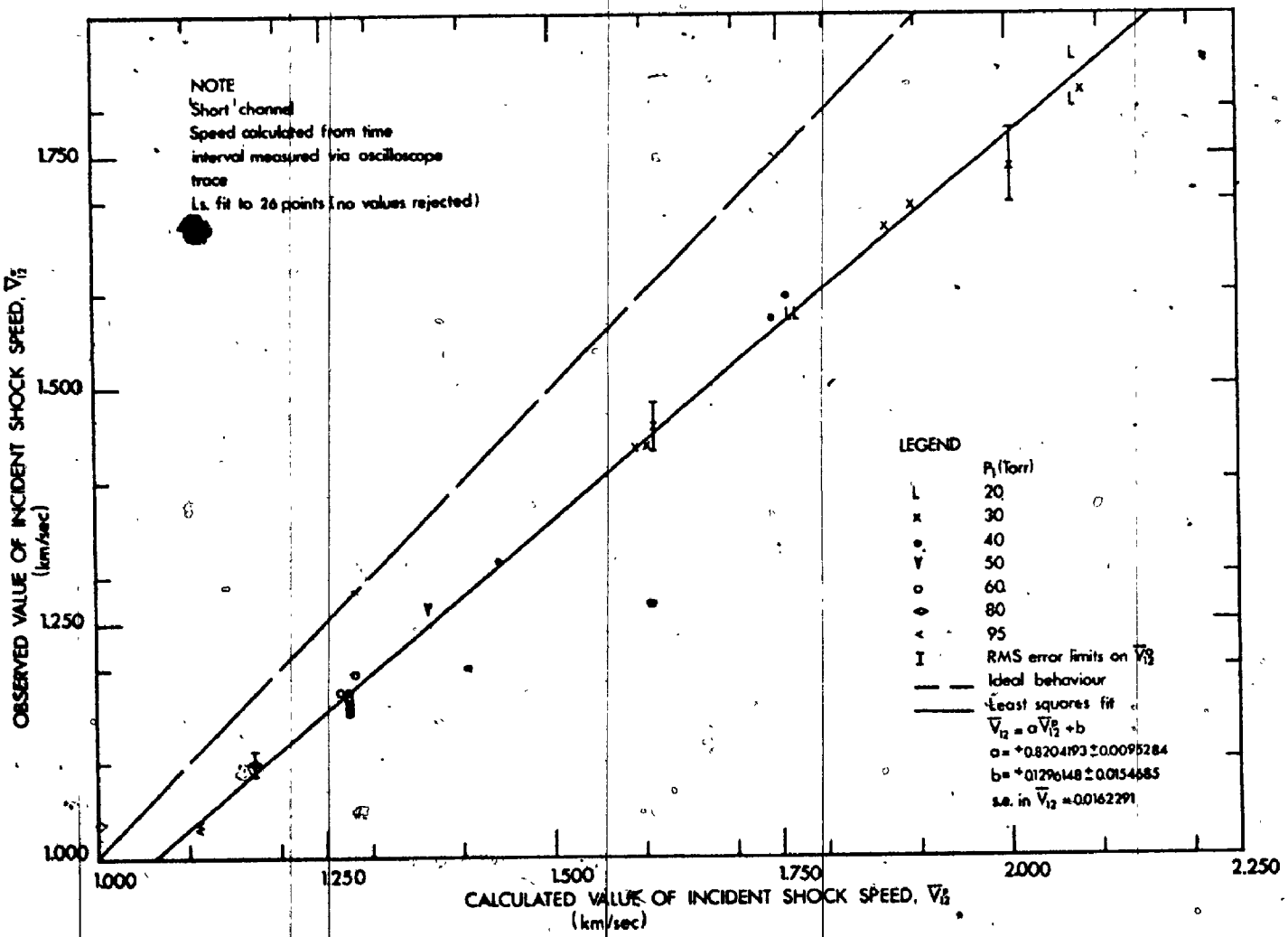

FIGURE 4-2

$\bar{V}_{12}$ VERSUS $\bar{V}_{12}^{c}$ FOR HYDROGEN DRIVEN SHOCK WAVES IN ARGON. (NO SAMPLE ADDED; 'SHORT' CHANNEL)

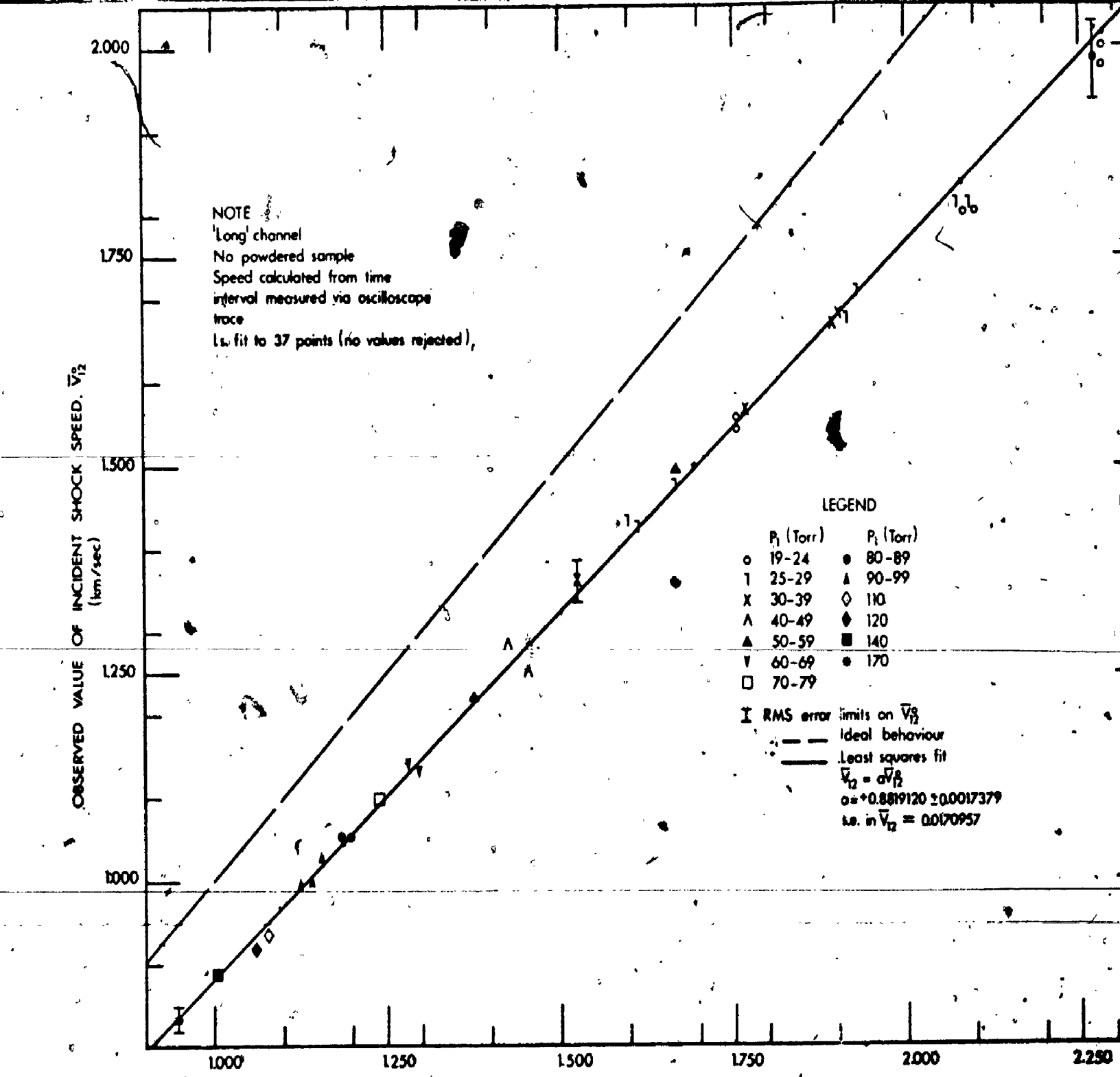

FIGURE 4-3

$\bar{V}_{12}^{o}$ VERSUS $\bar{V}_{12}^{s}$ FOR HYDROGEN DRIVEN SHOCK WAVES IN ARGON. (NO SAMPLE ADDED. 'LONG' CHANNEL)

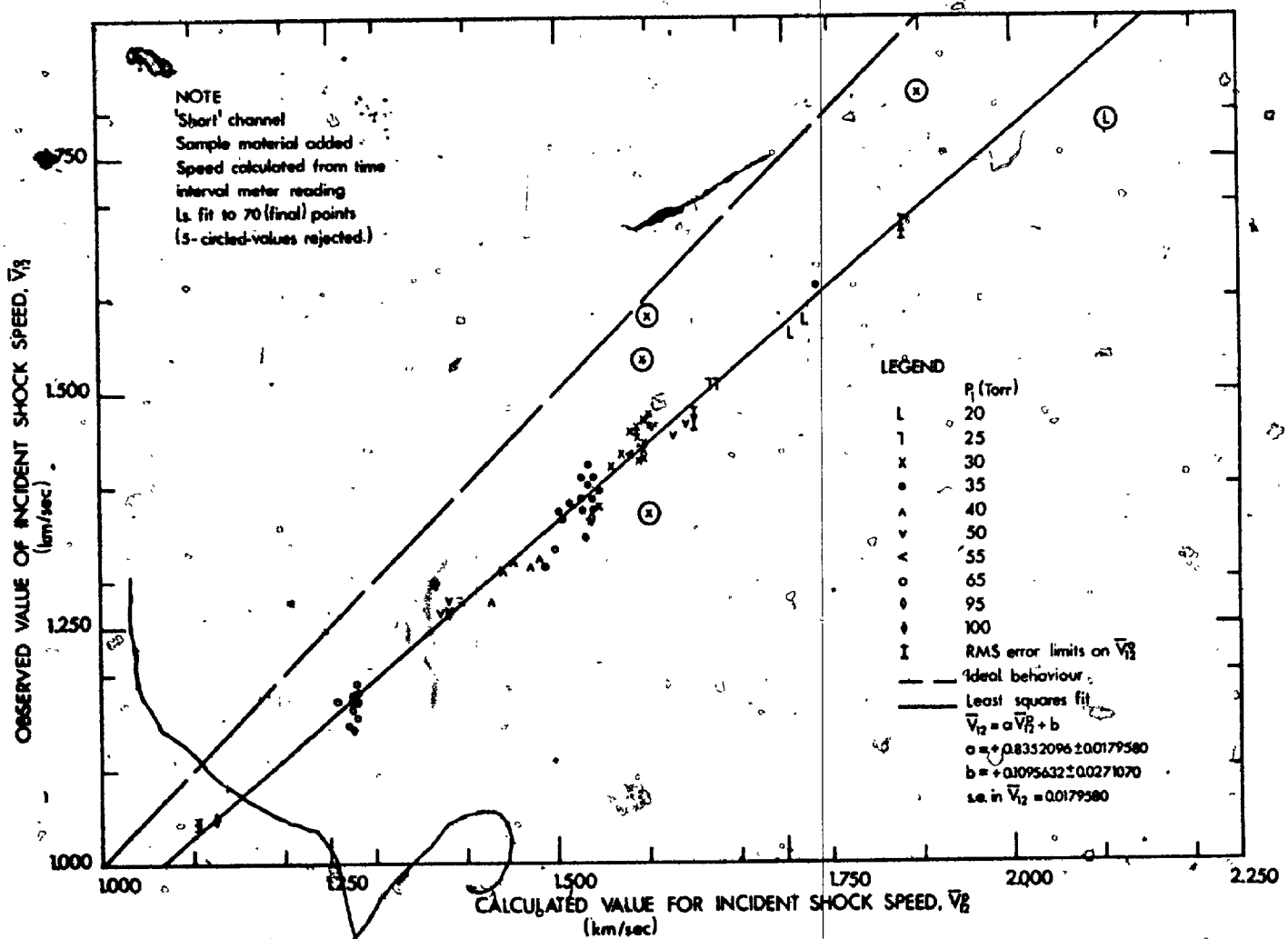

FIGURE 4-4

$\bar{V}_{12}$ VERSUS $\bar{V}_{12}^R$ FOR HYDROGEN DRIVEN SHOCK WAVES IN ARGON (VARIOUS POWDERED SAMPLE MATERIALS ADDED, 'SHORT' CHANNEL)

Channel configuration.

At a predicted speed of 2.00 km/sec, the shock is observed to travel at approximately 1.75 km/sec in both modifications. Consequently, both channel configurations produce the same attenuation of the shock between the time of its formation and passage between probes P_1 and P_2. However, at a predicted speed of 1.1 km/sec the shock front is found to travel at 1.03 km/sec in the 'Short' modification and at 0.97 km/sec in the 'Long' modification. Thus it would seem that weaker shocks attenuate more in the 'Long' Channel before reaching probe P_1. The possibility that the shock attenuates steadily during its passage between probes P_1 and P_2 is investigated in a later section when downstream time interval measurements are presented.

Linear least squares fits to data for both 'Short' and 'Long' modifications reproduce the observed shock speeds with a precision greater than the manufacturer's quoted 3% tolerance on the oscilloscope time base. For the elongated Channel section, a one-term fit has essentially the same standard error of estimate as a two-term fit. On the other hand, data for the 'Short' Channel requires a two-term fit, which has a standard error of estimate about half that found for a one-term fit to the same data.

The effect of powder sample addition upon shock speed in the 'Short' Channel can be deduced from consideration of Figs. 4-2, 4-4, as well as columns 1 and 2 of Table 4-1. In the 'Short' Channel, the incident shock front must travel

TABLE 4-1

Comparison of Incident Shock Speeds, $\bar{V}_{12}$, from Least Squares Fits to $\bar{V}_{12}^{o}$ versus $\bar{V}_{12}^{p}$ for Hydrogen Driven Shocks in Argon.

Source of Data For L.S. Fit	Fig 4-2	Fig 4-4	Fig 4-3	Table 4-2
Time Interval Measurement	'Scope	TIM	'Scope	TIM
Channel	Short	Short	Long	Long
Sample Added	No	Yes	No	No
S.E. in $\bar{V}_{12}$	0.016	0.018	0.017	0.022
$\bar{V}_{12}$ (km/sec) / $\bar{V}_{12}^{p}$ (km/sec)				
1.000	0.950	0.945	0.882	0.872
1.250	1.155	1.154	1.102	1.090
1.500	1.360	1.362	1.323	1.309
1.750	1.565	1.571	1.543	1.527
2.000	1.770	1.780	1.764	1.745
2.250	1.976	1.990	1.984	1.963

about 95 cm from the diaphragm station before encountering the sample. As it passes the sample holder, the metallic powder is scrubbed off the Mylar substrate and carried along in the gas flow of regions (2') and (2) behind the front. (Interactions between the sample and the heated slug of gas between shock front and Contact Surface could modify the shock front speed by causing changes in the common pressures and velocities across the Contact Surface.) Apparently, the sample sizes used were sufficiently small that sample@shock wave interactions did not significantly influence the incident shock speed. This conclusion follows from a comparison of fitted shock speeds versus predicted shock speeds given in Table 4-1, which shows that the mean speed between the locations of probes P_1 and P_2 is the same, within experimental error, whether or not a sample material is present in the purely Argon Test gas.

The data of Fig. 4-4 is of intrinsically higher precision than that of Fig. 4-2 because a TIM (time interval meter) was used in the evaluation of shock front transit time. Yet the data of Fig. 4-4 shows more scatter about the least-squares-fitted line than does the data of Fig. 4-2. This observation caused no concern for data scatter was expected. In fact, it is quite remarkable that the data of Figs. 4-2 and 4-3 shows so little scatter. Scatter in the observed shock speeds is controlled by the opening mechanism of the diaphragm. In the present experiments, the diaphragm consisted of from one to eight layers of Mylar. These were caused to burst by

slowly building up Chamber pressure until the membranes ruptured spontaneously. Variation in the tear pattern of the diaphragms and in the rate at which pressure was built up determined the way in which the diaphragm ruptured and allowed the driver gas to enter the Channel. These variables were different from shock to shock and so introduced scatter into the observed shock speed measurements.

Scattering of data about the least squares line in Fig. 4-5 is comparable with that shown in Fig. 4-4. Fig. 4-5 contains measured versus predicted shock speeds for eighty mole percent Ar to twenty mole percent H_2 test gas mixtures to which metallic powdered samples had been added. As Fig. 4-5 refers to the 'Long' Channel modification it may be compared with Fig. 4-3. The slopes of the two one-term fits differ by only 0.5%. This difference is just slightly greater than the sum of the standard deviations in the slopes. The difference in slopes should not be attributed to sample or Hydrogen addition to the Test gas. Rather, it is due to the use of a TIM and not oscilloscope traces in the measurement of shock front transit times. Reference to Table 4-2, a summary of shock speed measurements for Argon plus Hydrogen Test gas mixtures, indicates that the observed shock velocity is about 87.5% of the predicted value for Test gas Hydrogen content in the 0 - 20% range.

The first entry in Table 4-2 is based upon a completely different set of incident shock data from that presented in Fig. 4-3. Of course, the data covers the same range of shock

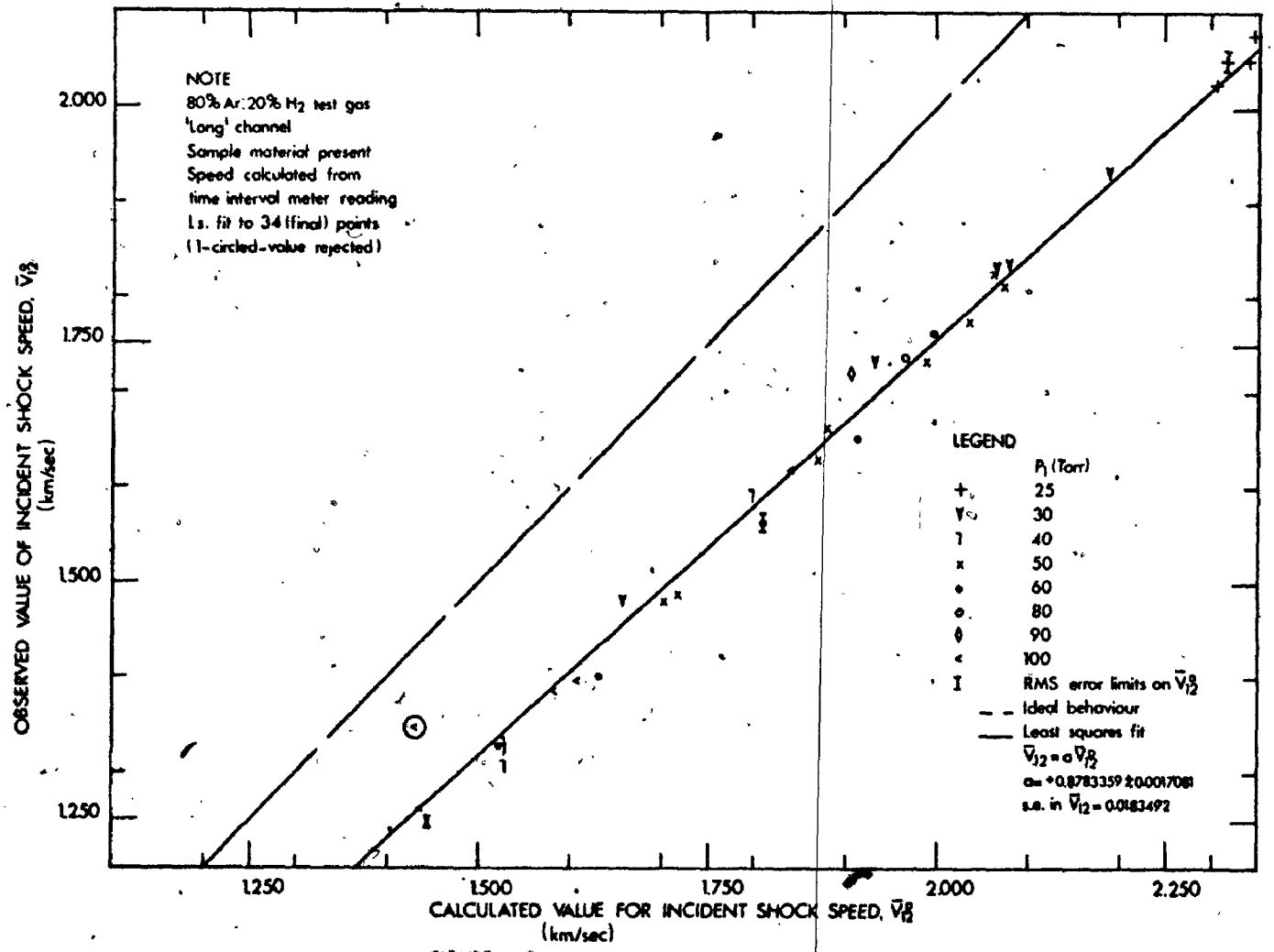

FIGURE 4-5

$\bar{V}_{12}$ VERSUS $\bar{V}_{12}^{R}$ FOR HYDROGEN DRIVEN SHOCK WAVES INTO AN 80% ARGON + 20% HYDROGEN INITIAL TEST GAS MIXTURE

TABLE 4-2

Influence of Ar:H_2 Test Gas Initial Composition upon the Least Squares Constant in Fits of the form $\bar{V}_{12} = a\bar{V}^{D}_{12}$ to $\bar{V}^{\circ}_{12}$ versus $\bar{V}^{D}_{12}$ data for Hydrogen driven Shocks. ($\bar{V}^{\circ}_{12}$ determined from TIM Readings.)

Initial % H_2	a	S.E. in $\bar{V}_{12}$ (km/sec)	Data Points Number	$\bar{V}^{\circ}_{12}$ Limiting Values (km/sec)
0**	0.8723 ± 0.0020	0.022	39(36)*	1.14/2.07
5	0.8729 ± 0.0012	0.017	59(54)	1.29/1.87
10	0.8762 ± 0.0020	0.021	31(31)	1.28/2.02
15	0.8791 ± 0.0036	0.028	20(20)	1.16/2.00
20	0.8783 ± 0.0017	0.018	35(34)	1.25/2.08

* For each H_2 concentration, the integer in parentheses is the number of points contributing to the fit. The integer preceding it is the number of data points initially available.

** Powdered sample material present for all other H_2 percentages.

conditions; but, for Fig. 4-8, oscillograms were employed in the determination of shock speed. Table 4-2 uses data from TIM measurements exclusively. The approximately 1% lower slope of the first entry in Table 4-2 in comparison with Fig. 4-3 is due in part to slightly different data scatter, in part to the use of an uncalibrated oscilloscope time-base and in part to the elimination of systematic observational bias in reading oscillograms by the use of automatic triggering of pulse amplifiers at pre-set voltage levels on the velocity probe output signals. Columns 3 and 4 of Table 4-1 compare the least-squares-fitted values of observed shock speeds in the 'Long' Channel determined by TIM and oscillogram measurements of shock transit times. Although the TIM data are about 1% lower in value than the others, the difference between fitted values of observed shock speed at any predicted speed is less than the sum of the standard errors of estimate in those fitted values. Possible sources of this difference have been mentioned above.

The hint of a slight increase in slope with increasing Hydrogen content given by the variation in the third decimal place within Table 4-2 may be a true indication. Yet the input data are not sufficiently precise to warrant such a conclusion. Table 4-2 supports the conclusion that incident shock speed determined by the transit time between probes P_1 and P_2 is about 87.5% of the theoretical value for Hydrogen driven shock waves into $Ar:H_2$ Test gas mixtures within the shock velocity range considered in this thesis, whether or

not a powdered sample is added to the Channel section.

4.1.2 Comparison of Incident Shock Transit Times over Two Contiguous Intervals

The preceding few paragraphs have treated the passage of the incident shock front between probes P_1 and P_2. The next few consider transit between probes P_2 and P_4. Reference to Fig. 4-1 will show that in this interval the shock must pass the transverse viewing windows before experiencing normal reflection at the end of the tube. If $\overline{V}^\circ_{24}$ denotes the mean speed between probes P_2 and P_4, then

$$\frac{\overline{V}^\circ_{24}}{\overline{V}^\circ_{12}} = \left(\frac{\Delta t^\circ_{12}}{\Delta t^\circ_{24}}\right)\left(\frac{\Delta x_{24}}{\Delta x_{12}}\right) = \frac{1}{a}\left\{\frac{\Delta x_{24}}{\Delta x_{12}}\right\} \qquad (4\text{-}1)$$

where a is the constant in a one-term linear least squares fit of Δt°_{24} vs Δt°_{12} data pairs observed for the same shock.

Two series of shock transit measurements were performed. In the first, the shock tube was operated in the customary mode for excitation and recording of emission and absorption spectra. In the second series of experiments, carefully machined inserts - placed in all window openings - converted the viewing 'head' into a uniform right circular cylindrical extension co-axial with the copper shock tube. In the latter configuration, probes P_2 and P_4 were separated by 22.9 ± 0.2 cm. The results obtained using this configuration are presented in Table 4-3.

For the experiments in which all inserts were used in the 'head', neither sample nor Hydrogen was added to the

TABLE 4-3

Comparison of values taken by the Least Squares Constant in Fits of the Form $\Delta t_{24} = a\Delta t^{\circ}_{12}$ to Δt°_{24} versus Δt°_{12} data for Hydrogen driven Shock Waves in Argon-Hydrogen Test gas mixtures.

Method of Measuring Δt°_{12}	Method of Measuring Δt°_{24}	Channel	Inserts	H_2 and Sample	a	S.E. in Δt_{24} (μsec)	Data Points Number	Δt°_{12} Limiting Values (μsec)
'Scope	TIM	Short	None	No	0.4870 ± 0.00085	1.7	26(24)†	253/565
'Scope	TIM	Long	None	No	0.4836 ± 0.00090	0.9	12(12)	255/335
TIM	TIM	Long	None	Yes*	0.4825 ± 0.00083	1.0	17(16)	250/383
TIM	'Scope	Long	All	No	$0.457_3 \pm 0.001_2$	1.7	19(19)	242/439
'Scope	TIM	Long	All	No	0.4571 ± 0.00069	1.5	34(33)	250/600

* Magnesium powder sample added to 10% or 15% Hydrogen content Test gases.

† The integer in parentheses is the number of data points included in the final fit. The number preceding it is the total number of data points available initially. Limiting values of time intervals are those actually included in the final fit.

Quoted error limits represent one standard deviation.

Argon Test gas. This procedure attempted to separate out the effects of shock attenuation that were not due to shock wave-sample interaction from those that were. Two independent sets of Δt°_{12} and Δt°_{24} data (for the same shock) are presented in Table 4-3. In those measurements, the oscilloscope time base had been calibrated against a crystal oscillator to reduce the error of time interval measurement. Both sets of data lead to the conclusion that $\Delta t_{24} = [0.457 \pm 0.001]\Delta t^{\circ}_{12}$. With this value for a and the probe separations given in Fig. 4-1, the ratio of mean speeds (with its rms error) in the two intervals is given by

$$\frac{\overline{V}^{\circ}_{24}}{\overline{V}^{\circ}_{12}} = 1.002 \pm 0.009_9$$

Consequently, when all inserts are used, the shock speed in the last 22.9 cm of the shock tube has the same value as in the preceding 50 cm within a 1% experimental error. (This error estimate is quite probably too large for the error in Δx_{24} - which dominates the rms error in the ration- is likely to be half that quoted. Such an error in Δx_{24} would lower the absolute rms error to 0.006_3.)

When the effects of sample addition and window bores are eliminated, the incident shock front travels the last 72.9 cm of this shock tube at constant velocity. Table 4-3 and Fig. 4-6 show that such is not the case when the window inserts are removed. (Table 4-4 gives requisite measurements of the 'head' internal dimensions.) The deviation from constant speed is directly attributable to the 16% volume increase

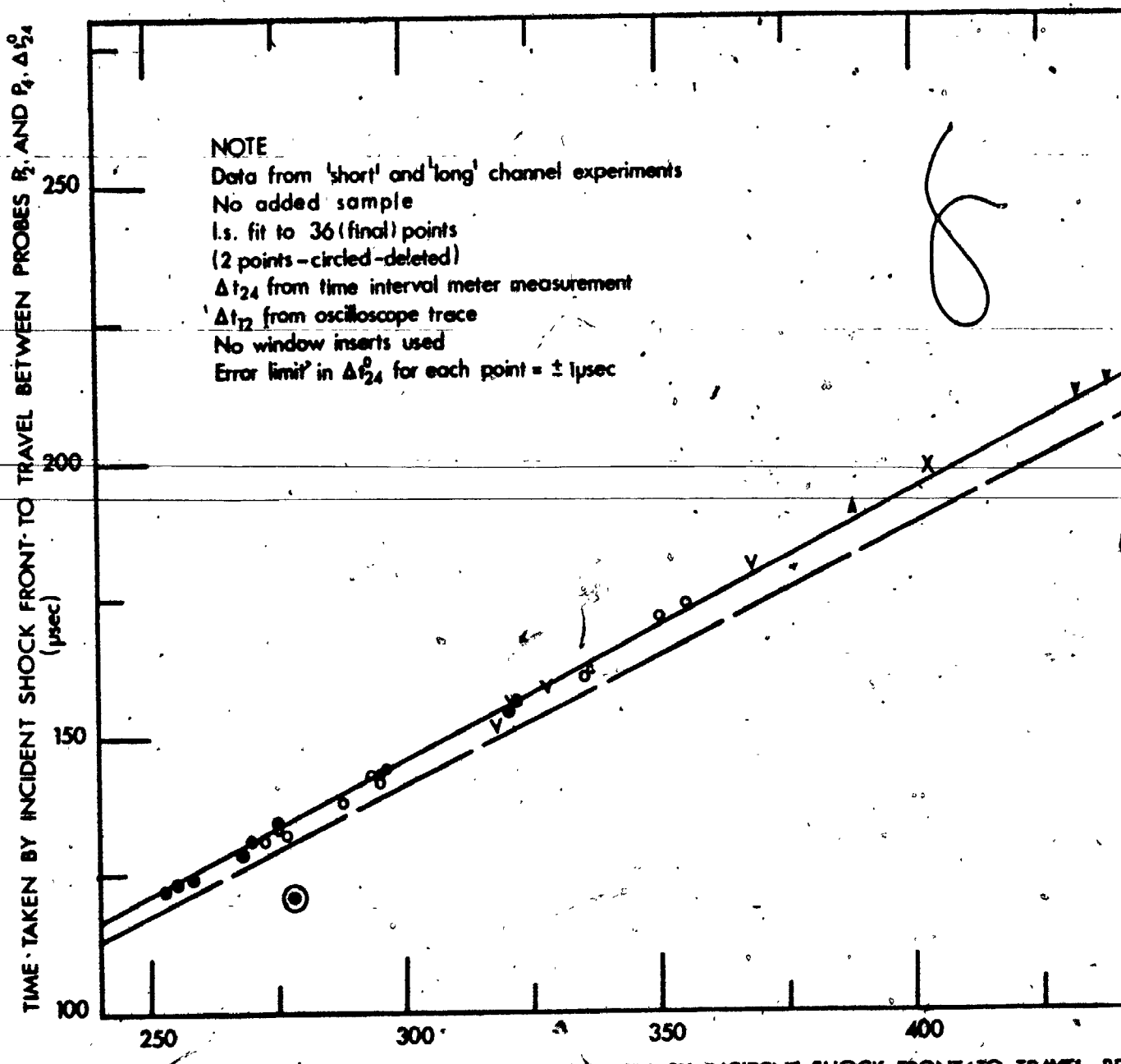

FIGURE 4-6

Δt^{o}_{24} VERSUS Δt^{o}_{12} FOR THE SAME HYDROGEN DRIVEN SHOCK WAVE IN ARGON. (COMBINED 'L

10

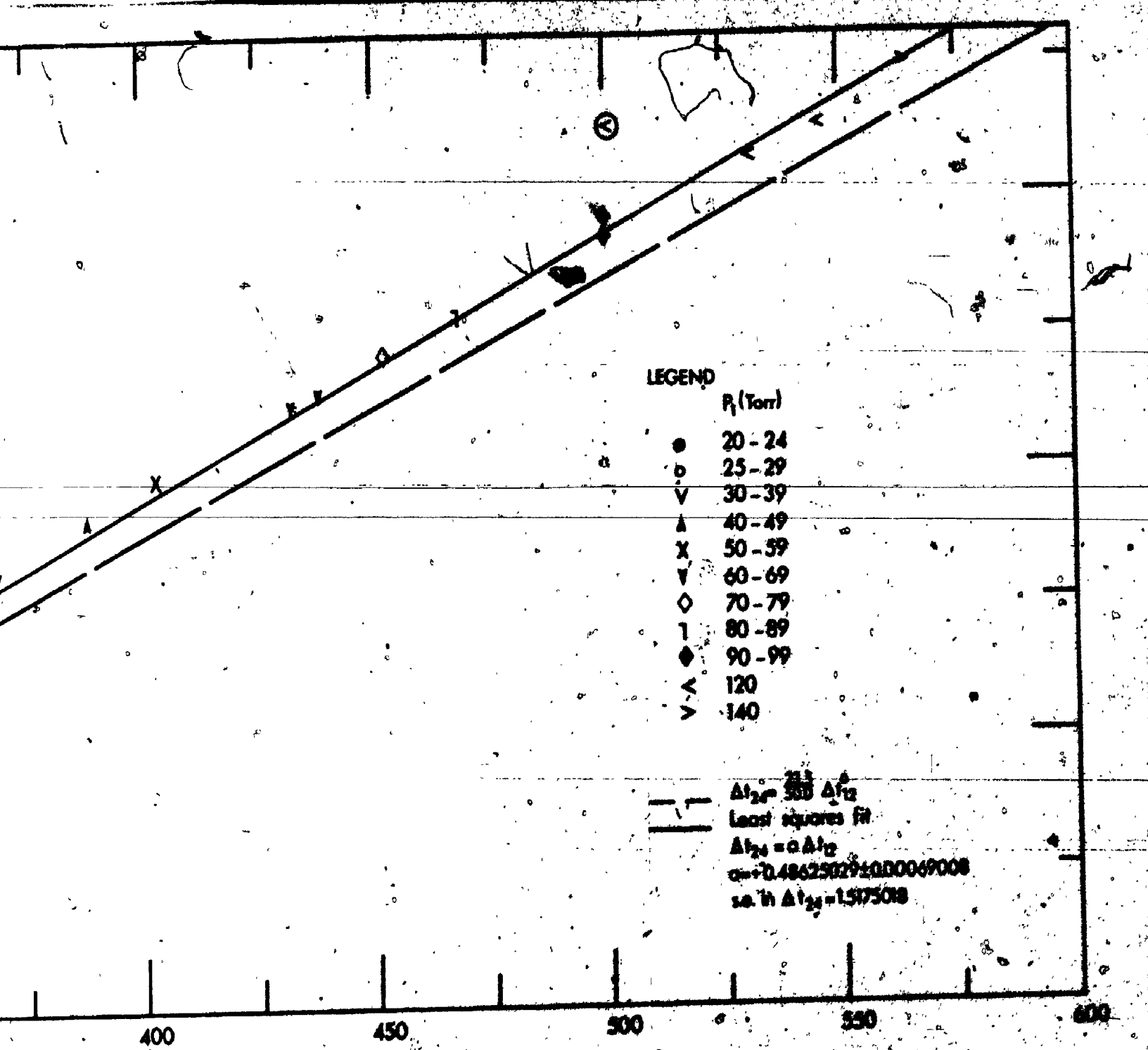

DENT SHOCK FRONT TO TRAVEL BETWEEN PROBES P_1 AND P_2, Δt_{12} (μsec)

K WAVE IN ARGON. (COMBINED 'LONG' AND 'SHORT' CHANNEL)

2 of 2

[redacted]

TABLE 4-4

Internal Dimensions and Volume of Shock Tube Viewing 'Head'

	Length (cm)	Diameter (cm)	Volume (cc)
Transverse Bore	*6.55	4.10	86.4_8
Longitudinal Bore	7.60	5.10	$155._{25}$
Volume of Transverse Bore not Common to Longitudinal Bore			25.1_5
End Window Support	0.60	4.10	7.9_2
Total Volume in 'Head' accessible to shock-heated gas			$188._{32}$
Distance from shock-reflecting end window to centre of Transverse Bore (cm)			5.20

* Measurement error in Length and Diameter is 0.005 cm

Common volume determined using integration by series expansion and by the procedure and tables of Hubbell (1964). Both methods yield 61.3_3 cc.

in the 'head' produced by the transverse bore which (as Fig. 4-6 illustrates) leads to an increase of 3.5% in the transit time between probes P_2 and P_4. It seemed reasonable to interpret the transit time increase as due to a decrease in mean speed over the interval Δx_w - from the shocks's first encounter with the window bore to the reflecting end wall - because spectroscopic observations were to be made in the reflected shock region after the reflected shock had passed the transverse bore (in the opposite direction).

Test gas shock-heated before the incident front's encounter with the side window bore continues to flow into this region with a speed greater than that of material shock-heated by passage through the shock front after the latter has reached the window location. The pressure disturbance equilibrates at a rate determined by the sound speed in the shock-heated matter. When the incident front has passed the transverse bore, its speed is still influenced by the effects of material entering that bore. The point-by-point calculations required to determine precisely the time-dependent behaviour of shocked gas within the transverse viewing region were not undertaken. They would have been most time-consuming and virtually irrelevant as the time-independent region (5) was to be the subject of spectroscopic investigation. The high temperature and pressure existing behind the reflected shock front and the flow of shock-heated material from region (2) into region (5) would quickly establish a uniform set of conditions behind the reflected shock front, after that front

had passed the side viewing location.

When the mean speed of the incident shock within a distance Δx_w of the end wall is identified by $\bar{V}_w$, then the ratio of $\bar{V}_w$ to the measured speed $\bar{V}^\circ_{12}$ may be expressed as

$$\frac{\bar{V}_w}{\bar{V}^\circ_{12}} = \frac{\left\{\frac{\Delta x_w}{\Delta x_{12}}\right\}}{\left\{\frac{\Delta t^\circ_{24}}{\Delta t^\circ_{12}}\right\} - \left\{\frac{\Delta x_{24} - \Delta x_w}{\Delta x_{12}}\right\}}, \qquad (4\text{-}2)$$

using the fact - established by the experiments using window inserts - that the shock travels the distance $(\Delta x_{24} - \Delta x_w)$ from probe P_2 with the mean speed $\bar{V}^\circ_{12}$. Thus, in the present case, with $\Delta x_w = 7.25$ cm (from Table 4-4) and $\Delta t_{24} = [0.486 \pm 0.001] \times \Delta t^\circ_{12}$ (from Fig. 4-6), the ratio of mean speeds is

$$\frac{\bar{V}_w}{\bar{V}^\circ_{12}} = 0.901 \pm 0.023$$

(The rms error is dominated by the measurement error in Δx_{24}. If the latter quantity were 0.1 cm - rather than the 0.2 assumed - the rms error in the ratio would be 0.012).) Had 0.483 been chosen for a instead of 0.486, the ratio of mean speeds would have been 0.918 with the same rms error.)

The above speed ratio was derived for Hydrogen driven shock waves in Argon from the data presented in Fig. 4-6. Those points are all values upon which the first two entries in Table 4-3 are based. Note that data points for 'Short' and 'Long' Channel configurations have been combined because

the 'Long' Channel data covers such a small range of Δt°_{12} values. Fig. 4-6 shows that the combined data scatter is very small and sustains the conclusion that the attenuation produced by the 'head' on a shock of known speed $\bar{V}^{\circ}_{12}$ is independent of the Channel configuration.

The third entry in Table 4-3 extends the last conclusion to shocks into Test gases containing Hydrogen and sample material. Once again the range of Δt°_{12} values is small, but the agreement with 'Long' Channel data in pure Argon is very encouraging. In fact, all three sets of data for the normal viewing 'head' show most satisfactory agreement. Consequently, just as velocity attenuation during the shock formation process was found to be unaffected by the Test gas Hydrogen and sample material content, so too the attenuation produced by changes in cross-sectional area within the viewing 'head' is independent of the Test gas composition. Therefore, within an experimental error of 1.5% - 2.5%, it may be assumed that the mean shock speed over the last 7.25 cm of the Channel is 10% lower than that measured over the interval Δx_{12}, i.e. is equal to $[0.90 \pm 0.02]U_1$.

4.1.3 Reflected Shock Transit Time Measurements

Reflected shock front transit times were measured only for H_2/Ar shocks. Of the reflected shock measurements, those using the 'Long' Channel equipped with all window inserts are presented in Fig. 4-7. There, two sets of data - derived from different series of shock runs - are plotted together.

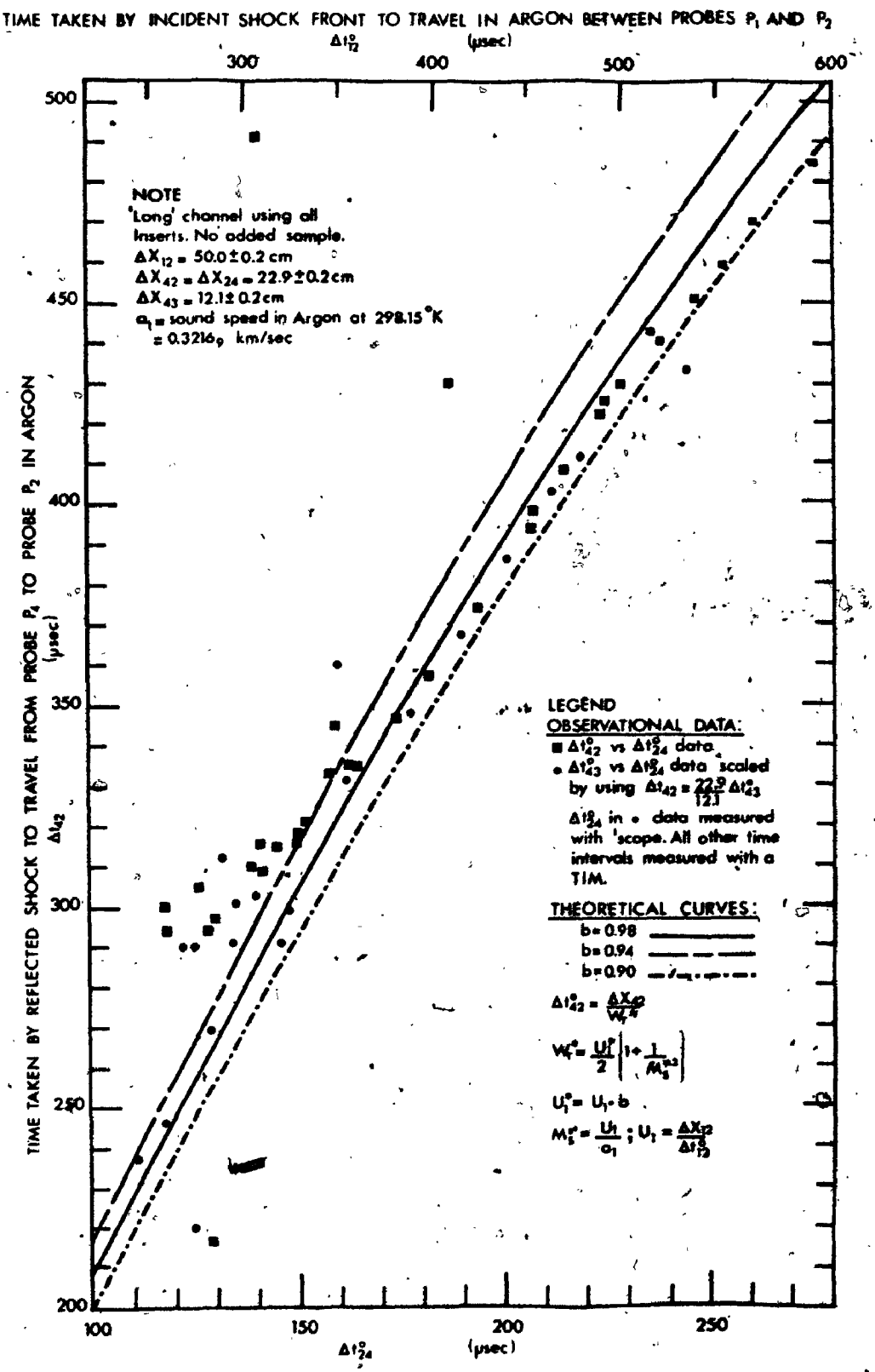

TIME TAKEN BY INCIDENT SHOCK FRONT IN ARGON TO TRAVEL FROM PROBE P_2 TO PROBE P_4

FIGURE 4-7

VARIATION OF REFLECTED SHOCK TRANSIT TIME WITH INCIDENT SHOCK TRANSIT TIME

In one set, transit times were measured over the distance Δx_{42}. In the other, the transit time Δt_{43} for the interval Δx_{43} (10.8 cm shorter than Δx_{42}) was the observed quantity. With Δt_{43} values scaled by the distance ratio - 22.9/12.1 - the two sets of points lie on a continuous curve for Δt_{12}>390 μsec. (Δt_{12}=390 μsec yields a shock speed of 1.32 km/sec and a Mach number of 4.10). By treating the point at Δt_{12}=350 μsec as a spurious reading, the scaled Δt_{43} values can be used to to extend the curve to Δt_{12}=310 μsec before these readings, too, show considerable scatter.

For Δt_{12}<350 μsec, the scatter in both sets of data has been interpreted as being caused by the arrival of the Contact Surface at the location of probe P_2 or P_3 before the arrival of the reflected shock front. The subsequent reflected shock front-Contact Surface interaction leads to increased transit times that are not determined solely by the reflected shock. These transit times are useless as a measure of the reflected shock speed since the interaction varies from shock to shock, depending on uncontrollable variations in the formation of the incident shock and the amount of diaphragm material carried along by the gas in region (2). On the other hand, for Δt_{12}>380 μsec, the two sets of data show that the shock crosses the intervals Δx_{43} and Δx_{42} at the same speed. Consequently, it may be asserted that the reflected shock front travels from the reflecting window to probe P_2 with constant velocity - for Δt_{12}>380 μsec.

Calculations, assuming ideal inviscid shock behaviour

indicate that the Contact Surface should traverse the distance between probes P_2 and P_3 in ~115 μsec for Δt_{12}=380 μsec and in 160 μsec for Δt_{12}=500 μsec. Consequently, the region of reliability of the Δt_{43} measurements should extend to Δt_{12}-values lower than those associated with Δt_{42} measurements. The data given in Fig. 4-7 certainly supports that contention. Thus, in that figure, all observed Δt_{42} data for Δt_{12}<380 μsec should be considered unreliable.

The cause of unreliable measurement resides in the pulse amplifier circuitry. These devices were designed to trigger TIMs or to provide sharp pulses on oscillograms when the output voltage of the heat transfer gauges was positive-going and had increased by a pre-set amount. No provision was made to abort on (or following) a negative-going voltage signal. When the contact surface moved past a probe, its voltage-time characteristic developed a negative slope as the resistance of the platinum film decreased, due to cooling of the probe by the expanded Driver gas. Examination of oscillograms showing output voltage-time curves of both probes P_2 and P_3 led to the above conclusions.

Theoretical values for the time taken by a constant speed reflected shock front to traverse the distance Δx_{42} have been evaluated using the relation

$$W_r^* = \frac{U_1^*}{2}\left\{1 + \frac{1}{M_s^{*2}}\right\} \qquad (4\text{-}3)$$

applicable to an ideal monatomic gas. (Derived by combining Eqs 54, 55, 67 and 68 of Parkinson (1957) and introducing the value of 5/3 for γ.) $U_1^*=bU_1$, with b an arbitrary attenuation factor and U_1 the measured incident shock speed. In Fig. 4-7, all the valid Δt_{42} values fall between the curves determined by b=0.94 and b=0.98 for $\Delta t_{12}>380$ μsec. Consequently, for the 'Long' configuration with the volume-increasing effects of the 'head' eliminated, the reflected shock speed may be interpreted as that characteristic of an incident shock of speed $[0.96\pm0.02]U_1$ - where U_1 is determined from Δt_{12} measurements.

Some data points with $\Delta t_{12}<350$ μsec lie very close to the b=0.94 curve. These points may represent valid measures, but the scatter of other points in this time domain precludes their use for reflected shock speed calculations. If they are valid, however, they may be used to infer that the Contact Surface and reflected shock front must meet very close to the location of probe P_3, because the Contact Surface has to be moving slowly enough that it will reach probe P_3 following the arrival of the incident front at probe P_2, after a time interval having a lower limit of $[\Delta t_{24}+\Delta t_{43}]$. This argument, when applied to the data accepted as valid, calls for automatic rejection of reflected front velocity determinations derived from Δt_{42} transit times associated with $\Delta t_{12}<390$ μsec. If the channel length is increased in any way, a greater value of Δt_{12} will be required as the lower limit for acceptable Δt_{42} data.

Table 4-3 shows that the incident front does take longer to cover distance Δx_{42} when the window inserts have been removed. Consequently, with the shock tube used in its 'spectroscopic' configuration ('Long' Channel with no inserts), observed Δt_{42} values will not lead to correct measures of the reflected wave speed when $\Delta t_{12}<390$ μsec. Examination of Fig. 4-8, which summarizes data taken when the window inserts were removed, indicates the onset of scatter (interpreted as due to Contact Surface arrival prior to reflected front) occurs about $390<\Delta t_{12}<400$ μsec as expected. The apparent division of valid data into the distinct response groups $400<\Delta t_{12}<500$ μsec and $500<\Delta t_{12}<575$ μsec most probably is due to a slight relative error in the two oscilloscope time ranges employed (0.1 msec/cm and 50 μsec/cm). As the accepted data lie between the theoretical limiting curves $0.85<b<0.95$, it was concluded that, for the 'Long' Channel without inserts configuration, the reflected shock speed could be taken as that corresponding to a shock of incident speed $[0.90\pm0.02]$ U_1 - with U_1 determined from Δt_{12} measurement. This result is in excellent agreement with the previous conclusion that the incident shock front travels through the viewing 'head' with a mean speed $[0.90\pm0.02]U_1$.

4.1.4 Reflected Shock Temperatures in Ar:H_2 Test Gases Evaluated from Δt_{12} Measurements

The earlier findings that Ar:H_2 mixtures exhibited the same behaviour both with respect to attenuation during shock

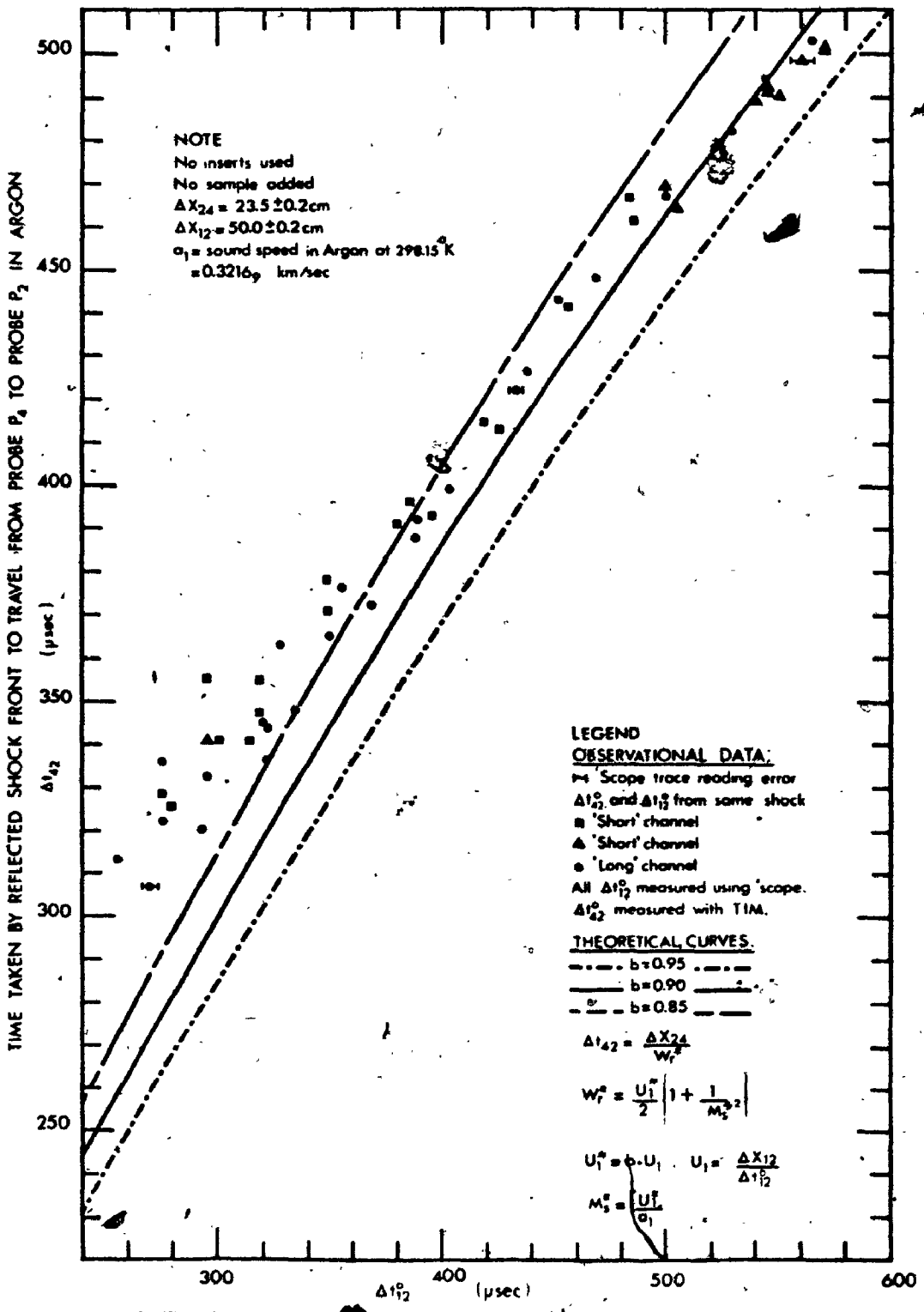

TIME TAKEN BY INCIDENT SHOCK FRONT TO TRAVEL IN ARGON FROM PROBE P_1 TO PROBE P_2

FIGURE 4-8

EFFECT OF OBSERVING 'HEAD' UPON REFLECTED SHOCK TRANSIT TIME

formation and later in response to passage past the transverse viewing windows, form the justification for the assumption that reflected shock front speeds in Ar:H_2 mixtures would exhibit the same behaviour across the viewing 'head' as that found for H_2/Ar shocks. (As Fig. 2-9 indicates, the equilibrium region will build out from the end wall at a speed considerably lower than this.) Thus all temperatures used for identifying spectra and oscillograms in the remainder of this document were evaluated by considering the incident shock speed through the observation region to be equal to $0.90U_1$ - with U_1 determined from Δt_{12} measurements.

The seven spectra shown in Chapter 6, for which spectrum synthesis was attempted, were obtained from $3.57<M_s<4.25$ Hydrogen driven shocks into Ar:H_2 Test gases containing 15% to 20% H_2. The corresponding transit times in pure Argon would be $435>\Delta t_{12}>366$ μsec. As the Δt_{43} measurements recorded in Fig. 4-7 have led to the conclusion that the Contact Surface and reflected shock front meet near probe P_3 for $\Delta t_{12}<310$ μsec, it is expected that the interaction for Ar:H_2 mixtures will occur between probes P_2 and P_3 - yet quite close to probe P_3. Perhaps for the lowest Δt_{12}-values the location of the interaction will be given a slight distance from probe P_3 towards the end wall.

4.2 Studies of Time-Resolved Shock-Excited Luminosity

Time-resolution of the shock-produced luminosity was undertaken initially to determine if the grey powder deposits

found on the observation windows after shock excitation of powdered samples would have adverse effects on the quantitative spectrophotometric experiments planned for MgH. The first of these studies involved the use of a Beckman & Whitley, Inc. Dynafax Framing Camera.

4.2.1 Framing Camera Records of Total Shock-Excited Luminosity

The Framing Camera was focused on one of the transverse viewing windows and operated at a rate of 25,000 frames per second, with a 2.6 μsec exposure per frame. Two records of shocks produced under identical initial conditions are presented as Fig. 4-9b and 4-9c. A plot of photographic image mean density vs time for record (b) is shown as Fig. 4-9a. The shock-reflecting end wall is located above the records in Fig. 4-9 - towards the graph - and the top of the window is at the right of each image.

At an arbitrary instant, t=0, the window appears clean and faintly illuminated by some readily excited luminosity in the reflected shock zone - presumably the Na-D lines. (Other studies using LS400 photo-detectors did indicate that Sodium radiation was the first to appear.) Within 100 μsec, the radiation becomes much more intense. However, during that early period the radiation pattern indicates turbulent mixing of radiating and non-radiating gas within the transverse bore. About 250 μsec after the radiation was first detected, it has reached a maximum intensity. For about 150 μsec on either

(a)

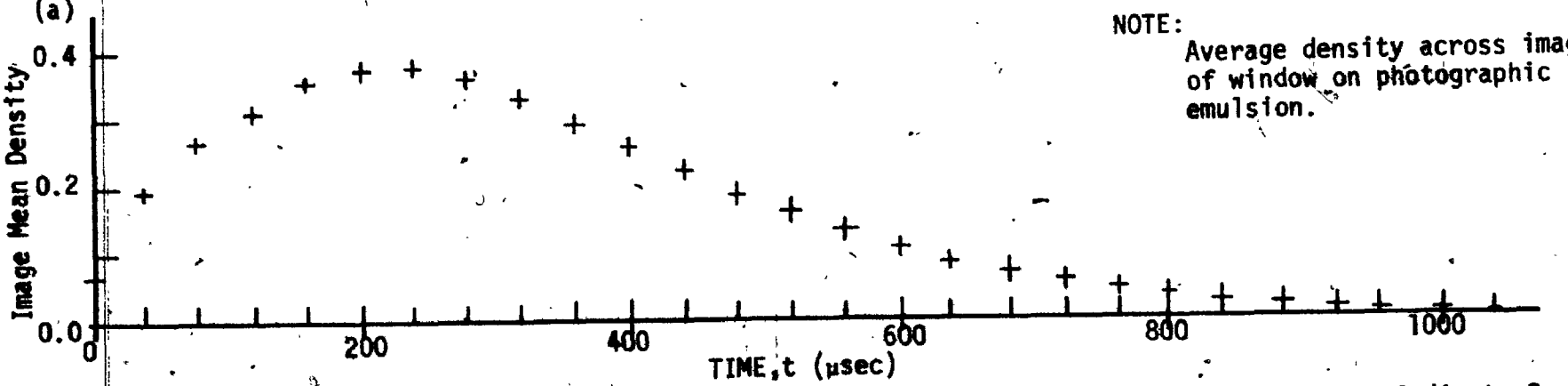

NOTE:
Average density across image of window on photographic emulsion.

Approximate Variation of Log_{10}(Emitted Shock Luminosity) for record (b) below. (Arbitrary Ordinate Scale)

(b)

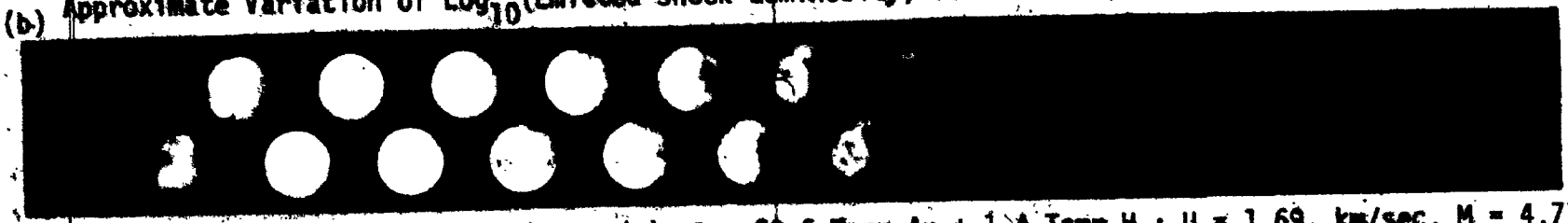

Shock Conditions for records (b) and (c): P_1= 28.6 Torr Ar + 1.4 Torr H_2; U_1= 1.69$_5$ km/sec, M_s= 4.71; P_5= 5.98 atm, T_5= 3880°K

(c)

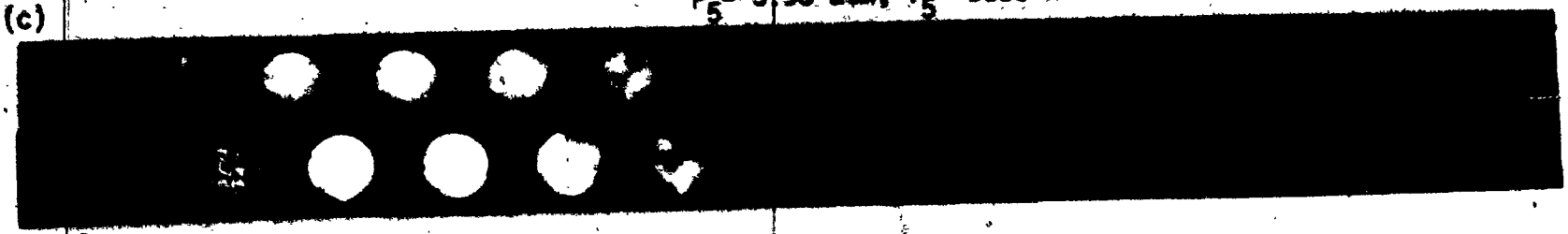

FIGURE 4-9

Framing Camera records - 2.6 μsec exposures at 40 μsec intervals of Luminosity from two separate runs using Ar:H_2 Test gases to which a Magnesium powder sample had been added. Camera focused on 4.10 cm diameter Transverse Viewing Window

side of this maximum, the observation window appears to be uniformly illuminated by shock-produced radiation. About 400 μsec after the arbitrary t=0, darkened regions appear on the photographs. Some of these are true deposits, others are cooler masses of gas mixing with those still emitting radiation. Record (b) clearly shows darkened areas on the quartz window for 600<t<950 μsec as a bright gaseous region apparently undergoes a clockwise rotation. Thus it appears that, for the first 500 μsec after initial detection of reflected shock luminosity, the formation of deposits on the viewing window should have minimal effect upon quantitative photometric studies of MgH.

The post-shock deposit on the quartz windows was not composed only of grey powder. Mixed at random in it were f fine shards of diaphragm material, and beneath it (usually imbedded in pits within the window) were bright silver spatters formed by collision of liquified sample droplets with the window surface. Photomicrographs showed that particle sizes in the deposit were at least a factor of 10 smaller than the 38 micron Magnesium sample size. These particles and the liquid droplets gradually pitted the windows until etching had so severely curtailed transmittance that it became necessary to install new windows.

During these studies to evaluate the effects of deposit formation, another interesting observation was made. It has already been mentioned; but its significance has not. For approximately 100 μsec after the reflected shock radiation

is detected, that radiation has a rather low intensity. This interval has been interpreted as an induction period during which significant concentrations of heated MgH are formed by chemical interactions within the reacting mixture. The rate at which these reactions produce electronically excited MgH molecules and Mg atoms cannot be determined from the time-resolution of total luminosity. It can be determined by time-resolution of spectral features particular to each species. Therefore, the following paragraphs are addressed to such investigations.

4.2.2 Time-Resolution of Radiation Emitted by Specific Species Behind the Reflected Shock Front

Two impurity features - the Na-D lines and the Ca I resonance line - plus two Mg I lines and the MgH (0,0) P-head were investigated. A Leeds and Northrup scanning spectrometer with its output fed into a Tektronix 535A oscilloscope was used to follow the time dependence of shock-excited luminosity. That luminosity was focused upon the 100 μ spectrometer entrance slit by a lens which produced a reduced image of the transverse observation window. Only one spectral feature could be observed per shock run.

Oscillograms illustrating the course of luminosity for Na I 5893Å, Ca I 4227Å and Mg I 5183Å radiations are shown in Fig. 4-10. The general features of the three time-dependent intensities are the same, indicating that these three emitters are present in the same region of the shocked gas mixture.

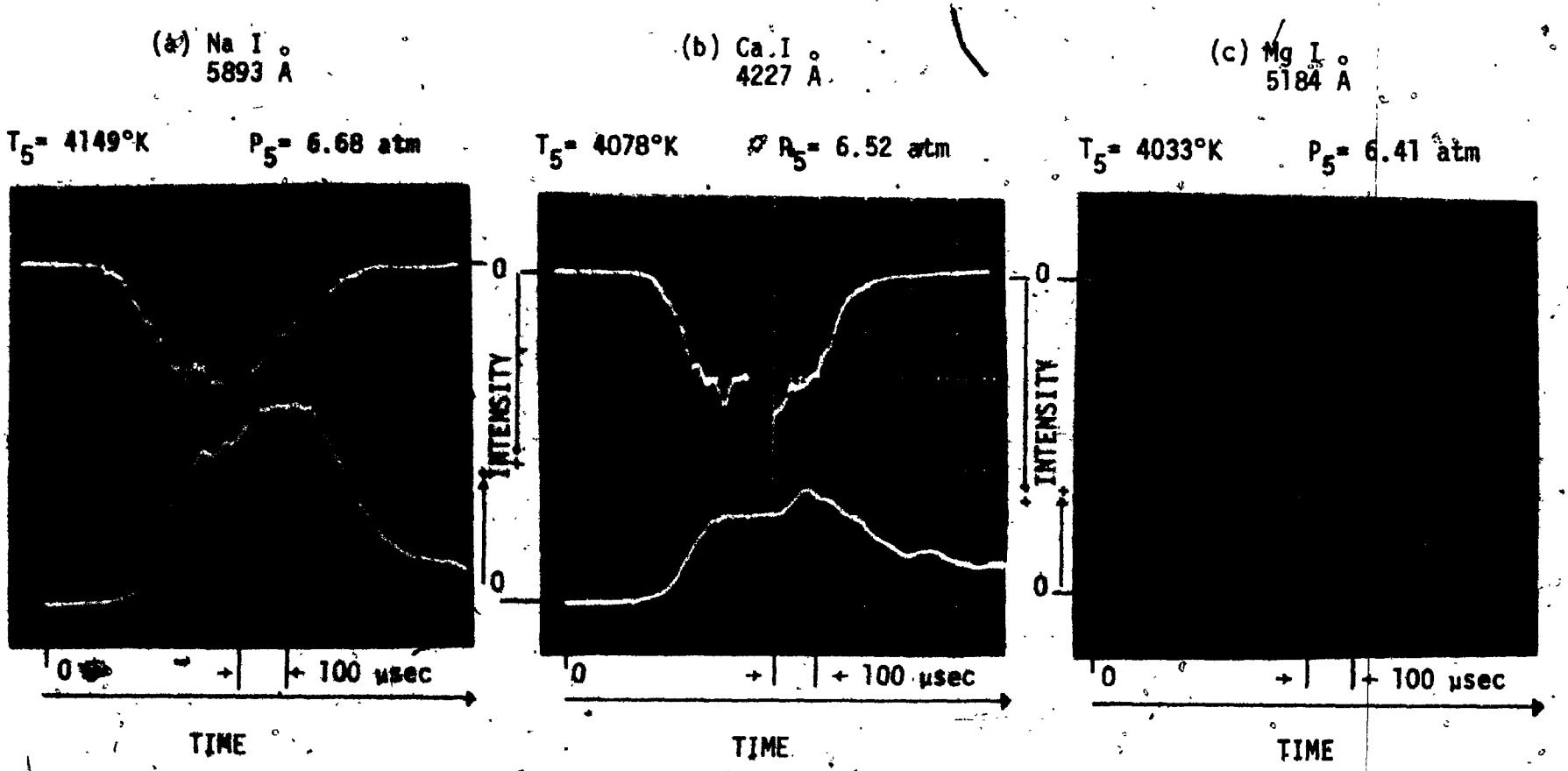

FIGURE 4-10

Time-Resolved Intensity of Three Strong Emission Lines Radiated by Ar:H_2 Test gas Shock-Heated within the Reflected Wave Region. Upper traces due to indicated Atomic Lines. Lower traces are [5905 ± 50] Å radiation detected by an LS 400 unit ~1.9 cm closer to probe P_3. All traces triggered by Incident Shock Front arrival at location of probe P_3.

The fact that the Na I intensity-time curve is not identical with the other curve superposed on the same oscillogram deserves some comment. That other curve is the output of an LS400 light detector located 1.9 cm closer to probe P_3 than the region focused on the spectrometer. The spectrometer field of view was wider than the narrow cone observed by the LS400. Finally, the LS400, although located behind filters that effectively limited its response to wavelengths in the range 5905±50Å, did not follow just the course of the Na I emissions. The LS400 response does seem to start within 50 μsec of the spectrometer response on each of the three oscillograms within Fig. 4-10; but the peak in the LS 400 response curve occurs later than the one in the spectrometer's output. The only significance attached to these observations was that response at the LS400's location was delayed about 50 μsec, with respect to the spectrometer due to the finite time required for the equilibrated region to build up between the two locations.

On the Mg I trace there exists a small blip in the response curve at t=150 μsec. If this is interpreted as the instant that the reflected shock front passes the spectrometer field of view, it is not until about 100 μsec later that the Mg I response has become an appreciable fraction of its maximum value. This behaviour is in excellent agreement with the results obtained from Framing Camera photographs.

In Fig. 4-10, all the spectrometer output curves show a 50 μsec wide intensity peak. This was caused by discharging

an FX-33 flash unit. (At the same time that time-resolved luminosity was being investigated, a calibration was being performed of a time delay circuit for controlling the flash unit.)

Intensity versus time curves for the Mg I 5528Å line and the MgH (0,0) P-head are shown in Fig. 4-11. The remarkable similarity of the three curves clearly shows that these radiations originate in the same regions of the viewing 'head' and are controlled by the same mechanism. The oscillograms indicate a linear increase in emitted intensity with time. Thus time-resolution of Mg I and MgH spectral features has shown that these emitters exist in the same region and have the same time-dependence of upper state population. These conclusions become all the more noteworthy when the LS 400 outputs for these shock runs are compared. Those output features change from shock to shock.

4.3 Impurity Radiation from the Shock Tube

Spectrograms obtained at T_5-values greater than 4000°K exhibit many atomic lines whether or not a sample material has been used. These lines belong to a large number of elements and seem to arise from the remains of previously introduced sample material lodged in regions of the shock tube inaccessible to the experimenter.

Such lines are a cause of grave concern when quantitative spectroscopic measurements are to be made, as allowance must be made for their presence. Thus as many lines (in the in-

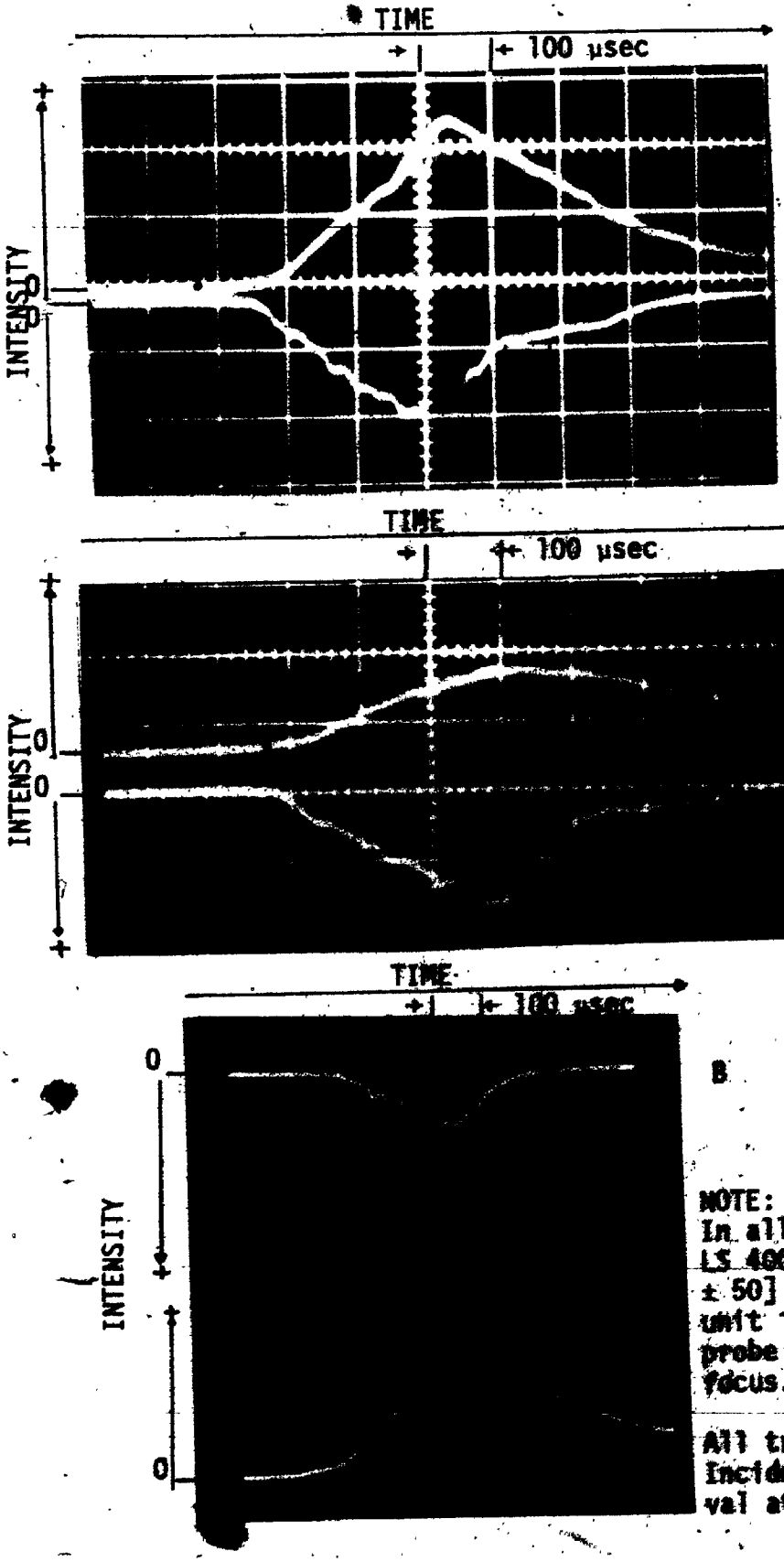

FIGURE 4-11

Time-Resolved Intensity of Mg I and MgH Radiations excited by Reflected Shock Wave. (Intensity scales have arbitrary units.)

TABLE 4-5

High Temperature Background Radiation from the Shock Tube (in the wavelength interval 4200Å - 6500Å) Emitted by Metallic Impurities.

Active Species	Wavelength (Å)	Multiplet (No.)	E_ℓ (eV)	E_u (eV)
BaI	*5535.484	$6^1S - 6^1P^\circ$ (2)	0.00	2.23
	6110.784 6063.117 6019.470 5971.699 5997.088	$5^3D - 5d6p\,^3P^\circ$ (7)	1.18	3.20
BaII	*4554.033 4934.086	$6^2S - 6^2P^\circ$ (1)	0.00	2.71
	6141.718 6496.896 5853.675	$5^2D - 6^2P^\circ$ (2)	0.70	2.71
CaI	*4226.728	$4^1S - 4^1P^\circ$ (2)	0.00	2.92
	6162.172 6122.219 6102.722	$4^3P^\circ - 5^3S$ (3)	1.89	3.89
	4454.781 4434.960 4425.441 4455.887 4435.688 4456.612	$4^3P^\circ - 4^3D$ (4)	1.89	4.66
	4302.527 4298.986 4318.652 4307.741 4283.010 4289.364	$4^3P^\circ - 4p^2\,^3P$ (5)	1.89	4.76

TABLE 4-5 (Contd.)

High Temperature Background Radiation from the Shock Tube (in the wavelength interval 4200Å - 6500Å) Emitted by Metallic Impurities.

Active Species	Wavelength (Å)	Multiplet (No.)	E_ℓ (eV)	E_u (eV)
CaI	5588.757 5594.468 5598.487 5601.285 5602.846 5581.971 5590.120	$3^3D - 3d4p\,^3D°$ (21)	2.51	4.72
	5270.270 5265.557 5262.244 5264.239 5261.706	$3^3D - 3d4p\,^3P°$ (22)	2.51	4.86
	5349.472	$3^1D - 3d4p\,^1F°$ (33)	2.70	5.00
	5857.454	$4^1P° - 4p^2\,^1D$ (47)	2.92	5.03
CuI	5105.541 5782.132	$4s^2\,^2D - 4^2P°$ (2)	1.38	3.80
	5218.202 5153.235 5220.070	$4^2P° - 4^2D$ (7)	3.80	6.17
MgI	5183.6042 5172.6843 5167.3216	$3^3P° - 4^3S$ (2)	2.70	5.09
NaI	*5889.953 5895.923	$3^2S - 3^2P°$ (1)	0.00	2.10

TABLE 4-5 (Contd.)

High Temperature Background Radiation from the Shock Tube (in the wavelength interval 4200Å - 6500Å) Emitted by Metallic Impurities.

Active Species	Wavelength (Å)	Multiplet (No.)	E_ℓ (eV)	E_u (eV)
TiI	5210.386	$a^3F - z^3F^\circ$	0.05	2.42
	5192.971	(4)		
	5173.742			
	5064.654	$a^3F - z^3D^\circ$	0.05	2.48
	5039.959	(5)		
	5014.185			
	*4981.732	$a^5F - y^5G^\circ$	0.84	3.33
	4991.067	(38)		
	4999.504			
	5007.209			
	5014.277			
	5016.162			
	5020.028			
	5022.871			
	5024.842			
	4533.238	$a^5F - y^5F^\circ$	0.84	3.57
	4534.782	(42)		
	4535.574			
	4535.920			
	4536.051			
	4555.486			
	4552.453			
	4548.764			
	4544.688			
	4512.734			
	4518.022			
	4522.798			
	4527.305			
ZrI	*4687.80	$a^5F - y^5G^\circ$	0.73	3.36
	4710.08	(43)		
	4739.48			
	4772.32			
	4815.62			

* - indicates a 'Raie Ultime'

terval 4000Å-6000Å) as possible were identified. They are listed in Table 4-5.

4.4 Pressure Measurements in Region (5)

The pressure in region (5) was not monitored during the present work. However, on two occasions the catastrophic failure of the end window placed a lower limit on the pressure achieved. On the first occasion, weakening of the window due to continual pitting was assumed to have decreased its strength. Following the second rupture, it was found that the window should have safely sustained a loading of 10 atmospheres while the calculated pressure within region (5) was 12 atmospheres. To prevent further occurrences of that nature, external brass supports were made to fit into the window retaining screw caps. Calculations based on information supplied by the Canadian General Electric Company Limited provided assurance that a support with a 3/4 inch diameter central hole would withstand pressures up to 25.4 atmospheres. Such supports were used with shocks for which the calculated P_5 value was greater than 20 atmospheres and no further window failures were encountered.

CHAPTER 5

Qualitative Spectroscopic Studies

From a consideration of the thermodynamics of metal-hydrogen-hydride systems, the author concluded that the diatomic hydrides MgH, BeH and AlH would be formed in quantities sufficient for quantitative spectroscopic analysis when Mg, Be and Al powders were shock-excited in Argon-Hydrogen test gas mixtures. Some results of experiments performed to test that hypothesis are presented in this chapter. Those results take the form of emission and absorption spectrograms, tables of observed atomic lines and Deslandres Arrays of detected bands. Bands belonging to the A - X transitions for all three hydrides were detected both in emission and in absorption.

Atomic lines and molecular features were identified with the aid of: 'Identification of Molecular Spectra' - Pearse & Gaydon (3rd ed., 1962); 'Spectra of Diatomic Molecules' - Herzberg (2nd ed., 1950); NBS Monograph 32 'Tables of Spectral-Line Intensities' - Meggers, Corliss & Scribner (1961); NBS Circular 467 'Atomic Energy Levels' - Moore (1949, 1958); 'A Multiplet Table of Astrophysical Interest' - Moore (revised ed., 1945); and the 'MIT Wavelength Tables'-- Harrison (1932).

Precision in wavelength estimation was achieved both by preparing large scale photographic enlargements from spectrograms and by making microdensitometer tracings of those spectrograms that expanded the apparent displacement between features by a factor of 50. In this way, it was ascertained that spectral features with a wavelength separation of less than 0.80 Å could be resolved.

Each set of spectra presented in the following pages is accompanied by a reference spectrum, a wavelength scale or both. In addition, each spectrum is identified by a set of calculated T_5 and P_5 values indicative of conditions within the reaction mixture when the spectrum was obtained. More complete information concerning the state of the shocked gas (based upon measured incident shock speed) is included within the tables forming Appendix B.

5.1 Studies of MgH

5.1.1 Emission Studies

The five emission spectra of Figure 5-1 are representative of those obtained when Magnesium powder was subjected to shock-excitation in an $Ar:H_2$ Test Gas mixture. As the spectra illustrate, bands of the MgH $A^2\pi - X^2\Sigma^+$ system and lines of the neutral Magnesium atom are prominent features of the luminosity from the shock tube. Table 5-1 is a list of all the Mg I lines detected in the shock-generated spectra. The

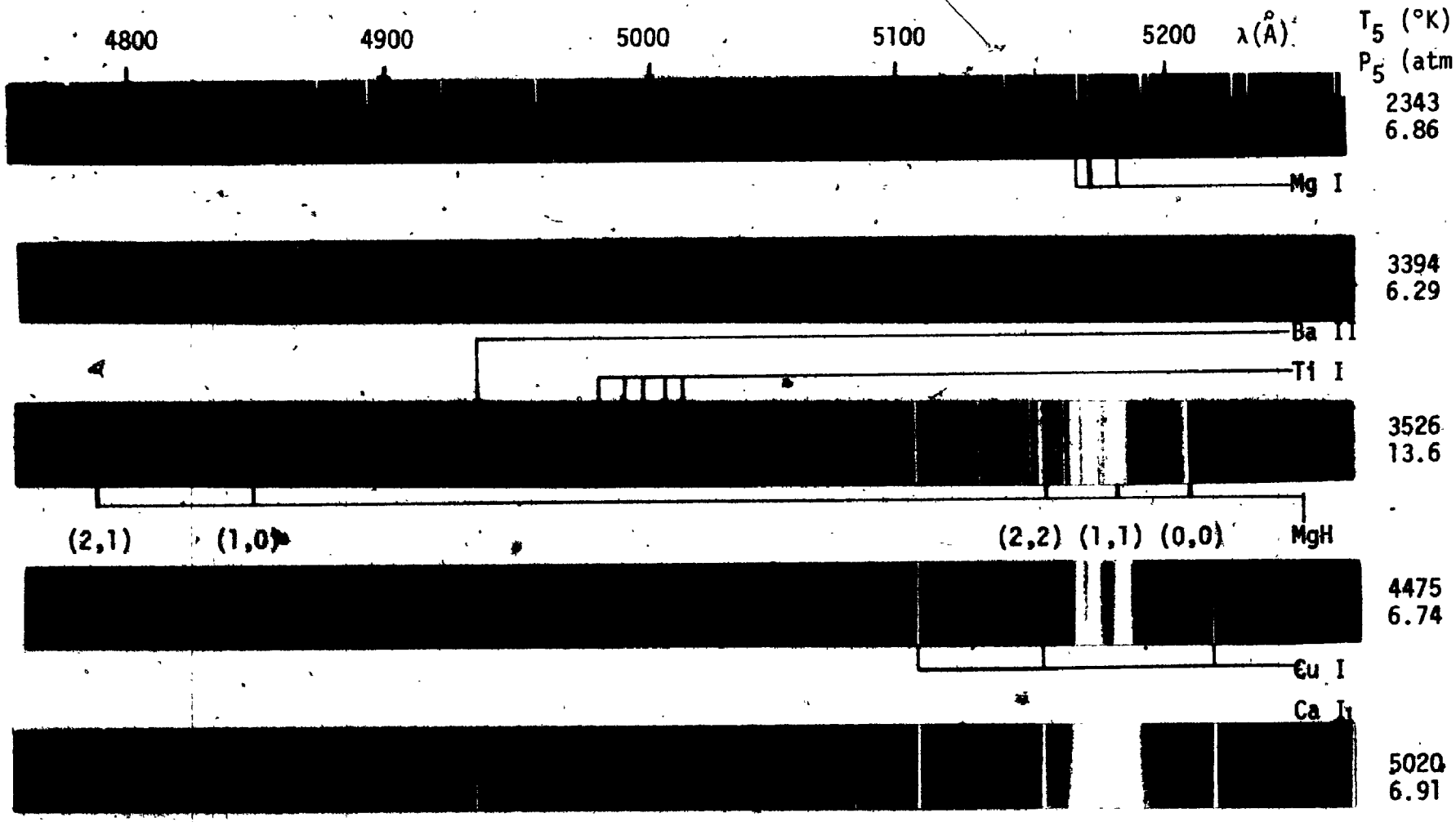

FIGURE 5-1

Emission Spectra of Luminosity from Magnesium samples shock-excited in Ar:H_2 Test Gases

identity of all MgH $A^2\Pi - X^2\Sigma^+$ bands detected in the shock-excited luminosity is presented in Table 5-2. The relative magnitudes of the Franck-Condon Factors, also listed in Table 5-2, give an approximation to the relative intensities of the emission bands. Thus, according to the relative FCF values, the $\Delta v=0$ sequence should be the most intense feature of the MgH spectrum - which it is.

The spectra of Fig. 5-1 cover the range of excitation temperatures $2300<T_5<5020°K$ and illustrate a feature of the shock-excitation process that was detected in earlier studies (McGregor, 1962). At low temperatures (provided that chemical reactions are fast enough) interaction between sample and Test Gas leads to predominance of molecular features in the emitted luminosity. At high temperatures - where molecular dissociation is appreciable - atomic and ionic lines are the dominant features of emission spectra. A mixture of atomic lines and molecular bands occur at intermediate temperatures.

At the highest temperature used to produce the spectra of Fig. 5-1, $T_5=5020°K$, atomic features do not arise solely from the added sample material - impurity lines occur as well. These impurities arise from remnants of past sample materials (lodged in portions of the facility inaccessible to the experimenter) being swept up by energetic shock waves.

The spectra of Fig. 5-1 that were excited at $T_5=2343°K$ and $3394°K$ illustrate a point about sample size. The second spectrum is fainter than the first yet the Mg I lines in it are more intense relative to the (0,0) P-head than is the case in the other spectrum. The second observation leads to the conclusion that the two spectra are correctly

ordered as functions of increasing temperature. The faintness of the second spectrum indicates that it was emitted by a smaller amount of sample material present in the hot gas than was present for the production of the first spectrum.

TABLE 5-1

Mg I Lines Detected in Luminosity from Magnesium Powder samples shock-excited in Ar:H_2 Test Gases.

Wavelength* (Å)	Multiplet (No.)	E_ℓ (eV)	E_u (eV)
4571.0956	$3^1S - 3^3P^\circ$ (1)	0.00	2.70
5183.6042 5172.6843 5167.3216	$3^3P^\circ - 4^3S$ (2)	2.70	5.09
5711.0880	$3^1P^\circ - 5^1S$ (8)	4.33	6.49
5528.4047	$3^1P^\circ - 4^1D$ (9)	4.33	6.56
4702.9909	$3^1P^\circ - 5^1D$ (11)	4.33	6.95
4351.9056	$3^1P^\circ - 6^1D$ (14)	4.33	7.16

*Standard Air Wavelengths from Risberg (1965), Multiplet designations, numbers and energy levels from Moore (1945).

TABLE 5-2

P-heads (Å in Standard Air) and Franck-Condon Factors for MgH $A^2\pi$ - $X^2\Sigma^+$ bands detected in the Luminosity produced by shock-exciting Magnesium Powder in Ar:H_2 Test Gases.

v' \ v"	0	1	2
0	5211.0 *0.944 0.944 0.941_4	5621.4 0.0518 0.0515 0.0538_7	
1	4845 0.0558 0.0556 0.0583_0	5182.3 0.839 0.838 0.828_4	5568.3 0.0929 0.0929 0.0994_5
2			5155.2 0.738 0.734 0.719_1

*Order of the three FCF entries:

McCallum, Jarmain & Nicholls (1970) using RKR potentials.
Popkie (1971) using RKR potentials.
Author using Morse potentials with constants determined by least squares fits to Guntsch (1939) $\Delta G(v+1/2)$ values. Dropped digit is indicative only of need to round off the third significant figure.

The third spectrum - the one emitted at T_5=3526°K - seems to have the greatest over-all intensity of Mg and MgH features - as if the largest amount of sample-shocked gas interaction had occurred for this case. All other spectra in Fig. 5-1 were recorded when the pressure behind the reflected shock front, P_5, was about 7 atm. For the third spectrum the pressure was ~14 atm. The observed enhancement led to the

question: 'If doubling P_5 can enhance Mg and MgH, will further increases in P_5 produce greater enhancement?'

Shock tube runs designed to yield high P_5 values resulted in the spectra shown in Fig. 5-2. The central spectrum was obtained with $P_5 \simeq 7$ atm - the others had P_5 values ca 14 and 20 atm respectively. Although the MgH $A^2\pi - X^2\Sigma^+$ system and the Mg I triplet at 5183 Å are still present with appreciable intensity, there seems to be no increase in the enhancement of these features over that found for $P_5 = 13$ atm in Fig. 5-1.

However, the spectra obtained at such high P_5 - values exhibit an unexpected feature - strong C_2-Swan band emissions. Subsequent experiments proved that the C_2-Swan system would often appear as an impurity over the temperature interval $3500 < T_5 < 4500°K$ when P_5 was 10 atm or higher. A list of the observed Swan bands is included as Table 5-3. The source of the Carbon impurity was attributed to thermal decomposition of the Mylar film sample support as it was carried downstream by the incident shock.

A close examination of the (0,1) Swan band in Fig. 5-2 will show that several rotational lines are missing. Emissions at these wavelengths have been completely absorbed by atomic lines of the Ca I $3^3D - 3d4p\,^3D°$ multiplet (ca 5590 Å).

5.1.2 Emission and Absorption Spectra from the same Hot Gas

The High Speed Shutter was arranged to uncover half the

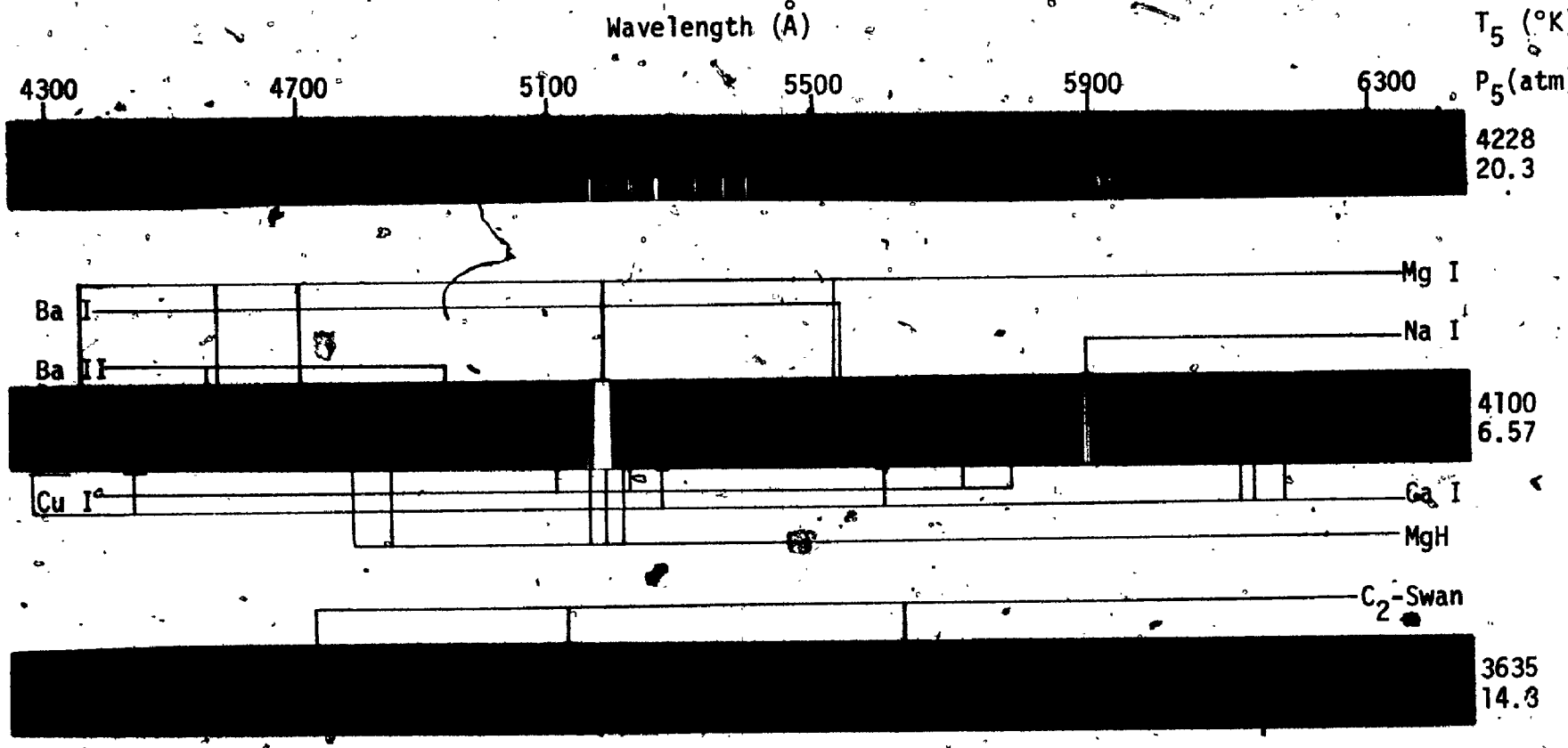

FIGURE 5-2

Change in Character of Luminosity from shock-excited Magnesium Powder Samples at High Pressure

TABLE 5-3

Heads (Å in Standard Air) of C_2-Swan Bands observed as Impurity Radiation Emitted from Ar:H_2 Test Gas Mixtures at Pressure $P_5 \geq 10$ atm.

v' \ v"	0	1	2	3	4	5
0	5165.2	5635.5				
1	4737.1	5129.3	5585.5			
2		4715.2	5097.7	5540.7		
3			4697.6		5501.9	
4						5470.3

spectrograph entrance slit for 250 μsec, close off the entire slit for 80 μsec and then to uncover the remaining half of the slit. An RCA 929 photo-tube, detecting Mg I and MgH luminosity (as shown in Fig. 3-14b), was intended to trigger discharge of the Multiblitz flash unit about 275 μsec after the initial portion of the spectrograph slit was uncovered. Consequently, an emission and an absorption spectrum could be obtained from the same shock-heated gas sample.

Fig. 5-3 shows the results of four attempts in the temperature range $3182 < T_5 < 4075$°K. Obviously, the system did not function entirely as planned for the two central spectra. In those cases, the flash unit was triggered just as the spectrograph slit was being closed off. The atomic lines having 'tapered' intensity on the spectrograms were caused

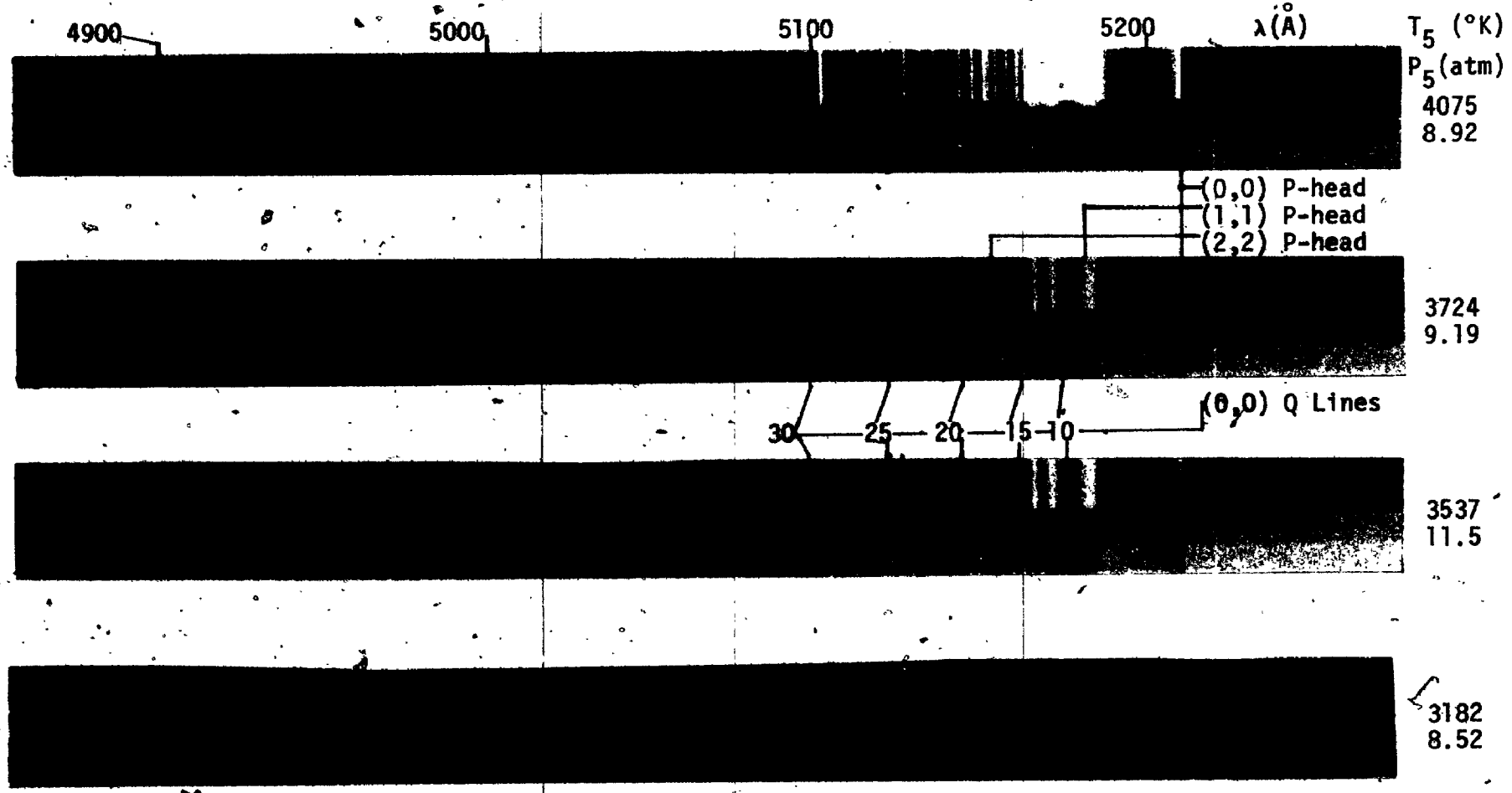

FIGURE 5-3

Emission and Absorption Spectra of the same hot gas containing Magnesium Sample material

by the moving slit of the High Speed Shutter unit being aligned not exactly parallel to the spectrograph slit. Thus it took a few microseconds more for the 'top' of the exposed slit length to be closed off than it did for the 'bottom'. The atomic lines of 'tapered' intensity were emitted by the Multiblitz unit in the 50-60 μsec period that its full discharge was building up.

The triggering malfunction notwithstanding, the four spectra of Fig. 5-3 establish three useful results:

i) Only for the T_5 = 4075°K spectrum do the Mg I lines appear in emission on top of the absorption continuum. Hence, this temperature is too great for use of the Multiblitz unit as a continuum source for quantitative absorption spectroscopy of the Mg I lines.

ii) The T_5=3182°K exposure involves essentially the same molecular and atomic lines in both the emission and absorption exposures. Small difference between the two on the print is due, probably, to lack of contrast in the photographic paper.

iii) For T_5>3200°K, the complexity of the absorption spectrum is less than that of the corresponding emission spectrum. Therefore, either the MgH absorption spectrum is characterized by a lower mean temperature than the emission spectrum, or the effective temperature of the Multiblitz continuum makes it unsuitable for quantitative studies at T_5>3200°K.

5.1.3 Absorption Studies

Additional absorption exposures were made to determine if the Multiblitz flash unit would be suitable for quantitative studies of the MgH spectrum. Fig. 5-4 shows some results. Absorption exposures ca 400 μsec duration were

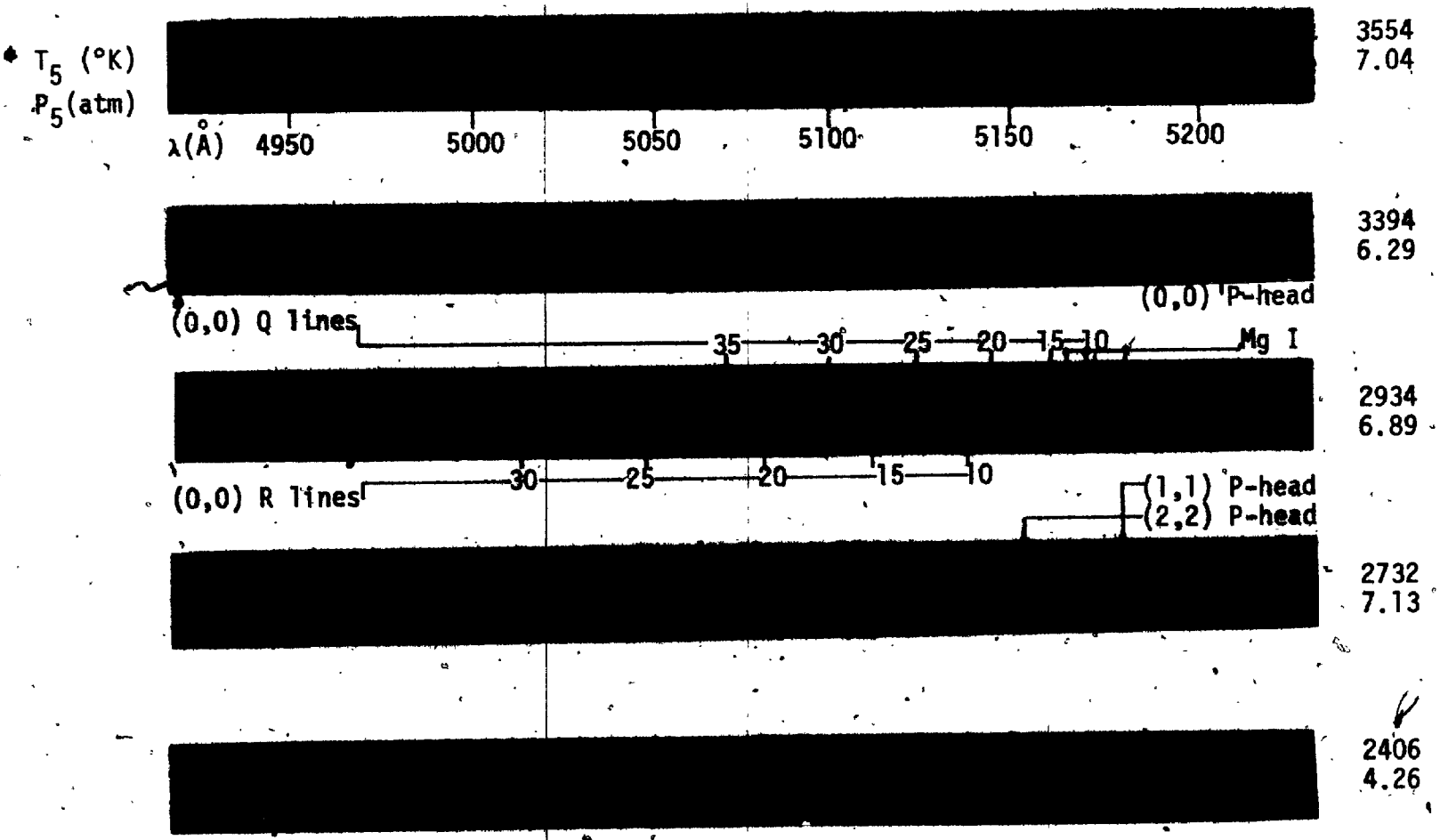

FIGURE 5-4

Absorption Spectra of the MgH $A^2\Pi$ - $X^2\Sigma^+$, $\Delta v=0$ sequence, recorded during the shock-excitation of Ar:H_2 Test Gas mixtures containing powdered Magnesium sample material. P-heads and some (0,0) band lines have been identified.

initiated about 200 μsec after incident shock reflection. Only light from the Multiblitz flash was permitted to enter the spectrograph by using the High Speed Shutter in a closed-open mode. The spectrograph slit was uncovered about 50 μsec after the Multiblitz unit had been triggered.

The spectra of Fig. 5-4 are arranged as a continuous function of T_5. However, it is difficult to say with conviction that the second spectrum from the top is located in its proper order without having an independent estimate of the gas temperature during the time the exposure was made. Perhaps the incident shock speed was incorrectly determined for this case. When compared with the others, the two uppermost of these five spectra do seem to be deficient in sample material. The lower three spectra, for which $T_5 < 3000$, would seem to indicate that the Multiblitz unit could be used as a source for quantitative absorption photometry. The only emission features present in these spectra are Xe I and Xe II lines originating in the flash tube. All of the spectra appear to be free from absorption lines due to impurities.

Nevertheless, Fig. 5-5a, a 50 μsec duration FX-33 flash exposure initiated about 150 μsec after shock reflection (with $T_5 = 4078°K$) shows the presence of a considerable number of impurity absorption lines - Cu I and Ti I, for example. Note also that the impurity lines are much sharper than the broader MgH absorption lines. Further, absorption by Mg I lines has removed almost the entire continuum at their wave-

(a) FX-33 Continuum of 50 μsec duration triggered ~150 μsec after shock reflection. Conditions behind the reflected shock front: T_5= 4078°K, P_5= 6.52 atm.

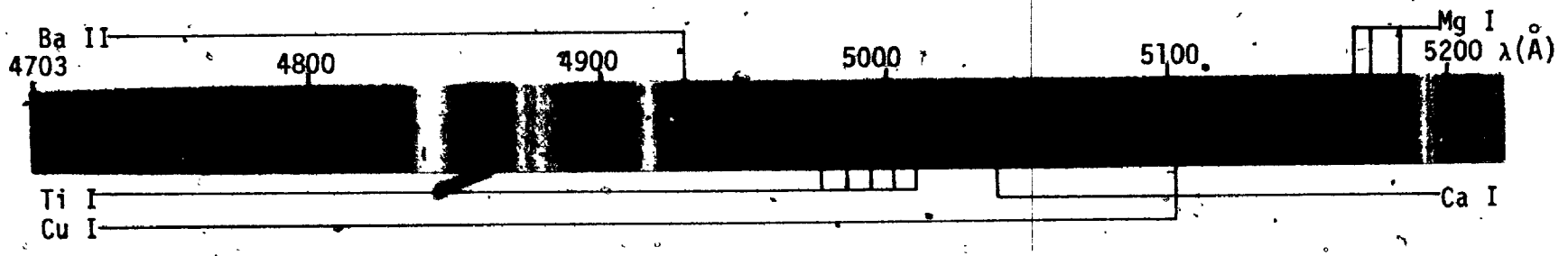

(b) Multiblitz Continuum of ~400 μsec duration triggered ~200 μsec after shock reflection. Conditions behind the reflected shock front: T_5= 3161°K, P_5= 9.67 atm.

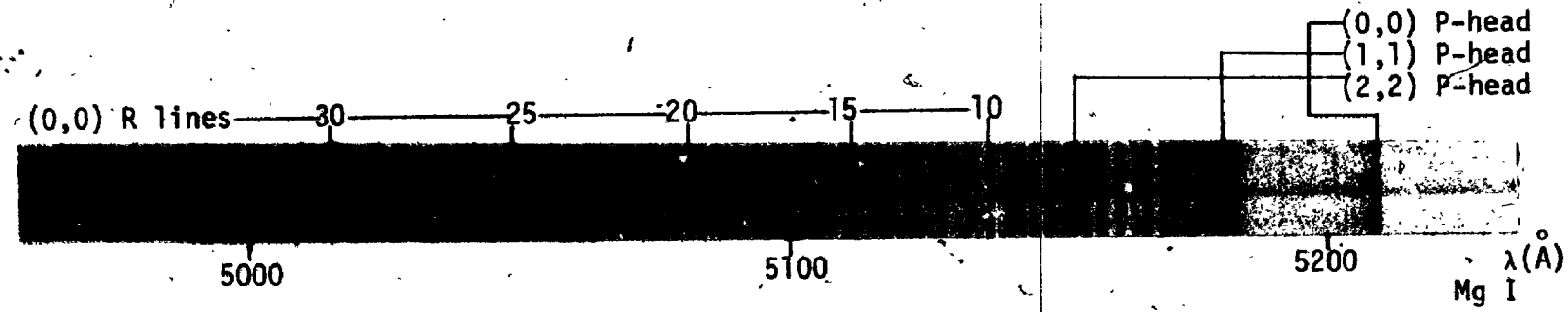

FIGURE 5-5

Comparison of Absorption Features characteristic of shock-produced MgH recorded when a) a High Intensity, Short-Duration Flash Continuum is passed through a high temperature Ar:H_2 shocked gas mixture, and b) a Long-Duration, Lower Intensity Flash Continuum is passed through a lower temperature shocked mixture. In both cases powdered Magnesium metal was added as a sample.

lengths. Attempts at quantitative spectroscopy of those lines would have to rely on the line wings rather than the central line profile for definitive results.

An exposure, at T_5=3161°K, using the Multiblitz flash triggered about 200 μsec after shock reflection - Fig. 5-5b - - gaves no indication of impurity lines originating within the shock tube and provided adequate absorption by MgH and Mg I lines for quantitative photometry.

In summary, the emission-absorption and absorption studies have shown that the Multiblitz continuum is adequate for quantitative spectroscopic studies on the MgH molecule and the Mg atom in the spectral range of the $\Delta v=0$ sequence of the $A^2\pi - X^2\Sigma^+$ band system of MgH provided that T_5 values are below ~3200°K and the exposure is started about 150-250 μsec after shock reflection. (That time interval allows the gas between the transverse viewing windows to equilibrate before the photographic exposure is made.)

5.2 BeH Studies

5.2.1 Emission Spectra

Shock excitation of finely divided (<38 micron diameter) Beryllium powder in Argon:Hydrogen mixtures produced an intense blueish-green output pulse of radiation after shock reflection. Spectra of the emitted luminosity revealed the $\Delta v=0$ sequence of the BeH $A^2\pi - X^2\Sigma^+$ band system to be the

sole feature of that molecule detected in the interval 4300 Å - 6000 Å. Furthermore, in that region only one Beryllium atomic line was tentatively identified. A list of the BeH bands, detected in the spectra via their rotational line distributions, is presented in Table 5-4 while Table 5-5 gives information about that lone Be I line.

The dearth of Be I and Be II lines is simply explained. In the spectral region from 4300 Å - 6000 Å there are three lines of atomic Beryllium at 4572.664 Å, 4548.538 Å and 4407.935 Å. The 4548 Å line would not be detectable in this experiment for its intensity has been found to be so low that the resonance line at 2348.61 Å is a factor of 3×10^7 more intense that it (Bozman et al., 1953). The 4572 Å line produced a blackening of the photographic emulsion that was just detectable. Moore (1945) gives the intensity ratio of the 4572 Å:4407 Å lines as 15:10. Thus it is not surprising that the 4407 Å line was also not detected. The high ionization potential of the Be atom (9.28eV) precludes the appearance of Be II lines under the shock excitation conditions used in these experiments.

The rotational structure of the (0,0) and (1,1) bands is identified in the absorption spectra of Fig. 5-8, for these spectra are less complex than the emission spectra of Fig. 5-6. In Fig. 5-6, the apparent doubling of lines in the spectrum taken at T_5=3235°K is <u>not</u> due to the doublet nature of the band system. (That doubling is unresolved in the present

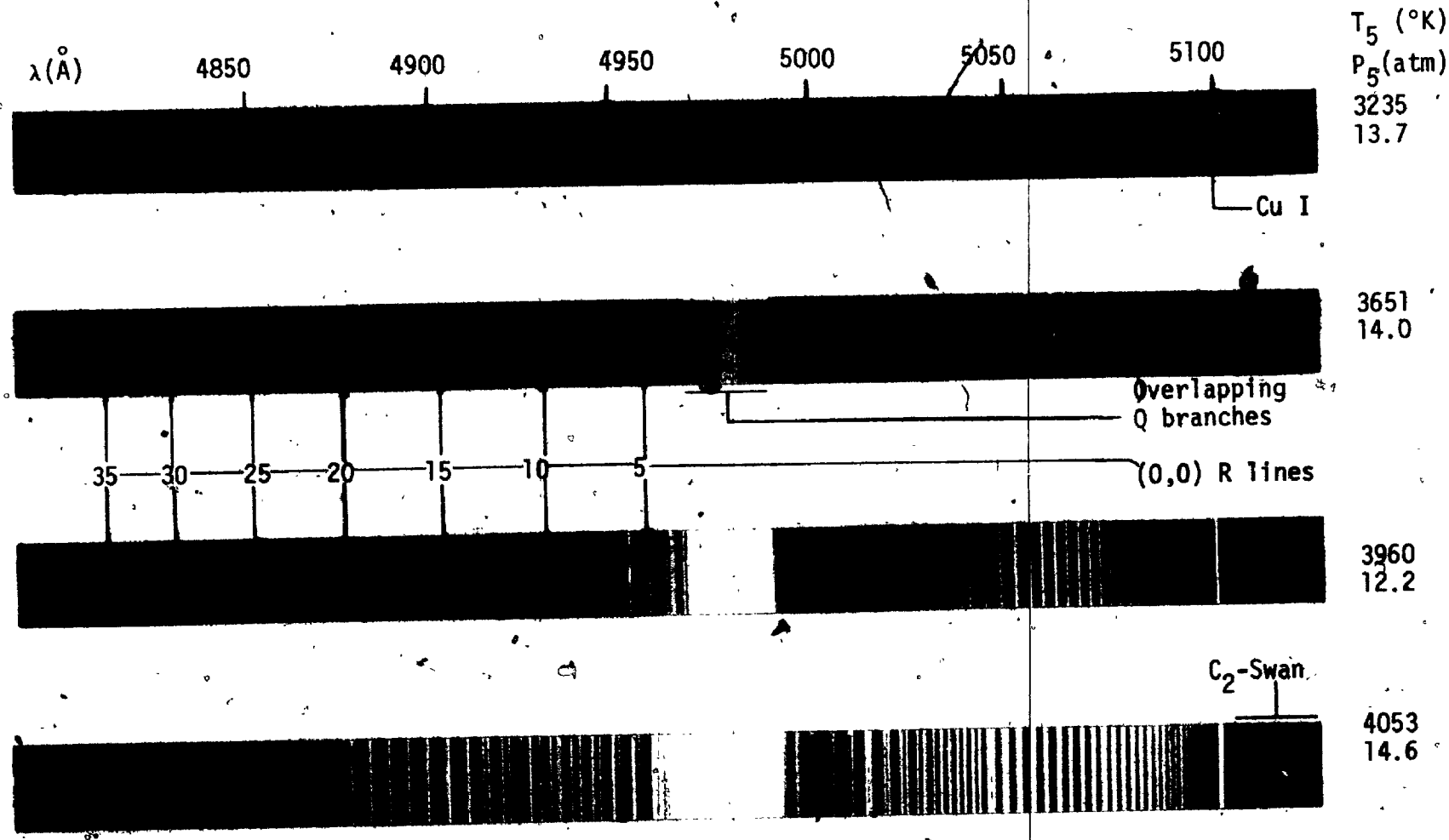

FIGURE 5-6

Emission Spectra of the BeH $A^2\Pi$ - $X^2\Sigma^+$ band system produced by shock-excitation of Beryllium powder samples in Ar:H_2 Test Gas mixtures. Note the increasing complexity of the spectrum as temperature increases due to increased population of higher vibrational levels.

TABLE 5-4

Band Origins (Å in Standard Air) and Franck-Condon Factors for BeH bands of the $A^2\pi - X^2\Sigma^+$ system observed when powdered Beryllium was Shock-excited in $Ar:H_2$ Test Gases.

Band	(0,0)	(1,1)	(2,2)	(3,3)	(4,4)
Origin	4988.3	4983.3	4980.5	4979.9	4981.4
FCF	0.997*	0.993	0.991	0.990	0.991
	0.997	0.993	0.990	0.990	0.990
	0.997_5	0.993_6	0.991_7	0.991_6	0.992_8

*McCallum & Nicholls (1971) using RKR potentials.
Popkie (1971) using RKR potentials.
Author using Morse potentials with constants obtained by least squares fits to Olsson's (1932) $\Delta G(v+1/2)$ values. The dropped integer is meant to indicate only the size of the next digit and not as a claim of greater precision.

Origins from Olsson's analysis.

TABLE 5-5

Beryllium Line Detected in Luminosity from Shock-excited Powder Samples of that Element.

Wavelength (Å)	Multiplet (No.)	E_ℓ (eV)	E_u (eV)
4572.671	$2^1P^\circ - 3^1D$ (3)	5.25	7.95

spectra.) It is caused by the slightly differing spacings between lines of the (0,0) and (1,0) bands. The lines of these bands are intermixed. Q-branch line spacing is very small for these BeH bands and so the overlap of two or three Q-branches from different bands produces the region of appar-

ently uniform intensity near the centre of the spectra.

As T_5 increases from 3235°K towards 4053°K, the region of overlapping Q-branches increases and more rotational lines appear in the R and P-branches between the lines of the (0,0) and (1,1) bands already present in the uppermost spectrum. At the highest temperature, the overlapping P-branches extend to wavelengths greater than that of the Cu I 5105 Å line beyond the measurements of Olsson (1932). Note also the presence of the C_2-Swan system lines in the lower three spectra as an impurity.

The Franck-Condon Factors quoted in Table 5-4 indicate that almost all the $A^2\pi - X^2\Sigma^+$ band system emission (and absorption) will occur in the $\Delta v=0$ sequence. This statement is based upon the facts that i) ΣFCF for fixed v' or v" must be unity (the FCFs in the table are almost unity themselves!) and ii) that the emission intensity is a product of other factors and an FCF.

FCFs based upon the Morse potential give essentially the same results as the more rigorous RKR potential. Thus the vibrational motion of the BeH molecule may be adequately approximated by the Morse oscillator.

5.2.2 Emission and Absorption Spectra from the Same Sample

The spectrum of Fig. 5-7 was produced by using the High Speed Shutter to allow one half of the spectrograph slit to remain uncovered for ~400 μsec following incident shock wave

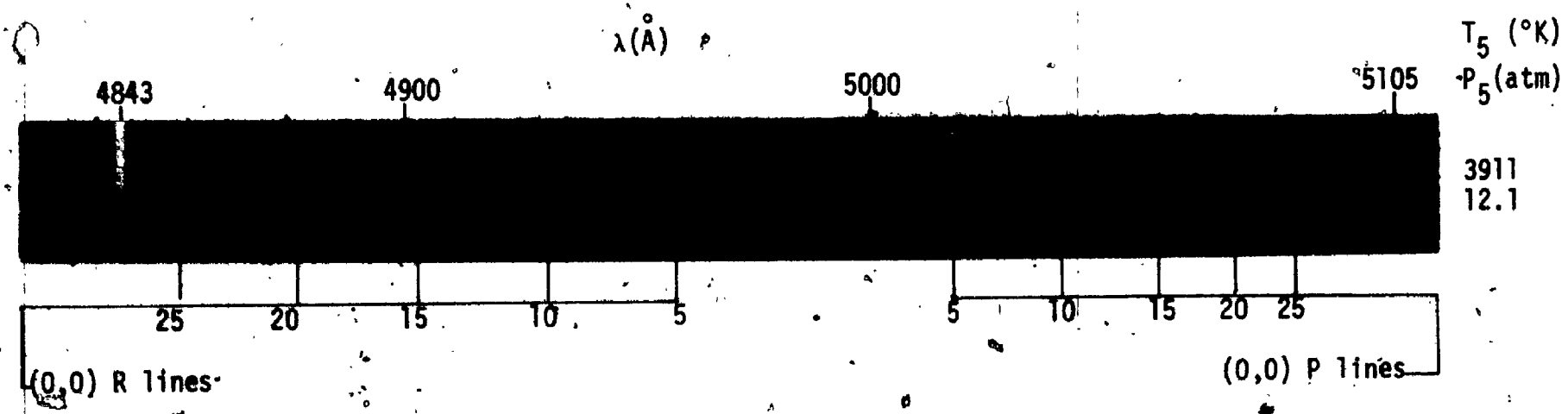

FIGURE 5-7

Emission and Absorption Spectra obtained from the same shock-excited Ar:H_2 Test Gas to which a Beryllium powder sample had been added. Some lines of the BeH $A^2\Pi - X^2\Sigma^+$ (0,0) band have been identified.

reflection. Then the shutter closed off the entire slit for 60 μsec as the Multiblitz flash unit was triggered prior to uncovering the second half of the spectrograph slit for about 500 μsec.

Comparison of the emission portion of Fig. 5-7 with the spectra of Fig. 5-6 indicates that the complexity of the former corresponds rather well with the complexity of the spectrum obtained at T_5=3960°K in Fig. 5-6.

A similar comparison of the absorption portion of Fig. 5-7 with the spectra of Fig. 5-8 indicates a complexity intermediate between the two spectra forming Fig. 5-8. A very rough estimate would be that the absorption spectrum of Fig. 5-7 corresponds to a temperature of 3000°K.

Thus the average temperature during the first 400 μsec following incident shock reflection is greater than the temperature of the shock-heated sample during the time interval 460 μsec<t<960 μsec. Consequently, to assure the highest effective temperatures for absorption spectra from any shock experiment, the absorption should be performed as soon as possible after shock reflection has occurred. Of course, proper allowance must be made for the finite time needed to establish local thermodynamic equilibrium at T_5 in the region used for performing the absorption studies.

5.2.3 Absorption Spectra

The two absorption spectra contained in Fig. 5-8 have

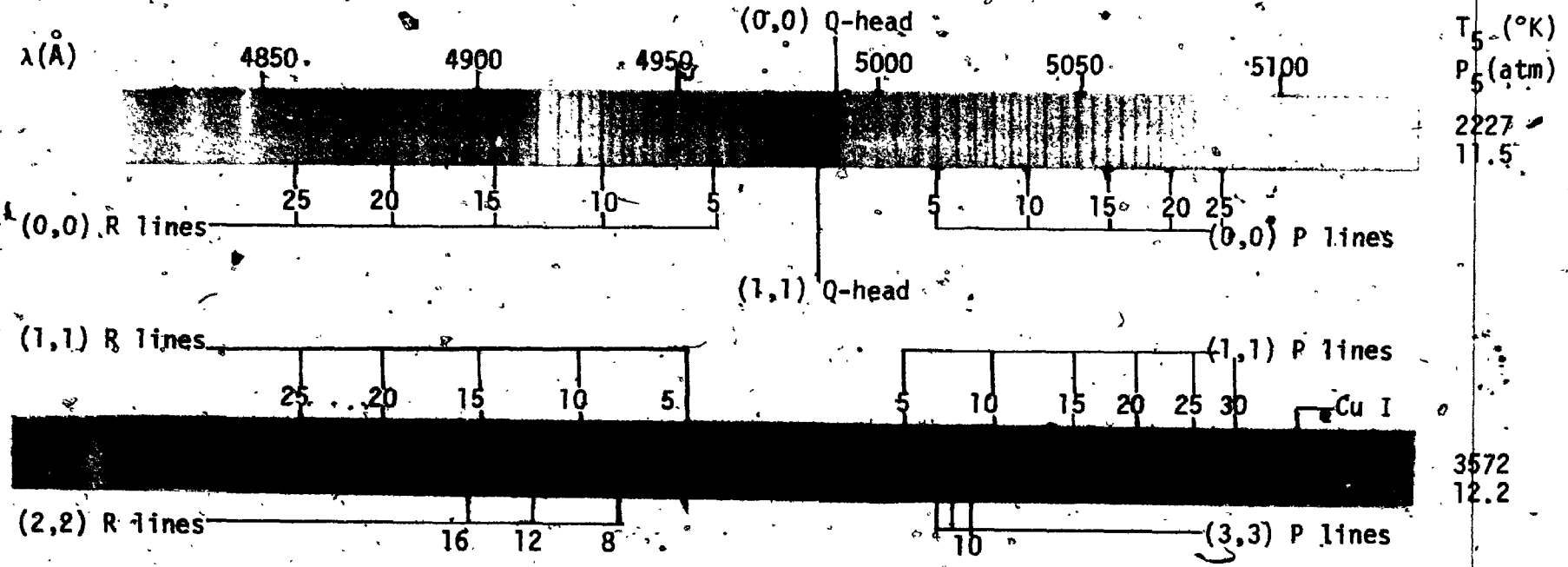

FIGURE 5-8

Absorption Spectra of the BeH $A^2\Pi - X^2\Sigma^+$ band system recorded during shock-excitation of Beryllium powder samples in Ar:H_2 Test Gas mixtures showing the increased population of vibrational levels v>0 with increased temperature behind the reflected shock front.

been labelled with the identity of P and R branch lines belonging to the (0,0) and (1,1) bands. Those identifications were made rather straightforward by use of Olsson's (1932) and Watson's (1928) measurements of rotational line wavenumbers. Notice, too, that it has been possible to indicate a few lines of the (2,2) R-branch and of the (3,3) P-branch.

The complexity of the higher temperature absorption spectrum compares quite well with that of the 3235°K emission spectrum shown in Fig. 5-6. It is not surprising that the apparent temperature for this exposure is about 300 K° lower than predicted. Both absorption spectra of Fig. 5-8 were obtained by triggering the Multiblitz flash unit about 325 μsec after incident shock reflection and then by using the High Speed Shutter to uncover, for the next 400 μsec, the initially covered spectrograph slit.

5.3 AlH Studies

5.3.1 Emission Spectra

Three spectra obtained from aluminium powder shock-excited at temperatures $3400 < T_5 < 4000$°K are presented in Fig. 5-9. Although bands of the AlH 4241 Å system are present, they are accompanied by bands of the AlO Green system - in particular, the AlO (1,0), (2,1), (3,2), (0,0), (1,1) and (2,2) bands can be readily discerned. Further, there seems to be a continuum underlying the AlH bands that has neither

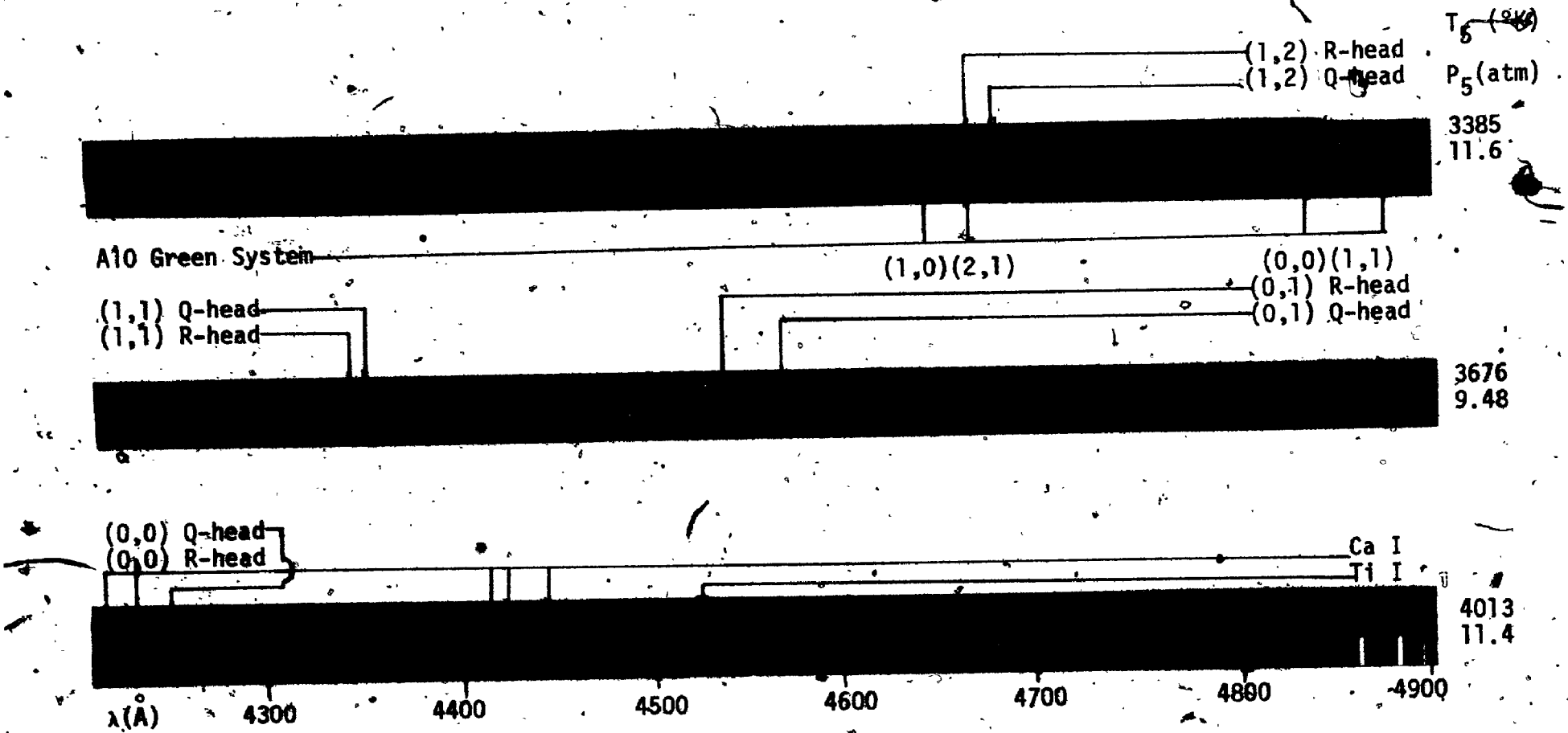

FIGURE 5-9

Emission Spectra of the AlH $A^1\Pi - X^1\Sigma$ band system generated by shock excitation of Aluminium powder samples in Ar:H_2 Test Gas mixtures.

the characteristics of incandescent particles nor of a light-leak in the spectrograph.

The continuum was ascribed to unresolved emission lines from the AlO molecule following a set of experiments in which a different source of Al powder was employed. The sample material used to produce the spectra of Fig. 5-9 had been exposed to the atmosphere for a considerable period of time. Although high purity (>99.9%Aℓ) powder had been purchased in a sealed, air-tight container, breakage of that seal had allowed an oxidation process to start. [Sidgwick (1950) states that aluminium quickly becomes covered by a layer of impervious oxide upon exposure to air.] Thus the results shown in Fig. 5-9 refer to shock-excitation of aluminium particles covered with a layer of oxide.

Emission spectra obtained using sample material from a freshly opened container did not show the oxide bands. However, the oxide bands have served a useful purpose for, by underlying the AlH features, they allowed the detection of AlH rotational lines in emission which would normally have been of too low an intensity to register on the photographic emulsion.

The spectra of Fig. 5-9 show that atomic features are more pronounced at the highest temperature while molecular features are more prominent at the lowest temperature. This results has come to be expected from shock-excited emission luminosity. No aluminium atomic lines were detected. The

prominent Al I lines at 3944.03 Å and 3961.93 Å lay beyond the violet limit for which the spectrograph had been focused.

Bands of the AlH $A^1\pi - X^1\Sigma$ system detected in emission are listed in Table 5-6 and the last rotational lines detected are recorded in Table 5-7.

5.3.2 Absorption Studies

The spectra of Fig. 5-10, showing strong absorption by AlH lines, were all obtained by use of the short-duration light pulse from an FX-33 flash tube. An RCA 929 photo-tube, detecting emissions from the Ca I 4226 Å line (and probably from the Al I 3944/3961 Å doublet), triggered discharge of the FX-33 about 350 μsec after shock reflection. Charging conditions for the capacitive energy storage unit were 38 μfd @ 1.3kV for Fig. 5-10a and 100 μfd @1.3kV for Fig. 5-10b. (Fig. 3-11 indicates an absorption flash duration ca 50 μsec for both sets of conditions.) Only aluminium powder that had not been appreciably exposed to the atmosphere was used as sample material.

Fig. 5-10a was produced by giving the print equal exposure times over the wavelength interval 4220 - 4680 Å so that it would indicate the over-all response of the optical system used to record the spectrum (configuration IV of Fig. 3-13)). For the remaining prints, the region 4320 - 4520 Å was given a lesser exposure than the region 4520 - 4900 Å in an attempt to show changes in rotational line absorption

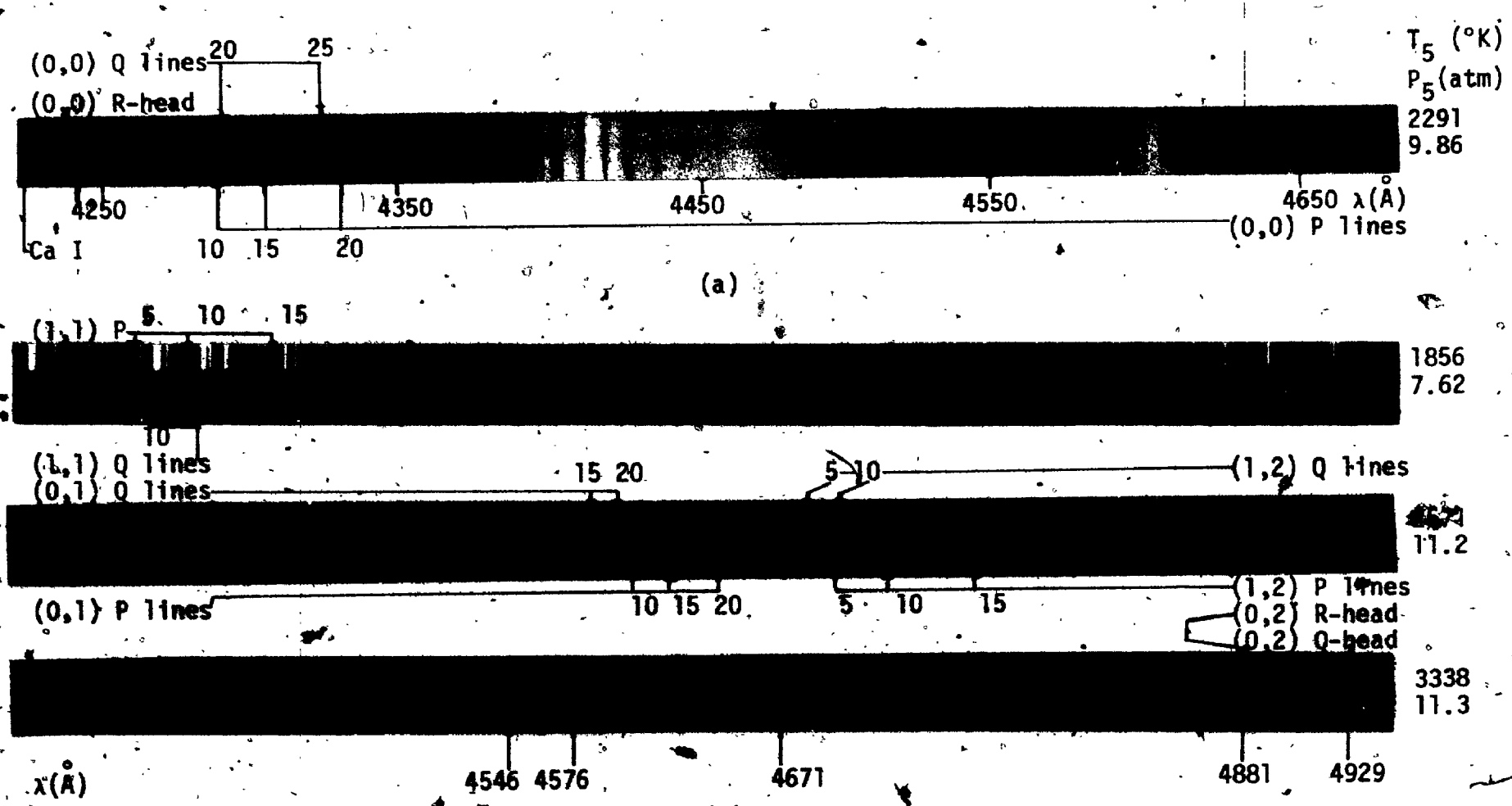

FIGURE 5-10

Absorption Spectra of the AlH $A^1\Pi$ - $X^1\Sigma$ band system resultant from shock-excitation of Aluminium powder samples in Ar:H_2 Test Gas Mixtures. Some rotational structure is identified.

TABLE 5-6

Standard Air Wavelengths (Å) of the AlH Band Heads detected in Emission and Absorption from Aluminium Powder Samples Shock-excited in Ar:H_2 Test Gas Mixtures.

v' \ v"	0	1	2	3	
0	4241.1	4546.5	4882		R-head
	(4259.5)	4576.4	4929.1		Q-head
1	4066.3	4353.1	4671.0	5024.2	
	(4072.6)	(4360.5)	(4680.7)	(5037.9)	

Data for (0,2) and (1,3) from Zeeman & Ritter (1954). The (0,2) R-head is an estimate from the present work. Remaining data from E. Bengtsson Knave (1932). The bracketed quantities are 'edges' of overlapped Q-branch lines. Quantities without brackets denote true heads in the sense that lines of higher J-value return upon lines of lower J-value.

features with reflected shock temperature, T_5. Film blackening below 4520 Å is very faint on the negatives due to greatly increased absorption by the (0,0) and (1,1) bands of AlH, with increase in T_5. Note how the wings of the AlH rotational lines have effectively absorbed all radiation below λ=4500 Å from the FX-33 discharge at T_5=3338°K. As T_5 increases towards 3338°K, so too does absorption by bands originating on the lower state vibrational levels v"=2 and 3. No bands involving the v"=4 level were detected.

For all the observed AlH absorption bands, it was noted that rotational lines of high J-value were much broader than those with low J-value. Measurements made upon densitometer tracings showed that the P(13) and P(14) lines of the (1,2) band were about 2 1/4 Å and 4 1/2 Å wide at the base compared

with a base width of 1Å for the Q(4) line of the same band. Although pressure broadening does affect the width of the AlH rotational lines, the markedly increased width at high J-values is attributable to predissociation resultant from an energy maximum in the $A^1\Pi$ state (Knave, 1932).

An investigation of the AlH predissociated spectrum was performed. Detailed results of that investigation will be given elsewhere. It is sufficient, for the present, to note that absorption spectra obtained in this work for P_5 approximately 9 atmospheres (about 1½ of that due to Hydrogen) showed structure and J-dependence in very good agreement with Figs 29e and 30c of Knave (1932). Those figures are densitometer traces of emission spectra obtained from an arc running between Aluminium electrodes in 9 atmospheres of Hydrogen.

5.4 Conclusions

The experimental results reported in this chapter support the conclusion that selected diatomic hydrides can be produced by the interaction of metallic powders with $Ar:H_2$ Test Gas mixtures during the shock-excitation process. The presence of the hydrides MgH, BeH and AlH was confirmed via emission and absorption spectrograms of the A-X electronic band systems of these molecules. No other band system attributable to these molecules was detected in the spectral region 4200Å - 6000Å.

In the absorption spectra of BeH and MgH, only the $\Delta v=0$

sequence was of sufficient strength to be positively identified. Absorption transitions involving the $\Delta v=-1$, 0, 1 and 2 sequences were detected for the AlH A-X system.

The emission spectra detected for BeH came from the $\Delta v=0$ sequence only; those for MgH came from the $\Delta v=-1$, 0 and 1 sequences; and the AlH emission spectra included all the AlH bands seen in absorption.

The effects of an energy maximum in the AlH $A^1\Pi$ state which leads to broadening of rotational lines due to predissociation were observed in both emission and absorption spectra. The observations made upon absorption spectra were in agreement with results reported by Bengtsson Knave (1932) based upon emission spectra obtained at high pressure (9 atm).

Provided that the shock-heated gas has a temperature, T_5, less than 3200°K, the Multiblit continuum is an adequate source for quantitative absorption spectrophotometry of the $\Delta v=0$ sequence of the MgH $A^2\Pi - X^2\Sigma^+$ band system.

CHAPTER 6

Quantitative Photographic Photometry of the MgH $A^2\Pi - X^2\Sigma^+$ $\Delta v=0$ Sequence

Bands of the $\Delta v=0$ sequence of the MgH $A^2\Pi - X^2\Sigma^+$ system overlap the MgI triplet 5167.3216 Å, 5172.6843 Å, 5183.6042 Å. This fact served as the basis for a method of determining the gf-values for individual MgH rotational lines and the "sum of the squares of the electronic transition moments" (Whiting & Nicholls, 1974), ΣR_e^2, for each of the vibrational bands from the known atomic oscillator strength of each line forming that triplet. The present chapter sets forth the procedure and the results obtained under the headings:

6.1 Theory of 'Parallel-Light' Absorption Spectroscopy

6.2 Application to Photographic Photometry of MgH

6.3 Results

6.4 Error Analysis

Underlying the entire theoretical framework are the assumptions:

i) Local Thermodynamic equilibrium exists within the absorbing system;

ii) The Ideal Gas Law holds in that system;

iii) Absorbing species are uniformly distributed throughout the system;

iv) The external source of illumination provides a plane-wave flux of energy to the system under study.

6.1 Theory of 'Parallel Light' Absorption Spectroscopy

Arnold, Whiting & Lyle (1969) have shown that, for plane-parallel radiation of specific intensity $I_\lambda^!$ (Watts/cm^2-μ-sr) incident upon one boundary of a gaseous layer in thermodynamic equilibrium characterized by temperature T, the spectral radiancy leaving the layer a distance z from the entry point is

$$I_\lambda = B_\lambda(T)\{1 - \exp(-k_\lambda z)\} + I_\lambda^! \exp(-k_\lambda z) \qquad (6\text{-}1)$$

with

$B_\lambda(T)$ = Planck Black-Body Function (W/cm^2-μ-sr)

$= 2hc^2\lambda^{-5}\{\exp(hc/kT\lambda) - 1\}^{-1}$

z = geometric path length (cm)

k_λ = absorption coefficient at wavelength λ corrected for stimulated emission (cm^{-1})

$k_\lambda z$ = optical depth of the gaseous layer

and

$$k_\lambda = \{E_\lambda\}/\{B_\lambda(T)\} \qquad (6\text{-}2)$$

E_λ = spectral emissive power due to spontaneous emission (W/cm^3-μ-sr)

$E = \int_{\Delta\lambda} E_\lambda d\lambda$ = total emissive power spontaneously emitted in a line with centre at λ_o (W/cm^3-sr)

Relation (6-2) is a statement of Kirchhoff's Law relating the absorption coefficient to the spontaneous emission spectral intensity. Thus the integrated absorption of a line having its centre at λ_o is related to the power emitted per unit solid angle in the line via the relation

$$k^\circ = \int_{\Delta\lambda} k_\lambda d\lambda = \int_{\Delta\lambda} \{E_\lambda d\lambda\}/B_\lambda(T)\} = \{B_{\lambda_o}(T)\}^{-1} \int_{\Delta\lambda} E_\lambda d\lambda = E/\{B_{\lambda_o}(T)\} \qquad (6\text{-}3)$$

where, in the interval $\Delta\lambda$ that k_λ is significantly greater than zero, the Planck Function may be taken as constant.

The next two subsections are given over to the development of expressions for k° appropriate to radiation from

atomic and molecular species.

6.1.1 Atomic Integrated Absorption Coefficient

Nicholls & Stewart (1962) give the entire power emitted per unit solid angle within a single line as

$$E = \frac{N_u h\nu A_{ul}}{4\pi} \times 10^{-7}, \quad (W/cm^3\text{-}sr) \qquad (6\text{-}4)$$

in which

$$h\nu = \frac{hc}{\lambda_0} = hc\{\Delta E_u - \Delta E_l\}$$

Substitution for the Einstein transition probability in terms of gf via

$$g_u A_{ul} = \frac{8\pi^2 c}{\lambda_0^3}\left\{\frac{e^2}{m_e c^2}\right\} g_l f_{lu}$$

and for the upper state population by means of the Maxwell-Boltzmann expression (Allen, 1963)

$$N_u = N_o^{at} \frac{g_u}{Z_{at}} \exp\left(-\frac{hc}{kT}\Delta E_u\right)$$

into (6-4) and the resultant expression into Eq. (6-3) yields

$$k^o = \left(\frac{\pi e^2}{m_e c^2}\right)\frac{2hc^2}{\lambda_0^3}\left\{\frac{g_l f_{lu}}{B_{\lambda_0}(T)}\right\}\frac{N_o^{at}}{Z_{at}} \cdot \exp\left(-\frac{hc}{kT}\Delta E_u\right) \times 10^{-7} \qquad (6\text{-}5)$$

The integrated absorption coefficient for a single atomic line is obtained from Eq. (6-5) by substitution for $B_{\lambda_0}(T)$ and is

$$k^o_{at} = \left(\frac{\pi e^2}{m_e c^2}\right)\lambda_0^2 (g_l f_{lu}) \frac{N_c^{at}}{Z_{at}} \exp\left(-\frac{hc}{kT}\Delta E_l\right)\left\{1 - \exp\left(-\frac{h\nu}{kT}\right)\right\} \times 10^{-7} \qquad (6\text{-}5a)$$

When the atomic line is part of a multiplet, use of the gf-sum rule (Allen, 1963)

$$\Sigma g_l f_{lu} = g_t f_{lu}$$

valid for Russell-Saunders coupling of angular momenta, leads to the relation

$$k^{o}_{at} = \left[N^{at}_{o} \Sigma g_l f_{lu}\right]\left(\frac{\pi e^2}{m_e c^2}\right)\frac{\lambda_0^2}{Z_{at}}\cdot\frac{g_l}{g_t}\cdot\exp\left(-\frac{hc}{kT}\Delta E_l\right)\left\{1 - \exp\left(-\frac{h\nu}{kT}\right)\right\}\times 10^{-7} \qquad (6\text{-}6)$$

In the last expression, only the quantities within the square braces are - in general - unknown. The other terms in the equation are either fundamental constants or quite precisely known properties of atomic energy levels. N^{at}_{o}, the total atomic species concentration, is at the experimenter's disposal as a control parameter and $\Sigma g_l f_{lu}$ is experimentally determinable. Currently, there is a good deal of active experimentation (summarized by Wiese, Smith & Miles, 1969; Martinson, 1974) and theoretical effort (viz Bates & Altick, 1973) directed towards improvement in the presently accepted values for Magnesium atomic gf-values.

In later computations reported in this work, allowance will be made for refinements in gf-values and so it is convenient - at this time - to introduce the expression

$$k^{o}_{at} = \{N^{at}_{o} \Sigma g_l f_{lu}\} k^{*}_{at} \qquad (6\text{-}7)$$

in which k^{*}_{at} is determined solely by the properties of the two atomic energy levels involved in the transition and the choice of coupling scheme (Russell-Saunders).

A similar relation will now be developed for individual molecular lines.

6.1.2 Integrated Absorption Coefficient for a Molecular Line Of a $^2\Pi - {}^2\Sigma$ Vibrational Band

3 4

OF/DE

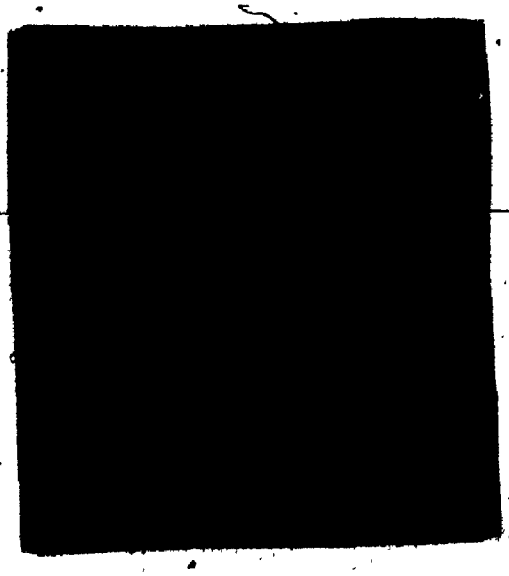

Starting once more with relation (6-4) and substituting (again from Allen, 1963) for the Einstein A-coefficient

$$g_u A_{ul} = \frac{64\pi^4}{3h\lambda^3} \tilde{S}$$

in which $\tilde{S}$ is the Line Strength and

$g_u = 2J' + 1$ $\quad$ J' = upper rotational level total angular momentum quantum number.

yields

$$E^{mol} = \frac{16\pi^3 c}{3\lambda^4} \tilde{S} \left\{ \frac{N_u}{2J'+1} \right\} \times 10^{-7} \qquad (6\text{-}8)$$

for the power emitted into the line per steradian. The upper state population of one Λ-component of $a^2\Pi - {}^2\Sigma$ transition ($N(n,v,N,J,p)$ of Tatum's 1967 paper) is given by Tatum as

$$N_u = N_o^{mol} \frac{(2J'+1)}{Z_{mol}} \exp\left(-\frac{hc}{kT}\{T'_e + G'(v) + F'_i(N)\}\right) \qquad (6\text{-}9)$$

That relation may be written in terms of the measured line centre wavelength and the lower state energy as

$$N_u = N_o^{mol} \frac{(2J'+1)}{Z_{mol}} \exp\left(-\frac{hc}{kT}\{\Delta E'' + 1/\lambda_0\}\right) \qquad (6\text{-}9a)$$

(refer to Appendix A and the Nomenclature section for explanatory details of the notation that is standard)

with

$\Delta E''$ - the energy of the lower rotational state of the transition above the level $v''=N''=T''_e=0$.

N_o^{mol} - the number density of the molecular species in particles per cubic centimetre.

Z_{mol} - the partition function for the molecular species.

Note that J' rather than N' must be used in evaluating the multiplicity of the upper rotational level.

Haycock (1963) has expressed the Line Strength, $\tilde{S}$, by the relation

$$\bar{S} = \{|Re(\bar{r}_{v'v''})|^2 q_{v'N'v''N''i'}\}S_J \qquad (6\text{-}10)$$

with

$|Re(\bar{r}_{v'v''})|^2$ - square of the electronic transition moment

$q_{v'N''v'N''i'}$ - Franck-Condon Factor with allowance for vibration-rotation interaction. Rotational term values are labelled $F_{vi}(N)$ with i specifying the spin doublet component.

S_J - Honl-London Factor for the line normalized to yield $\sum_{J'} S_J=(2J'+1)(2S''+1)$ and $\sum_{J''} S_J=(2J''+1)(2S''+1)$ following Schadee (1971). S_J is a shorthand notation for $S_{v'N'v''N''i'}$ - the more appropriate notation.

$\bar{r}_{v'v''}$ - $\bar{r}$-centroid for the $(v'v'')$ vibrational band.

after invoking the Born-Oppenheimer approximation to justify considering the electronic and vibrational motions as only weakly coupled while regarding the coupling between vibration and rotation as being much stronger. The same approach has been followed in this work.

The final expression for E^{mol} results from substitution for N_u from Eq (6-9) and for $\bar{S}$ from (6-10), followed by the replacement of the theoretically defined electronic transition moment by an experimentally determinable average (Arnold et al., 1969; Arnold & Nicholls, 1972). The latter replacement is defined via

$$|Re(\bar{r}_{v'v''})|^2 = \frac{\Sigma\Sigma|Re(\bar{r}_{v'v''})|^2}{(2-\delta_{0,\Lambda'})(2S'+1)} \qquad (6\text{-}11)$$

with

$\sum_{p'}\sum_{\Sigma\Sigma'}|Re(\bar{r}_{v'v''})|^2$ - this double summation is performed over all electric dipole transitions between non-degenerate states of specified parity p and with Σ-values $\pm\frac{1}{2}$.

so that

$$E^{mol} = \left\{\frac{16\pi^3 c}{3\lambda^4}\right\} N_u q_{v'v''} \left\{\frac{S_J \cdot \Sigma\Sigma|Re(\bar{r}_{v'v''})|^2 \times 10^{-7}}{(2-\delta_{0,\Lambda'})(2S'+1)(2J'+1)}\right\} \qquad (6\text{-}12)$$

is the expression ultimately taken by Eq (6-8) when the dependence of Honl-London and Franck-Condon Factors on rotational quantum numbers has been suppressed.

Finally; by combining (6-12) with (6-9a), by substitution of this result for E^{mol} in relation (6-3) and by inserting the full expression for $B_{\lambda_o}(T)$, the integrated absorption coefficient corrected for stimulated emission of a rotational line in a $^2\Pi$ - $^2\Sigma$ electronic transition is found to be

$$k^o_{mol} = \left[N^{mol}_o \frac{\Sigma\bar{\Sigma}|Re(\bar{r}_{v'v''})|^2}{2(2S'+1)}\right]\left\{\frac{8\pi^3}{3hc}\right\}\left\{\frac{S_J}{Z_{mol}}\right\}\cdot q_{v'N'v''N''}\cdot$$

$$\exp\left(-\frac{hc}{kT}\Delta\bar{E}''\right)\left\{1 - \exp\left(-\frac{h\nu}{kT}\right)\right\}x10^{-7} \qquad (6\text{-}13)$$

For a $^2\Pi$ - $^2\Sigma$ transition, the factor $(2 - \delta_{o,\Lambda'})$ has the value two (2) as $\Lambda'=1$. There is a k^o_{mol} for each spin component of the electronic band system. Thus S_J is the Honl-London Factor for a single line. (There are separate contributions from both the $P_1(N)$ and $P_2(N)$ lines, say, rather than an averaged value for the close P_1 and P_2 components of the same spin doublet.)

As in the atomic case, the integrated absorption coefficient for a molecular line may be expressed as a product of experimentally variable quantities and factors that are numeric constants or well known properties of the rotational levels. When this is done, the result is

$$k^o_{mol} = \{N^{mol}_o \Sigma Re^2\}k^*_{mol} \qquad (6\text{-}14)$$

in which ΣRe^2 is an abbreviation for $\dfrac{\Sigma\bar{\Sigma}|Re(\bar{r}_{v'v''})|^2}{(2S'+1)}$

Now that expressions are available for the integrated absorption coefficient of atomic and molecular lines, the absorption coefficient of the plane-parallel gaseous layer can be determined at each wavelength λ. This evaluation is performed in the following paragraphs.

6.1.3 Absorption Coefficient and Optical Depth of the Medium as a Function of Wavelength

k^o is the absorption coefficient integrated over an entire absorption line of centre (peak absorption) λ_0. This line contributes to the absorption at arbitrary λ an amount determined by k^o and by some normalized distribution function characteristic of the line shape. In the present study, molecular rotational and atomic lines were all assumed to have shapes determined by the Voigt Profile (van de Hulst & Reesinck,1947; Posener,1959;Young,1965) - a profile which has been found to represent the combined effects of thermal (Doppler) and collisional broadening very well. (Refer to Appendix A for specific details of the methods employed in the evaluation of the profile and the distance from the line centre beyond which the line was assumed to have negligible absorption.)

Consequently, contributions by atomic and molecular lines at wavelength λ were represented by

$$k_{\lambda_{at}} = b_{at}(|\lambda-\lambda_0|)k^o_{at}$$

$$k_{\lambda_{mol}} = b_{mol}(|\lambda-\lambda_0|)k^o_{mol}$$

where the distribution functions b_{at} and b_{mol} were not ,in

general, the same. Both distributions, however, were normalized to unity and were determined by the properties of the absorber and its environment.

When several molecular and atomic lines make contributions to the absorption coefficient at the same wavelength, the optical depth within the medium is given by

$$k_\lambda z = \sum_{v'v''} \sum_{N'N''} k^o_{mol} b_{mol}(|\lambda-\lambda_0|)z + \sum_i k^o_{at} b_{at}(|\lambda-\lambda_0|)z \qquad (6\text{-}15)$$

The first summation is over all rotational lines (N',N") of every (v',v") vibrational band that make non-zero contributions to k_λ; the second summation represents the contributions from all atomic lines. Implicit in equation (6-15) is the assumption that atomic and molecular absorbers are present in the entire absorption path at a temperature T.

Written in terms of factors which are basically fixed quantities and those that are experimentally controllable, the optical depth becomes

$$k_\lambda z = N_o^{mol} \Sigma Re^2 z \left[\sum_{v'v''} \sum_{N'N''} k^*_{mol} b_{mol}(|\lambda-\lambda_0|)\right] + N_o^{at} \Sigma g_l f_{lu} z \left[\sum_i k^*_{at} b_{at}(|\lambda-\lambda_0|)\right] \qquad (6\text{-}15a)$$

Insertion of this expression in relation (6-1) and knowledge of the intensity, I'_λ, initially incident upon the absorbing layer allow a complete determination of the absorption features exhibited by the species within the absorption medium. The experimentally adjustable parameters in Eq (6-15a) - those outside the square braces - are all the data

needed for the determination of ΣRe^2 relative to the sum $\Sigma g_l f_{lu}$. The ratio of these factors is

$$R_{at}^{mol} = \frac{\text{Coefficient of } k^*_{mol} \text{ sum}}{\text{Coefficient of } k^*_{at} \text{ sum}}$$

$$\therefore \quad R_{at}^{mol} = \frac{N_o^{mol}}{N_o^{at}} \frac{\Sigma Re^2}{\Sigma g_l f_{lu}} \qquad (6\text{-}16)$$

Equation (6-16) is the basis of the present method for evaluating the sum of the squares of the electronic transition moment. The ratio of molecular concentration to atomic concentration - as a result of thermodynamic equilibrium between reacting species, H, Mg and MgH - is fixed by the temperature, T, at which equilibrium is established and by the dissociation energy of the MgH molecule. Thus a knowledge of T, the MgH dissociation energy and an experimental evaluation of R_{at}^{mol} allows ΣRe^2 to be expressed as a multiple of $\Sigma g_l f_{lu}$. During experimentation, the coefficients of the k^*_{mol} and k^*_{at} sums may be treated as independently adjustable parameters.

6.1.4 Instrumental Response to the Absorption Beam

During the present studies, a plane-parallel beam of specific intensity I'_λ impinged upon the shock-heated gas through one of the transverse viewing windows. It left the absorbing region with specific intensity I_λ due to the interaction with the gaseous sample. When this emergent radiation was focussed upon the spectrograph slit, the specific intensity detected at the instrument's focal curve

at a location corresponding to wavelength λ' was

$$I^{fc}(\lambda') = \int I_\lambda g(|\lambda-\lambda'|)d\lambda \qquad (6\text{-}17)$$

in which $g(|\lambda-\lambda'|)$ is a normalized (to unity) slit function. In essence, the spectrograph - instead of producing a very sharp line-image at the location corresponding to wavelength λ - distributed the intensity I_λ (given by Eq (6-1)) over an area of the focal curve corresponding to a range of wavelengths.

When, as in the present experiments, $I^{fc}(\lambda')$ falls upon a photographic emulsion, it produces a response that is transformed into emulsion blackening which is some function of the total radiation impinging on each small area of the emulsion. Variation of blackening across the emulsion may be (and in these studies was) determined by using a recording microdensitometer. Owing to the finite size of the microdensitometer scanning slit and the magnification factor of its linkages and optical system, the density reading given by the instrument is an average over the width of its scanning slit image Δs_d. All radiation falling on the photographic emulsion over the image width Δs_d contributes to the blackening that evokes the microdensitometer response. Consequently, the radiation responsible for producing the plate blackening which is recorded as a density response $D(\lambda'')$ is a convolution of the radiation specific intensity incident upon the focal curve of the spectrograph and a slit function $h(|\lambda'-\lambda''|)$ that gives the microdensitometer response function to wavelength λ'

$$I_{dens}(\lambda'') = \int_0^{\infty} I^{fc}(\lambda')h(|\lambda'-\lambda''|)d\lambda' \qquad (6\text{-}18)$$

$I_{dens}(\lambda'')$ is the total radiation - of all wavelengths - falling upon the photographic emulsion (and appropriately summed over the spectrograph and microdensitometer slit response functions) that contributes to the density reading $D(\lambda'')$ at a position on the microdensitometer record corresponding to the wavelength λ''.

The functional relationship between $I_{dens}(\lambda'')$ - and so, ultimately, I_λ - and $D(\lambda'')$ can be evaluated experimentally in the manner outlined below.

6.1.5 Emulsion Calibration using Absorption Beam and Standard Lamp Exposures

Emulsion calibrations were performed in the usual manner by passing light from a tungsten strip-filament lamp operated at fixed filament current through a step density attenuator and on to the spectrograph slit. The optical arrangement for this procedure is illustrated by Fig 3-14.

An additional calibration technique was employed both to allow correction for possible reciprocity failure within the photographic emulsion and to produce more calibration points. This method consisted, essentially, of passing the radiation I_λ emergent from the shock tube through a focussing system that formed an image on the step density attenuator and then re-focussed that image on the slit of a stigmatic spectrograph. The resultant exposure appeared as a series of bands having different blackening on the developed emulsion.

When this procedure was employed (again, refer to Fig 3-14 for the proper experimental arrangement and to Fig 3-13 for a schematic diagram of the system) the tungsten lamp standardizing exposures were performed through the same optical system as the absorption flash calibrations.

The density of a particular feature in the i-th band of the attenuated absorption spectrum will correspond with light incident on the spectrograph focal curve - given by Eqs (6-17) and (6-18) as -

$$I^{fc}(a_i,\lambda') = \int_0^\infty I_\lambda a_i g(|\lambda-\lambda'|)d\lambda = a_i I^{fc}(\lambda')$$

$$I_{dens}(a_i,\lambda'') = \int_0^\infty I^{fc}(a_i,\lambda')h(|\lambda'-\lambda''|)d\lambda' = a_i I_{dens}(\lambda'')$$

when a_i, the attenuation produced by step i, is such a slowly varying function of wavelength that it may be taken as constant over the wavelength interval corresponding to the combined spectrograph and microdensitometer slit image widths. (In these studies, a_i satisfied that condition.) Using regions in which no absorption from the incident beam occurs, a calibration curve of $D(a_i,\lambda'')$ versus $\mathrm{Ln}\left\{\frac{I_{dens}(a_i,\lambda'')}{I_{dens}(\lambda'')}\right\}$ may be prepared on the assumption that I_λ may be treated as slowly variable over the combined slit image widths. (This restriction was met in the present experiments as the combined width of spectrograph and microdensitometer slits never exceeded 5 Å in those spectra subjected to quantitative spectrophotometric analysis.)

By combining calibration curves obtained from the tungsten lamp and absorption flash exposures - weighted in

favour of the absorption points -- a composite curve may be obtained. In the present work, the only significant difference between the separate calibrations occurred in the "toe" region of the H-D curve. Here preference was given to the absorption flash points.

Once an acceptable calibration curve is available, it may be approximated by a series of straight-line segments. Then, computer evaluation of $I_{dens}(\lambda)$ and $I'_{dens}(\lambda)$ followed by two slit function convolutions can be used to obtain $Ln\left\{\frac{I_{dens}(\lambda)}{I'_{dens}(\lambda)}\right\}$ values for which responses - corresponding to pen deflections on the microdensitometer tracings - may be determined from the calibration curve and a graphical output produced. ($I'_{dens}(\lambda)$ is intensity of unattenuated absorption beam.)

With a fixed temperature for the absorbing species equilibrium, the coefficients of the k^*_{mol} and k^*_{at} sums of Eq (6-15a) may be varied until the computer graphical output simulates the original microdensitometer tracing to an acceptable precision. A more detailed description of the method used for calculation of graphical output points is given in Appendix A section A.3.

The application of the above theoretical development to the practical case of the MgH A-X system is presented in the next few paragraphs.

6.2 Application to Photographic Photometry of MgH

6.2.1 Input Spectroscopic Parameters for Mg and MgH

Data used for the Mg I triplet are listed in Table 6-1.

TABLE 6-1

Input Parameters for the Mg I $3s3p\,^3P^o$ - $3s4s\,^3S$ Transition

Data				
Risberg (1965) Meissner (1938) Mundie & Meissner (1944)	Standard Air Wavelength	5183.6042	5172.6843	5167.3216
	Wavenumber of line centre	19286.225	19326.939	19346.997
	$3s4s\,^3S$ Term Value (cm^{-1})	41197.403	41197.403	41197.403
	$3s3p\,^3P^o$ Term Value (cm^{-1})	21911.178	21870.464	21850.405
Allen (1963)	Lower State Degeneracy	5	3	1
	Upper State Degeneracy	3	3	3
	gf-value for each line	0.583	0.350	0.116

The gf-value for each line is based upon $\Sigma g_l f_{lu} = 1.05$ given by Allen (1963).

For the MgH molecule, reconstructed rotational line wavenumbers were employed. Constants from which they were derived are given in the band re-analysis of Appendix D. The wavenumbers and lower state energy values used in the calculations are given in Table A-2 for the (0,0) band for $0 \leq N \leq 50$. As the $A^2\Pi$ state of MgH is close to Hund's case b, satellite branches have negligible rotational strength factors for $N > 5$ to 10. Therefore, only lines of the six Main Branches were included in the present treatment. The ranges of N-values used was $0 \leq N \leq 50$ for the (0,0) band, $0 \leq N \leq 30$ for the (1,1) band and $0 \leq N \leq 20$ for the (2,2) band. It was felt that good estimates of lower state energy and line wavenumbers could not be made for higher N-values.

Rotational line strength factors (Hönl-London factors) for MgH were calculated for every line used from Earl's (1935) formulae re-normalized to

$$\sum_{N_i} S_{v'N_i'v''N_i''} = (2S+1)(2J_i+1)$$

where N_i is the N-value of the i-spin component and J_i is the value of J associated with N_i. S has the same value in the Pi and Sigma states. (The summation expressess the same condition as was stated below Eq (6-10).) Some of the Hönl-London Factors used are presented as a function of N in Table 6-2.

Franck-Condon Factors <u>not</u> taking vibration-rotation interaction into account have already been presented in Table

TABLE 6-2

Rotational Line Strength Factors, $S_{v'N'v''N''}$, for the Main Branches of the MgH $A^2\Pi$ - $X^2\Sigma^+$ $\Delta v=0$ Sequence.

N	R_1	Q_1	P_1	R_2	Q_2	P_2
			(0,0)			
0	0.8133	0.6666				
5	3.6146	5.8310	2.2574	3.2568	4.7672	1.5665
10	6.1718	10.9022	4.7531	5.7530	9.8838	4.1562
15	8.6952	15.9315	7.2520	8.2519	14.9230	6.6878
20	11.2078	20.9474	9.7514	10.7514	19.9425	9.2036
25	13.7158	25.9573	12.2511	13.2512	24.9541	11.7130
30	16.2212	30.9641	14.7510	15.5710	29.9619	14.2192
35	18.7251	35.9690	17.2508	18.2508	34.9674	16.7237
40	21.2281	40.9727	19.7507	20.7507	39.9715	19.2270
45	23.7305	45.9757	22.2506	23.2506	44.9747	21.7296
50	26.2324	50.9780	24.7506	25.7506	49.9772	24.2316
			(1,1)			
0	0.7976	0.6666				
5	3.6052	5.8185	2.2542	3.2534	4.7515	1.5553
10	6.1661	10.8946	4.7511	5.7510	9.8750	4.1494
15	8.6911	15.9261	7.2506	8.2506	14.9170	6.6832
20	11.2047	20.9432	9.7504	10.7504	19.9380	9.2000
25	13.7132	25.9539	12.2503	13.2503	24.9505	11.7102
30	16.2190	30.9612	14.7503	15.7503	29.9589	14.2169
			(2,2)			
0	0.7954	0.6666				
5	3.6038	5.8167	2.2537	3.2529	4.7493	1.5537
10	6.1653	10.8935	4.7508	5.7507	9.8738	4.1485
15	8.6906	15.9254	7.2504	8.2504	14.9162	6.6826
20	11.2043	20.9426	9.7503	10.7503	19.9374	9.1996
25	13.7128	25.9534	12.2502	13.2502	24.9500	11.7098
30	16.2187	30.9608	14.7502	15.7502	29.9584	14.2166

5-2. There, values determined for the Morse vibrator are compared with the more rigorous RKR-values and the largest difference between the two sets of values amounts to 2.6% for the (2,2) band.

As hydrides have large values of B_v and D_v relative to non-hydrides, it seemed that Haycock's (1963) approach using the Morse-Pekeris rotating-vibrator model (Pekeris, 1934) to include rotational effects within the Franck-Condon factors was preferable to the neglect of these effects. As a consequence $q_{v'N'_i v''N''_i}$ was calculated for every rotational line included in the synthesized spectrum. Table 6-3 lists some of the Franck-Condon factors that were employed; Table 6-4 gives $\bar{r}$-Centroids for the various rotational lines.

Slight discrepancies between the present values and the tabulations of Haycock may be traced to the use of slightly different molecular constants.

6.2.2 Temperature, Pressure and Concentration Data

The T_5-value, calculated on the assumption that the incident shock travelled the last 7.0cm of the shock-tube length at $0.90U_1$ (Refer to Chapter 4), was adopted as the equilibrium temperature during the emission or absorption of the MgH A-X band system. Consequently, the composition and particle densities given by the shock-tube programmes for this T_5-value and a powder sample of 2.5 mgm mass were accepted as the characteristics of the MgH molecules' environment. (The graphs at the end of Chapter 2 - in particular, Figs 2-10 and 2-11 - show that the size of the sample has a minor effect on the shocked-gas temperature when the sample is less than 5mgm.)

TABLE 6-3

Franck-Condon Factors Including Vibration-Rotation Interaction, $q_{v'N'v''N'}$ for the MgH $A^2\Pi - X^2\Sigma^+$ $\Delta v=0$ Sequence.

N	R_1	Q_1	P_1	R_2	Q_2	P_2
			(0,0)			
0	0.94170	0.94118				
5	0.94391	0.94124	0.93900	0.94400	0.94135	0.93910
10	0.94582	0.94203	0.93651	0.94589	0.94101	0.93658
15	0.94744	0.94062	0.93388	0.94750	0.94067	0.93395
20	0.94871	0.93999	0.93110	0.94878	0.94004	0.93117
25	0.94957	0.93908	0.92814	0.94963	0.93913	0.92821
30	0.94993	0.93783	0.92500	0.94999	0.93787	0.92503
35	0.94972	0.93616	0.92149	0.94978	0.93621	0.92157
40	0.94887	0.93400	0.91766	0.94894	0.93406	0.91778
45	0.94727	0.93127	0.91338	0.94740	0.93136	0.91360
50	0.94482	0.92786	0.90854	0.94510	0.92805	0.90898
			(1,1)			
0	0.82865	0.82717				
5	0.83484	0.82737	0.82106	0.83518	0.82777	0.82154
10	0.84015	0.82670	0.81418	0.84042	0.82700	0.81449
15	0.84458	0.82547	0.80683	0.84489	0.82578	0.80716
20	0.84796	0.82355	0.79902	0.84833	0.82393	0.79943
25	0.85012	0.82075	0.79070	0.85043	0.82122	0.79114
30	0.85102	0.81675	0.78191	0.85076	0.81730	0.78200
			(2,2)			
0	0.71838	0.71608				
5	0.72787	0.71642	0.70670	0.72823	0.71707	0.70729
10	0.73583	0.71519	0.69594	0.73601	0.71546	0.69616
15	0.74226	0.71782	0.68436	0.74240	0.71304	0.68452
20	0.74648	0.70924	0.67181	0.74676	0.70943	0.67199
25	0.74693	0.70449	0.65735	0.74834	0.70396	0.65814
30	0.74056	0.69906	0.63871	0.74633	0.69534	0.64244

TABLE 6-4

$\bar{r}$-Centroids (Å) Including Vibration-Rotation Interaction for the MgH $A^2\Pi - X^2\Sigma^+$ $\Delta v=0$ Sequence.

N	R_1	Q_1	P_1	R_2	Q_2	P_2
			(0,0)			
0	1.72902	1.72869				
5	1.73187	1.73122	1.73070	1.73188	1.73125	1.73072
10	1.74078	1.73962	1.73857	1.74079	1.73963	1.73858
15	1.75483	1.75316	1.75159	1.75484	1.75317	1.75160
20	1.77390	1.77174	1.76967	1.77391	1.77174	1.76967
25	1.79782	1.79517	1.79263	1.79782	1.79517	1.79263
30	1.82637	1.82327	1.82027	1.82637	1.82327	1.82027
35	1.85930	1.85579	1.85235	1.85930	1.85578	1.85235
40	1.89634	1.89244	1.88859	1.89631	1.89241	1.88857
45	1.93717	1.93293	1.92869	1.93708	1.93283	1.92861
50	1.98144	1.97692	1.97232	1.98122	1.97667	1.97212
			(1,1)			
0	1.77766	1.77754				
5	1.78153	1.78092	1.78041	1.78155	1.78094	1.78300
10	1.79092	1.78980	1.78880	1.79092	1.78981	1.78880
15	1.80575	1.80414	1.80264	1.80575	1.80414	1.80264
20	1.82590	1.82381	1.82184	1.82590	1.82381	1.82184
25	1.85121	1.84866	1.84623	1.85119	1.84865	1.84622
30	1.88148	1.87846	1.87562	1.88140	1.87844	1.87557
			(2,2)			
0	1.8311	1.83105				
5	1.83513	1.83463	1.83421	1.83514	1.83465	1.83424
10	1.84498	1.84407	1.84325	1.84499	1.84408	1.84326
15	1.86064	1.85931	1.85811	1.86065	1.85932	1.85812
20	1.88196	1.88025	1.87868	1.88197	1.88026	1.87868
25	1.90869	1.90671	1.90473	1.90875	1.90669	1.90476
30	1.94044	1.93849	1.93596	1.94073	1.93832	1.93611

In the absence of ionization, and as an equilibrium exists in shock tube region (5), the relative numbers of MgH molecules and Mg atoms are fixed by the dissociation reaction

$$Mg + H \rightleftarrows MgH$$

Schadee (1965,p320) has considered this type of equilibrium. His analysis leads to the result

$$\left\{\frac{N_o^{mol}}{N_o^{at}}\right\} = N_H\left\{\frac{h^2}{2\pi\mu_{MgH}kT}\right\}^{\frac{3}{2}}\left(\frac{Q_{MgH}^{int}}{Q_H^{int}\ Q_{Mg}^{int}}\right)\cdot\exp(+D_o/kT) \qquad (6\text{-}19)$$

with

D_o = energy separation between the lowest accessible MgH state and the zero level of the infinitely separated atoms.

Q_i^{int} = internal partition function referred to the lowest energy state attainable by species i.

$N_o^{mol} = N_o^{MgH}$ = the total number density of MgH molecules in the reaction zone regardless of their energy state.

$N_o^{at} = N_o^{Mg}$ = the number density of Magnesium atoms in the reaction region regardless of energy state.

N_H = the number density of Hydrogen atoms within the hot gas regardless of their energy states.

The ratio N_o^{mol}/N_o^{at} was obtained from the shock-parameter computer programme described in Chapter 2. That programme, using the thermodynamic data of Heimel et al. (1963), used D_o=2.00 eV=46,110 cal/mole for the energy required to dissociate a ground state MgH molecule into 3^1S Mg I and 1^2S H atoms. For any other value for the dissociation energy, D_o^* say,

$$\left\{\frac{N_o^{MgH}}{N_o^{Mg}}\right\}^*_{D_o^*} = \left\{\frac{N_o^{MgH}}{N_o^{Mg}}\right\}_{D_o} \cdot \exp\left\{\frac{(D_o^* - D_o)}{kT}\right\} \qquad (6\text{-}20)$$

The dissociation energy of MgH is not well established. Estimates of it and corresponding values for the exponential term in Eq (6-20) are given in Table 6-5. It is believed that the adopted value for D_o is an appropriate choice in view of Gaydon's (1968) estimate: namely, $D_o^* = 2.1 \pm 0.5$ eV.

It was earlier remarked, in passing, that the number ratio of Magnesium atoms to Magnesium Hydride molecules would be determined by the dissociation reaction in the absence of ionization. It is time to determine whether or not Magnesium ionization was negligible. That is done in the next section.

6.2.3 The Amount of Mg II in the Reaction Zone

Order of magnitude calculations made with the Saha equation (Allen, 1963) and an Ionization Potential of 7.64eV for Mg I yield

$$\left\{\frac{N_o^{MgII} \cdot N_e}{N_o^{MgI}}\right\} = 2.5 \times 10^{+8} \quad \text{at } 3000^oK \text{ , and}$$

$$= 4.4 \times 10^{+1} \quad \text{at } 2000^oK$$

On the worst-case assumption that all the electrons are provided by the Magnesium ionization $\left\{N_o^{MgII} / N_o^{MgI}\right\}$ takes values 1.3×10^{-3} and 1.3×10^{-4} at 3000^oK when N_o^{MgI} is assumed to be 10^{+14} and 10^{+16} particles per cc, respectively. Those, concentration values are roughly the ones obtained for distributing a 2.5 mgm Magnesium powder sample uniformly throughout shock tube Region (5). The ion/neutral ratio obtained

above is an over-estimate for electrons are produced much more readily in the shock-heated gas from Calcium, Barium and Sodium impurities. (Lines of ionized Barium have been identified in some of the spectra located in Chapter 5.) Thus an upper limit of 0.1% has been found for the fraction of Magnesium ionized in the shock-tube at temperatures $< 3000^{\circ}K$. Higher particle densities within the reaction zone than those already considered will lead to a suppression of the ionization. Thus the 0.1% limit can be taken as a firm upper bound and so be used to justify the neglect of what few ions of Magnesium that may be present in the Test gas.

TABLE 6-5

Effect of Change in Estimated Dissociation Energy on N_o^{MgH}/N_o^{Mg}

Source	D_o^* eV	$(N_o^{MgH}/N_o^{Mg})^* = w(N_o^{MgH}/N_o^{Mg})$ w at: $2000^{\circ}K$	$3000^{\circ}K$
Lippincott et al. (1961)	1.76	0.25	0.40
Heimel et al. (1963)	2.00	1.00	1.00
Gaydon (1968)	2.10±0.5	1.79	1.47
Herzberg (1950)	2.49 (max)	17.1	6.62

6.2.4 Method for Determining Best Fit Control Parameters

In Section 6.1.1, Eq (6-15a), the quantities

$N_o^{mol}\Sigma Re^2 z$ and $N_o^{at}\Sigma g_l f_{lu} z$

appear as coefficients of the k^*_{mol} and k^*_{at} sums. Before preparation of synthesized microdensitometer tracings, initial values were assumed for these entities. Then, during the fitting process, the assumed values were scaled independently as follows:

$$N_o^{mol}\Sigma Re^2 z = \mu(N_o^{mol\dagger}\Sigma Re^{\dagger 2} z^\dagger) \qquad (6\text{-}21a)$$

$$N_o^{at}\Sigma g_l f_{lu} z = \alpha(N_o^{at\dagger}\Sigma g_l f_{lu}^\dagger z^\dagger) \qquad (6\text{-}21b)$$

where the daggers indicate initially assumed values. (Note that it is implicitly assumed throughout these calculations that the geometric path length is exactly the same for atoms as for molecules.) The initial concentrations of MgH and Mg correspond to a distributed sample size of 2.5 mgm Magnesium.

The initial stage of the fit consists of varying μ of Eq. (6-21a) until the computed spectrum and the microdensitometer tracing reach a best fit. This fit was determined by superposing, on a light box, the original tracing and the synthesized replica of it. The possible range of μ was found by performing the fit in the region of the (0,0) P-head. The value of μ was further refined by extending the fit so that the best possible reproduction of the spectrum could be obtained in regions where there was no overlap with atomic Magnesium lines.

With μ determined - and so maintained fixed - α was

varied until the best fit was obtained for that portion of the microdensitometer tracing that possessed combined Mg I and MgH lines (5160 - 5190 Å).

Finally, with μ & α both known, an estimate of ΣRe^2 was made. The equation allowing that evaluation is derived below.

6.2.5 Evaluation of ΣRe^2

From equation (6-16),

$$R_{at}^{mol} = \frac{\text{Coefficient of } k^*_{mol} \text{ sum}}{\text{Coefficeint of } k^*_{at} \text{ sum}} = \frac{N_o^{mol} \Sigma Re^2 z}{N_o^{at} \Sigma g_1 f_{1u} z}$$

and in terms of the scale factors and initially assumed values,

$$R_{at}^{mol} = \left\{\frac{\mu}{\alpha}\right\}\left(\frac{N_o^{mol\dagger}}{N_o^{at\dagger}}\right)\frac{\Sigma Re^{\dagger 2}}{\Sigma g_1 f_{1u}^{\dagger}}$$

Allowing for the possibility of using a dissociation energy other than that initially assumed, and noting that Eq (6-20) applies, equating the above two expressions for R_{at}^{mol} yields

$$\left[\exp\left\{\frac{D_o^* - D_o}{kT}\right\}\right]\frac{\Sigma Re^2}{\Sigma g_1 f_{1u}} = \left\{\frac{\mu}{\alpha}\right\}\frac{\Sigma Re^{\dagger 2}}{\Sigma g_1 f_{1u}^{\dagger}}$$

which leads directly to the desired result

$$\Sigma Re^2 = \frac{\Sigma\Sigma |Re(\bar{r}_{v',v''})|^2}{(2S+1)} = \left\{\frac{\mu}{\alpha}\right\}\Sigma g_1 f_{1u}\left\{\frac{\Sigma Re^{\dagger 2}}{\Sigma g_1 f_{1u}^{\dagger}}\right\}\exp\left(-\frac{D_o^* - D_o}{kT}\right) \qquad (6\text{-}22)$$

In the case that $D_o^* = D_o$ and the gf-sum is the same for both initially assumed and later scaled data, the estimated value for ΣRe^2, $\Sigma Re^{\dagger 2}$, is to be multiplied just by the ratio of the molecular to atomic scaling constants to yield the

revised estimate for the average value of the "sum of the squares of the electronic transition moments".

6.3 Results

Results obtained from computer synthesis of microdensitometer traces are presented in two parts: a group of four figures that illustrates the degree to which observed spectra were simulated; and a discussion of the numeric values found from the successful simulation of six absorption spectra.

6.3.1 Computer-simulated Microdensitometer Traces

Figures 6-1, 6-2, 6-3 and 6-4 will indicate the type of visual results obtained. Figures 6-1, 6-3 and 6-4 are photographic reductions of simulated traces. Figure 6-2 contains photographic records of the seven spectra whose simulation was attempted.

The three tracings in Figure 6-1(which corresponds with the 2606^{o}K spectrum of Fig 6-2) are presented to illustrate the versatility of the present computational scheme. The dotted points are separated by 0.01" measured along the wavelength axis on the original plotter output; and the absorption continuum level is assumed to be the straight line that passes through the "highest" points on Trace A. Trace A corresponds with the absorption spectrum that would be obtained from the shock-heated gas if Mg were present and MgH absent. This result was obtained by setting the scale factor μ (defined by Eq 6-21a) to zero. Trace C shows the result to be expected when MgH is present but Mg

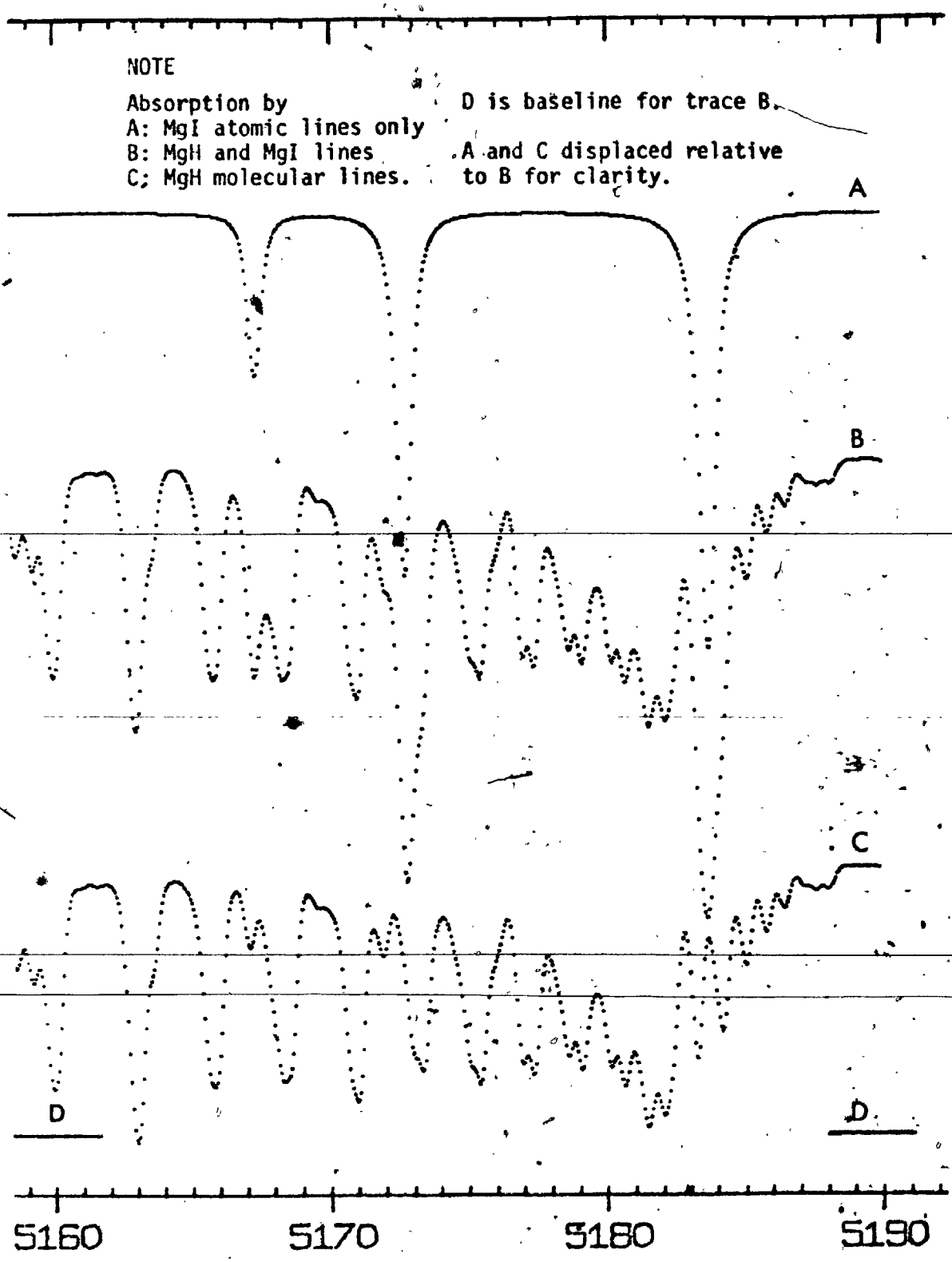

FIGURE 6-1

Computer-Simulated Densitometer Traces of Film Exposure by an Absorption Continuum passed through SHOCK-HEATED GAS at T_5= 2606°K, P_5= 10.90 atm.

is not. (That result was attained by setting the scaling factor α to zero.) Finally, Trace B was obtained by using the best-fit values for both α and μ.

On Trace A, allowance for absorption due to the far wings of the Mg I lines is detectable as far as 4 Å from the line centre. (A greater allowance than this was made when evaluating the absorption coefficient array.) The folly of attempting relative or absolute intensity measurements on the Mg I lines in the presence of MgH is clearly evident in Traces B & C. The Mg I lines are overlapped by rotational structure of both the (0,0) and (1,1) bands of the $A^2\Pi - X^2\Sigma^+$ system. Note, in particular, the 5183 Å line for which no trace of the two overlapped MgH rotational lines is apparent.

On the other hand, the MgH lines are so badly overlapped both by each other and by the wings of the Magnesium lines that only by computer-synthesis of the spectrum can sufficient detail be included to allow for a precise determination of ΣRe^2.

Figure 6-3 illustrates the best fit obtained between simulated and original traces; Figure 6-4 is the worst fit. In both these spectra, the continuum level is too low over the range 5188 - 5192 Å due to the presence of a Xenon line in the flash continuum that was not included in the computer simulation. Some discrepancies between simulated and real line positions are probably due to the use of reconstructed line wavenumbers rather than the observed quantities. However, part of the discrepancy is due to the superposition

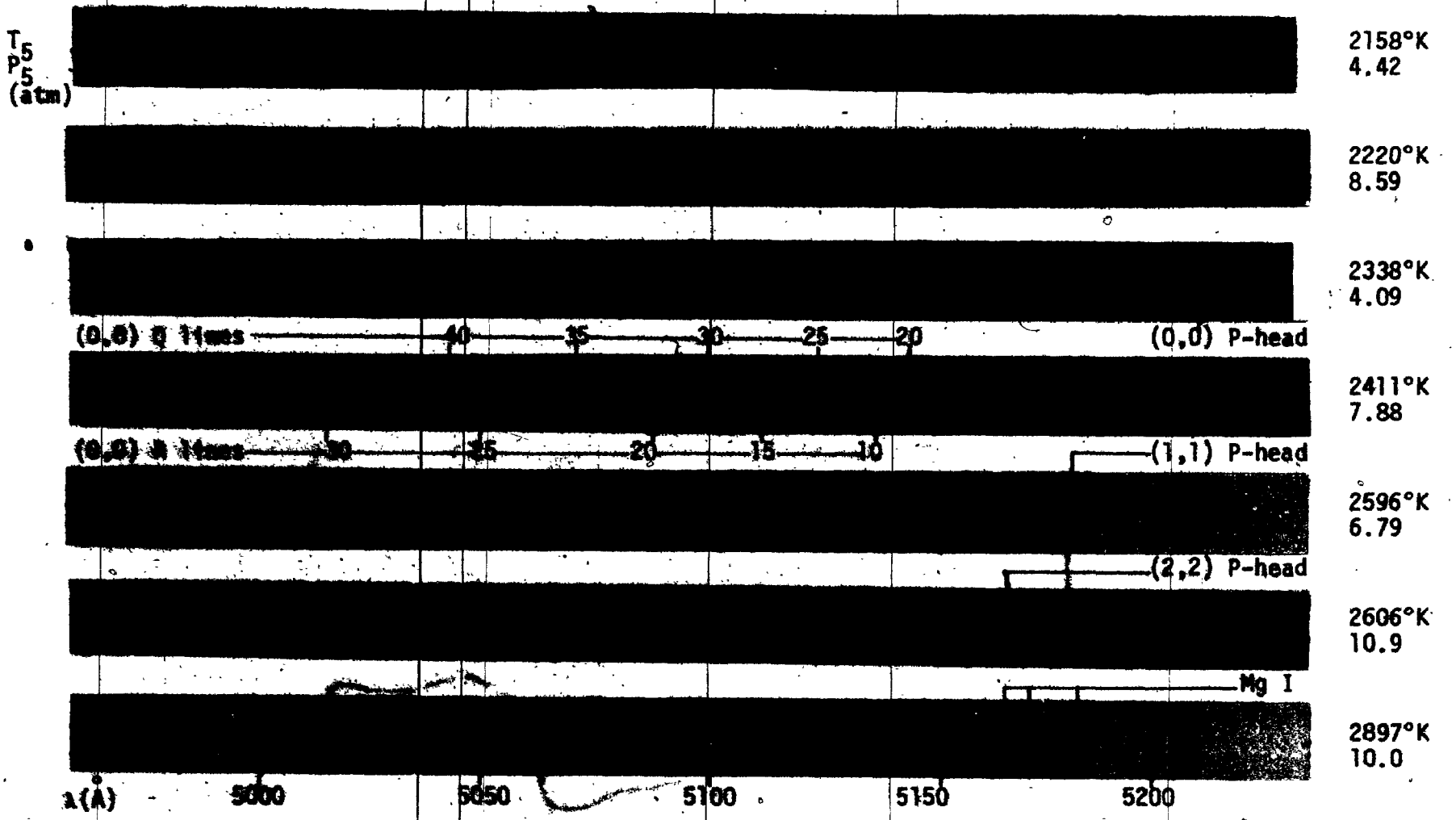

FIGURE 6-2

MgH $A^2\Pi$ - $X^2\Sigma^+$ $\Delta v=0$ sequence Absorption Spectra (recorded during shock-excitation of Magnesium powder samples in Ar:H_2 gas mixtures) for which Computer-Synthesis of Microdensitometer traces was attempted.

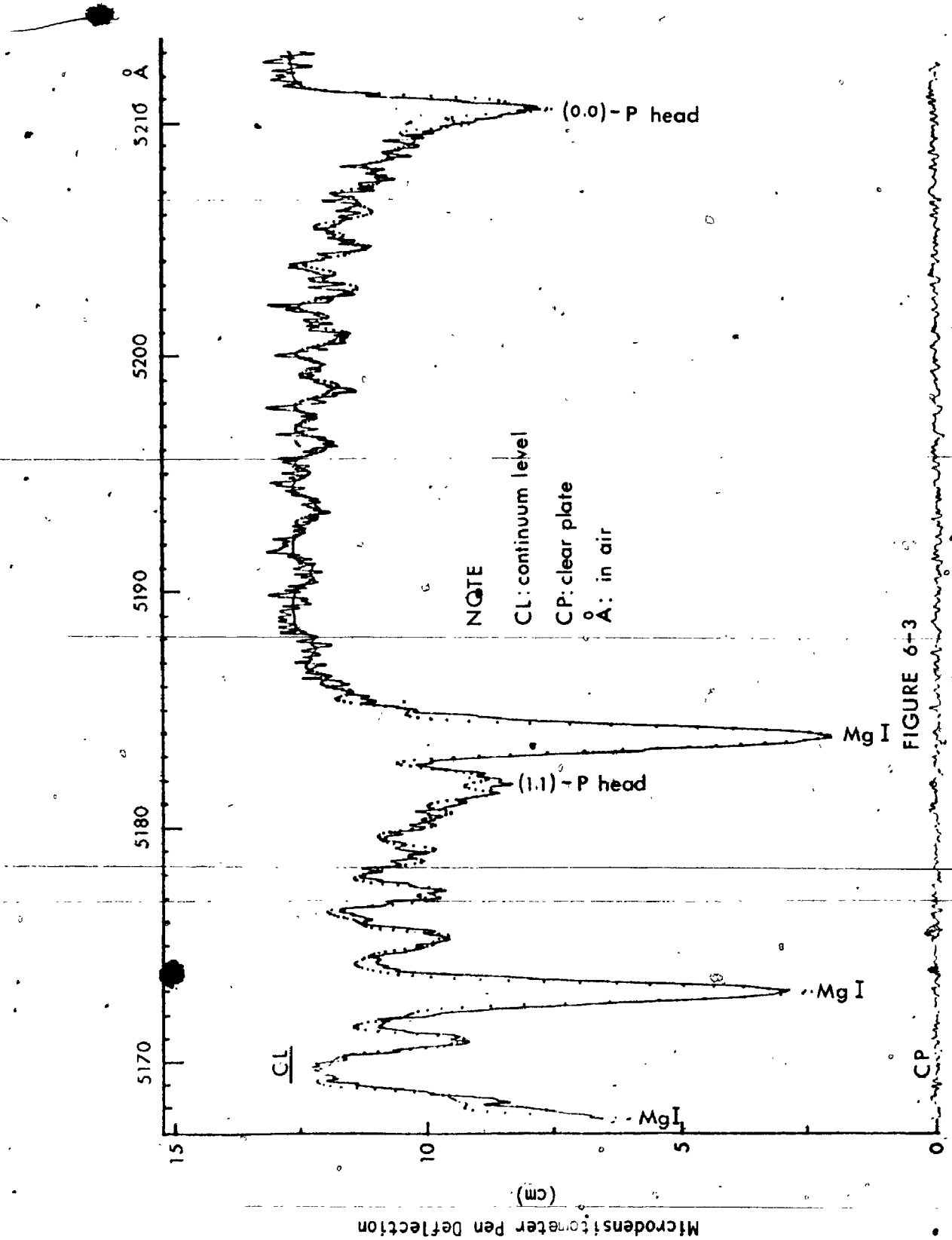

FIGURE 6-3

Microdensitometer Trace (Continuous Curve) and Computer Simulation of it (Dotted Curve) for an Emulsion Exposed to a Flash Continuum which had been passed through a SHOCK-HEATED Argon:Hydrogen mixture containing MgH and Mg Absorbers at T_5= 2897°K, P_5= 10.01 atm.

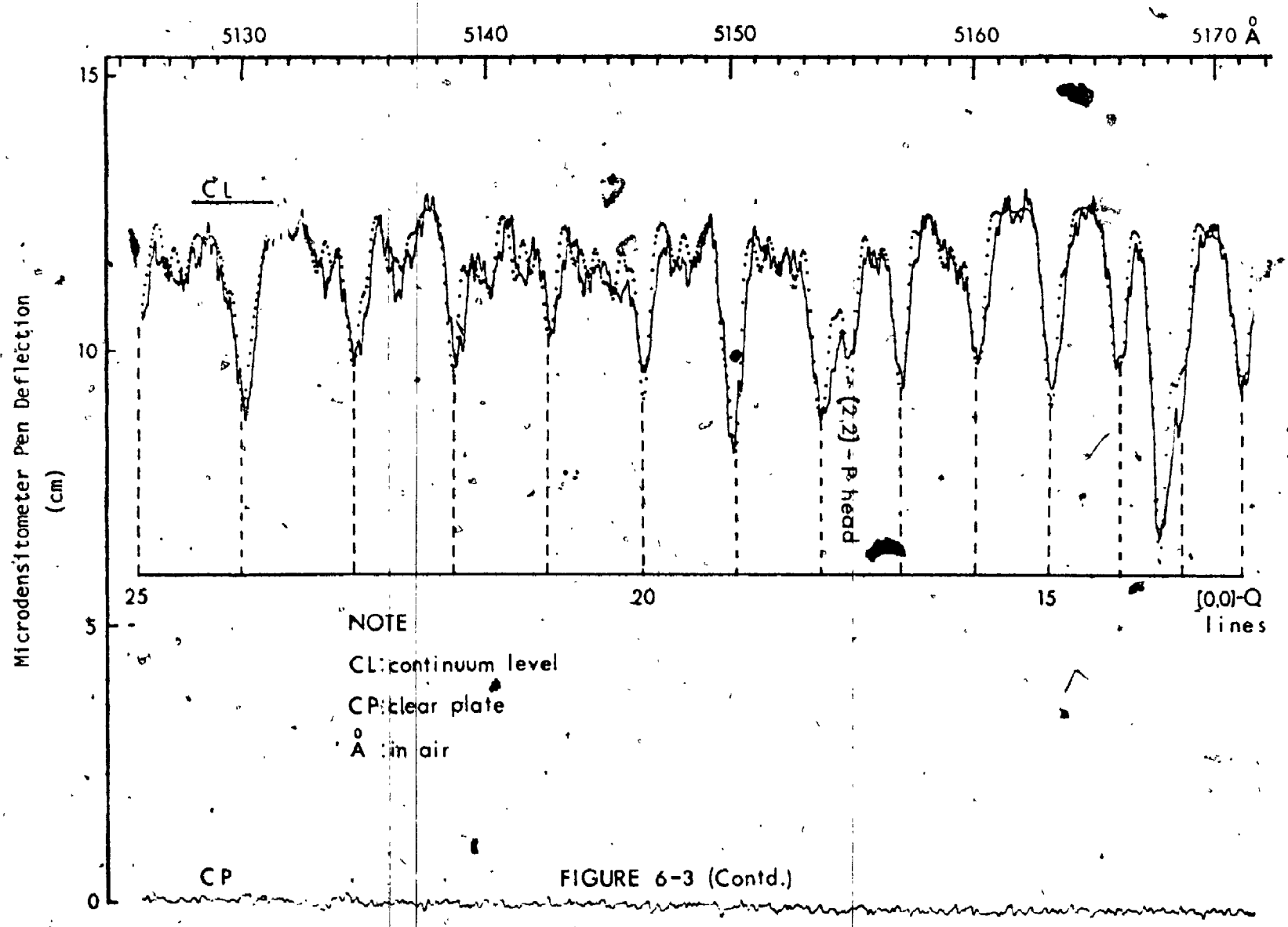

FIGURE 6-3 (Contd.)

Microdensitometer Trace (Continuous Curve) and Computer Simulation of it (Dotted Curve) for an Emulsion Exposed to a Flash Continuum which had been passed through a SHOCK-HEATED Argon:Hydrogen mixture containing MgH and Mg Absorbers at T_5 = 2897°K, P_5 = 10.01 atm.

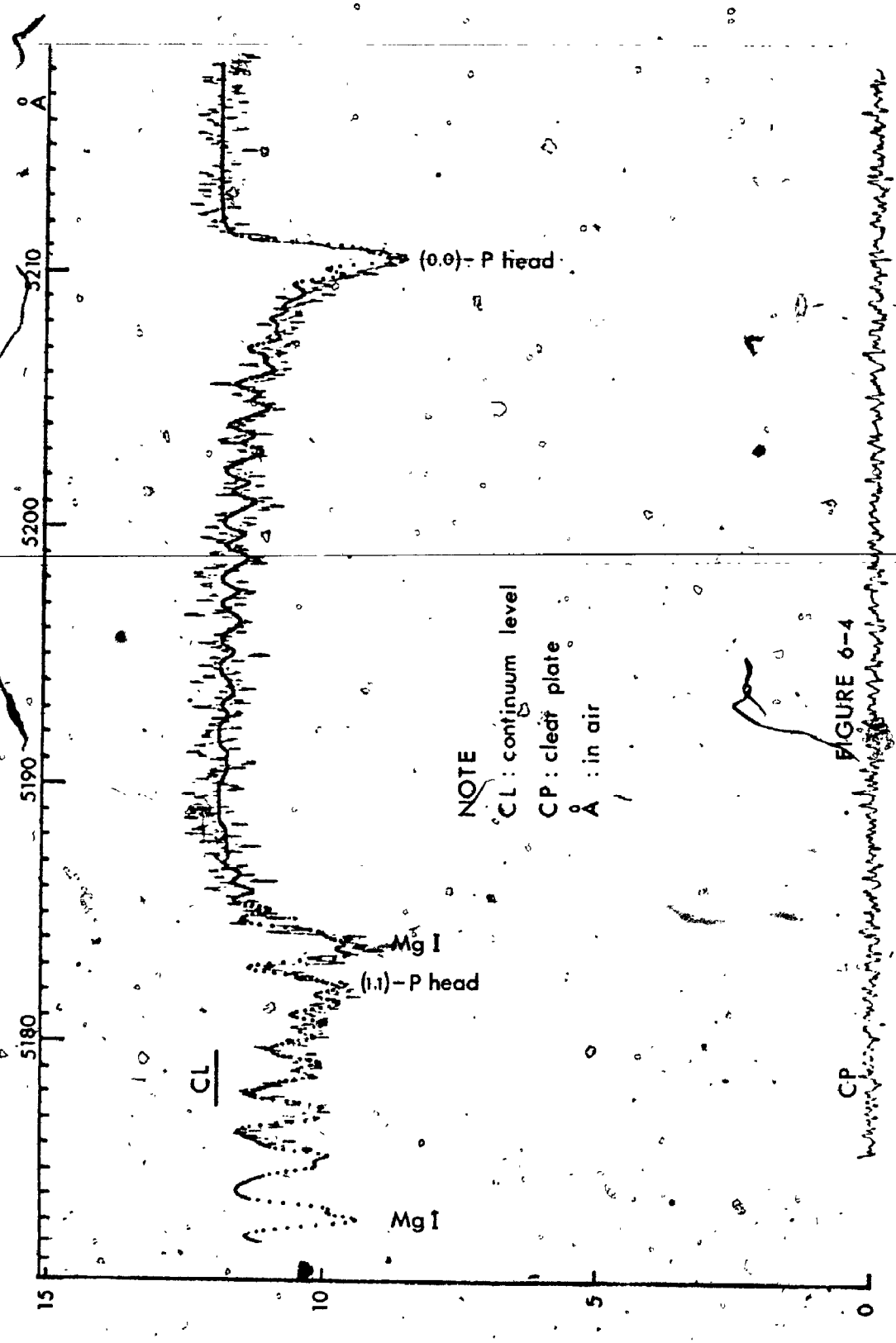

FIGURE 6-4

Microdensitometer Trace (Continuous Curve) and Computer Simulation of it (Dotted Curve) for an Emulsion Exposed to a Flash Continuum which had been passed through a SHOCK-HEATED Argon:Hydrogen mixture containing MgH_o and Mg Absorbers at T_5= 2220°K, P_5= 8.59 atm.

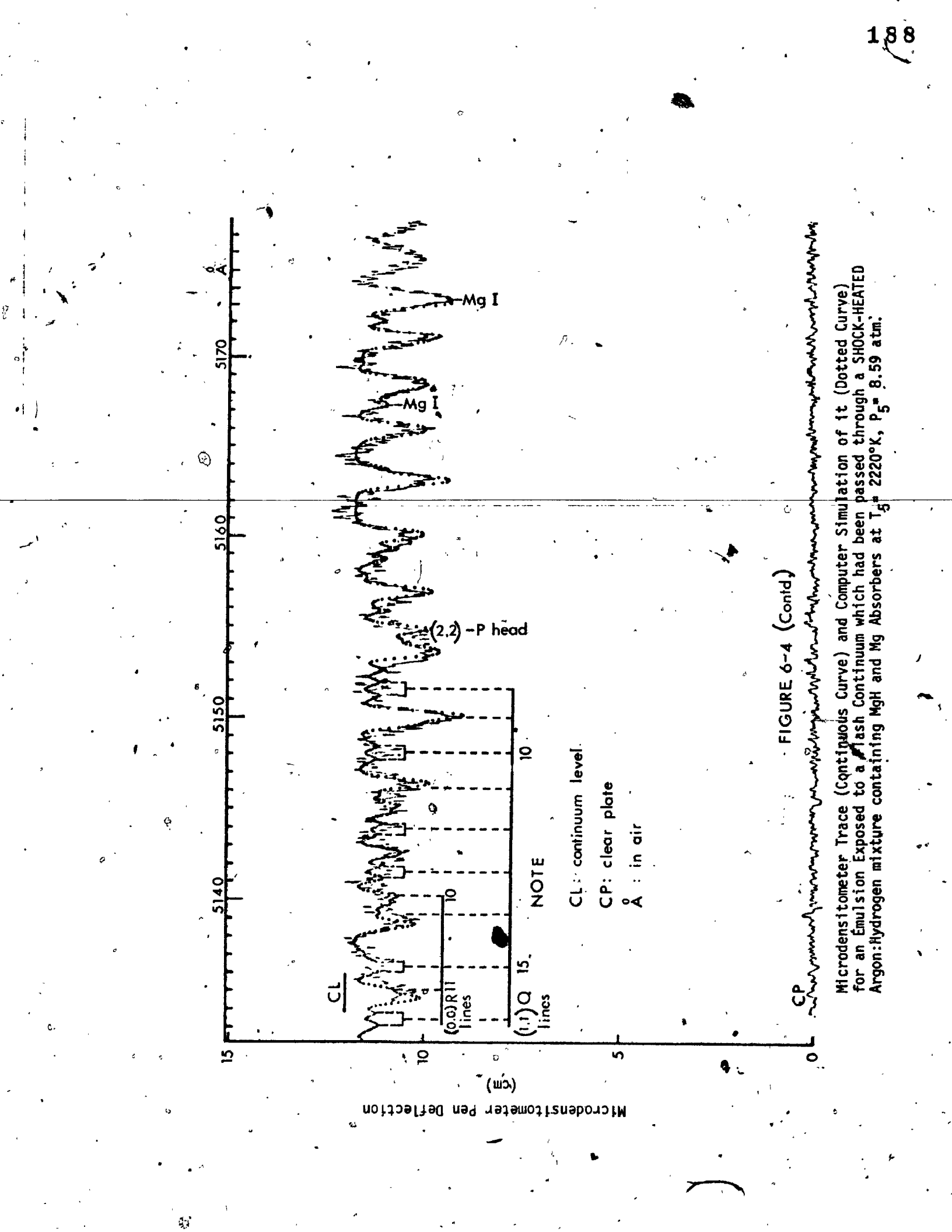

FIGURE 6-4 (Contd.)

Microdensitometer Trace (Continuous Curve) and Computer Simulation of it (Dotted Curve) for an Emulsion Exposed to a Flash Continuum which had been passed through a SHOCK-HEATED Argon:Hydrogen mixture containing MgH and Mg Absorbers at T_5 = 2220°K, P_5 = 8.59 atm.

of information from two photographic negatives in the production of these figures. Some differences in the amount of absorption should be attributed to inclusion of too few lines of the Main Branches. Still, neglect of the (3-3) band does not affect the spectral regions shown. Estimates for the (3,3) P-head (based upon data of Appendix D) lead to a value less than 5125 Å for the longest wavelength portion of the (3,3) band.

Figure 6-4 is based upon unacceptable scaling factor α and μ values. It is an unacceptable simulation for, although it reproduces the absorption spectrum between 5175 & 5212 Å quite well, it overestimates the absorption between 5130 & 5145 Å. This effect might be due to use of an incorrect temperature during the synthesis. However, this spectrum was very insensitive to small variations in the α scaling factor. Thus it is believed to have yielded a poor estimate for ΣRe^2.

6.3.2 Experimental Values obtained for ΣRe^2

Of the seven spectra presented in Fig 6-2, synthesis of six has been successfully completed. For the seventh spectrum, characterized by a reflected shock temperature of 2158°K, the absorption features were too faint to allow an adequate comparison with the synthesized spectrum due to emulsion graininess. Another cause for rejection of the synthesized output is given in the following paragraph.

Hurle (1967), when measuring the Hydrogen-atom recombination rates behind shock waves, found equilibrium between

H and H_2 (for an initial loading of 13.2 Torr of a 60% H_2 to 40% Ar mixture) 15μsec after passage of an incident front with U_1=3.34km/sec. He observed a luminous front (T:observed, 3560°K;theoretical, 3550°K) followed by a relaxation zone until equilibrium (T,P:observed, 2908°K 1.12atm;theoretical, 2925°K 1.13atm) was reached. That shock-heated gas temperature is comparable with those used in this work. At the higher initial loading pressures employed here, it is expected that equilibrium was reached behind the reflected shock front in about 15μsec also. Consequently, as the reflected front - in this work - had to advance from the end wall past the transverse viewing windows (7.25cm) before the spectrograph slit was uncovered (to prevent unwanted exposure of the film), the delay time between shock reflection and slit opening had to be >140μsec for the temperatures associated with the spectra of Fig 6-2. Except for the 2158°K case, the above constraint was met by use of a 150μsec delay. For the 2158°K exposure, the delay was 25μsec. Synthesis was attempted regardless to find out if the luminosity of the front was sufficient to affect the recorded absorption features. Unfortunately, owing to emulsion graininess, the small amount of absorption recorded was insufficient to permit the test. Results for the remaining six spectra are presented in Table 6-6. There ΣRe^2 is given in atomic units (ea_0= $2.5415496 \times 10^{-18}$ esu-cm).

Line shape factors and line half-widths (both evaluated at 5183 Å) are quoted for each absorber at every temperature.

TABLE 6-6

Experimentally Determined $\Sigma Re^2/(ea_o)^2$ Values
Based Upon $D_o = 2.00eV$, $\Sigma g_1 f_{1u} = 1.05$

T_5 (^oK)	$\overline{P_5}$ (atm)	Line Shape a	w_d, w_c w_v (Å)	Scale Factor μ	Scale Factor α	$\Sigma Re^2/(ea_o)^2$ (atomic units)
2220	8.59	7.63	0.019 0.163 0.164	1.1±0.1	6.0±2.0	0.0255±0.0088
		3.70	0.017 0.077 0.081			
2338	4.09	3.45	0.018 0.076	0.5±0.1	1.0±0.1	0.0697±0.016
		1.67	0.080 0.018 0.037 0.044			
2411	7.88	6.45	0.018 0.143 0.146	1.5±0.1	5.0±0.5	0.0418±0.0050
		3.13	0.018 0.067 0.071			
2596	6.79	5.18	0.019 0.119 0.122	1.2±0.05	2.4±0.1	0.0697±0.0041
		2.51	0.019 0.056 0.062			
2606	10.91	8.28	0.019 0.191 0.193	2.2±0.1	6.5±0.5	0.0472±0.0042
		4.01	0.018 0.086 0.089			
2897	10.01	6.85	0.019 0.166 0.168	2.3±0.1	5.0±0.5	0.0641±0.0070
		3.27	0.019 0.075 0.079			

Note that line shape factors and line half-widths are entered in the order: atomic then molecular and w_d, w_c then w_v.

It is worth noting that ΣRe^2 values are derived from lines whose shape factors range between 1.67 and 4.01 for the MgH rotational lines and between 3.45 and 8.28 for Mg I. Clearly, the absorption region must have been optically thick for MgH and Mg I radiations.

Estimates of uncertainty are given beside the experimentally obtained values of the scaling factors μ and α. They were determined by halving the difference between the quoted value and the value nearest it which gave a detectable difference in the fit. The estimated uncertainties in ΣRe^2 are rms deviations due only to uncertainties in μ and α.

Calculation of the mean value from Table 6-6 yields $\Sigma Re^2/(ea_0)^2=0.0530\pm0.0073$ when all data are included. As the value of 0.0255 is more than 3 standard deviations (0.0219) from the mean, it was rejected and the accepted value for the mean found to be $\Sigma Re^2/(ea_0)^2=0.0585\pm0.0059$. In deriving this value the following data were used: $\Sigma g_1 f_{1u}=1.05$, $D_0=2.00$eV.

In addition to the results summarized in Table 6-6, synthesized microdensitometer traces were produced for six of the Fig 6-2 spectra at reflected shock temperatures corresponding to the measured incident shock speed, U_1. It was impossible to obtain fits that represented the spectra well for wavelength intervals greater than 75 Å. In addition to yielding less satisfactory fits, these conditions produced a much greater scatter in the observed estimates of ΣRe^2. Similar simulations were performed for reflected shock temperatures corresponding to incident shock front speeds of

$0.80U_1$, $0.85U_1$ and $0.95U_1$ for the 2897°K spectrum. The overall fits that best represented the original tracings occurred when $0.90U_1$ was used for calculating the reflected shock conditions. Then a reasonable fit of the MgH spectrum could be made over a 200 Å interval.

6.3.3 $\Sigma Re^2/(ea_0)^2$ Using Best Available Estimate for $\Sigma g_l f_{lu}$

The quantity $\Sigma g_l f_{lu}$ should be considered in the form $(g_t f_{lu})\ \Sigma(g_l/g_t)$ which more clearly indicates it to be a product of a weighted oscillator strength for the entire triplet and the sum of relative weight factors -- customarily referred to as relative oscillator strengths. Thus error in $\Sigma g_l f_{lu}$ arises both from $(g_t f_{lu})$ and $\Sigma(g_l/g_t)$. These terms are considered separately below.

6.3.3.1 Relative gf-values for the Mg I 5167 - 5183 Å lines

The results of Table 6-6 are predicated upon gf-values given by Allen (1963) which are averages of laboratory experimental results (Kersten & Ornstein,1941;Allen,1957) and theoretical estimates (Trefftz,1949,1950; Bates & Damgaard, 1950). Other gf-values are available and some are presented in Table 6-7.

It may be seen that experimental values for the relative intensities of the Mg I lines (which are linearly proportional to the gf-values) deviate from Russel-Saunders Coupling by not more than ±5% except for the data of Corliss et al. (1962). After discarding the latter value on the basis

TABLE 6-7

Relative gf-values for the Mg I $3s3p\,^3P^o$ - $3s4s\,^3S_1$ Triplet

Source	λ(Å) 5183	λ(Å) 5172	λ(Å) 5167	Claimed %Error	Technique
a) Experimental:					
1941 Kersten et al.	100	59.4	19.8		Carbon Arc em.
1962 Corliss et al.	100	54	18.5		Copper Arc em.
1962 Penkin et al.	100	60	20	5-10	Hooks & absorp.
1964 Aarts & Bosch	100	61	21	6	Furnace em.
b) Theoretical:					
1963 Allen	100	60	20		L-S coupling
1964 Helliwell	100	60	20		Semi-empirical
1968b Warner	100	59.9	20		Intermediate
c) Values adopted for this work:	100	60	20	5	

(Schaefer, 1971) of arc demixing and lack of local thermodynamic equilibrium in the arc, it was concluded that for the present work the lines of the Mg I triplet could be assumed to follow L-S coupling within a ±5% error bound.

6.3.3.2 Absolute Value for $g_t f_{lu}$

A fairly precise estimate of the absolute value for $g_t f_{lu}$ is much more difficult to obtain due to the lack of close agreement among the published values.

Since 1962, there has been great activity in the experimental measurement of atomic gf-values using Hanle-effect, phase-shift, anomalous dispersion and Beam-foil techniques. Work completed before 1969 has been critically reviewed by Weise, Smith & Miles (1969). Martinson (1974) has surveyed Beam-foil results produced since that time. Accompanying this resurgence of experimental interest has been a host of theoretical calculations. Some of this recent data applicable to the Mg I $3s3p\,^3P^o$ - $3s4s\,^3S_1$ transition is presented in Table 6-8; while Table 6-9 contains some of the available data for the $3s^2\,^1S_o$ - $3s3p\,^1P_1$ transition. (Percentage errors in f_{lu} and A_{lu} are the same as those quoted with the lifetime measurements.) The transitions and their relation to the lowest lying energy levels of the Mg atom are depicted in Figure 6-5.

Exclusive of the Corliss & Bozman data, lifetime measurements for the $3s4s\,^3S_1$ state average 12.4nsec with an approximately ±20% spread. The agreement is heartening; but the spread in data would lead to an unacceptably high uncertainty

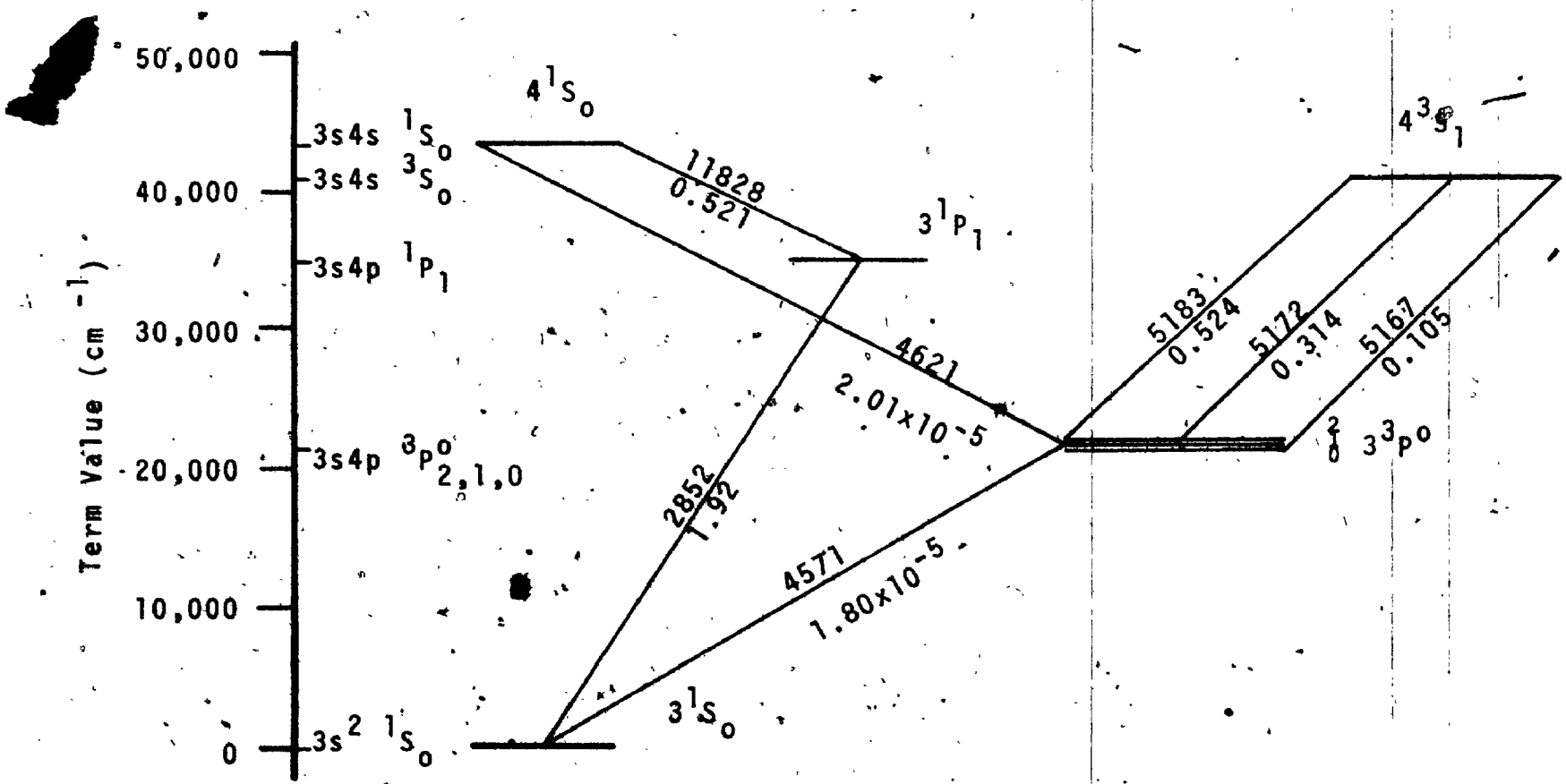

FIGURE 6-5

Lowest Lying Levels of Mg I (after: Risberg, 1965; Risberg & Swenmson, 1965). Air Wavelengths and Warner's (1968b) calculated gf-values are indicated for Observed Transitions. Energy separations of 3^3P^0-levels have been exaggerated.

TABLE 6-8

Lifetime, Absorption f-value and Transition Probability (A_{ul}) for the Mg I Triplet $3s3p\,^3P^0 - 3s4s\,^3S_1$ about 5167-5183 Å.

Source	Lifetime (nsec)	f_{lu}	A_{ul} x10^{+8} sec^{-1}	Technique
a) Experimental Values:				
1962 Corliss & Bozman	2.70	0.498	3.71	Arc in emission
1964 Aarts & Bosch	11.8	0.113	0.844	Arc in emission
1970 Berry, Bromander et al.	13. ± 1.	0.103	0.769	Beam-foil
1971 Schaefer	14.8 ± 0.7	0.0907	0.676	Delayed-coincidence
1972 Andersen, Mohave et al.	10.1 ± 0.8	0.133	0.990	Beam-foil
b) Theoretical Values:				
1950 Trefftz	10.05	0.134	0.995	SCF-polarization included
1964 Helliwell	9.5	0.14	1.05	Semi-empirical
1967 Weiss	9.62	0.139	1.04	SCF
1967 Zare	11.1	0.12	0.89	SCF
1968a Warner	19.0	0.0708	0.527	STFD-intermediate coupling
1968b Warner	12.8	0.105	0.782	STFD-intermediate coupling
c) Critically Averaged "best values":				
1963 Allen	11.5	0.116	0.869	
1969 Weise, Smith & Miles	9.62 ± 0.96	0.139	1.04	
d) Value adopted for this work:	10.0 ± 0.8	0.134	1.00	

NOTE: SCF stands for Self-Consistent Field.
STFD represents Scaled Thomas-Fermi-Dirac Wavefunctions.

TABLE 6-9

Lifetime, Absorption f-value and Transition Probability $(A_{ul})_0$ for the $3s^2{}^1S_0$ - $3s3p{}^1P_1$ Mg I Resonance Transition at 2852.13Å

Source	Lifetime (nsec)	f_{lu}	A_{ul} $\times 10^{+8}$ sec^{-1}	Technique
a) Experimental Value:				
1958 Ostrovskii et al.	3.05±0.8	1.2	3.28	Hooks & abs.
1961 Ostrovskii et al.	2.9 ±0.7	1.25	3.44	Hooks & abs.
1962 Corliss & Bozman	3.3	1.1	3.01	Arc emission
1962 Demtröder	3.29±0.16	1.11	3.04	Phase-shift
1964 Hulpke et al.	1.99±0.08	1.84	5.03	Phase-shift
1964 Lurio	1.99±0.08	1.85*	5.03	Hanle-effect
1966 Smith & Gallagher	2.03±0.06	1.80	4.95	Hanle-effect
1970 Andersen et al.	2.2 ±0.2	1.67*	4.56	Beam-foil
1970 Berry et al.	1.5 ±0.2	2.4	6.56	Beam-foil
1971 Smith & Liszt	1.9 ±0.3	1.86*	5.26	Phase-shift
1973 Lundin et al.	2.09±0.10	1.75	4.78	Beam-foil
b) Theoretical Value:				
1950 Bates & Damgaard	2.29	1.60	4.37	Coulomb app.
1950 Trefftz	1.662	1.674*	4.542*	SCF
1964 Helliwell	1.98	1.85	5.06	Semi-empirical
1967 Weiss	2.13	1.72	4.70	SCF
1967 Zare	2.36	1.55	4.24	SCF
1968a Warner	2.27	1.61	4.40	STFD-intermed.
1968b Warner	1.91	1.92	5.25	STFD-intermed.
1973 Bates & Altick	2.12	1.73	4.73	SCF
c) Critically Assessed "best values":				
1963 Allen	2.29	1.6	4.37	
1969 Weise, Smith & Miles	2.02	1.81	4.95	
d) Value Recommended after this comparison	2.05±0.10	1.78	4.88	

NOTES:

All theoretical studies have included some degree of configuration interaction. SCF is short for Self-consistent Field. Warner used Scaled Thomas-Fermi-Dirac (STFD) one-electron wavefunctions and an intermediate angular momentum coupling scheme that employed measured values of relative line intensities.

* Denotes a value given by the original author which is of a precision different from the remainder of the tabulation.

in ΣRe^2. The theoretical estimates have the same ±20% spread and cluster around 10.6nsec when Warner's (1968a) data is rejected. (Presumably, this calculation suffered from the use of an inappropriate experimental value. Refer to the note below Table 6-9.)

In an effort to establish f_{lu} for the 5167 - 5183 Å triplet more precisely, data for the 2852 Å resonance and the 4571 Å intercombination lines were examined carefully. However, only one experimental result - an atomic beam absorption measurement $f_{lu} = (5.0\pm1.0)\times10^{-6}$ (Boldt,1958)-was found for the intersystem combination line. Data for the resonance line is much more extensive and is presented in Table 6-9 where the recommended lifetime listed in section d) was determined after rejection of data due to Ostrovskii, Demtröder and Berry,Bromander & Buchta.

Lurio (1964) and Smith & Liszt (1971) criticize Demtröder's value on the basis that radiation entrapment vitiated it. Corliss & Bozman's data was not included for the reasons mentioned earlier. Data of Ostrovskii et al. suffered from an inexact value for the Magnesium vapour density (Lurio, 1964) and so were not used in the averaging process.

Andersen, Mølhave & Sørensen (1972) claim that Beam-foil data yield just as precise measurements of upper state lifetimes as do other techniques when requisite cascade corrections are applied. Lundin et al.'s (1973) value in Table 6-9 - itself corrected for cascade - bears out this contention. For at 2.09±0.10, it agrees extremely well with the Hanle-effect

value of 2.03±0.06 (Smith & Gallagher,1966) and the phase-shift measurement of [illegible]99 ± 0.08 (Hulpke et al., 1962).

Andersen et al. (1972) find Schaefer's results to have a systematic error; and further fault the same results as well as those of Berry, Bromander & Buchta for lack of cascade correction. Therefore, of the experimental values listed in Table 6-8, only those of Andersen et al. (1972) and Aarts & Bosch (1964) might be considered reliable. After weighing these two values, the available theoretical estimates for f_{1u} and the averaged value suggested by Weise, Smith & Miles (1969), it was decided to adopt $f_{1u} = 0.134 \pm 0.011$ as the best available estimate for the absorption oscillator strength. This value leads to $\Sigma g_1 f_{1u} = 1.20_6 \pm 0.11_4$ (~9.5%) when the 5% error bound for assumed L-S coupling is combined with the uncertainty in f_{1u} to yield the rms error of the summation.

6.3.3.3 Variation of $\Sigma Re^2/(ea_0)^2$ and the (0,0) MgH $A^2\Pi - {}^2\Sigma^+$ Absorption Oscillator Strength with $\Sigma g_1 f_{1u}$ and D_0^* values.

Now that an estimate for $\Sigma g_1 f_{1u}$ better than Allen's (1963) value is available for the MgI triplet, revised values for $\Sigma Re^2/(ea_0)^2$ may be calculated. Table 6-10 contains such values. Individual $\Sigma Re^2/(ea_0)^2$-values were determined from the spectrum synthesis scaling factors of Table 6-6 and Eq (6-22) was employed to take the change in dissociation energy into account. For each D_0^*-value new averages were calculated and yielded the results in column 2 of Table 6-10.

TABLE 6-10

Effect of D_0^* and $\Sigma g_1 f_{1u}$ Values on (0,0) Absorption Oscillator Strength and $\Sigma Re^2/(ea_0)^2$

D_0^* (eV)	$\Sigma g_1 f_{1u}$(Allen)		$\Sigma g_1 f_{1u}$(Table 6-8)	
	$\Sigma Re^2/(ea_0)^2$	$f_{0,0}$	$\Sigma Re^2/(ea_0)^2$	$f_{0,0}$
1.76	0.174 ±0.019	0.0096	0.200 ±0.028	0.011
2.00	0.0585±0.0059	0.0033	0.0672±0.0093	0.0037
2.10	0.0372±0.0038	0.0021	0.0427±0.0059	0.0024
2.49	0.0064±0.0009	0.00036	0.0078±0.0013	0.00043

TABLE 6-11

Transition Probability and Absorption Oscillator Strength Data for the $\Delta v=0$ Sequence of the MgH $A^2\Pi - X^2\Sigma^+$ System

Band	(0,0)	(1,1)	(2,2)	(3,3)
* $f_{e1}(\lambda)$	0.00394	0.00396	0.00398	0.00400
$f_{v'v''}$	0.0037	0.0036	0.0029	0.0025
$S_{v'v''}$(A.U.)	0.12_7	0.11_1	0.096_6	0.082_5
$A_{v'v''}(sec^{-1})$	$2.3\times10^{+5}$	$2.1\times10^{+5}$	$1.8\times10^{+5}$	$1.6\times10^{+5}$
Origin (cm^{-1})	19284.7	19387.3	19484.7	19592.0
$q_{v'v''}$	0.9414	0.8284	0.7191	0.6141

* $f_{e1}(\lambda)$ and other quantities in Table 6-11 are evaluated with wavelength corresponding to the band origin.

(The results for the 2158°K spectrum were not included in any average.) Errors quoted in that table are rms values entering through the average value and the error in the summation. The $f_{0,0}$ values given in Table 6-10 possess the same percentage errors as the $\Sigma Re^2/(ea_0)^2$.

The notation used throughout this chapter, except for ΣRe^2 which is defined by Eq. (6-14), has been that of Schadee (1967, 1971) and Arnold & Nicholls(1972). $\Sigma Re^2/(ea_0)^2$ used here is related to $\Sigma|Re(\bar{r}_{v',v''})/ea_0|^2$ via

$$\Sigma|Re(\bar{r}_{v',v''})/ea_0|^2=(2S+1)\left\{\Sigma Re^2/(ea_0)^2\right\} \qquad (6\text{-}23)$$

$S''=S'=S=\frac{1}{2}$= spin multiplicity of both upper and lower electronic states.

Throughout the computer synthesis it has been assumed that the same ΣRe^2 applied to all bands of the $\Delta v=0$ sequence. Thus, adopting the more concise notation ΣRe^2 as there is no variation in this quantity with r-Centroid, the related band parameters given by Schadee(1967) $f_{el}(\lambda)$, $f_{v',v''}$, $A_{v',v''}$ and the Band Strength $S_{v',v''}$ given by Nicholls & Stewart (1962) take the functional form

$$S_{v',v''}=q_{v',v''}(2S''+1)\left\{\Sigma Re^2/(ea_0)^2\right\}= \text{Band strength in atomic units} \qquad (6\text{-}24)$$

$$f_{el}(\lambda)=\left\{\frac{f_{v',v''}}{q_{v',v''}}\right\}= \text{Wavelength dependent electronic Oscillator strength for absorption.} \qquad (6\text{-}25)$$

$$f_{v',v''}=\left\{\frac{8\pi^2 m_e c}{3he^2}\right\}\left\{\frac{q_{v',v''}}{\sum_{v'}q_{v',v''}}\right\}\left\{\frac{\Sigma Re^2}{2-\delta_{0,\Lambda}}\right\}= \text{absorption oscillator strength for the } (v',v'') \text{ band} \qquad (6\text{-}26)$$

$$\tilde{A}_{v'v''} = q_{v'v''}\left\{\frac{64\pi^3}{3h\lambda^3}\right\}\left\{\frac{\Sigma Re^2}{2 - \delta_{0,\Lambda'}}\right\} = \text{Spontaneous emission transition probability} \quad (6\text{-}27)$$

Values for the first four bands of the $\Delta v=0$ sequence of the MgH $A^2\Pi - X^2\Sigma^+$ system determined from

$$\frac{\Sigma Re^2}{(ea_o)}^2 = 0.0672 \pm 0.0093 \quad \text{A.U.}$$

(the value which the author feels is the best estimate) and Eqs (6-24) to (6-27) are given in Table 6-11.

Using the dissociation energy of Heimel et al. (1963) and the $\Sigma g_l f_{lu}$ value determined from Table 6-8, the author concluded that the sum of the squares of the transition moments (given via Eq (6-23)) resultant from these experiments is

$$\sum_{p''p'} \sum_{\Sigma''\Sigma'} \left\{\frac{Re(\bar{r}_{v'v''})}{(ea_o)}\right\}^2 = 0.13_4 \pm 0.02 \text{ A.U.}$$

6.3.4 Comparison with Other Experimental Values

When the present researches were begun, there was no experimentally determined oscillator strength for the MgH $A^2\Pi - X^2\Sigma^+$ band system. In the interim, three experimental determinations have been published. They are listed below

Schadee (1965)	$f_{0,0} = 8.0\times10^{-3}$	±10%
Main et al. (1967)	$f_{\Delta v=0} \leq 2.0\times10^{-3}$	±50%
Mallia (1968)	$f_{0,0} = 0.0243 \pm 0.020$	non LTE
	$= 0.0105 \pm 0.020$	LTE

Schadee's and Mallia's results are derived from study of weak solar absorption lines and both presuppose the MgH dissociation energy to be 2.49eV. In Table 6-10, the (0,0) band oscillator strength corresponding to 2.49 eV dissociation energy is 0.00043 a factor of 20 smaller than Schadee's result and between a 25th and a 40th of Mallia's claimed result. Both observers assumed models for the Sun's photospheric structure in the derivation of the band oscillator strength. In fact, Mallia considered six different models and obtained six estimates of $f_{0,0}$ ranging from 8.5×10^{-3} to 3×10^{-2}. It is difficult to place much credence in his claimed values for non Local Thermodynamic Equilibrium models and Local Thermodynamic Equilibrium models. His range of f-values casts doubt on the validity of Schadee's result as well for it, too, was based upon a model atmosphere calculation.

It appears that Main used 1.85eV for the MgH dissociation energy. A graph of the present results yields an interpolated value of $f_{0,0} = 7 \times 10^{-3}$ for this dissociation energy. This number is about three and a half times Main's upper limit. However the agreement is reasonably satisfactory. There were so many competing reactions in Main's rocket exhaust source that error in the thermochemical data for one species could have changed the concentrations drastically. To the contrary, in the present work, the only unknown thermochemical datum is the MgH dissociation energy and allowance for that has been made in this comparison.

6.49

Main's published wavelength-intensity graph for the radiation from his rocket exhaust shows a low dispersion trace in which MgH and Mg emissions are indistinguishable. They are completely overlapped one by the other. At wavelengths greater than 5175Å, the MgH features are superposed upon the wing of an unidentified 5252Å transition that is over 100Å wide at the baseline. For wavelengths less than 5050Å, MgH features are overlapped and masked by the much stronger emission from $\Delta v=0$ bands of the MgO $B^1\Sigma^+ - X^1\Sigma^+$ system. Main makes special note of an unidentified background underlying his MgH bands and ascribes it 'possibly' to MgO (B-A). The background is ignored in his later calculations.

Consequently, Main's conclusions regarding MgH and MgO (B-X) are of questionable validity. At 4000°K, his calculated temperature, many lines of the MgH $\Delta v=0$ R-branches with wavelength less than 5050Å have appreciable intensity. These lines fall in the region of the MgO (B-X) system and were undoubtedly included as part of the MgO (B-X) measurement with the result that they vitiate Main's conclusions regarding the MgO f-number. A more important consequence for the present work, is the corollary that the MgO-overlapped R-branch radiation was not included in his MgH intensity measurement. Therefore it is likely - as the details of his calculations are not given in sufficient particularity to determine otherwise - that Main included only a portion of the $\Delta v=0$ MgH sequence radiation without allowing for the remainder. Consequently, his resultant f-number should be

considered an under-estimate of the true value.

Finally, his result could have been influenced by self-absorption - particularly in the region of the Mg I triplet. Many times, shock-tube emission spectra taken by the author have shown considerable absorption at the centre of strong atomic lines.

For all the above reasons, the author believes that Main's result was too low and that the value obtained in the present study more closely approximates to the true value.

6.4 Error Analysis

Much of the error evaluation has already been done. As was mentioned in the last section, thermochemical data are well determined for the system studied: Ar, H_2, H, Mg and MgH being the predominant species. Only for MgH - via its dissociation energy - is there an uncertainty in the significant information. Accounting for possible values of the dissociation energy by the method just performed is a good way of taking into account possible changes in D_o^*. Indeed it might be advisable, at a later date if warranted then, to compute points for a continuous curve of f-vs-D_o^*. There is sufficient information

in this chapter to allow that calculation to be made.

As the thermochemical data for the Test gas mixture is so well known, it is expected that the calculated temperatures will be quite close to thosethat actually occurred. The shock speed studies of Chapter 4 showed how the irregularity in viewing 'Head' cross-section could be allowed for. Hurle's (1967) and more recent works have shown that for Hydrogen-Argon mixtures, calculated and observed Test gas conditions agree very well in the equilibrium behind the shock front.

A serious source of error in this type of experiment is emulsion calibration. It is felt that the effects of Reciprocity Law failure have been minimized in this work. The last statement is particularly true for five of the seven spectra studied quantitatively. For those five cases, the absorption flash - passed through a step density attenuator - served to define the calibration in addition to the standard lamp. The other two spectra were recorded on the same film strip. It was cut from the same film role as two other strips (one preceding it, the other following it) which were subjected to absorption flash calibration. Those two film strips had remarkably similar calibration curves. Of course, the two-absorption-exposure-strip still had two standard lamp exposures impressed upon it. These efforts notwithstanding, emulsion calibration is still an important source of error. The fact that the method employed is a relative intensity determination means that the determina-

of the calibration curve need not be an absolute one. This decreases the error introduced into derived values by use of such a curve.

Emulsion calibration errors are, still, probably the most important single cause for the spread in the experimentally determined ratio μ/α. Certainly, pains were taken to maintain precision in the computer calculations. Uncertainties in calculated values must be sought in the input data - such as in the collision cross-sections. Those are likely to furnish the second most important source of error in this experiment. Those cross-sections are not known precisely. Averages for a particular family of elements are not so satisfactory data as particular values previously determined for a given family member.

On the basis of calibration error and uncertainty in the collision cross-sections, the error bounds for the "sum of the squares of the transition moments" seems a bit low. This error bound contains within it the uncertainty in the value for ΣRe^2 derived from the raw computer output. The latter uncertainty was taken as one standard deviation. A reasonable value for the error bound on the final value of ΣRe^2 would thus seem to be 20 - 25%. Consequently as the final result of this experiment, the MgH $A^2\Pi - X^2\Sigma^+$ is found to have a "sum of squares of the transition moments" given by

$$\sum_{p',p''} \sum_{\Sigma',\Sigma''} \left| \frac{Re(\bar{r}_{v'v''})}{(ea_o)} \right|^2 = 0.13 \pm 0.03 \left\{ \begin{array}{l} \text{based upon} \\ D_o = 2.00\,\text{eV} \\ \Sigma g_1 f_{1u} = 1.20_6 \pm 0.11_4 \end{array} \right.$$

CHAPTER 7

Conclusions & Suggestions for Further Work

In the interest of brevity, the main conclusions of this work are listed in point form within Section 7.1. Some amplification of them is included in the suggestions of Section 7.3.

7.1 Conclusions

1) The shock-excitation of Magnesium powder in an Ar-H_2 Test gas does yield MgH molecules behind the reflected shock front.
2) There is sufficient MgH formed within the shock tube to permit quantitative absorption spectrophotometry of the MgH $A^2\Pi - X^2\Sigma^+$ band system.
3) Shock parameters for the MgH, Mg, H, H_2 and Ar mixture were evaluated by the methods outlined in Chapter 2 (plus Appendix C) and served as data for the remaining chapters.
4) Shock speed studies provided a means of relating the reflected shock speed to the measured incident shock front speed and so allowed correction for non-uniformity in the cross-section of the observation

region.

5) This method of hydride production was attempted using Beryllium and Aluminium as sample materials and resulted in the formation of the BeH and AlH molecules as witnessed by emission and absorption spectra of Chapter 5.

6) The data of Guntsch(1939) and Balfour(1970) were re-analysed so that reconstructed wavelengths and a set of consistent energy levels could be used in the synthesis of microdensitometer tracings.

7) A series of computer programmes was developed which allowed good simulation of microdensitometer traces of the MgH spectra.

8) A value for "the sum of the squares of the electronic transition moments" - common to the (0,0), (1,1) & (2,2) bands - was determined to be 0.13 ± 0.03 atomic units.

7.2 Suggestions for Equipment Improvements

The basic limitations of the present shock tube could be removed by:

1) Replacement of the viewing 'Head' with one of more suitable geometry.

2) Addition of pressure sensitive and recording gauges for the determination of P_2 and P_5.

3) Provision of a line-reversal temperature measuring device for on-line routine operation.

4) Use of scribed metal diaphragms instead of Mylar to

remove C_2-Swan contamination which is particularly noticeable at P_5-values greater than 10 atmospheres.

7.3 Suggestions for Further Experimentation

The following suggestions include extensions of the present studies to other hydrides, to the determination of atomic optical collision cross-sections and to an investigation of predissociation in AlH.

7.3.1 Further Investigations of the MgH $A^2\Pi$ - $X^2\Sigma^+$ system

The MgH A-X system has been identified and studied as a contributor to the radiation balance in rocket exhaust gases (Main, 1967), in the solar photosphere (Laborde, 1957, 1961; Schadee, 1965; Withbroe, 1968), in sunspots (Branch, 1970) and in the atmospheres of K- and M-type stars (Merchant Boesgaard, 1968). For determinations of heat balances or number densities of species within these environments, a good value for the MgH A-X "sum of squares of the electronic transition moments" is vital. Unfortunately, it is not yet possible to perform ab initio $\Sigma\Sigma|\mathrm{Re}(\bar{r}_{v',v''})|^2$ calculations with any hope of obtaining a realistic value. The recent theoretical values for $f_{0,0}$ of 0.2501 (Hennecker & Popkie, 1971) and 0.192 or 0.188 (Popkie, 1971) for the A-X system are strongly at variance with Schadee's (1965) 0.0080 and the present result 0.0037.

Until theoretical treatments and experimental measurements for molecular transitions can yield comparable results such as those now possible for atomic systems (compare f_{3u} values of 0.133 (Andersen et al., 1972), 0.139 (Weise et

al., 1969) and Froese Fischer's theoretical 0.135 (1975) for the Mg I 5167Å - 5183Å triplet.), continued efforts must be made to improve molecular f-numbers. At present, the author foresees the most fruitful approach as being the experimental one for the theoretical complexities have not yet been overcome even for the lightest hydrides. Thus additional studies of the MgH A-X system are recommended. They should be extended beyond the scope of this study to include bands of other Δv sequences.

As the relative intensity method outlined in this work would be directly applicable to high-temperature furnace studies, it is suggested that such an approach be taken. If some method can be devised to overcome species de-mixing, then photo-electric scanning techniques could be employed to reduce uncertainties in the resultant f-value possibly by as much as a factor of five. A furnace study of MgH A-X would be a worthwhile investigation.

7.3.2 Investigations of Other Hydride Spectra

7.3.2.1 Intensity Measurements

The present relative intensity technique can be applied to spectral studies of any metal, Me, that has hydride bands, MeH and atomic lines Me I in spectroscopically accessible regions. Three metals that could be quantitively investigated without significant modification of the present computer programmes are Cu, Ca and Al as their diatomic hydrides either overlap lines of the corresponding element or lie close to

them. Thus the requisite spectra could be obtained with one setting of an appropriate spectrograph.

However, it is not a requirement of the method that atomic and molecular lines be recorded within the same spectral region. For example, beam-splitting techniques could be used for separate detection of atomic and molecular features. Then, for example, the atomic line could be monitored photo-electrically to yield an absolute concentration of the atomic species. Modification of the microdensitometer trace simulation programme would then allow only a variation in μ (see Eq 6-21a) via changes in the assumed value for ΣRe^2. (Based on the assumption that the optical path for atomic and molecular absorbers was the same within the shock tube.) It is recommended that a study of the BeH A-X system be performed using this technique.

For MeH and Me (Me stands for any metallic element.) species whose f-numbers are already known from other studies, this relative intensity shock-tube technique could lead to the establishment of better estimates of the molecular dissociation energy. Thus experiments treating this problem are suggested.

7.3.2.2 AlH Predissociation

AlH predissociation was particularly evident in the higher Test gas pressure spectra of these studies. Thus it seems likely that the height of the potential maximum above the bottom of the excited state well could be determined more precisely by using shock-excitation techniques. Therefore, the writer suggests the undertaking of a study of AlH

predissociation particularly at P_5 values greater than 10 atmospheres.

7.3.3 Atomic Optical Collision Cross-Sections

The great sensitivity of atomic line widths to the value used for the optical collision cross-section establishes the need to know these parameters for collision systems. A programme devoted to the measurement of line widths and shifts in the presence of foreign gases would be a useful undertaking for a shock-tube spectroscopist. In particular, attention should be focussed upon non-resonance atomic lines and the pressure range $2<P_5<40$ atmospheres. These areas are almost inaccessible to the ballistic compressor technique followed by Ch'en & Henry (1973).

In the relative intensity method for f-number determination employed in the present work, collision cross-sections were needed for non-resonance lines. It is quite likely that they will be of equal usefulness to later investigators.

APPENDIX A

Details of Intermediate Calculations performed in the Computer synthesis of MgH Absorption Spectra

A set of computer programmes was developed for the IBM 1130 which would produce graphical output duplicating microdensitometer tracings of recorded absorption spectra. The programme listings and fine details of the methods used will not be given. It is sufficient to note that the techniques employed were fashioned after those used by Whiting, Arnold & Lyle (1967, 1969) and Drake (1966) because the author had access to listings of both programmes.

As the IBM 1130 has a much smaller storage facility - even in the 16K modification used - and is a slower machine than the computers used by Arnold et al. and Drake, synthesis of spectra was performed using modular programming techniques. Results of each step could then be stored upon disc data files and serve as input to following modules.

The basic steps in the synthetic spectrum computation are outlined below.

A.1 Steps in the Generation of Synthesized Spectra

The computations can be subdivided into the following stages -

i) Storage in disc data files of MgH rotational line wavenumbers, lower state rotational degeneracy, lower state energy, Honl-London and Franck-Condon factors for lines of the six main branches of the (0,0),(1,1) and (2,2) bands of the $A^2\Pi - X^2\Sigma^+$ band system.

ii) Preparation of a disc storage file with the data of i) arranged in ascending order of wavenumber and each datum tagged to the appropriate rotational level of the lower state.

iii) Distribution of the wavelength-dependent absorption coefficient for Mg I lines into a storage array having entries at $\Delta\lambda$=0.01Å intervals with the aid of an appropriate Voigt Profile for the lines.

iv) Distribution of MgH rotational line contributions into a separate molecular absorption coefficient storage array using a different Voigt Profile from that employed in iii) but at the same 0.01Å intervals.

v) Point by Point evaluation of I_λ/I' (via Eq 6-1) and storage of the results for a 10Å interval in a core storage array with entries at 0.01Å intervals.

vi) Preparation of points for the graphical output by evaluation of emulsion response to the radiation of v) that would fall in the spectral interval viewed by the Joyce-Loebl Mark IIIC microdensitometer final viewing slit.

vii) Plotting of output points on a synthesized microdensitometer pen response versus wavelength graph. The plotter available was used at its maximum resolution; namely 0.01" intervals between plotted points.

viii) Recycling. Steps v),vi) and vii) were present in the same programme. Consequently, at the end of each 10Å stretch, completion of step vii) signalled a branch to step v). Care was taken to have sufficient data points in the core array so that proper convolution of spectrograph and microdensitometer response functions could be made for all output points.

Some of the major details in these programmes are explained in the ensuing paragraphs. Slit functions will be treated shortly but first the treatment of the rotational line shape will be described.

A.2 Line Shapes - Molecular Rotational & Atomic

The same treatment was followed in both cases - only the extent of wing contributions differed between the two. Therefore, it is appropriate to discuss both of them at this time.

A.2.1 Basic Relationships

In the present investigations, atoms and molecules of the Test gas were subjected to conditions: $4<P_5<15$ atmospheres, $2200<T_5<3000^{0}K$. At such temperatures, the Doppler line half-width of a spectrum line is given by

$$w_d=\left[\frac{2kT\ln(2)}{mc^2}\right]^{\frac{1}{2}}\cdot\frac{1}{\lambda_0} \qquad (cm^{-1}) \qquad (A-1)$$

and the collision half-width, w_c, by (Jeans, 1954, p252)

$$w_c=\frac{1}{\pi c}\cdot\sum_j N_j\sigma_{ij}^2\left\{(8\pi kT)\left[\frac{1}{M_i}+\frac{1}{M_j}\right]\right\}^{\frac{1}{2}} \quad (cm^{-1}) \qquad (A-2)$$

with N_j - Number of collision partners of type j per cm^3

σ_{ij}^2 - Optical collision cross-section for line broadening are much greater than Natural or Stark broadening line widths. As only Doppler and Collisional broadening mechanisms were significant within the Test gas, the line shape was represented by the classical Voigt Profile. Consequently, k_λ/k^0 was expressed as

$$b(|\lambda-\lambda_0|) = \frac{1}{w_d}\left[\frac{\ln(2)}{\pi}\right]^{\frac{1}{2}}H(a,x) \qquad (A-3)$$

$$H(a,x) = \frac{a}{\pi}\int_{-\infty}^{+\infty}\frac{\exp(-y^2)}{a^2+(x-y)^2}\,dy \qquad (A-4)$$

$$x=\left[\frac{1}{\lambda}-\frac{1}{\lambda_0}\right]\left[\frac{\ln(2)}{w_d}\right]^{\frac{1}{2}}. \qquad (A-5)$$

$$a = \left\{\ln(2)\right\}^{\frac{1}{2}} \frac{w_c}{w_d} = \text{Line Shape Parameter} \qquad \text{(A-6)}$$

where the notation is similar to that of Penner (1959) and Drake (1965). Several recent studies have been made of H(a,x) (Posener, 1959; Young, 1965; Armstrong, 1967) and led to convenient methods for its evaluation (Armstrong, 1967; Hummer, 1965). Whiting (1968) has given a convenient approximation for the Voigt line half-width, w_v

$$w_v = \frac{w_c}{2} + \left\{\left(\frac{w_c}{2}\right)^2 + w_d^2\right\}^{\frac{1}{2}} \qquad \text{(A-7)}$$

which was used only as an indicator of the computer-simulated line profile width. For line wings, i.e. for $|x|>52.4$, the asymptotic series given by Plass & Fivel (1953) was used in the form -

$$H(a,x) = \left(\frac{a}{\sqrt{\pi}\,x^2}\right)\left\{1 + \left(\frac{3}{2} - a^2\right)\frac{1}{x^2} + \left(\frac{15}{4} - 5a^2 + a^4\right)\cdot\frac{1}{x^4}\right.$$
$$+ \left(\frac{105}{8} - \frac{105}{4}a^2 + \frac{21}{2}a^4 - a^6\right)\cdot\frac{1}{x^6}$$
$$+ \left(\frac{945}{16} - \frac{315}{2}a^2 + \frac{189}{2}a^4 - 18a^6 + a^8\right)\cdot\frac{1}{x^8}$$
$$\left. + \left(\frac{10,395}{32} - \frac{17,325}{16}a^2 + \frac{3465}{4}a^4 - \frac{495}{2}a^6 + \frac{55}{2}a^8 - a^{10}\right)\cdot\frac{1}{x^{10}} + \ldots\right\} \qquad \text{(A-8)}$$

For $a>5.0$, computer time was saved with no significant sacrifice of precision by retaining only the first three terms within the curly braces (i.e. to the end of the first line of the equation!).

Armstrong (1967) has demonstrated that

$$\int_{-\infty}^{+\infty} H(a,x)\,dx = \sqrt{\pi}$$

and as $H(a,x)=H(a,-x)$ - for positive a, the only values of significance in the present study - because $H(a,x)$ is an even function of the variable x

$$\int_{0}^{+\infty} H(a,x)\,dx = \frac{\sqrt{\pi}}{2} \qquad \text{(A-9)}$$

A.2.2 Evaluation of $b(|\lambda-\lambda_0|)$ during Profile Generation

For the MgH 5211 Å $\Delta v=0$ sequence, only the spectral range $4800<\lambda<5250$ Å need be treated. Owing to the wavelength dependence of the Doppler line width in this interval, the Line Shape parameter, a, varies about ±3% from its value at 5025 Å. Allowance for this variation was made using the following two-dimensional interpolation scheme. All contributions from a particular line were determined before any contributions from the next line were evaluated.

Card decks containing previously evaluated H(a,x)-values were fed to the computer and their contents stored in a disc storage file. (The H(a,x)-values had been evaluated using either the Gauss-Hermite procedure suggested by Posener,1959 or from the real part of the Complex Probability Integral by methods suggested by Faddeeva & Terentev, 1961.) A set of $H(a_c,x)$ - a_c being the Line Shape parameter associated with the centre of a wavelength interval being treated - was entered into one file and another file was loaded with $DelH(a_c,x)$ values determined from

$$DelH(a_c,x) = \{H(a_c,x) - H(a^*,x)\}/(a^*- a_c)$$

so that H(a,x) for each line could be evaluated at the appropriate wavelength via

$$H(a^*,x) = H(a_c^*,x) + (a_c - a)\,\mathrm{Del}H(a_c,x) \qquad (A\text{-}10)$$

With $x_1 < x < x_2$, a linear interpolation between $H(a,x_1)$ and $H(a,x_2)$ evaluated from Eq (A-10) gave the desired H(a,x) value. Tests of this approximation proved that it provided H(a,x)-values that were within 0.5% of values prepared for the same a-value via the general programmes used to furnish the punched decks of H(a,x)-values for fixed a when a and a* were both within 3-5% of a_c.

Prepared punched decks of input Voigt Profile values agreed with the tabulations of Faddeeva & Terentsev (1961) with a precision of 1 digit in the sixth figure. (A later comparison of the punched deck output with values generated by the programmes listed by Armstrong, 1967 - run in double precision on the IBM 370/158-gave agreement to 1 digit in the sixth significant figure, the precision claimed by Armstrong. The punched deck output agreed to the eighth significant figure with the listings given by Hummer, 1965) The interpolation routine sacrificed some of this precision by producing errors of ±4 in the fourth significant figure in the test cases considered.

The maximum value for $|x|$, $|x_{max}|$, beyond which contributions were assumed zero was determined by numerically evaluating the integral

$$\int_0^{\infty} H(a_c,x)\,dx = x\,x\,\frac{\sqrt{\pi}}{2}$$

using Simpson's Rule and determining values of $|x_{max}|$ for xx values of 0.95,0.96,0.97,0.98 and 0.99 for every prepared card deck. The $H(a_c,x)$-values for 525 values of x at $\Delta x \equiv 0.1$ intervals were read from each card deck. Further values for the numeric integration were provided by Eq (A-8).

Generally, for MgH rotational lines $|x_{max}|$ corresponding to xx=0.95 was found to yield quite acceptable results. For Mg I lines $|x_{max}|$ corresponding to xx=0.98 or 0.99 was selected to allow for the far wings as the atomic features present on the spectrograms were usually much stronger than the molecular ones.

For each line $b(|\lambda-\lambda_0|)$-values were determined at 0.01 Å intervals and the appropriate contributions stored in the atomic or molecular absorption coefficient array. If some contribution were already present at that wavelength location, the contribution from the current line was added to it and the result stored in the location.

The appropriate a_c-value for use with rotational or atomic lines was a prerequisite to the entry of $H(a_c,x)$ and $H(a^*,x)$ data into storage arrays. This a_c-value could only be determined after knowledge of the Test gas mixture composition, temperature and pressure - data provided by the shock tube programmes - was available. However that data alone was insufficient. In addition, the collision cross-sections for broadening of the Mg I and MgH lines by the other species present in the mixture were needed as well. In fact, until the work of Ch'en & Henry was published in 1973, there was

TABLE A-1

Collision Cross-Sections used as Profile Input Data

Lines Broadened	Collision Pairs	σ^2 ($\mathring{A}^2$)	Data Source
MgH	MgH:Ar, MgH:Mg, MgH:MgH	16	Penner (1959)
	MgH:H_2, MgH:H	8	
Mg I	Mg:Ar, Mg:Mg, Mg:MgH	36	Ch'en & Henry (1973a,b)
	Mg:H_2, Mg:H	13	

insufficient data to make a realistic estimate for the collision width of Mg I atomic lines within the shock-heated Test gas. Therefore, a brief summary of the reasons behind the choices for σ^2 presented in Table A-1 is in order and is presented below.

A.2.3 Optical Collision Cross-Sections

In determining w_c - the collisional broadening half-width-from Eq (A-2), values of σ^2 are required for all possible pair collision partners.

A value of $\sigma^2=16\ \mathring{A}^2$ found by Penner (1959) for rotational line broadening of the CO-fundamental vibration spectrum by CO:Ar collisions was used for MgH:Ar collisions. No collision

cross-sections were found in the open literature for MgH. Penner's work and Drake's (1966) thesis indicate that order of magnitude estimates are acceptable for molecular collision cross-sections. In their report on BeO, Drake,Tyte & Nicholls (1967) found order of magnitude estimates for σ^2 to be sufficiently accurate.

Table A-1 lists values for collision cross-sections used in the current work. Values of 16 and 8 $\mathring{A}^2$ apply strictly to broadening of rotational lines in the CO-fundamental vibration band by CO:Ar and CO:H_2 respectively. They are adopted, here, for MgH:Ar and MgH:H_2 collisions in the absence of other data. Because MgH:Ar and MgH:H_2 collisions will normally be the most frequent at temperatures employed in these experiments, MgH:Mg and MgH:MgH cross-sections were assumed to be the same as that for MgH:Ar as the colliding pairs have roughly the same reduced mass. A similar argument was used to justify taking 8 $\mathring{A}^2$ as the cross-section for MgH:H collisions after comparison with the reduced mass of the MgH-H_2 pair. Errors in cross-sections for MgH:Mg, MgH:MgH and MgH:H are expected to be of minor significance for the main collision partners are MgH-Ar and MgH-H_2 pairs.

Contrary to the molecular case, σ^2 for atoms varies strongly with collision partner as shown by the works of Margenau & Watson (1936), Ch'en & Takeo (1957) and Ch'en & Henry (1973a,b). The value chosen for Mg:Ar collisions is an average of the cross-sections for collision of Ca I, Ba I and Sr I with Argon atoms as measured using the resonance

lines. Following a comparison of Ch'en & Takeo's (1957) results for the alkali atoms, the Mg:H_2 cross-section was taken to be that found by Ch'en & Henry (1973b) for Group IIa elements with Helium. For the alkalis, Ch'en & Takeo had found a comparable effect of line broadening using Hydrogen and Helium as the broadening species.

The two broadening parameters for Mg collisions, listed in Table A-1, were obtained from data obtained experimentally at temperatures akin to those used in the shock-tube studies. Ch'en & Henry report temperatures of 2450^{o}K and 2500^{o}K and a range of densities which includes those found in the shock heated Test gas.

Ch'en & Henry (1973a) predict a shift of the Mg I line centres due to collision. So, provision was made in the computer programmes to allow a variable shift of the Mg I triplet relative to the MgH rotational lines. Shifts required to match observed spectra were found to agree with the estimates given by Ch'en & Henry.

A.3 Slit Functions and Convolutions

After an examination of faint lines recorded from a low pressure Mercury source and from an iron arc running in air, it was concluded that a triangular slit function could adequately represent the effect of the spectrograph on the incoming radiation. Thus

$$g(|\lambda-\lambda^{\dagger}|) = \frac{2}{\Delta s_s}\left\{1 - \frac{2}{\Delta s_s}|\lambda^{\dagger} \lambda|\right\} \qquad \left\{\begin{array}{c} \lambda^{\dagger} - \frac{\Delta s_s}{2} < \lambda \\ \lambda < \lambda^{\dagger} + \frac{\Delta s_s}{2} \end{array}\right\} \quad (A\text{-}11)$$

$$g(|\lambda-\lambda^{\dagger}|) = 0 \quad . \qquad \text{otherwise}$$

with Δs_s (a wavelength-dependent quantity) representing the base width of the triangular function in wavelength units.

When the spectra, reported in Chapter 6, were recorded, the spectrograph slit width varied between 30 and 60 microns. Calibration of the slit width settings using a 1P21 photomultiplier verified those widths. The spectra were recorded in the second diffraction order and Δs_s found to vary with the geometrical slit width and plate factor according to

$$\Delta s_s = 2(\text{geometric slit width in mm})(\text{Plate Factor in } \tfrac{\text{Å}}{\text{mm}})$$

As the Plate Factor was ~10.8 Å/mm at 5000 Å (refer to Fig 3-7), Δs_s had a range of 0.65 Å - 1.30 Å. Provision was made to compute Δs_s at each output wavelength from an externally specified slit width during the convolution operations.

Over the spectral range of the spectrograph slit width, it was found experimentally that the flash absorption continuum could be treated as constant in intensity - except in the vicinity of a pressure broadened Xenon emission line. Thus the convolution of Equation (6-17) yielded

$$I^{fc}(\lambda') = \int_0^{\infty} I_{\lambda} g(|\lambda-\lambda'|)\,d\lambda \qquad \text{in general}$$

and

$$I^{fc}(\lambda') = I_{\lambda'} \qquad \text{for specific intensity constant over the spectrograph slit free spectral range}$$

because $\int_{-\infty}^{\infty} g(|\lambda-\lambda^{\dagger}|)\,d\lambda = 1.$

Consequently for most of the spectral range covered,

$$\frac{I^{fc}(\lambda')}{I'_{\lambda'}} = \int_0^\infty \frac{I_\lambda}{I'_{\lambda'}}\, g(|\lambda-\lambda'|)d\lambda$$

and was evaluated over the slit function width by Simpson's Rule for the more than sixty profile points that lay within the free spectral range Δs_s. (Recall that the synthesized spectrum was evaluated at 0.01 Å intervals.

The effects of the Joyce-Loebl Mark IIIC microdensitometer's slit function were more difficult to determine. In this unit, the recorded spectrum is scanned by an entrance slit whose enlarged image is projected upon a 'final viewing slit' of width Δs_d. This width is a function of the optical components in the scanning light path and the Plate Factor of the emulsion being scanned. For the spectra of Chapter 6, the 'final viewing slit' had a geometric width in the range 200 - 300 microns. Using the typical value of 220μ, the interval on the recorded spectrum whose enlarged image fell between the jaws of the 'final viewing slit' was about 0.02 Å when a 5X objective was used and 0.10 Å for a 10X objective. With the 10X objective inserted, the microdensitometer 'final viewing slit' scans between one-seventh and one-tenth of the recorded spectrograph slit image.

As the 'final viewing slit' was much larger than its diffraction width, a rectangular slit function of width Δs_d was used to represent it. Thus

$$h(|\lambda-\lambda''|) = \frac{1}{\Delta s_d} \qquad \left\{ \begin{array}{l} \lambda'' - \frac{\Delta s_d}{2} < \lambda \\ \lambda < \lambda'' + \frac{\Delta s_d}{2} \end{array} \right\} \quad \text{(A-12)}$$

$h(|\lambda - \lambda''|) = 0$ otherwise

when there was an odd number of Intensity values in the interval covered by the 'final viewing slit' and when the outer Intensity points fell at the location of the slit jaws. Of course, this was not the common case and special end corrections had to be provided. Fewer than ten (10) profile points normally fell between the 'final viewing slit' jaws. Thus, it was assumed that the Intensity variations in this region could be treated as continuous and a series of parabolae were fitted to every three-point sequence (the basis of Simpson's Rule). The area under these points was determined and summed when the points lay between the slit jaws. The points just external to the jaws were used in conjunction with those near the ends to compute the end corrections.

In the output graphs (the microdensitometer linkage was normally used at the 50X (nominal) value), points were plotted at increments of 0.01" on the traces - corresponding to wavelength increments of ~0.05Å. Spectrograph slit convolutions were performed at wavelengths corresponding to these output points. They were kept in a temporary storage array - one member being removed from the bottom of the array as the newest member was added at the top. These entries were sufficient to allow proper convolution with the microdensitometer slit function. It was noted that, as the microdensitometer output density value was a function of the total radiation incident on the emulsion within the range covered by the jaws of the 'final viewing slit', $I_{dens}(\lambda'')$ must be evalu-

ated before taking logarithms to calculate the correct density response from the calibration curve.

For those regions in which the absorption flash luminosity, I'_λ could be considered constant over the spectral range of the spectrograph entrance slit, the convolution of the microdensitometer slit function with the attenuated radiation falling within the microdensitometer slit's jaws could be expressed as

$$\frac{I_{dens}(\lambda'')}{I'_{dens}(\lambda'')} = \frac{I_{dens}(\lambda'')}{I'_{\lambda''}} = \int_0^\infty \left(\frac{I^{fc}(\lambda)}{I'_{\lambda''}}\right) h(|\lambda-\lambda''|)\,d\lambda$$

When the logarithm of the above ratio was evaluated, the output simulated-response of the microdensitometer pen could be determined from the line-segment representation of the emulsion calibration curve which had been stored in the computer during data entry.

The final piece of information needed for the complete evaluation of the synthesized spectrum is the absolute Intensity of the flash continuum used in the production of the absorption spectra. It was determined in the manner outlined below.

A.4 Absolute Intensity of the Flash Continuum I'_λ

The intensity of the Multiblitz output was determined relative to a tungsten strip-filament lamp itself recently calibrated at the National Research Council of Canada Laboratories in Ottawa. The tungsten lamp was operated under those steady conditions for which its output intensity was

known. During this comparison, luminosity from both sources passed through the complete optical path shown in Fig 3-13,IV and through the spectrograph before detection by a 1P21 photomultiplier mounted at the location of the spectrograph plate-holder. The output signal of the 1P21 was passed through a precision attenuator before being used to produce oscillograph time vs intensity records as the flash continuum was much more intense than the output of the standard lamp.

When absorption spectra were recorded and the high-speed shutter was being employed to limit the time-duration of light pulses falling upon the photographic emulsion, the following procedure was used. A 1P21 was mounted on the plate-holder to detect radiation ca 6000 Å (but not the Na D-lines) and the film strips used to record the absorption spectra were cut sufficiently short that no radiation of wavelength greater than 5950 Å, say, fell upon them. The attenuated time-intensity oscillograph traces of the 1P21 output obtained during the process of recording absorption spectra were compared individually with previous calibration traces and with tungsten lamp output traces. From this information and the calculated temperature of the shock-heated absorbing layer, the quantity $B_\lambda(T_5)/I'_\lambda$ was determined for each spectrum. The latter ratio is the multiplier of the emission term in Equation (6-1) when the ratio I_λ/I'_λ is taken.

Usually the ratio $B_\lambda(T_5)/I'_\lambda$ was less than 2×10^{-3}. Yet, sometimes it became as high as 4×10^{-2} due to a slightly erratic behaviour of the high-speed shutter. Therefore, provision

was made in the computer programme which produced the synthesized spectrum for external adjustment of this ratio. Emulsion calibrations showed that the ratio $B_\lambda(T_5)/I'_\lambda$ could be taken to be constant over the spectral interval 5000Å to 5300Å except for regions containing pressure-broadened Xenon lines.

A.5 Reconstructed Line Wavenumbers, Energy Levels and Intermediate computations of A, gf and f.

Table A-2 lists lower state energies and reconstructed wavenumbers for all of the (0,0) band lines employed in this work. In addition, Einstein A-coefficients, gf-values and absorption oscillator strengths - f - are quoted for each line. These calculations were performed specifically for the 2897°K spectrum of Figure 6-2 and employ $\Sigma Re^2/(ea_0)^2$ = 0.0641 atomic units. That value is slightly lower than the one finally adopted; namely 0.0672 ± 0.0093. However, the listing will be useful for relative intensity measures.

TABLE A-2

Characteristics of the MgH $A^2\Pi - X^2\Sigma^+$ System (0,0) Band Rotational Lines.

P_1-Branch

N"	Reconstituted Vacuum Wavenumber (cm^{-1})	Sigma State Energy (cm^{-1})	Einstein A Coefficient (sec^{-1}) $x10^{-5}$	gf $x10^{+1}$	f $x10^{+3}$
0					
1	19261.67	11.47	2.285	0.036_9	0.923_5
2	19252.88	34.41	2.676	0.086_6	1.443^5
3	19243.84	68.79	2.884	0.140^6	1.751
4	19235.11	114.59	3.001	0.195	1.946
5	19226.93	171.78	3.073	0.249	2.077
6	19219.39	240.31	3.121	0.304	2.172
7	19212.55	320.14	3.154	0.359	2.242
8	19206.44	411.20	3.179	0.413	2.297
9	19201.07	513.44	3.197	0.468	2.340
10	19196.45	626.77	3.211	0.523	2.376
11	19192.60	751.10	3.223	0.577	2.405
12	19189.53	886.36	3.232	0.632	2.429
13	19187.24	1032.44	3.239	0.686	2.450
14	19185.74	1189.23	3.246	0.740	2.468
15	19185.02	1356.62	3.252	0.795	2.483
16	19185.10	1534.49	3.257	0.849	2.497
17	19185.97	1722.71	3.261	0.903	2.509
18	19187.65	1921.14	3.266	0.957	2.520
19	19190.12	2129.63	3.270	1.012	2.529
20	19193.39	2348.04	3.274	1.066	2.538
21	19197.46	2576.20	3.278	1.120	2.546
22	19202.33	2813.96	3.282	1.174	2.553
23	19208.00	3061.14	3.286	1.228	2.559
24	19214.46	3317.56	3.290	1.283	2.565
25	19221.71	3583.04	3.294	1.337	2.571
26	19229.75	3857.39	3.299	1.391	2.576
27	19238.57	4140.41	3.304	1.445	2.581
28	19248.18	4431.90	3.308	1.499	2.585
29	19258.56	4731.66	3.314	1.554	2.590
30	19269.70	5039.48	3.319	1.608	2.594
31	19281.61	5355.13	3.324	1.662	2.597
32	19294.27	5678.40	3.330	1.717	2.601

TABLE A-2 (Contd.)

Characteristics of the MgH $A^2\pi - X^2\Sigma^+$ System (0,0) Band Rotational Lines.

P_1-Branch

N"	Reconstituted Vacuum Wavenumber (cm^{-1})	Sigma State Energy (cm^{-1})	Einstein A Coefficient (sec^{-1}) $x10^{-5}$	gf $x10^{+1}$	f $x10^{+3}$
33	19307.67	6009.06	3.336	1.771	2.605
34	19321.81	6346.87	3.343	1.826	2.608
35	19336.67	6691.62	3.349	1.880	2.611
36	19352.24	7043.05	3.356	1.935	2.614
37	19368.52	7400.94	3.363	1.989	2.617
38	19385.49	7765.03	3.370	2.044	2.620
39	19403.13	8135.08	3.378	2.098	2.623
40	19421.44	8510.84	3.385	2.153	2.626
41	19440.39	8892.06	3.393	2.208	2.628
42	19459.97	9278.49	3.401	2.262	2.631
43	19480.16	9669.87	3.410	2.317	2.633
44	19500.95	10065.96	3.418	2.372	2.635
45	19522.32	10466.49	3.427	2.427	2.638
46	19544.24	10871.21	3.436	2.481	2.640
47	19566.69	11279.86	3.445	2.536	2.642
48	19589.66	11692.19	3.454	2.591	2.644
49	19613.11	12107.94	3.464	2.646	2.646
50	19637.04	12526.86	3.473	2.701	2.648

TABLE A-2 (Contd.)

Characteristics of the MgH $A^2\Pi - X^2\Sigma^+$ System (0,0) Band Rotational Lines.

P_2-Branch.

N''	Reconstituted Vacuum Wavenumber (cm^{-1})	Sigma State Energy (cm^{-1})	Einstein A Coefficient (sec^{-1}) $x10^{-5}$	gf $x10^{+1}$	f $x10^{+3}$
0					
1					
2					
3	19249.61	68.76	1.669	0.054	0.900
4	19239.39	114.54	2.342	0.114	1.423
5	19230.35	171.70	2.667	0.173	1.730
6	19222.26	240.21	2.848	0.231	1.926
7	19215.05	320.01	2.960	0.288	2.060
8	19208.68	411.04	3.033	0.345	2.157
9	19203.12	513.24	3.084	0.401	2.229
10	19198.38	626.53	3.121	0.457	2.285
11	19194.44	750.83	3.149	0.513	2.330
12	19191.30	886.05	3.171	0.568	2.366
13	19188.96	1032.09	3.188	0.623	2.397
14	19187.43	1188.85	3.202	0.678	2.422
15	19186.70	1356.21	3.214	0.733	2.443
16	19186.77	1534.04	3.224	0.788	2.462
17	19187.65	1722.23	3.232	0.842	2.478
18	19189.33	1920.63	3.240	0.897	2.492
19	19191.81	2129.11	3.247	0.952	2.504
20	19195.09	2347.50	3.253	1.006	2.515
21	19199.17	2575.65	3.260	1.061	2.525
22	19204.05	2813.40	3.265	1.115	2.534
23	19209.73	3060.57	3.271	1.169	2.542
24	19216.20	3316.98	3.277	1.224	2.550
25	19223.46	3582.46	3.282	1.278	2.557
26	19231.51	3856.81	3.288	1.333	2.563
27	19240.34	4139.83	3.293	1.387	2.569
28	19249.95	4431.32	3.299	1.441	2.574
29	19260.33	4731.06	3.305	1.496	2.579
30	19271.49	5038.85	3.311	1.550	2.584
31	19283.41	5354.47	3.317	1.605	2.588
32	19296.08	5677.69	3.323	1.659	2.593

TABLE A-2 (Contd.)

Characteristics of the MgH $A^2\Pi - X^2\Sigma^+$ System (0,0) Band Rotational Lines.

P_2-Branch

N"	Reconstituted Vacuum Wavenumber (cm^{-1})	Sigma State Energy (cm^{-1})	Einstein A Coefficient (sec^{-1}) $\times 10^{-5}$	gf $\times 10^{+1}$	f $\times 10^{+3}$
33	19309.51	6008.27	3.330	1.714	2.597
34	19323.69	6345.99	3.337	1.768	2.601
35	19338.61	6690.60	3.344	1.823	2.604
36	19354.25	7041.87	3.351	1.878	2.608
37	19370.62	7399.54	3.358	1.932	2.611
38	19387.71	7763.35	3.366	1.987	2.614
39	19405.51	8133.07	3.374	2.042	2.617
40	19424.01	8508.42	3.382	2.096	2.620
41	19443.19	8889.14	3.390	2.151	2.623
42	19463.06	9274.98	3.399	2.206	2.626
43	19483.61	9665.66	3.408	2.261	2.629
44	19504.82	10060.92	3.417	2.316	2.632
45	19526.68	10460.48	3.426	2.371	2.634
46	19549.19	10864.07	3.436	2.426	2.637
47	19572.34	11271.42	3.445	2.481	2.639
48	19596.11	11682.25	3.455	2.536	2.642
49	19620.50	12096.29	3.466	2.591	2.644
50	19645.49	12513.27	3.476	2.647	2.647

TABLE A-2 (Contd.)

Characteristics of the MgH $A^2\Pi$ - $X^2\Sigma^+$ System (0,0) Band Rotational Lines.

R_1-Branch

N''	Reconstituted Vacuum Wavenumber (cm^{-1})	Sigma State Energy (cm^{-1})	Einstein A Coefficient (sec^{-1}) $x10^{-5}$	gf $x10^{+1}$	f_{abs} $x10^{+3}$
0	19287.29	0.00	2.802	0.090	4.517
1	19301.15	11.47	3.319	0.160	4.007
2	19315.29	34.41	3.488	0.224	3.738
3	19329.92	68.79	3.557	0.285	3.568
4	19345.12	114.59	3.590	0.345	3.452
5	19360.92	171.78	3.608	0.404	3.367
6	19377.33	240.31	3.619	0.462	3.303
7	19394.37	320.14	3.628	0.521	3.253
8	19412.01	411.20	3.635	0.579	3.214
9	19430.27	513.44	3.643	0.636	3.182
10	19449.13	626.77	3.650	0.694	3.156
11	19468.58	751.10	3.658	0.752	3.135
12	19488.61	886.36	3.666	0.810	3.117
13	19509.20	1032.44	3.675	0.869	3.102
14	19530.36	1189.23	3.684	0.927	3.089
15	19552.06	1356.62	3.694	0.985	3.079
16	19574.29	1534.49	3.704	1.044	3.070
17	19597.04	1722.71	3.715	1.102	3.062
18	19620.29	1921.14	3.727	1.161	3.055
19	19644.03	2129.63	3.738	1.220	3.050
20	19668.25	2348.04	3.750	1.279	3.045
21	19692.93	2576.20	3.763	1.338	3.042
22	19718.05	2813.96	3.776	1.398	3.039
23	19743.61	3061.14	3.789	1.457	3.036
24	19769.58	3317.56	3.803	1.517	3.034
25	19795.95	3583.04	3.816	1.577	3.032
26	19822.70	3857.39	3.831	1.637	3.031
27	19849.81	4140.41	3.845	1.697	3.031
28	19877.28	4431.90	3.860	1.757	3.030
29	19905.07	4731.66	3.874	1.818	3.030
30	19933.19	5039.48	3.890	1.879	3.030
31	19961.59	5355.13	3.905	1.939	3.030
32	19990.28	5678.40	3.920	2.000	3.031

TABLE A-2 (Contd.)

Characteristics of the MgH $A^2\pi - X^2\Sigma^+$ System (0,0) Band Rotational Lines.

R_1-Branch

N"	Reconstituted Vacuum Wavenumber (cm^{-1})	Sigma State Energy (cm^{-1})	Einstein A Coefficient (sec^{-1}) $x10^{-5}$	gf $x10^{+1}$	f_{abs} $x10^{+3}$
33	20019.23	6009.06	3.936	2.061	3.031
34	20048.42	6346.87	3.952	2.123	3.032
35	20077.84	6691.62	3.968	2.184	3.033
36	20107.46	7043.05	3.984	2.245	3.034
37	20137.27	7400.94	4.000	2.307	3.035
38	20167.25	7765.03	4.016	2.368	3.036
39	20197.37	8135.08	4.032	2.430	3.038
40	20227.62	8510.84	4.048	2.492	3.039
41	20257.98	8892.06	4.064	2.554	3.040
42	20288.42	9278.49	4.081	2.616	3.042
43	20318.93	9669.87	4.097	2.678	3.043
44	20349.48	10065.96	4.113	2.740	3.044
45	20380.06	10466.49	4.129	2.802	3.046
46	20410.64	10871.21	4.145	2.864	3.047
47	20441.20	11279.86	4.161	2.926	3.048
48	20471.71	11692.19	4.177	2.988	3.049
49	20502.16	12107.94	4.192	3.050	3.050
50	20532.52	12526.86	4.208	3.112	3.051

TABLE A-2 (Contd.)

Characteristics of the MgH $A^2\Pi - X^2\Sigma^+$ System (0,0) Band

Rotational Lines

R_2-Branch

N''	Reconstituted Vacuum Wavenumber (cm^{-1})	Sigma State Energy (cm^{-1})	Einstein A Coefficient (sec^{-1}) $x10^{-5}$	gf $x10^{+1}$	f_{abs} $x10^{+3}$
0					
1	19306.90	11.47	4.507	0.145	7.251
2	19319.54	34.39	4.097	0.198	4.938
3	19333.29	68.76	3.933	0.252	4.207
4	19347.93	114.54	3.846	0.308	3.851
5	19363.35	171.70	3.794	0.364	3.641
6	19379.51	240.21	3.761	0.420	3.503
7	19396.35	320.01	3.739	0.477	3.406
8	19413.86	411.04	3.726	0.534	3.334
9	19432.03	513.24	3.717	0.590	3.280
10	19450.82	626.53	3.713	0.647	3.237
11	19470.22	750.83	3.711	0.705	3.203
12	19490.23	886.05	3.713	0.762	3.175
13	19510.81	1032.09	3.716	0.819	3.152
14	19531.97	1188.85	3.720	0.877	3.133
15	19553.67	1356.21	3.726	0.935	3.117
16	19575.92	1534.04	3.733	0.993	3.104
17	19598.68	1722.23	3.741	1.051	3.092
18	19621.95	1920.63	3.750	1.110	3.083
19	19645.71	2129.11	3.760	1.168	3.075
20	19669.95	2347.50	3.770	1.227	3.068
21	19694.65	2575.65	3.781	1.286	3.062
22	19719.79	2813.40	3.793	1.345	3.057
23	19745.35	3060.57	3.805	1.405	3.053
24	19771.33	3316.98	3.817	1.464	3.050
25	19797.70	3582.46	3.830	1.524	3.047
26	19824.45	3856.81	3.844	1.584	3.045
27	19851.57	4139.83	3.857	1.644	3.044
28	19879.03	4431.32	3.871	1.704	3.042
29	19906.81	4731.06	3.885	1.764	3.041
30	19934.92	5038.85	3.900	1.824	3.041
31	19963.31	5354.47	3.915	1.885	3.040
32	19991.99	5677.69	3.930	1.946	3.040

TABLE A-2 (Contd.)

Characteristics of the MgH $A^2\Pi - X^2\Sigma^+$ System (0,0) Band Rotational Lines.

R_2-Branch

N"	Reconstituted Vacuum Wavenumber (cm^{-1})	Sigma State Energy (cm^{-1})	Einstein A Coefficient (sec^{-1}) $x10^{-5}$	gf $x10^{+1}$	f_{abs} $x10^{+3}$
33	20020.94	6008.27	3.945	2.007	3.040
34	20050.13	6345.99	3.960	2.068	3.041
35	20079.55	6690.60	3.976	2.129	3.041
36	20109.20	7041.87	3.991	2.190	3.042
37	20139.04	7399.54	4.007	2.252	3.043
38	20169.07	7763.35	4.023	2.313	3.043
39	20199.27	8133.07	4.039	2.375	3.044
40	20229.63	8508.42	4.055	2.436	3.045
41	20260.13	8889.14	4.071	2.498	3.047
42	20290.76	9274.98	4.087	2.560	3.048
43	20321.50	9665.66	4.104	2.622	3.049
44	20352.35	10060.92	4.120	2.684	3.050
45	20383.28	10460.48	4.136	2.746	3.051
46	20414.29	10864.07	4.152	2.808	3.052
47	20445.37	11271.42	4.168	2.870	3.054
48	20476.50	11682.25	4.185	2.933	3.055
49	20507.68	12096.29	4.201	2.995	3.056
50	20538.89	12513.27	4.217	3.057	3.057

TABLE A-2 (Contd.)

Characteristics of the MgH $A^2\Pi - X^2\Sigma^+$ System (0,0) Band Rotational Lines.

Q_1-Branch

N''	Reconstituted Vacuum Wavenumber (cm^{-1})	Sigma State Energy (cm^{-1})	Einstein A Coefficient (sec^{-1}) $x10^{-5}$	gf $x10^{+1}$	f $x10^{+3}$
0	19273.14	0.00	4.581	0.074	3.698
1	19275.82	11.47	5.699	0.184	4.599
2	19278.21	34.41	6.228	0.302	5.025
3	19280.89	68.79	6.479	0.418	5.226
4	19284.09	114.59	6.613	0.533	5.333
5	19287.89	171.78	6.669	0.647	5.395
6	19292.33	240.31	6.747	0.761	5.436
7	19297.43	320.14	6.785	0.874	5.463
8	19303.21	411.20	6.813	0.987	5.483
9	19309.67	513.44	6.837	1.100	5.498
10	19316.80	626.77	6.856	1.212	5.509
11	19324.62	751.10	6.874	1.325	5.519
12	19333.13	886.36	6.890	1.437	5.527
13	19342.30	1032.44	6.905	1.550	5.534
14	19352.16	1189.23	6.920	1.662	5.540
15	19362.68	1356.62	6.934	1.775	5.546
16	19373.87	1534.49	6.949	1.887	5.551
17	19385.72	1722.71	6.964	2.000	5.556
18	19398.23	1921.14	6.979	2.113	5.561
19	19411.38	2129.63	6.994	2.226	5.565
20	19425.18	2348.04	7.009	2.339	5.570
21	19439.61	2576.20	7.025	2.453	5.574
22	19454.67	2813.96	7.042	2.566	5.579
23	19470.35	3061.14	7.059	2.680	5.583
24	19486.64	3317.56	7.076	2.794	5.587
25	19503.53	3583.04	7.094	2.908	5.592
26	19521.02	3857.39	7.112	3.022	5.596
27	19539.10	4140.41	7.131	3.136	5.601
28	19557.75	4431.90	7.150	3.251	5.605
29	19576.96	4731.66	7.170	3.366	5.609
30	19596.73	5039.48	7.190	3.481	5.614
31	19617.04	5355.13	7.210	3.596	5.618
32	19637.89	5678.40	7.232	3.711	5.623

TABLE A-2 (Contd.)

Characteristics of the MgH $A^2\Pi$ - $X^2\Sigma^+$ System (0,0) Band Rotational Lines.

Q_1-Branch

N"	Reconstituted Vacuum Wavenumber (cm^{-1})	Sigma State Energy (cm^{-1})	Einstein A Coefficient (sec^{-1}) $x10^{-5}$	gf $x10^{+1}$	f $x10^{+3}$
33	19659.26	6009.06	7.253	3.826	5.627
34	19681.14	6346.87	7.275	3.942	5.632
35	19703.51	6691.62	7.297	4.058	5.636
36	19726.37	7043.05	7.320	4.174	5.640
37	19749.70	7400.94	7.343	4.290	5.645
38	19773.49	7765.03	7.366	4.406	5.649
39	19797.73	8135.08	7.390	4.523	5.654
40	19822.39	8510.84	7.414	4.640	5.658
41	19847.47	8892.06	7.439	4.756	5.662
42	19872.96	9278.49	7.464	4.873	5.667
43	19898.83	9669.87	7.489	4.990	5.671
44	19925.07	10065.96	7.514	5.107	5.675
45	19951.66	10466.49	7.539	5.225	5.679
46	19978.60	10871.21	7.565	5.342	5.683
47	20005.86	11279.86	7.591	5.459	5.687
48	20033.42	11692.19	7.617	5.577	5.691
49	20061.27	12107.94	7.643	5.694	5.694
50	20089.39	12526.86	7.669	5.812	5.698

TABLE A-2 (Contd.)

Characteristics of the MgH $A^2\Pi - X^2\Sigma^+$ System (0,0) Band

Rotational Lines

Q_2-Branch

N"	Reconstituted Vacuum Wavenumber (cm^{-1})	Sigma State Energy (cm^{-1})	Einstein A Coefficient (sec^{-1}) $x10^{-5}$	gf $x10^{+1}$	f_{abs} $x10^{+3}$
0					
1					
2	19283.96	34.39	5.033	0.162	4.058
3	19285.14	68.76	6.019	0.291	4.862
4	19287.45	114.54	6.391	0.412	5.151
5	19290.68	171.70	6.571	0.529	5.295
6	19294.73	240.21	6.673	0.645	5.374
7	19299.54	320.01	6.737	0.759	5.423
8	19305.11	411.04	6.781	0.873	5.455
9	19311.41	513.24	6.813	0.986	5.478
10	19318.42	626.53	6.839	1.099	5.495
11	19326.15	750.83	6.861	1.212	5.508
12	19334.57	886.05	6.880	1.324	5.519
13	19343.69	1032.09	6.898	1.437	5.528
14	19353.50	1188.85	6.914	1.550	5.535
15	19363.99	1356.21	6.930	1.663	5.542
16	19375.15	1534.04	6.946	1.775	5.548
17	19386.98	1722.23	6.961	1.888	5.553
18	19399.46	1920.63	6.977	2.001	5.559
19	19412.60	2129.11	6.992	2.114	5.564
20	19426.39	2347.50	7.008	2.227	5.568
21	19440.81	2575.65	7.025	2.341	5.573
22	19455.86	2813.40	7.041	2.454	5.578
23	19471.53	3060.57	7.059	2.568	5.582
24	19487.81	3316.98	7.076	2.682	5.587
25	19504.69	3582.46	7.094	2.796	5.591
26	19522.17	3856.81	7.112	2.910	5.596
27	19540.24	4139.83	7.131	3.024	5.600
28	19558.87	4431.32	7.151	3.139	5.605
29	19578.08	4731.06	7.170	3.253	5.609
30	19697.83	5038.85	7.191	3.368	5.614
31	19618.14	5354.47	7.211	3.483	5.618
32	19638.97	5677.69	7.232	3.599	5.623

TABLE A-2 (Contd.)

Characteristics of the MgH $A^2\Pi - X^2\Sigma^+$ System (0,0) Band Rotational Lines.

Q_2-Branch

N"	Reconstituted Vacuum Wavenumber (cm^{-1})	Sigma State Energy (cm^{-1})	Einstein A Coefficient (sec^{-1}) $x10^{-5}$	gf $x10^{+1}$	f_{abs} $x10^{+3}$
33	19660.33	6008.27	7.254	3.714	5.627
34	19682.20	6345.99	7.276	3.830	5.632
35	19704.58	6690.60	7.298	3.945	5.636
36	19727.44	7041.87	7.321	4.061	5.641
37	19750.78	7399.54	7.344	4.177	5.645
38	19774.59	7763.35	7.368	4.294	5.650
39	19798.86	8133.07	7.392	4.410	5.654
40	19823.57	8508.42	7.416	4.527	5.658
41	19848.71	8889.14	7.440	4.644	5.663
42	19874.27	9274.98	7.465	4.760	5.667
43	19900.24	9665.66	7.490	4.877	5.671
44	19926.61	10060.92	7.516	4.995	5.676
45	19953.36	10460.48	7.542	5.112	5.680
46	19980.48	10864.07	7.568	5.229	5.684
47	20007.97	11271.42	7.594	5.347	5.688
48	20035.80	11682.25	7.620	5.464	5.692
49	20063.97	12096.29	7.647	5.582	5.696
50	20092.46	12513.27	7.674	5.700	5.700

APPENDIX B

This appendix contains three tables - one for each sample material shock-excited in $Ar-H_2$ Test Gas mixtures. These tables list initial pressures within the shock tube, measured values of the Incident Shock Front speed and calculated values for P_5 and T_5 plus estimates of the mole fraction (X_{MeH}) of the appropriate hydride (MgH, BeH or AlH) in the equilibrated region behind the Reflected Shock Front. P_5, T_5 and X_{MeH} values have been rounded-off from computer print-out. The three sets of (P_5, T_5, X_{MeH})-values, which are presented for each set of initial pressure conditions, correspond to the assumptions:

i) U_1 equals measured shock front speed. No sample is present.

ii) U_1 equals measured shock front speed. A 2.5 mgm powdered sample is present.

iii) U_1 is 10% slower than the measured speed. A 2.5 mgm powdered sample is present.

The calculations presuppose that $T_1=T_4=298.15°K$ as, initially, both Channel and Chamber were at room temperature. In all cases, the shock front speed was determined from the time interval taken by the front to travel 50.0 cm.

TABLE B-1

Shock Excitation Conditions Applied to Magnesium Powder Samples.

Figure Number	Measured Incident Shock Front Speed (km/sec)	Diaphragm Bursting Pressure (psia H_2)	Initial Channel Pressure (Torr) Ar : H_2	MgH Mole Fraction $x10^{+4}$	P_5 (atm)	T_5 (°K)
4-9	1.69_5	181	28.6:1.4	0.0	6.95	4645
				0.49	7.46	4583
				0.82	5.98	3880
4-10	1.78_6	194	28.5:1.5	0.0	8.10	5170
				0.36	8.56	5080
				0.74	6.68	4149
	1.76_7	187	28.5:1.5	0.0	7.83	5028
				0.40	8.30	4946
				0.77	6.52	4078
	1.75_4	186	28.5:1.5	0.0	7.66	4939
				0.43	8.14	4861
				0.80	6.41	4033
4-11	1.78_6	194	28.5:1.5	0.0	8.10	5170
				0.36	8.56	5080
				0.74	6.68	4149
	1.70_1	187	28.5:1.5	0.0	6.98	4585
				0.55	7.48	4528
				0.88	6.00	3858
	1.73_0	185	28.5:1.5	0.0	7.34	4772
				0.48	7.83	4703
				0.84	6.22	3951
5-1	1.20_5	226	72.0:8.00	0.0	8.01	2730
				0.76	8.55	2722
				0.60	6.86	2343
	1.83_2	193	24.0:6.00	0.0	7.26	3700
				2.64	7.76	3691
				2.51	6.29	3394
	1.53_3	298	85.5:4.50	0.0	16.08	3976
				0.58	16.65	3972
				0.61	13.58	3526

TABLE B-1 (Contd.)

Shock Excitation Conditions Applied to Magnesium Powder Samples.

Figure Number	Measured Incident Shock Front Speed (km/sec)	Diaphragm Bursting Pressure (psia H_2)	Initial Channel Pressure (Torr) Ar : H_2	MgH Mole Fraction $x10^{+4}$	P_5 (atm)	T_5 (°K)
5-1	1.77_3	191	29.0:1.00	0.0	8.16	5705
				0.16	8.64	5605
				0.38	6.74	4475
	1.76_7	191	29.5:0.50	0.0	8.34	6315
				0.32	8.76	6214
				0.11	6.91	5020
5-2	1.76_0	306	95.0:5.00	0.0	25.27	5022
				0.34	25.79	5005
				0.51	20.30	4228
	1.77_3	190	28.5:1.50	0.0	7.92	5074
				0.39	8.39	4989
				0.76	6.57	4100
	1.57_2	306	85.5:4.50	0.0	17.03	4113
				0.55	17.60	4107
				0.61	14.32	3635
5-3	1.93_8	308	31.5:3.50	0.0	11.24	4770
				1.02	11.65	4722
				1.38	8.92	4075
	1.89_4	301	34.0:6.00	0.0	11.21	4117
				1.84	11.65	4103
				1.87	9.19	3724
	1.76_1	319	51.0:9.00	0.0	13.73	3884
				1.55	14.24	3879
				1.50	11.50	3537
	1.58_7	189	46.7:8.25	0.0	9.83	3500
				1.55	10.39	3497
				1.43	8.52	3182
5-4	1.93_1	254	24.0:6.00	0.0	8.41	3887
				2.67	8.86	3875
				2.59	7.04	3554

TABLE B-1 (Contd.)

Shock Excitation Conditions Applied to Magnesium Powder Samples.

Figure Number	Measured Incident Shock Front Speed (km/sec)	Diaphragm Bursting Pressure (psia H_2)	Initial Channel Pressure (Torr) Ar : H_2	MgH Mole Fraction $\times 10^{+4}$	P_5 (atm)	T_5 (°K)
5-4	1.83_2	187	24.0:6.00	0.0	7.26	3700
				2.64	7.76	3691
				2.51	6.29	3394
	1.50_6	131	41.5:8.50	0.0	7.83	3252
				1.66	8.39	3247
				1.47	6.89	2934
	1.41_2	124	50.0:10.0	0.0	8.18	3072
				1.39	8.74	3066
				1.19	7.13	2732
	1.33_7	68	32.0:8.00	0.0	4.67	2761
				1.66	5.22	2745
				1.36	4.26	2406
5-5	1.65_0	254	48.0:12.0	0.0	11.27	3471
				1.78	11.83	3467
				1.61	9.67	3161
	1.76_7	186	28.5:1.50	0.0	7.83	5028
				0.40	8.30	4946
				0.77	6.52	4078
6-1	1.39_7	202	80.0:20.0	0.0	12.97	2967
				1.12	13.52	2962
				0.93	10.91	2606
6-2	1.24_7	69	40.0:10.0	0.0	4.96	2528
				1.28	5.49	2510
				0.99	4.42	2158
	1.26_3	134	80.0:20.0	0.0	10.24	2593
				0.92	10.77	2585
				0.71	8.59	2220
	1.31_2	69	32.0:8.00	0.0	4.47	2699
				1.61	5.02	2682
				1.29	4.09	2338

TABLE B-1 (Contd.)

Shock Excitation Conditions Applied to Magnesium Powder Samples.

Figure Number	Measured Incident Shock Front Speed (km/sec)	Diaphragm Bursting Pressure (psia H_2)	Initial Channel Pressure (Torr) Ar : H_2	MgH Mole Fraction $\times 10^{+4}$	P_5 (atm)	T_5 (°K)
6-2	1.33_0	134	64.0:16.0	0.0	9.26	2778
				1.15	9.80	2770
				0.93	7.88	2411
	1.40_1	130	48.0:12.0	0.0	7.81	2942
				1.46	8.36	2934
				1.22	6.79	2596
	1.39_7	202	80.0:20.0	0.0	12.97	2967
				1.12	13.52	2962
				0.93	10.91	2606
	1.44_9	201	68.0:12.0	0.0	11.72	3240
				1.19	12.29	3236
				1.04	10.01	2897

TABLE B-2

Shock Excitation Conditions Applied to Beryllium Powder Samples.

Figure Number	Measured Incident Shock Front Speed (km/sec)	Diaphragm Bursting Pressure (psia H_2)	Initial Channel Pressure (Torr) Ar : H_2	BeH Mole Fraction x10^{+4}	P_5 (atm)	T_5 (°K)
5-6	1.53_8	237	63.0:7.00	0.0	12.11	3626
				3.11	15.92	3597
				3.23	13.68	3235
	1.73_6	303	49.5:5.50	0.0	12.70	4097
				3.14	16.29	4040
				3.57	14.00	3651
	1.92_3	312	31.5:3.50	0.0	10.97	4695
				3.14	14.20	4460
				4.24	12.24	3960
	†1.75_4	32[illegible]	52.3:2.75	0:0	13.89	4952
				1.08	17.31	4742
				1.85	14.62	4053
5-7	1.90_1	301	31.5:3.50	0.0	10.57	4594
				3.30	13.91	4387
				4.34	12.06	3911
5-8	1.23_8	128	85.0:15.0	0.0	10.24	2678
				3.08	13.77	2614
				2.92	11.52	2227
	1.71_8	241	40.5:4.50	0.0	10.12	4011
				3.66	13.92	3948
				4.15	12.18	3572

† All windows were supported by external brass spacers having a 1" diameter central opening. Calculations indicate that windows were capable of withstanding 14.3 atm overpressure. The end window shattered following shock reflection in this case.

TABLE B-3

Shock Excitation Conditions Applied to Aluminium Powder Samples

Figure Number	Measured Incident Shock Front Speed (km/sec)	Diaphragm Bursting Pressure (psia H_2)	Initial Channel Pressure (Torr) Ar : H_2	Al Mole Fraction $x10^{+4}$	P_5 (atm)	T_5 (°K)
5-9	1.58_7	245	63.0:7.00	0.0	13.00	3747
				1.12	14.10	3742
				1.45	11.63	3385
	1.74_8	243	40.5:4.50	0.0	10.60	4096
				1.04	11.61	4076
				1.46	9.48	3676
	*1.72_4	281	52.3:2.75	0.0	13.20	4761
				0.26	14.22	4709
				0.58	11.43	4013
5-10a	*1.34_8	136	75.0:25.0	0.0	11.37	2677
				3.34	12.32	2656
				4.70	9.86	2291
5-10b	1.24_4	130	70.0:30.0	0.0	8.79	2215
				5.77	9.62	2185
				8.73	7.62	1856
	*1.38_9	193	80.0:20.0	0.0	12.81	2947
				2.40	13.83	2934
				3.19	11.17	2571
	*1.56_7	251	63.0:7.00	0.0	12.63	3697
				1.16	13.74	3693
				1.50	11.33	3338

* Speed estimated by comparison with other shocks having identical initial conditions - except, perhaps, for the nature of the sample material.

APPENDIX C

SOLUTION OF SHOCK TUBE EQUATIONS

Economical solution of the equations introduced in Chapter 2 requires a set of good starting values and a rapidly convergent iteration scheme. The means of acquiring both are discussed below.

C.1 Incident Shock Starting Values

Initial estimates of temperature and pressure ratios across the incident shock front were obtained from

$$P_{2*1} = \left\{\frac{2\gamma_1}{\gamma_1+1}\right\} M_s - \left\{\frac{\gamma_1-1}{\gamma_1+1}\right\} \qquad (C\text{-}1)$$

$$T_{2*1} = \frac{\{2 + (\gamma_1-1)M_s^2\}}{(\gamma_1+1)} \left\{\frac{P_{2*1}}{M_s^2}\right\} \qquad (C\text{-}2)$$

relations quoted by Wright (1961) for ideal gases with constant specific heat ratio, γ. M_s is the incident shock Mach number defined by

$$M_s = \{U_1\}/\{a_1\}$$

The density ratio across the shock, ρ_{2*1}, was found from Eq (2-16) using the above estimates of P_{2*1} and T_{2*1}. WM_{2*} was set equal to WM_1 as no dissociation or chemical reaction occurs in region (2*). Evaluation of γ_1 and a_1 is discussed in section C.3 .

Starting values for region (2) were assumed to be the final values obtained for region (2*).

C.2 Reflected Shock Starting Values

Starting values of temperature and molar mass were chosen to be

$$T_{5*1} = 2 \cdot T_{21} \qquad (C\text{-}3)$$

$$WM_{5*} = WM_2 \qquad (C\text{-}4)$$

so that $P_{5*1} = 2\rho_{5*1}$ (by application of Eq (2-16)). The starting value for ρ_{5*1} was obtained from

$$\rho_{5*1}^2 - \rho_{5*1}\left\{\left(\frac{\rho_{21}}{2}\right)\cdot\left(3 + \frac{\rho_2 V_2}{P_2}\right)\right\} + \frac{\rho_{21}^2}{2} = 0 \qquad (C\text{-}5)$$

an expression which results from combining Eq (2-28) with (2-29) and introducing the starting values for T_{5*}, WM_{5*} from (C-3) and (C-4) via the equation of state, relation (2-16).

The final values for region (5*) were used as starting values for region (5).

C.3 Evaluation of K_{p1}, K_{p2}, γ_k and a_k

Only the reactions

$$H + H \rightleftharpoons H_2$$

$$Mg + H \rightleftharpoons MgH$$

were considered to occur with significant yield in the shock-heated mixture. When the heat bath (the shock-heated gas) is in local thermodynamic equilibrium, the Law of Mass Action requires that K_{p1} and K_{p2}, defined by

$$K_{p1} = \frac{[H_2]}{[H]^2} \qquad K_{p2} = \frac{[MgH]}{[Mg][H]}$$

be functions solely of temperature. The equilibrium constants (the K_ps) are related to changes in the molar Gibbs Free Energy (Mayer & Mayer, 1940, page 240) by

$$H_2: \quad (\Delta \bar{F}^\circ_T)_f = (\bar{F}^\circ_T)_{H_2} - 2(\bar{F}^\circ_T)_H = -RT\ln(K_{p1}) \qquad (C\text{-}6)$$

$$MgH: \quad (\Delta \bar{F}^\circ_T)_f = (\bar{F}^\circ_T)_{MgH} - (\bar{F}^\circ_T)_{Mg} - (\bar{F}^\circ_T)_H = -RT\ln(K_{p2}) \qquad (C\text{-}7)$$

Owing to these two chemical reactions, even though each species, i, within the shock heated test gas may be treated as a perfect gas following Eq (2-16) with molar specific heat capacities satisfying

$$\bar{C}_{p_i}(T) - \bar{C}_{V_i}(T) = R$$

the resultant mixture <u>will not</u>, <u>in general</u>, satisfy that equality. The correct relationship between $\bar{C}_p$ and $\bar{C}_V$ <u>for the mixture</u> may be obtained using Vardya's (1964) treatment.

As each species, individually, is treated as a perfect gas, total enthalpy, H, and total internal energy, E, of a fixed mass of the test gas will satisfy the relations

$$E = \sum_{i=1}^{r} n_i \bar{E}_i$$

$$H = \sum_{i=1}^{r} n_i \bar{H}_i$$

where the overbar indicates a molar value and n_i is the mole number of species i at temperature T. Due to the chemical reactions, n_i-values change with temperature and so a contribution is made both to $\bar{C}_p$ and $\bar{C}_V$ owing to those changes. For constant mass of an r-component reacting system

$$C_V = \left(\frac{\partial \bar{E}}{\partial T}\right)_V = \sum_{i=1}^{r} n_i \bar{C}_{V_i} + \sum_{i=1}^{r} \bar{E}_i \left(\partial n_i / \partial T\right)_V \qquad \text{(C-8)}$$

$$C_p = \left(\frac{\partial \bar{H}}{\partial T}\right)_p = \sum_{i=1}^{r} n_i \bar{C}_{p_i} + \sum_{i=1}^{r} \bar{H}_i \left(\partial n_i / \partial T\right)_p \qquad \text{(C-9)}$$

$$n = \sum_{i=1}^{r} n_i \qquad \text{(C-10)}$$

Molar values of C_p and C_V are obtained after division of (C-8) and (C-9) by n.

In Argon-Hydrogen mixtures, dissociation increases the number of moles present in a fixed mass of the mixture. When a metallic sample material is present, formation of its monohydride decreases the number of moles in the mixture. At temperatures where no chemical reactions occur, n is fixed and the second summation term in (C-8) or (C-9) makes no contribution to C_V or C_p. Such a situation exists in region (1) when the test gas has had no interaction with the shock wave. A similar case results from interaction with shock waves strong enough to produce a completely atomic test gas mixture.

However, in the present studies, temperatures and pressures in the shocked mixture were usually such that appreciable concentrations of both diatomic and monatomic hydrogen were present and the full relations (C-8) and (C-9) had to be used to determine γ ($\gamma=C_p/C_V$). Knowledge of γ in the incident shock regions is important for deciding whether or not the interaction between Contact Surface and Reflected Shock Front is "tailored" (Wittliff et al, 1959).

In the reacting mixture the sound speed, a, is given (Vardya, 1964; Rowlinson, 1958) by

$$a^2 = \left(\frac{\gamma P}{\rho}\right)\cdot\left\{1 - \left(\partial \ln(n)/\partial \ln(P)\right)_T\right\}^{-1} = \left(\frac{\gamma P}{\rho}\right)\left\{1-\frac{P}{n}\left(\frac{\partial n}{\partial P}\right)_T\right\}^{-1} \qquad \text{(C-11)}$$

which becomes the more familiar

$$a^2 = \left(\frac{\gamma P}{\rho}\right) \qquad \text{(C-12)}$$

for a mixture with constant mole numbers, i.e. in the absence of chemical reactions.

Omission of the second summations in (C-8) and (C-9) and the { }-term in (C-11) leads to significant error even for shocks travelling at 1.45 km/sec. For example, when such a shock travels into a 15% H_2:85% Ar mixture with P_1=80 Torr, γ and a behind the incident shock (T_2=1800°K) are 0.1% and 0.15% lower than values predicted neglecting those contributions. At still higher temperatures these effects become much more important. In the reflected region of the same shock tube experiment (T_5=3200°K), γ and a are calculated to

be respectively 15% and 8.7% below the values obtained when the rate of change of mole numbers is not included. (All thermodynamic state function data employed in these computations were evaluated using the polynomial expressions of Heimel et al (1963)).

C.4 Temperature Estimators and Convergence Criteria

Equations (2-13) and (2-33), the enthalpy change equalities, were each treated as separable relations (refer to Eq (2-14) and (2-15).) -

$$\text{L.H.S.} = \Delta h(T)$$

$$\text{R.H.S.} = \Delta h(\rho)$$

Early desk calculator computations showed $\Delta h(T)$ to be a much more rapidly varying function of T than $\Delta h(\rho)$ was of ρ. In addition, it was found that the chosen temperature

T was too low when $\xi = \Delta h(T) - \Delta h(\rho) > 0$

T was too high when $\xi = \Delta h(T) - \Delta h(\rho) < 0$

T was acceptable when $|\xi| = |\Delta h(T) - \Delta h(\rho)| < 0.02$ cal/gm.

Once Eqs (C-1) and (C-5) had been used to obtain starting values, the first estimate of an improved temperature, T', for region (k) was found from

$$T' = \frac{\Delta h(\rho)}{\Delta h(T)} \cdot T \qquad (C\text{-}13)$$

an estimator based upon the starting values and derived by the following heuristic argument:

The starting value for T is close enough to the true

value that h(T) may be considered proportional to T (i.e. $\Delta h(T)=b'T$). $\Delta h(\rho)$ is so slowly varying that it may be considered constant. Consequently any change in ξ should result from a change in $\Delta h(T)$. Therefore, to produce a change of $-\xi$ in the $(\Delta h(T)-\Delta h(\rho))$ difference, the temperature must change by an amount $\Delta T=(T'-T)$ given by

$$\Delta(\Delta h(T)) = b'\Delta T = -\xi = -(\Delta h(T)-\Delta h(\rho))$$

$$\frac{\Delta(\Delta h(T))}{\Delta h(T)} = \left(\frac{T'-T}{T}\right) = -\left(\frac{\Delta h(T)-\Delta h(\rho)}{\Delta h(T)}\right)$$

from which (C-13) follows.

This estimator is useful for starting an iteration but results in too slow a convergence. Much faster convergence is obtained by considering ξ itself to be a linear function of temperature. Thus, with

$$\xi_1(T)=a+bT \qquad \text{and} \qquad \xi_2(T')=a+bT'$$

a further estimate of temperature $(T''=-a/b)$ is obtained by requiring $\xi_3(T'')$ to be zero. Thus the previous estimators were necessary to provide the two (ξ,T) initial values. Subsequent temperature estimates are based upon iterations using $\xi(T)$. In general, $\xi(T)$ values oscillate between positive and negative quantities. Acceptable values for T and ρ are found within six to ten iterations even in those cases for which chemical reaction is appreciable.

C.5 The Iterative Solution

Prior to shock initiation, the quantities P_1, P_4, T_1,

4 4

OF/DE

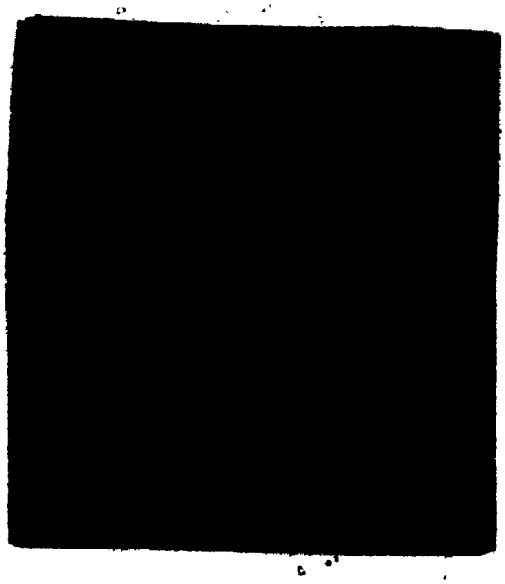

T_4, γ_4, I, [I] and WT_I (where I represents species I, and WT_I is the molar mass of I) are known. From them the initial mole fractions, molar mass, density, ϕ_1 and ϕ_2 are determined using Eqs (2-3), (2-5), (2-16), (2-20), and (2-24) respectively. The specific heat ratio , γ_1, and sound speed, a_1, are evaluated from Eqs (C-8), (C-9) and (C-11).

C.5.1 Incident Shock Iteration Scheme

With the aid of U_1, the incident shock speed, starting values for region (2*) are obtained from relations (C-1) and (C-2). Then the iteration proceeds in the following stages:

1) Using P_k and T_k values, the partial pressure of each species is determined using Eqs (2-18) to (2-25). The mole fractions are found from Eq (2-3), the molar mass via (2-5) and ΔE_{Dk} from (2-27).
2) Eq (2-17) is employed to determine the density ratio, ρ_{k1}.
3) For the current values of P_k, T_k and ρ_k, $\Delta h(T_k)$ and $\Delta h(\rho_k)$ are computed.
4) $\xi=\Delta h(T_k)-\Delta h(\rho_k)$ is calculated and stored with the corresponding T_k value.
5) (a) If $|\xi|<0.02$ cal/gm, the iteration is complete and the current estimates of P_k, T_k and ρ_k are accepted as final values.
   (b) When $|\xi|>0.02$ cal/gm, a new temperature estimate T_k' is made using the methods outlined in

section C.4.

6) A new pressure estimate, P_k', based upon T_k' is obtained from Eq (2-12).

7) The iteration loops back to step (1) and continues cycling until $|\xi| < 0.02$ cal/gm.

After final values for region (2*) are available, the initial values for region (2) are set equal to them and the above iteration process is repeated from step (1). Once final values for region (2) are known, the theoretical pressure ratio P_{41} is evaluated from (2-35).

C.5.2 Reflected Shock Iteration Scheme

This process is quite similar to the one just described. Starting values for T_k, ρ_k and P_k are evaluated from relations (C-3), (C-4) and (C-5). ΔE_{D5*} is set equal to ΔE_{D2}.

1) The partial pressure of each species is determined by using P_k, T_k and relations (2-18) to (2-25). Mole fractions are obtained from (2-3), the molar mass via (2-5) and ΔE_{DK} from (2-27).

2) (a) If U_k is specified, ρ_{k1} is determined from Eq (2-31).

   (b) When U_k is unknown, ρ_{k1} is found from Eq (2-34) and U_k from (2-31).

3) $\Delta h(T_k)$ and $\Delta h(\rho_k)$ are calculated from polynomial expansions and Eq (2-26) respectively.

4) $\xi = \Delta h(T_k) - \Delta h(\rho_k)$ is evaluated and stored with the

current T_k value.

5) (a) If $|\xi|<0.02$ cal/gm, the iteration is stopped and the existing estimates of T_k, ρ_k and P_k are accepted as final values.

(b) When $|\xi|>0.02$ cal/gm, a new temperature estimate is found by the methods discussed in section C.4.

6) When U_k is not specified initially, a new density estimate, ρ_k', is obtained from Eq (2-34) and a new U_k' value found from Eq (2-31).

7) An improved estimate of the pressure, P_k', is determined via Eq (2-32).

8) The cycle is repeated from step (1) until $|\xi|<0.02$ cal/gm.

When final values for region (5*) have been calculated, they are used as starting values for region (5) and the iteration begun once more.

Occasionally, the second estimate of T_5 given by relation (C-13) is lower than T_2, or even negative, due to the estimated size of ΔE_{D5} resulting from the use of starting values. In such cases, another estimator of T_5 (namely $T_5 = 0.66T_{5*}$) is used to provide the second set of (ξ,T) values required to start off the $(\xi\text{-}T)$ iteration scheme described in section C.4. With this improvement, the sequences of steps outlined in sections C.5.1 and C.5.2 have been found

to give physically acceptable results even for shocks into pure diatomic Hydrogen that completely dissociates behind the reflected shock front. Experience has shown that region (5) starting values seem to be most sensitive to powdered sample addition when there is 35%-40% Hydrogen present in Argon-Hydrogen test gas mixtures. Even in those extreme cases, the iteration scheme for any region now requires no more than 12 cycles to achieve acceptable convergence.

C.6 Example of Program Convergence

Data presented in Tables C-1 and C-2 were obtained via an option of the computer program which prints out values of selected shocked gas parameters at the completion of each cycle of the iteration scheme just described. Calculated values contained in the first table refer to a typical shock, without powdered sample addition, propagating through an $Ar:H_2$ (85:15 mole percent) mixture. Results presented in Table C-2 refer to an identical shock to which powdered Magnesium has been added as a sample. Five milligrams of this element are assumed to have vaporized in the region behind the incident shock front and reached thermal and chemical equilibrium with the other species present in the test gas mixture.

The changes in temperature, pressure and molar mass (decrease in temperature, increase in pressure, decrease in molar mass) behind the incident shock as a result of sample

Table C-1

Iterative Solution for a Shock of Speed 1.50 km/sec Propagating into an Argon-Hydrogen Mixture with T_1=298°K and P_1=80.0 Torr (68.0 Torr Argon + 12.0 Torr Hydrogen). Results are rounded off to 5 significant figures.

Region	P(atm)	T(K°)	WM(gm)	X_{Ar}	X_{H_2}	X_H	Δh(T) cal/gm	Δh(ρ) cal/gm
1	0.1053	298.15	34.255	0.85000	0.15000	0.00000	0.00	0.00
2*	2.3173	1808.9	34.255	0.85000	0.15000	0.00000	234.90	231.83
	2.3344	1785.2	34.255	0.85000	0.15000	0.00000	231.16	232.60
	2.3290	1792.7	34.255	0.85000	0.15000	0.00000	232.35	232.86
2	2.3290	1792.7	34.253	0.84996	0.14995	0.00009	232.36	232.23
	2.3297	1791.7	34.253	0.84996	0.14995	0.00008	232.20	232.26
	2.3295	1792.0	34.253	0.84996	0.14995	0.00008	232.25	232.25
5*	12.115	3584.1	34.253	0.84996	0.14995	0.00008	521.03	531.69
	12.136	3657.4	34.253	0.84996	0.14995	0.00008	533.02	536.81
	12.182	3697.9	34.253	0.84996	0.14995	0.00008	539.64	538.86
	12.174	3691.0	34.253	0.84996	0.14995	0.00008	538.51	538.51
5	12.174	3691.0	32.859	0.81535	0.10313	0.08152	546.27	409.39
	11.267	2766.2	34.114	0.84652	0.14529	0.00820	388.75	485.67
	11.578	3149.6	33.804	0.83883	0.13489	0.02627	452.47	471.54
	11.717	3243.5	33.686	0.83589	0.13092	0.03319	468.39	466.91
	11.722	3236.8	33.696	0.83613	0.13123	0.03264	467.24	468.02
	11.724	3239.1	33.693	0.83605	0.13113	0.03282	467.64	467.80
	11.725	3239.7	33.692	0.83603	0.13110	0.03287	467.74	467.77
	11.725	3239.8	33.692	0.83603	0.13110	0.03288	467.76	467.77

Table C-2

Iterative Solution for the Shock of Table C-1 when a 5 mgm Magnesium Sample is Present in Regions 2, 5* and 5.

Region	P(atm)	T(K°)	WM(gm)	X_H x10^{+3}	X_{Mg} x10^{+3}	X_{MgH} x10^{+3}	Δh(T) cal/gm	Δh(ρ) cal/gm
2	2.3295	1792.0	34.179	0.084	7.549	0.062	240.58	224.24
	2.4101	1670.2	34.180	0.027	7.554	0.057	221.29	227.82
	2.3872	1705.0	34.180	0.038	7.553	0.059	226.79	226.86
	2.3869	1705.4	34.180	0.038	7.553	0.059	226.85	226.85
5*	13.085	3410.8	34.180	0.038	7.553	0.059	501.46	527.83
	13.250	3590.2	34.180	0.038	7.553	0.059	530.79	538.05
	13.334	3658.4	34.180	0.038	7.553	0.059	541.96	541.55
	13.330	3654.7	34.180	0.038	7.553	0.059	541.36	541.36
5	13.330	3654.7	32.928	73.479	7.095	0.237	548.33	425.13
	12.458	2833.5	34.015	9.807	7.348	0.227	408.39	490.18
	12.743	3161.2	33.743	25.775	7.274	0.240	463.01	477.25
	12.860	3230.2	33.660	30.616	7.254	0.242	474.71	474.50
	12.869	3229.2	33.662	30.530	7.254	0.242	474.53	474.99
	12.869	3229.9	33.661	30.582	7.254	0.242	474.65	474.93
	12.871	3231.0	33.659	30.667	7.254	0.242	474.85	474.86

addition are in accord with Nayfeh's (1966) findings for ablating Teflon spheres.

The decrease in both temperature and pressure for region 5 relative to region 5* is due to the difference in mole fractions of the components in these two regions. Region 5* is a zone of frozen dissociation and chemistry. To reach the equilibrium characteristic of region 5, some kinetic energy is removed from the mixture to produce further dissociation of the hydrogen and so temperature falls. The increase in density arises from the non-linear dependence of pressure upon temperature, the requirement of momentum conservation and the thermodynamic constraint imposed by the equation of state.

APPENDIX D

A Re-analysis of the v=0,1 and 2 Vibrational Levels of the MgH $A^2\Pi$ - $X^2\Sigma^+$ Band System

In synthesizing an absorption spectrum via computer, it is of the utmost importance to use correct rotational line positions or the computer-generated spectrum cannot be made to reproduce the experimental spectrum faithfully. Early attempts to reconstruct the observed wavenumbers for lines of the MgH $A^2\Pi$ - $X^2\Sigma^+$ band system with the aid of electronic, vibrational and rotational constants determined by Guntsch (1939) and Khan (1962) disclosed significant differences between observed and calculated values for J≥10. (J is the quantum number associated with total angular momentum in the vector model of the diatomic molecule.) Thus, a re-analysis of Guntsch's data was undertaken to obtain a consistent set of constants (particularly D_v and H_v values) that would represent the observations and which might permit a modest extrapolation to lines of higher J-value. While this analysis was in progress, further measurements for the (0,0) and (0,1) bands were published by Balfour (1970). These new data served as additional input for the present analysis.

In the analysis reported below, least squares techniques assuming a weight of unity for each data point were used. This

contrasts with the graphical treatments used by Guntsch which assign weights that are functions of $(J+1/2)^{-1}$. Most of the theoretical expressions employed in the analysis may be found in Herzberg (1950). Therefore, they are mentioned only briefly. The least squares - derived rotational constants for the $^2\Pi$ state are not the true values of B_v and D_v. They are effective values. The analysis was designed to provide only a set of term values for each v' and v" level valid to reasonably high J. As upper state term values may be obtained from those of the lower state by addition of observed line wavenumbers (Refer to Eq (D-1)), it was decided to determine the upper state energy levels in this way. Hence a re-analysis of the lower state became mandatory to assure consistency of the derived quantities.

A description of the MgH 5211 Å band system structure is presented next, both as an aid to understanding the details of the ensuing analysis and as requisite background for the theoretical relations associated with computer-generation of spectra outlined in Chapter 6.

D.1 The Structure of $^2\Pi - {}^2\Sigma^+$ Band Systems

D.1.1 Vector Notation, Λ-type Doubling and Coupling Cases

The rotational term values of the MgH $A^2\Pi - X^2\Sigma$ bands can be represented in terms of Hund's case a or b for angular momentum coupling within diatomic molecules. These models are

treated briefly below using conventional motation. Angular momentum quantities associated with the electronic motions are designated $\vec{\Lambda}$, $\vec{\Sigma}$ and $\vec{\Omega}$ while the rotation of the nuclei is represented by $\vec{R}$.

$\vec{\Lambda}$ is the component of $\vec{L}$ (the resultant orbital angular momentum of all electrons in the molecule) along the internuclear axis about which $\vec{L}$ precesses. The possible values of $\vec{\Lambda}$ ($\Lambda=0,1,2,3\ldots,L$) are indicated by the labels [as $f(\Lambda)$] Σ, $\Pi,\Delta,\Phi,\ldots$ used to denote electronic states of the molecule. $\vec{\Lambda}$ may be oriented either parallel or anti-parallel to the internuclear axis. Hence, in all electronic states for which $\Lambda>0$ (thereby excluding Σ states) there is a double degeneracy - Λ-type doubling - resultant from the two possible $\vec{\Lambda}$ orientations.

$\vec{\Sigma}$ is the component of $\vec{S}$ (the resultant of all the electron spins) directed parallel to the internuclear axis when $\Lambda>0$. $\vec{\Sigma}$ is undefined for $\Lambda=0$. There are $(2S+1)$ allowed values of $\vec{\Sigma}$,

$$\vec{\Sigma} = S, S-1, S-2, \ldots, -S.$$

Thus a particular molecular electronic state has a spin multiplicity of $(2S+1)$.

$\vec{\Omega}$, the total electronic angular momentum about the internuclear axis is defined by $\vec{\Omega} = \vec{\Lambda} + \vec{\Sigma}$ with magnitude $\Omega = |\vec{\Lambda} + \vec{\Sigma}|$.

International spectroscopic nomenclature includes information concerning $\vec{\Lambda}$, $\vec{\Sigma}$ and $\vec{\Omega}$ in the designation of molecular

states via the notation $^{2S+1}f(\Lambda)_{\Omega}$.

When $\Lambda=0$, $f(\Lambda)=\Sigma$ and, although $\vec{\Sigma}$ and $\vec{\Omega}$ are undefined, the spin multiplicity of the state is formally identified with $(2S+1)$. Spin multiplets become detectable when the effects of interactions between nuclear and electronic motions are taken into account. When $\Lambda=1$, $f(\Lambda)=\Pi$. So the upper, A, state of the MgH 5211 Å band system has two spin components identified as $A^2\Pi_{\frac{1}{2}}$ and $A^2\Pi_{\frac{3}{2}}$.

The Λ-type degeneracy of the spin multiplet components is removed when interaction between $\vec{L}$ and $\vec{R}$, occurring in the rotating molecule, establishes Λ-components (labelled c and d) of slightly different energy within each spin component. Consequently the A state of MgH consists of four term series:

$$A^2\Pi^c_{\frac{1}{2}}, A^2\Pi^d_{\frac{1}{2}}, A^2\Pi^c_{\frac{3}{2}}, A^2\Pi^d_{\frac{3}{2}}.$$

In the $^2\Pi$ state, coupling between electronic and nuclear rotational motions can be described by Hund's case a for slow rotation of the nuclei and by case b for fast nuclear rotation. For Hund's case a, the electronic motion is strongly coupled to the internuclear axis and Ω is a good quantum number. As Fig. D-1a illustrates, the total electronic angular momentum vector, $\vec{\Omega}$, and the nuclear rotation angular momentum vector, $\vec{R}$, combine to yield $\vec{J}$, the total angular momentum vector, which has possible values -

$$J=\Omega,\Omega+1,\Omega+2,\Omega+3,\ldots$$

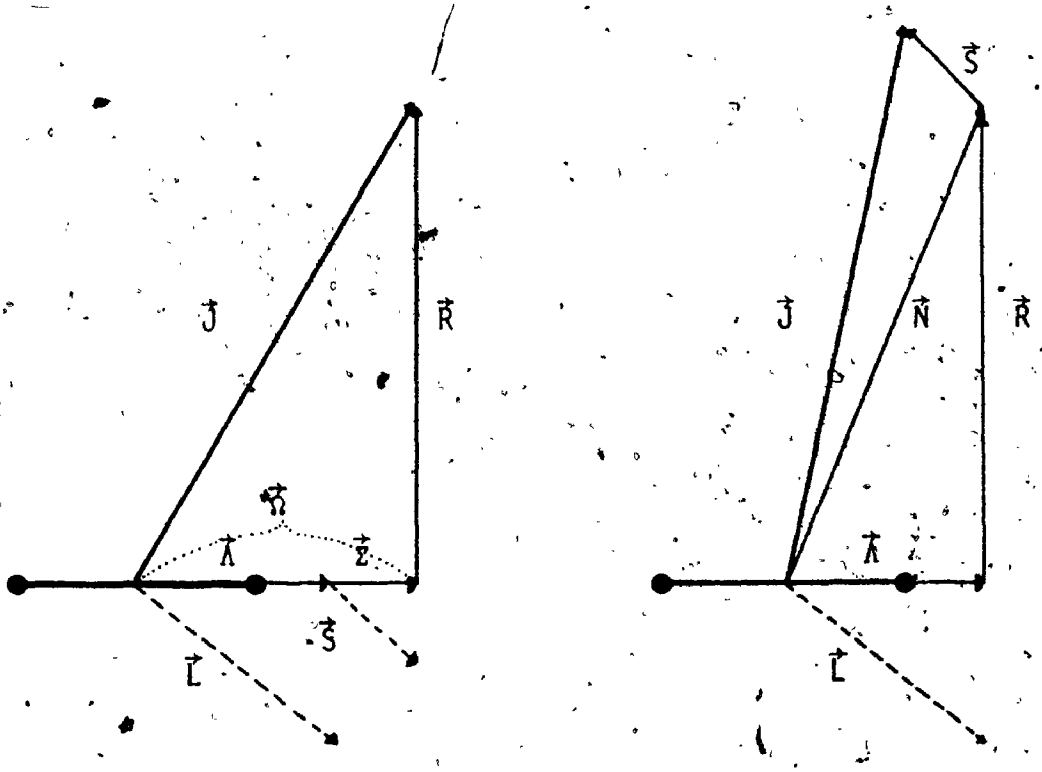

a) Hund's Case a

b) Hund's Case b

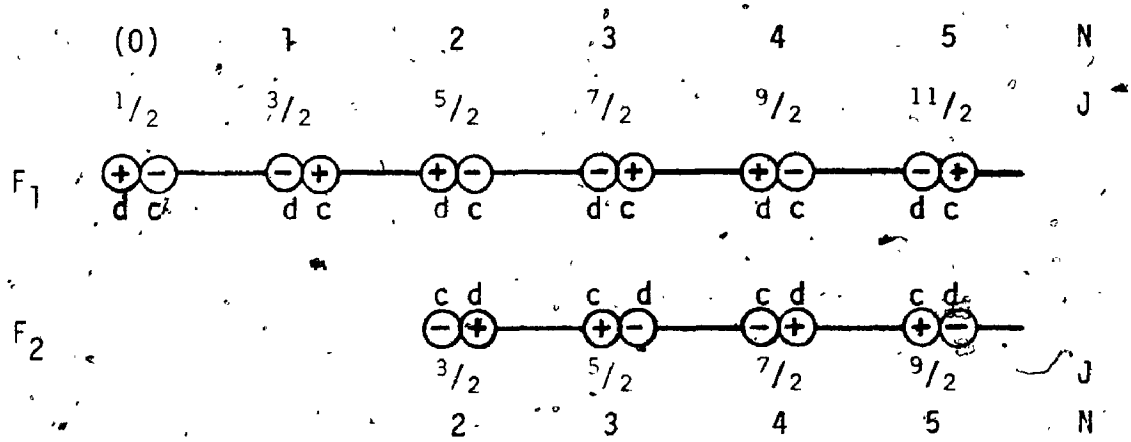

c) Parity of Levels and Λ-components of a Regular $^2\Pi$ State in a $^2\Pi$ - $^2\Sigma^+$ Transition (after Mulliken, 1931)

FIGURE D-1

Coupling Cases and Symmetry Properties for a Regular $^2\Pi$ State

Levels with $J<\Omega$ do not occur. Hund's case b coupling is characterized by weak or zero coupling of $\vec{S}$ to the internuclear axis with the result that $\vec{\Sigma}$ and $\vec{\Omega}$ are not defined. However, $\vec{R}$ and $\vec{\Lambda}$ form a resultant $\vec{N}$, the total angular momentum neglecting spin, which in turn forms a resultant, $\vec{J}$, with $\vec{S}$ as Fig. D-1b shows. $\vec{N}$ has the possible values

$$N=\Lambda,\Lambda+1,\Lambda+2,\Lambda+3,\ldots$$

while J may take the values

$$J=N+S,N+S-1,N+S-2,\ldots,|N-S|$$

in general. (The case J=S must be considered separately.)

The spin multiplicity in both electronic states of a $^2\Pi - {}^2\Sigma^+$ transition is 2. So the spectral lines of the vibrational bands may be considered either as J-doublets or N-doublets. (For each J-value there are two possible N-values and vice versa. Once again the J=S rotational levels lead to special cases.) The following treatment is based on N-doublets as the energies of the two spin components associated with each N-value are closer than those associated with each J-value for the MgH bands. Rotational contributions to the term values are considered either as F_1-levels (N=J-1/2) or as F_2-levels (N=J+1/2). When it is necessary to identify Λ-components of spin doublets, within the F_1-levels say, recourse is made to the notation $F_1^c(N)$ and $F_1^d(N)$. Fig. D-1c may be used to clarify the term components within the $^2\Pi$ state.

D.1.2 Term Values, the Band Origin and Branches of $^2\Pi$-$^2\Sigma^+$ Vibrational Band

The vacuum wavenumber of a spectral line may be evaluated from

$$\nu = T' - T'' \qquad (D\text{-}1)$$

in which T' = the term value (cm^{-1}) for the upper level
T'' = the term value for the transitions lower level.

and $$T = T_e + G_e(v) + F^k_{evi}(J) \qquad (D\text{-}2)$$

with T_e = the electronic energy associated with the state e.

$G_e(v)$ = energy due to vibration of the molecule in the vth vibrational level of the eth electronic state.

$F^k_{evi}(J)$ = energy due to rotation with total angular momentum J for the kth Λ-component of the ith spin component in the vth vibrational level of the eth electronic state.

Substitution from Eq (D-2) into (D-1) leads to

$$\nu = \nu_0 + F'(J') - F''(J'') \qquad (D\text{-}3)$$

with the band origin, ν_0, given by

$$\nu_0 = T'_e - T''_e + G'(v') - G''(v'') \qquad (D\text{-}4)$$

Double primes stand for all suppressed identifiers required to specify the lower rotational level. Single primes represent those which characterize the upper state of the transition. Wavenumbers for rotational lines of any (v',v") band may be evaluated from (D-3) when the band origin and the rotational term values are known.

The selection-rules for dipole radiation [$\Delta J = J' - J'' = -1, 0, +1$ with $J' = 0 \not\leftrightarrow J'' = 0$] restrict possible branch types to three

- P, Q and R. (Symmetry properties of the molecular rotational states and the parity selection rule +↔- require that all Main branch transitions in a $^2\Pi$ - $^2\Sigma^+$ band system with $\Delta J=0$ terminate on c-levels and those with $\Delta J=\pm 1$ end on d-levels of Λ-doublets. The converse holds true for Satellite branches. [Mulliken, 1931]). As a rotational transition may occur in any one of four possible ways for each branch type [$F_i'(J') \longleftrightarrow F_j''(J'')$; i=1,2 and j=1,2], twelve branches exist. Those for which i=j are designated the Main branches and have $\Delta J=\Delta N$. The remainder are known as Satellite branches and for them $\Delta J \neq \Delta N$. ΔN may be found for any Satellite branch from the transition written in J-notation in the following manner:

i) Subtract 1/2 from J-value of F_1-levels.

ii) Add 1/2 to J-value of F_2-levels.

iii) Subtract the modified lower state J-value from the modified upper state J-value to obtain ΔN which specifies the form of the branch.

Table D-1 gives expressions in both J and N notation for the branches of $^2\Pi$ - $^2\Sigma^+$ bands as a function of the lower state J or N value. The form of each Satellite branch is specified in the N-notation expressions via a superscript to the left of the branch type.

D.2 Re-analysis of the $^2\Sigma^+$ State

A re-analysis of the lower electronic state was performed to obtain rotational constants that would adequately represent levels of

TABLE D-1

The Twelve Branches of a $^2\Pi - {}^2\Sigma$ Vibrational Band

$P_1(J) = \nu_0 + F_1^{d\prime}(J-1) - F_1''(J)$	$P_1(N) = \nu_0 + F_1^{d\prime}(N-1) - F_1''(N)$
$P_2(J) = \nu_0 + F_2^{d\prime}(J-1) - F_2''(J)$	$P_2(N) = \nu_0 + F_2^{d\prime}(N-1) - F_2''(N)$
$P_{21}(J) = \nu_0 + F_2^{c\prime}(J-1) - F_1''(J)$	$^{Q}P_{21}(N) = \nu_0 + F_2^{c\prime}(N) - F_1''(N)$
$P_{12}(J) = \nu_0 + F_1^{c\prime}(J-1) - F_2''(J)$	$^{O}P_{12}(N) = \nu_0 + F_1^{c\prime}(N-2) - F_2''(N)$
$Q_1(J) = \nu_0 + F_1^{c\prime}(J) - F_1''(J)$	$Q_1(N) = \nu_0 + F_1^{c\prime}(N) - F_1''(N)$
$Q_2(J) = \nu_0 + F_2^{c\prime}(J) - F_2''(J)$	$Q_2(N) = \nu_0 + F_2^{c\prime}(N) - F_2''(N)$
$^{O}Q_{21}(J) = \nu_0 + F_2^{d\prime}(J) - F_1''(J)$	$^{R}Q_{21}(N) = \nu_0 + F_2^{d\prime}(N+1) - F_1''(N)$
$Q_{12}(J) = \nu_0 + F_1^{d\prime}(J) - F_2''(J)$	$^{P}Q_{12}(N) = \nu_0 + F_1^{d\prime}(N-1) - F_2''(N)$
$R_1(J) = \nu_0 + F_1^{d\prime}(J+1) - F_1''(J)$	$R_1(N) = \nu_0 + F_1^{d\prime}(N+1) - F_1''(N)$
$R_2(J) = \nu_0 + F_2^{d\prime}(J+1) - F_2''(J)$	$R_2(N) = \nu_0 + F_2^{d\prime}(N+1) - F_2''(N)$
$R_{21}(J) = \nu_0 + F_2^{c\prime}(J+1) - F_1''(J)$	$^{S}R_{21}(N) = \nu_0 + F_2^{c\prime}(N+2) - F_1''(N)$
$R_{12}(J) = \nu_0 + F_1^{c\prime}(J+1) - F_2''(J)$	$^{Q}R_{12}(N) = \nu_0 + F_1^{c\prime}(N) - F_2''(N)$

molecular rotation for N>15. These constants were later used when lower state rotational contributions were included in the evaluation of band origins.

D.2.1. $^2\Sigma^+$ State Rotational Analysis

As all $^2\Sigma$ states can be represented by Hund's coupling case b, the energies of the spin doublets may be expressed as (Herzberg, 1950; Kovacs, 1969)

$$F_{vi}(N)=B_v[N(N+1)]-D_v[N(N+1)]^2+H_v[N(N+1)]^3+\gamma_v f_i(N) \quad (D\text{-}5)$$

F_1-levels: $i=1$, $f_1(N)=+N/2$

F_2-levels: $i=2$, $f_2(N)=-(N+1)/2$

in which γ_v is a measure of the magnetic interaction between $\vec{S}$ and $\vec{N}$. D_v and H_v are centrifugal distortion coefficients normally important in hydrides for N>10.

The lower state rotational constants B''_v, D''_v, H''_v and γ''_v were derived from the combination differences

$$\Delta_2F''_{vi}(N)=F''_{vi}(N+1)-F''_{vi}(N-1)=R_i(N-1)-P_i(N+1) \quad (D\text{-}6)$$

Substitution from Eq (D-5) into (D-6) followed by some algebraic manipulation yields a relation for the combination differences in terms of the rotational constants -

$$\Delta_2F''_{vi}(N)=B''_v\{2[2N+1]\}-D''_v\{4[2N+1](N(N+1)+1)\}$$
$$+H''_v\{2[2N+1](3[N(N+1)]^2+10[N(N+1)]+4)\}+f_i(\gamma) \quad (D\text{-}7)$$

F_1-levels: $i=1$, $f_1(\gamma)=+\gamma''_v$ in $\Delta_2F''_{v1}$

F_2-levels: $i=2$, $f_2(\gamma)=-\gamma''_v$ in $\Delta_2F''_{v2}$.

Use of the non-standard notation

$$i=3,\ f_3(\gamma)=0 \quad \text{in} \quad \Delta_2F''_{v3}=[\Delta_2F''_{v1}(N)+\Delta_2F''_{v2}(N)]/2$$

allows Eq (D-7) to be applied to the average of the $\Delta_2F''_v(N)$-values.

A computer program capable of performing a least squares fit to an expression of the form

$$Y = C_1z_1(x) + C_2z_2(x) + C_3z_3(x) + C_4z_4(x) + \ldots$$

was available. (The $z_i(x)$ are arbitrary functions of x subject to the constraint that all the $z_i(x)$'s must be linearly independent.) Both the number of constants and the order of their evaluation could be set upon each call to the program. When the fit was complete, the program would return values for the C_i, standard deviations for the C_i and the standard error of Y-estimate. By identifying B''_v,D''_v,H''_v and γ''_v with the C_i's and the $z_i(x)$'s with the functions of N in Eq (D-7), the computer program could accomplish the analysis for the lower state rotational constants.

A set of input $\Delta_2F''_{vi}(N)$ values was obtained from all measured bands having the same lower vibrational level [(0,1), (2,1) and (1,0) for v"=1] using lines from the P and R branches of the same (v',v") band. Effective rotational constants which best reproduce the $\Delta_2F''_{v1}(N)$'s and $\Delta_2F''_{v2}(N)$'s are listed in Table D-2 to the number of digits used in the reconstruction of rotational line wavenumbers from them. The precision of those values may be assessed by comparison with the "true"

TABLE D-2

Effective Rotational Constants (cm^{-1}) for the MgH $A^2\Pi$ - $X^2\Sigma$ System Needed to Reproduce Observed Rotational Line Wavenumbers

State	v	Valid for Main Branches	$B_{v_{eff}}$	$D_{v_{eff}}$ x 10^{+4}	$H_{v_{eff}}$ x 10^{+8}	$\gamma_{v_{eff}}$	A_v
Sigma	0	P,Q,R	5.7364724*	3.5218736**	1.1395494	0.0	-
			5.7339303	3.4839279	0.94785183	0.0	-
	1	P,Q,R	5.5555623	3.5417864	0.97895699	0.0	-
			5.5570831	3.5439956	0.93362470	1.1418033	-
	2	P,Q,R	5.3666240	3.5220538	0.0	0.0	-
			5.3669316	3.5255497	0.0	0.0	-
Pi	0	P,R	6.0945290	3.5220538	1.1006348	0.0	35.0
			6.0955100	3.6746237	1.0352254	0.0	35.0
		Q	6.0932063	3.6732316	1.1410571	0.0	35.0
			6.0923578	3.6516333	1.0041175	0.0	35.0
	1	P,R	5.9062404	3.8225882	2.1609425	0.0	36.0
			5.9057569	3.6650042	0.0	0.0	36.0
		Q	5.9001272	3.6086888	0.0	0.0	36.0
			5.9019302	3.6090200	0.0	0.0	36.0
	2	P,R	5.7009614	3.3132555	-8.7726820	0.0	36.0
			5.7335324	4.0575617	0.0	0.63383492	36.0
		Q	5.7076258	3.8885269	3.0550633	0.0	36.0
			5.6999876	3.3950990	-4.1479319	0.0	36.0

* F_1-levels
* F_2-levels

** Values read $D_{v_{eff}} = 3.5218736 \times 10^{-4}$.

values of B''_v, D''_v and H''_v - obtained from the $\Delta_2 F''_{v3}(N)$ values - which are given in Table D-3.

Table D-3 contains not only an analysis of the combined data of Guntsch and Balfour, but also gives a comparison of the present values with those obtained by Guntsch and Balfour separately. The close agreement between the three sets of B''_v-values was expected as was the discrepancy between the D''_v-values. The latter are influenced greatly by the inclusion of an H''_v term. Such an inclusion is justified when data with $N \geq 30$ is used in determining the constants. The slight differences between the B''_v-values found by the present treatment and the ones found separately by Guntsch and Balfour from their data is probably due to the rejection criterion employed (No $\Delta_2 F''_{v3}(N)$-value was retained if its residual was greater than three times the standard error of estimate in $\Delta_2 F''_{v3}(N)$) and not to the use of Eq (D-7) instead of the customary power series -

$$\Delta_2 F''_{v1}(N) = \{4B''_v - 6D'' + \frac{27H''_v}{4}\}[N+1/2] - \{8D''_v - 34H''_v\}[N+1/2]^3 + 12H''_v[N+1/2]^5 + f_i(\gamma). \quad \text{(D-8)}$$

Eq (D-7) was used because it yielded individual constants with their standard deviations directly. Preliminary tests, using only the data of Guntsch, indicated that the constants obtainable from Eqs (D-8) and (D-7) had the same values.

Comparison of the standard errors of estimate in the fitted values of $\Delta_2 F''_{v3}(N)$ for separate analyses of the data of

TABLE D-3

Rotational Constants (cm^{-1}) for the $^2\Sigma^+$ State derived from Averaged $\Delta_2F''_v(N)$-values.

Analysis	v"	B_v	D_v x10^{+4}	H_v x10^{+8}	Points Number	N-values Included in fit	S.E. of Estimate
Combined Data	0	$5.7347_7 \pm 0.0004_7$ 5.732_9	$3.496_7 \pm 0.007_3$ 3.3	$1.01_1 \pm 0.03_3$ 0.4	90(83)	2 - 36	0.089
	1	$5.5544_2 \pm 0.0005_2$ 5.551_9	$3.52_0 \pm 0.01_2$ 3.4	$0.84_1 \pm 0.07_4$	74(68)	3 - 30	0.074
	2	$5.366_7 \pm 0.001_2$ 5.356_6	$3.52_0 \pm 0.02_0$ 3.5		50(49)	5 - 23	0.21
	3	$5.171_3 \pm 0.002_0$ 5.172^3	$3.68_8 \pm 0.03_6$ 3.7		11(11)	8 - 19	0.13
Guntsch Data	0	$5.7343 \pm 0.0007_9$	$3.47_9 \pm 0.01_3$	$0.87_2 \pm 0.06_5$	55(51)	4 - 34	0.11
	1	$5.554_8 \pm 0.001_0$	$3.52_7 \pm 0.03_2$	$0.90_5 \pm 0.29_4$	45(42)	8 - 24	0.079
Balfour Data	0	$5.7342 \pm 0.0006_2$ 5.7328	$3.490 \pm 0.008_9$ 3.44	$0.99_7 \pm 0.03_8$	35(34)	2 - 36	0.073
	1	$5.5538 \pm 0.0007_2$ 5.552	$3.51_5 \pm 0.01_4$ 3.39^5	$0.83_2 \pm 0.07_7$	29(27)	3 - 31	0.066

Note: Guntsch's values for the rotational constants appear below the present estimates in the "Combined Data" section. Balfour's values are under the present ones in the "Balfour Data" section. The number of points included in the final fit is given in parentheses following the initial number of points. Quoted N values refer to $\Delta_2F(N)$s actually included in the final fit. Indicated errors equal one standard deviation.

Guntsch and of Balfour shows that these data are of comparable precision. Thus, combining rotational line wavenumbers from both sources in the determination of the constants for v"=0,1 is justified. Data for the v"=2,3 levels is due entirely to Guntsch and does not extend to sufficiently large N to justify the use of an H''_v term. Attempts to evaluate one yield a "constant" that is comparable in size to its own standard deviation. Neither the data of Guntsch nor that of Balfour is of sufficiently high precision to permit determination of the true γ''_v-values. These seem to be smaller than the combined errors of measurement entering into the relation normally used for their evaluation. A fact that Guntsch noted!

B''_v-values determined for the combined data may be represented by

$$B''_v = 5.8220-0.1727[v''+1/2]-0.003775[v''+1/2]^2 \qquad (D-9)$$

with a reproducibility of one unit in the fourth place of decimals.

D.2.2 $^2\Sigma^+$ State Vibrational Constants

The lower state vibrational constants were determined by a method first suggested by Jenkins & McKellar (1932) which consists of evaluating

$$\Delta G''(v+1/2)=G''(v''+1)-G''(v'') \qquad (D-10)$$

from differences in the wavenumbers of lines occurring in the same branch and having the same N-value in (v',v"+1) and (v', v") bands. These differences yield

$$\Delta_1\nu_i(N) = R_{(v',v''+1),i}(N) - R_{(v',v''),i}(N) = Q_{(v',v''+1),i}(N) - Q_{(v',v''),i}(N)$$
$$= P_{(v',v''+1),i}(N) - P_{(v',v''),i}(N)$$

It is a straightforward matter to show that

$$\Delta_1\nu_i(N) = \Delta G''(v+1/2) - F''_{v,i}(N) + F''_{v+1,i}(N) \qquad (D\text{-}11)$$

by substitution from Eq (D-2) and that $\Delta_1\nu_i(N)$ is related to the differences between rotational constants of the two Sigma state vibrational levels via

$$\Delta_1\nu_i(N) = \Delta G''(v+1/2) - \{B''_v - B''_{v+1}\}[N(N+1)] + \{D''_v - D''_{v+1}\}[N(N+1)]^2$$
$$- \{H''_v - H''_{v+1}\}[N(N+1)]^3 - \{\gamma''_v - \gamma''_{v+1}\}f_i(N) \qquad (D\text{-}12)$$

F_1 - levels: $i=1$, $f_1(N)=N/2$
F_2 - levels: $i=2$, $f_2(N)=-(N+1)/2$

Average: $i=3$, $f_3(N)=-1/4$ with $\Delta_1\nu_3(N) = \dfrac{[\Delta_1\nu_1(N) + \Delta_1\nu_2(N)]}{2}$

as a result of further substitution from (D-5) into (D-11). Because H_v and γ_v are such small quantities, differences between their values in neighbouring vibrational levels lead to negligible terms in (D-12). Consequently, $\Delta_1\nu_1 = \Delta_1\nu_2$ to this degree of approximation.

Thus six estimates of $\Delta G''(v+1/2)$, $\{B''_v - B''_{v+1}\}$, $\{D''_v - D''_{v+1}\}$ and their associated uncertainties were determined from the Main branches for selected pairs of bands. These preliminary results showed that retention of the term in $\{D''_v - D''_{v+1}\}$ was essential although there

was considerable scatter among the estimates of its value. They also showed that there was close agreement between the $\Delta G''(v+1/2)$ and $[B''_v - B''_{v+1}]$ differences found from Q-branch lines and those evaluated from P and R-branch lines.

A simultaneous least squares fit to all data sets derived from Guntsch's observations yielded the values recorded in Table D-4. For comparison purposes, differences between appropriate rotational constants appearing in Table D-3 have been included in Table D-4. The agreement between the two sets of results is quite satisfactory.

Finally, the Sigma state vibrational constants were obtained from the $\Delta G''(v+1/2)$ values using the customary power series expansion for $G(v)$

$$G(v) = \omega_e(v+1/2) - \omega_e x_e(v+1/2)^2 + \omega_e y_e(v+1/2)^3 \qquad \text{(D-13)}$$

which leads to

$$\Delta G(v+1/2) = \{\omega_e + \frac{\omega_e y_e}{4}\} - 2\omega_e x_e(v+1) + 3\omega_e y_e(v+1)^2 \qquad \text{(D-14)}$$

when terms up to $\omega_e y_e$ are included. (For a Morse oscillator only the first two terms appearing on the right in Eq (D-13) are non-zero.) When the present results were inserted into (D-14) the constants given in Table D-5 were obtained. Also contained in that table are vibrational constants derived by Guntsch, Morse constants found by Khan and the Morse constants determined in the present analysis that best represent $\Delta G''(v+1/2)$ values. The vibrational energies, $G(v)$, predicted by these four sets of constants are approximately the same. Certainly the two Morse fits are equivalent. They both give energy levels about 2.0-2.3 cm^{-1} higher than those predicted by the present three term fit which

TABLE D-4

Determination of $\Delta G''(v+1/2)$ and Differences between Lower Electronic State Rotational Constants (cm^{-1}) in Vibrational levels v" and v"+1.

v"	$\Delta G''(v+1/2)$	$B''_v - B''_{v+1}$	$D''_v - D''_{v+1}$ $\times 10^{+4}$	Band Pairs Utilized
0	*1432.02 ± 0.06	†$0.1808 \pm 0.0004_4$	$-3.2_0 \pm 0.6_3$	(0,0) (0,1)
		$0.1803 \pm 0.0007_0$	-2.4 ± 1.4	(1,0) (1,1)
1	$1368.6_4 \pm 0.1_4$	$0.187_0 \pm 0.001_4$	-7.0 ± 2.9	(0,1) (0,2)
		$0.187_7 \pm 0.001_3$	0.0 ± 2.3	(1,1) (1,2)
				(2,1) (2,2)
2	$1301.3_4 \pm 0.1_2$	$0.194_1 \pm 0.001_2$	-18.6 ± 2.5	(2,2) (2,3)
		$0.195_4 \pm 0.002_3$	-16.8 ± 4.2	

* Guntsch gives 1432.2,1367.9 and 1302.7.

† The first entry comes from the analysis suggested by Jenkins & McKellar (1932). The second entry is obtained by subtracting values located in Table D-3 and evaluating the rms error in the result.

TABLE D-5

$^2\Sigma^+$ State Vibrational Constants and G(v) Values in cm^{-1}. Comparison of Three Term and Morse Fits.

	This Work	Guntsch	This Work (Morse)	Khan (Morse)
ω_e	1491.6_4	1495.7	1498.0_1	1497.0
$\omega_e x_e$	28.7_5	31.5	32.6_7	32.4
$\omega_e y_e$	-0.16_3	-0.15	-	-
G(0)	738.53	739.96	740.8	740.4
G(1)	2170.57	2172.17	2173.5	2172.6
G(2)	3539.21	3540.03	3540.8	3540.0
G(3)	4840.55	4842.64	4842.8	4842.6

in turn, yields G(v) values about 1.5 cm^{-1} below those found by Guntsch.

D.3 The $^2\Pi$ State Analysis

The examination of the $^2\Pi$ state was not so complete as that of the $^2\Sigma$ state. That earlier analysis had shown the reliability of Guntsch's work. Consequently his values for the coupling constant, A_v, were accepted. Effective rotational constants for the Λ-components and band origins were extracted from his data. No attempt was made to determine the constants governing the Λ-doubling itself.

Effective upper state rotational constants finally adopted for use in reconstructing rotational line wavenumbers are listed in Table D-2. The method of their evaluation is discussed in the following sub-section.

D.3.1 $^2\Pi$ Rotational Analysis

Hill and Van Vleck (1928) give for the energy due to rotation in a $^2\Pi$ state intermediate between Hund's coupling cases a and b -

$$F_{vi}(J) = B_v\{(J+1/2)^2 - 1 \pm \tfrac{1}{2}[4(J+1/2)^2 + Y(Y-4)]^{\frac{1}{2}}\} \qquad (D\text{-}15)$$

F_1 - levels, i=1 use the - sign

F_2 - levels, i=2 use the + sign

in the absence of centrifugal distortion, $Y=A_v/B_v$ and A_v is a constant denoting the amount of coupling between $\vec{\Sigma}$ and $\vec{\Lambda}$. In the MgH 5211 Å band system, the $^2\Pi$ state is close to Hund's case b. Therefore, addition of centrifugal distortion and spin-splitting terms (applicable to case b) to Eq (D-15) plus expression of the rotational term values in N-notation yields

$$F_{v1}(N) = B_v\{(N+1)^2 - 1 - \tfrac{1}{2}[4(N+1)^2 + Y(Y-4)]^{\frac{1}{2}}\} - D[N+1/2]^4 \qquad (D\text{-}15a)$$

$$+ Hv[N+1/2]^6 + \gamma_v N/2$$

$$F_{v2}(N) = B_v\{N^2 - 1 + \tfrac{1}{2}[4N^2 + Y(Y-4)]^{\frac{1}{2}}\} - D_v[N+1/2]^4 + H_v[N+1/2]^6 - \gamma_v(N+1)/2 \qquad \text{(D-15b)}$$

Combination differences for the upper state Λ-component levels were evaluated from measured line wavenumbers by employing the usual relations-

$$\Delta_2 F_i^{c\prime}(N) = Q_i(N+1) - Q_i(N-1) - P_i(N+1) + R_i(N-1)$$

$$\Delta_2 F_i^{d\prime}(N) = R_i(N) - P_i(N)$$

Equation (D-15) may be used to relate these differences to a set of rotational constants for each Λ-component via

$$\Delta_2 F_1'(N) = B_v'\{4(N+1) + \tfrac{1}{2}\{[4N^2 + Y(Y-4)]^{\frac{1}{2}} - [4(N+2)^2 + Y(Y-4)]^{\frac{1}{2}}\}\}$$
$$-D_v'[2N+1]([2N+1]^2+4) + H_v'[2N+1](\tfrac{3}{8}[2N+1]^4 + 5[2N+1]^2 + 6) + \gamma_v \qquad \text{(D-16a)}$$

$$\Delta_2 F_2'(N) = B_v'\{4N + \tfrac{1}{2}\{[4(N+1)^2 + Y(Y-4)]^{\frac{1}{2}} - [4(N-1)^2 + Y(Y-4)]^{\frac{1}{2}}\}\}$$
$$-D_v'[2N+1]([2N+1]^2+4) + H_v'[2N+1](\tfrac{3}{8}[2N+1]^4 + 5[2N+1]^2 + 6) - \gamma_v \qquad \text{(D-16b)}$$

Introduction of a non-standard notation, once more, and use of Eqs (D-16a,b) leads to

$$\Delta_2 F_3'(N) = [\Delta_2 F_1'(N) + \Delta_2 F_2'(N+1)]/2$$
$$= B_v'[4(N+1)] - D_v'[4(N+1)][2(N+1)^2 + 3.5] + H_v'[4(N+1)][3(N+1)^4 + 17.5(N+1)^2 + 183/16]. \qquad \text{(D-17)}$$

which may be used to evaluate the other rotational constants without recourse to the coupling constant A_v.

TABLE D-6

Rotational Constants (cm^{-1}) for the $^2\Pi$ State derived from $\Delta_2F_3'(N)$-values.

Analysis	v'	B_v	D_v $\times 10^{+4}$	H_v $\times 10^{+8}$	Data Points Number	N-values Included in Fit	S.E. of Estimate
Combined Data	0	$6.0951 \pm 0.0002_6$	$3.681_9 \pm 0.003_7$	$1.11_2 \pm 0.01_6$	113(104)	3 - 37	0.058
		$6.0930 \pm 0.0004_6^6$	$3.672_1 \pm 0.007_2$	$1.14_4 \pm 0.03_3^6$	110(106)	3 - 36	0.10
	1	$5.9027 \pm 0.0006_6$	$3.627 \pm 0.007_5$		60(56)	5 - 25	0.13
		$5.9008 \pm 0.0008_9^6$	$3.60_6 \pm 0.01_1^5$		49(48)	6 - 24	0.15
	2	$5.712_9 \pm 0.002_6$	$3.88_1 \pm 0.05_5$		35(35)	6 - 18	0.30
		$5.707_5 \pm 0.002_4^6$	$3.72_5^5 \pm 0.04_7$		36(36)	6 - 18	0.28
	3	$5.501_0 \pm 0.006_8$	$3.6_7 \pm 0.1_6$		9(9)	8 - 16	0.33
		$5.474_9 \pm 0.009_9^8$	$3.1_1^7 \pm 0.1_9^6$		7(7)	11 - 17	0.37
Guntsch Data	0	$6.0942 \pm 0.0005_6$	$3.659 \pm 0.009_4$	$0.95_6 \pm 0.04_5$	53(52)	3 - 34	0.082
		$6.0913 \pm 0.0009_6^6$	$3.62_6 \pm 0.01_7^4$	$0.83_5^6 \pm 0.08_9^5$	51(51)	4 - 33	0.14
Balfour Data	0	$6.0947 \pm 0.0003_3$	$3.677_4 \pm 0.004_5$	$1.09_7 \pm 0.01_8$	60(57)	3 - 37	0.054
		$6.0933 \pm 0.0004_6^3$	$3.675_7 \pm 0.006_5$	$1.16_0 \pm 0.02_8^8$	59(56)	3 - 36	0.071

Note: For each v'-value, the first entry is the rotational constant appropriate to the P and R-branches. The second entry applies to the Q-branches. Consequently, in Mulliken's notation, for v'=0 the combined data yield B_0^d=6.0951 and B_0^C=6.0930. Quoted errors represent one standard deviation.

TABLE D-7

"True" Rotational Constants (cm^{-1})
for the $A^2\Pi$ State of MgH

v	B_v	D_v x10^{+4}	H_v x10^{+8}
0	6.0941	3.677	1.13
	6.0834	3.6	
1	5.901_8	3.6_2	
	5.892_5	3.7	
2	5.710	3.80	
	5.699	3.8	
3	5.48_8	3.4	
	5.51_1	4.0	

The first entry is an arithmetic average of the c and d-level values from Table D-6. The second is the value quoted by Guntsch. Balfour gives $B_0' = 6.0936\ cm^{-1}$ and $D_0' = 3.57 \times 10^{-4} cm^{-1}$. For Guntsch data alone, the present analysis yields $B_0' = 6.0928\ cm^{-1}$, $D_0' = 3.64 \times 10^{-4} cm^{-1}$ and $H_0' \approx 0.89 \times 10^{-8} cm^{-1}$.

The effective rotational constants used to reconstruct P,Q and R branch lines that are listed in Table D-2 were computed by least squares fitting of data to Eq (D-16a,b). A fixed value for A_v and an assumed value of B_v were used to provide Y values for the first fit. Then the least squares procedure was iterated (for Y changed with each estimator of B_v although A_v was maintained constant.) until differences were negligible between rotational constants evaluated upon successive iterations.

Table D-6 contains effective rotational constants for the c and d Λ-components determined from Eq (D-17). These results differ considerably from those of Table D-2 in part as a result of smoothing performed

during the averaging that takes place in calculating $\Delta_2F_3(N)$ and in part due to inclusion of H_v- and γ_v-dependent terms in the solutions of Eq (16a and b).

It is customary to quote the arithmetic average of the effective A-component constants as the "true" value of B_v, D_v, etc. This is done in Table D-7 where Guntsch's results have also been included for comparison. With the exception of B_0', the agreement is quite satisfactory. The discrepancy between B_0' values may be traced to Guntsch's failure to include an H_0' term in his analysis. Clearly, the present estimate of B_0' is quite close to Balfour's estimate of that quantity. Had the H_0' term been omitted, the present treatment would have yielded a fit to Guntsch's data with $B_0' = 6.0846 \pm 0.0012$ cm^{-1}, $D_0' = [3.471 \pm 0.0089] \times 10^{-4}$ cm^{-1} and a standard error of estimate equal to 0.23 cm^{-1}.

The upper state B_v-values may be represented by

$$B_v = 6.1825 - 0.1723(v+1/2) - 0.0074(v+1/2)^2$$

with a reproducibility of 6 units in the third decimal place.

D.3.2 $^2\Pi$ State Vibrational Analysis

The underlying purpose of analysing the $^2\Pi$ state was to determine reliable estimates for the band origins, ν_0. In his work, Guntsch had subtracted rotational term values from P-head measurements to yield two values of ν_0 for each band. Khan, in his re-appraisal of Guntsch's thesis, gave $\nu_e = 19234.5$ cm^{-1} as the system origin and Morse constants for both upper and lower vibrational levels. Some doubt existed that the Morse model could give an adequate representation of the MgH A and X states. Therefore, origins were derived for all the bands Guntsch had measured

and vibrational constants for the Pi state extracted from them. The origins were determined in the following manner.

Quantities $\Delta\nu^d(N)$ and $\Delta\nu^c(N)$, defined by Eqs (D-18a,b), were computed.

$$\Delta\nu^d(N) = \nu_0 + \tfrac{1}{2}[\, F_1^{d\prime}(N) + F_2^{d\prime}(N+1)\,] \qquad \text{(D-18a)}$$
$$= \tfrac{1}{2}\{\,[R_1(N-1) + F_1''(N-1)\,] + [R_2(N) + F_2''(N)\,]\,\}$$
$$= \tfrac{1}{2}\{\,[P_1(N+1) + F_1''(N+1)\,] + [P_2(N) + F_2''(N)\,]\,\}$$

$$\Delta\nu^c(N) = \nu_0 + \tfrac{1}{2}[\, F_1^{c\prime}(N) + F_2^{c\prime}(N+1)\,] \qquad \text{(D-18b)}$$
$$= \tfrac{1}{2}\{\,[Q_1(N) + F_1''(N)\,] + [Q_2(N+1) + F''(N+1)\,]\,\}$$

(Note that $\Delta\nu^d(N)$ and $\Delta\nu^c(N)$ are Term Values for the mean of J-doublets.) These quantities are related to the Pi state effective rotational constants through

$$\Delta\bar{\nu}^i(N) = [\nu_0 - \tfrac{\gamma_v^i}{2}] + B_v^i[(N+1)^2 - 1] - D_v^i[(N+1)^4 + \tfrac{3}{2}(N+1)^2 + \tfrac{1}{16}] \qquad \text{(D-19)}$$
$$+ H_v^i[(N+1)^6 + \tfrac{15}{4}(N+1)^4 + \tfrac{15}{16}(N+1)^2 + \tfrac{1}{64}]$$

when the upper state rotational term values are given by Eq (D-15). Previously, rotational analyses had shown that terms in γ_v were negligible. Therefore, a least squares treatment, performed on data for each (v',v") band separately, using Eq (D-19) yielded estimates of ν_0 and of the Pi state rotational constants simultaneously. However, all these quantities are sensitive to values chosen for the Sigma state rotational constants. (Eq (D-18) stipulates the addition of calculated rotational term values for the lower state to the measured line wavenumbers.) Therefore, to maintain consistency, the band origins were evaluated using for the Sigma state only those rotational constants which are presented in the "Combined

data section of Table D-3. Results of this analysis are presented in Table D-8. Information on the first page of that table refers exclusively to data of Guntsch. None of the bands considered there have been measured to such large N-values that evaluation of an H_v' term was justified. H_v' terms are required for those bands considered on the second page of Table D-8. On that page, band origins based upon the measurements due to Guntsch are compared with those derived from Balfour's data and other estimates based upon the combined data of both observers.

Origins derived from Q-branches agree very well with those found from P and R-branches in the v"-progressions having v'=0,1. Agreement is not so good for bands originating on v'=2. The greatest disagreement in origin location occurs with the (3,2)-band for which the two estimates differ by 1.4 cm^{-1}. It also appears, from Table D-8, that there is a systematic difference of 0.15 cm^{-1} between the (0,0) rotational line measurements of Balfour and Guntsch. Therefore Pi state results based upon the combination of data sets are of questionable validity for the (0,0) band. For this reason and because Balfour's measurements extend to $Q_2(48)$ while those of Guntsch terminate at $Q_2(38)$, it is recommended that ν_{00} be taken as 19284.70 cm^{-1}.

Estimates of B_v', D_v' and H_v' contained in Table D-8 are in remarkably good agreement with those located in Table D-6. Consider bands originating on v'=1 or v'=2 for example. The slight changes in B_2' and B_1' estimates with v' gives an indication of the small effect that the choice of Sigma state rotational constants has had upon the Pi state constants. As the rotational constants listed in Table D-6 were not subject to influence by the choice of $^2\Sigma$ state constants while those present in Table D-8 were and because the two sets of values are so nearly equal for given v',

TABLE D-8

Band Origins and Rotational Constants (cm^{-1}) for the $A^2\Pi$ State of MgH Derived from Term Values

Band & Data	ν_0	B_v	D_v x10+4	H_v x10+8	Points Number	N-values Included in Fit	S.E. of Estimate
(3,2)	$20892.4_8 \pm 0.2_9$	$5.493_7 \pm 0.003_5$	$3.47_5 \pm 0.08_9$		22(22)	7 - 17	0.25
Guntsch	$20893.8_4 \pm 0.5_3$	$5.479_0 \pm 0.004_8$	$3.15_4 \pm 0.09_9$		9(9)	10 - 18	0.16
(2,3)	$18182.8_6 \pm 0.1_9$	$5.711_1 \pm 0.002_2$	$3.85_7 \pm 0.05_1$		24(24)	6 - 18	0.20
Guntsch	$18183.2_7 \pm 0.0_{60}$	$5.706_8 \pm 0.000_{57}$	$3.73_3 \pm 0.01_1$		14(14)	7 - 20	0.051
(2,2)	$19484.0_8 \pm 0.1_3$	$5.714_6 \pm 0.001_4$	$3.93_4 \pm 0.03_1$		27(26)	6 - 19	0.15
Guntsch	$19484.9_4 \pm 0.0_{84}$	$5.704_2 \pm 0.001_0$	$3.66_9 \pm 0.02_5$		16(16)	4 - 19	0.12
(2,1)	$20853.1_1 \pm 0.1_3$	$5.716_5 \pm 0.001_4$	$3.94_9 \pm 0.03_1$		30(29)	4 - 20	0.22
Guntsch	$20853.7_7 \pm 0.0_{62}$	$5.708_0 \pm 0.000_{67}$	$3.72_1 \pm 0.01_4$		16(16)	5 - 20	0.078
(1,2)	$18018.61 \pm 0.02_6$	$5.9043 \pm 0.0002_2$	$3.651_8 \pm 0.003_7$		40(40)	4 - 24	0.063
Guntsch	$18018.65 \pm 0.03_4$	$5.9026 \pm 0.0002_9$	$3.630_2 \pm 0.004_8$		19(19)	5 - 23	0.050
(1,1)	$19387.27 \pm 0.05_9$	$5.9033 \pm 0.0004_1$	$3.641 \pm 0.005_8$		37(35)	7 - 25	0.095
Guntsch	$19387.31 \pm 0.08_8$	$5.9009 \pm 0.0005_5$	$3.602 \pm 0.006_7$		25(25)	4 - 28	0.18
(1,0)	20819.44 ± 0.030	$5.9008 \pm 0.0002_1$	$3.602 \pm 0.002_8$		47(43)	4 - 26	0.074
Guntsch	$20819.60 \pm 0.1_2$	$5.8990 \pm 0.0007_6$	$3.58_6 \pm 0.01_0$		18(18)	8 - 25	0.13
(0,2)	$16484.08 \pm 0.09_5$	$6.0935 \pm 0.0008_6$	$3.57_3 \pm 0.01_7$		19(19)	8 - 20	0.078
Guntsch	$16484.01 \pm 0.02_6$	$6.0931 \pm 0.0002_3$	$3.59_9 \pm 0.00_{43}$		15(15)	7 - 21	0.025

TABLE D-8 (Contd.)

Band Origins and Rotational Constants (cm^{-1}) for the $A^2\Pi$ State of MgH Derived from Term Values

Band & Data	ν_0	B_v	D_v $\times 10^{+4}$	H_v $\times 10^{+8}$	Points Number	N-values Included in Fit	S.E. of Estimate
(0,1)							
Combined	†$17852.66 \pm 0.01_6$	$6.0953 \pm 0.0001_6$	$3.686 \pm 0.004_1$	$1.12_4 \pm 0.02_9$	96(93)	2 - 31	0.051
Data	$17852.71 \pm 0.01_7$	$6.0935 \pm 0.0001_3$	$3.678 \pm 0.002_7$	$1.15_1 \pm 0.01_5$	51(51)	2 - 35	0.042
Guntsch	$17852.55 \pm 0.02_7$	$6.0963 \pm 0.0003_5$	$3.71_5 \pm 0.01_2$	$1.3_9 \pm 0.1_1$	38(38)	5 - 25	0.035
Data	$17852.7_0 \pm 0.1_0$	$6.0930 \pm 0.001_2$	$3.65_2 \pm 0.03_8$	$0.8_7 \pm 0.3_6$	17(17)	8 - 24	0.052
Balfour	$17852.69 \pm 0.01_5$	$6.0946 \pm 0.0001_7$	$3.675 \pm 0.004_2$	$1.07_0 \pm 0.02_8$	58(56)	2 - 31	0.043
Data	$17852.72 \pm 0.00_7$	$6.0928 \pm 0.0000_6$	$3.665 \pm 0.001_2$	$1.08_5 \pm 0.00_7$	34(34)	2 - 25	0.017
(0,0)							
Combined	$19284.65 \pm 0.09_8$	$6.094_3 \pm 0.001_4$	$3.66_4 \pm 0.02_3$	$1.0_2 \pm 0.1_0$	141(137)	1 - 41	0.098
Data	$19284.66 \pm 0.08_1$	$6.092_6 \pm 0.002_7$	$3.65_8 \pm 0.03_2$	$1.0_6 \pm 0.0_{99}$	81(76)	3 - 47	0.081
Guntsch	$19284.55 \pm 0.04_2$	$6.0937 \pm 0.0003_1$	$3.646_4 \pm 0.005_5$	$0.90_0 \pm 0.02_6$	70(68)	1 - 38	0.087
Data	$19284.57 \pm 0.05_3$	$6.0911 \pm 0.0003_9$	$3.616_7 \pm 0.006_9$	$0.79_1 \pm 0.03_3$	35(35)	3 - 37	0.12
Balfour	$19284.73 \pm 0.04_5$	$6.0941 \pm 0.0003_0$	$3.660_6 \pm 0.004_8$	$1.00_3 \pm 0.02_0$	71(67)	1 - 41	0.052
Data	$19284.70 \pm 0.02_0$	$6.0920 \pm 0.0003_7$	$3.652_2 \pm 0.004_1$	$1.04_5 \pm 0.01_2$	46(42)	4 - 47	0.020

†For each band and data set entry, the first number refers to constants valid for P and R branches. The second entry holds for Q branches. The error estimate equals one standard deviation.

it is thought that the band origins are of considerable precision.

Except for the (0,0) and (0,1) bands where Q-branch estimates were used and the (1,0) band for which the P and R branch estimate was used, ν_0 was determined by the arithmetic average of the two available estimates. The results of these calculations and $\Delta G(v+1/2)$-values derivable from them are set forth in Table D-9. Upper state vibrational constants that satisfy Eq (D-13) or the Morse model are compared in Table D-10 where it is seen that the vibrational term values of Guntsch are ~1.8 cm^{-1} below those found by the author. This agreement is very satisfactory. As in the $^2\Sigma$ case, the two Morse fits are essentially equivalent and both lie consistently below the G(v) vs (v+1/2) curve that describes the vibrational potential in terms of the present three term fit.

Two estimates of the system origin, ν_e, were obtained for every band entered in Table D-9 - one based upon the three term fit, the other upon Morse fits. (The Morse-derived values exhibit much more scatter than the others.) An arithmetic average of all available ν_e estimates of a particular type locates the system origin at

ν_e= 19226.8 cm^{-1} - Three term fits to G(v)

ν_e= 19235.8 cm^{-1} - Morse fits to G(v)

above the bottom of the $X^2\Sigma^+$ state potential well. From these values of ν_e and the vibrational constants derived during the course of this study, origins for all bands with v'<4 and v"<4 have been calculated and listed in Table D-11.

D.4 Reconstruction of Rotational line Wavenumbers

The synthesis of microdensitometer traces - considered in Chapter 6 - centred on the $\Delta v=0$ sequence of the MgH 5211 Å system. Initially,

TABLE D-9

Deslandres Array of Band Origins (cm^{-1}) with $\Delta G(v+1/2)$ for MgH $A^2\Pi - X^2\Sigma^+$

v' \ v"	0		1		2		3
0	19284.70	(1432.00)	17852.70	(1368.65)	16484.05		
	(1534.7)		(1534.60)		(1534.58)		
1	20819.4	(1432.1)	19387.30	(1368.67)	18018.63		
			(1466.2)		(1465.9)		
2			20853.5	(1369.0)	19484.5	(1301.4)	18183.1
					(1408.7)		
3					20893.2		

TABLE D-10

$^2\Pi$ State Vibrational Constants and G(v) Values in cm^{-1}.
Comparison of Three Term and Morse Fits.

	This Work	Guntsch	This Work (Morse)	Khan (Morse)
ω_e	1614.0_3	1611.3	1595.6_7	1598.4
$\omega_e x_e$	42.7_8	40.5	31.4_8	31.9
$\omega_e y_e$	1.8_8	1.4	-	-
G(0)	796.56	795.70	790.0	791.2
G(1)	2331.16	2330.55	2322.7	2325.8
G(2)	3797.16	3797.00	3792.4	3796.6
G(3)	5205.86	5203.45	5199.3	5203.6

TABLE D-11

Predicted Band Origins (cm^{-1}) for MgH $A^2\Pi - X^2\Sigma^+$ System
Comparison of Three Term and Morse Fits.

v' \ v"	0	1	2	3	
0	19284.7	17852.7	16484.1	15182.7	- Three Term
	19284.9	17852.3	16484.9	15182.9	- Morse Fit
1	20819.3	19387.3	18018.7	16717.3	
	20817.6	19385.0	18017.6	16715.6	
2	22285.3	20853.3	19484.7	18183.3	
	22287.4	20854.7	19487.4	18185.4	
3	23694.0	22262.0	20893.4	19592.0	
	23694.2	22261.6	20894.2	19592.2	

it was assumed that reconstruction of lines from bands involving $v<4$ would be required. However, Guntsch's measurements for the (2,3) and (3,2) bands contain all the information available about the vibrational levels $v''=3$ and $v'=3$. That data is rather skimpy particularly for the (3,2) band in which combination differences with $N<8$ cannot be evaluated and for which Q-branch constants are based upon data having $10<N<18$. It was felt that wavenumbers for lines of the (3,3) band could not be calculated with a precision comparable to that of the other bands in the sequence. Consequently, wavenumbers used in the synthesis were determined only for lines of the (0,0),(1,1) and (2,2) bands. The effective origins that were used in conjunction with the rotational constants of Table D-2 are ν_{00}= 19284.70 cm^{-1}, ν_{11}= 19387.25 cm^{-1} and ν_{22}= 19484.90 cm^{-1}.

Wavenumbers of rotational lines determined by this reconstruction agree with the available measurements to the precision indicated in Table D-12. Reconstructed line wavenumbers for the Main Branches of the (0,0) band are listed for $0<N<50$ in appendix A, Table 6-2.

D.5 Further Improvements in Line Wavenumber Reconstruction

A better correspondence between reconstructed and observed rotational line positions must await observational data of higher precision. More precise values for B_v, D_v and H_v cannot be extracted from the available measures. The vibrational constants, in particular, need further refinement. Currently their values hinge on fragmentary measures of the (3,2) and (2,3) bands. Other bands having $v>3$ should be measured to put the vibrational analysis on a firmer footing. However, as the MgH $A^2\Pi - X^2\Sigma^+$ sequences show great overlapping, measurements of even the (3,3) band

TABLE D-12

Reconstructed Minus Observed Line Wavenumbers for the Main Branches of the MgH 5211Å system

Mean Deviation	Band (0,0)	(1,1)	(2,2)
$<0.3\ cm^{-1}$	R_1, Q_1, P_1, R_2, P_2	R_1, Q_1, P_1	R_1, Q_1, P_1, Q_2
$\sim 0.4\ cm^{-1}$	Q_2		
$\sim 0.6\ cm^{-1}$		R_2, Q_2, P_2	R_2, P_2

will require the use of spectrographs having plate factors about ten times those used by Balfour and Guntsch. Balfour states that his measurements were made upon plates with a reciprocal dispersion ~1.2Å/mm. Consequently a plate factor of 0.15Å/mm would be an appropriate choice for obtaining data of the requisite precision.

REFERENCES

a) General Background

Abramowitz, M. & Stegun, I.A. 1964. NBS Applied Mathematics Series. 55. Handbook of Mathematical Functions. (1966 printing)

Allen, C.W. 1963. Astrophysical Quantities. 2nd Ed. (Athlone Press, London)

Dole, M. 1954. Introduction to Statistical Thermodynamics. (Prentice-Hall, New York)

Ferri, A. 1961. Agardograph #41, Fundamental Data from Shock Tube Experiments. (Pergamon, New York)

Gaydon, A.G. & Hurle, I.R. 1963. The Shock Tube in High Temperature Chemical Physics. (Reinhold, New York)

Gaydon, A.G. & Wolfhard, H.G. 1970. Flames: Their Structure, Radiation And Temperature. 3rd Ed. Rev. (Chapman & Hall, London)

Harrison, G.R. 1932. Wavelength Tables. (MIT Press, Cambridge)

Herzberg, G. 1950. Molecular Spectra & Molecular Structure I. Spectra of Diatomic Molecules. 2nd Ed. (D. Van Nostrand, New York)

Hurd, D.T. 1952. An Introduction to the Chemistry of the Hydrides. (Wiley, New York)

Jeans, J.H. 1954. The Dynamical Theory of Gases. (Dover)

Kovacs, I. 1969. Rotational Structure in the Spectra of Diatomic Molecules. (American Elsevier, New York)

Mayer, J.E. & Mayer, M.G. 1940. Statistical Mechanics. (Wiley, New York)

Meggers, W.F., Corliss, C.H. & Scribner, B.F. 1961. NBS Mono 32-Part I. Tables of Spectral Line Intensities Arranged by Elements.

Mitchell, A.C.G. & Zemansky, M.G. 1961. Resonance Radiation & Excited Atoms. (Cambridge University Press, Reprint of 1934 Ed.)

Moore, C.E. 1945. NBS Technical Note 36. A Multiplet Table of Astrophysical Interest. Revised Edition (1959 Reprinting of 1945 Ed.)

Moore, C.E. 1949. NBS Circular 467. Atomic Energy Levels. Vol. I.

Moore, C.E. 1952. NBS Circular 467. Atomic Energy Levels. Vol. II.

Moore, C.E. 1958. NBS Circular 467. Atomic Energy Levels. Vol. III.

Natrella, M.G. 1963. NBS Handbook 91: Experimental Statistics (1966 Printing)

Nicholls, R.W. & Stewart, A.L. 1962. "Allowed Transitions" in Atomic & Molecular Processes. Ed. D.R. Bates. (Academic Press, New York)

Oswatitsch, K. 1956. Gas Dynamics (Academic Press, New York)

Pearse, R.W.B. & Gaydon, A.G. 1963. The Identification of Molecular Spectra. 3rd Ed. (Chapman & Hall, London)

Penner, S.S. 1959. Quantitative Molecular Spectroscopy And Gas Emissivities. (Addison-Wesley, Reading, Mass.)

Reif, F. 1965. Fundamentals of Statistical And Thermal Physics. (McGraw-Hill, New York)

Topping, J. 1957. Errors of Observation and Their Treatment. 3rd Ed. (Chapman & Hall, London)

Wright, J.K. 1961. Shock Tubes (Methuen, London)

b) Articles and Other Cited Works

Aarts, J. & Bosch, G. 1964. Physica, Vol 30, #8, pp 1673-1681

Allen, C.W. 1957. Mon. Not. Roy. Astr. Soc., Vol 117, #6, pp 622-628

Andersen, T., Desesquelles, J., Jessen, K.A.& Sørensen, G. 1970. J.Q.S.R.T., Vol 10, 1143-1150

Andersen, T., Mølhave, L. & Sørensen, G. 1972. Astrophys. J., Vol 178, #2, pp 577-582

Armstrong, B.H. 1967. J.Q.S.R.T., Vol 7, pp 61-88

Arnold, J.O. 1968. J.Q.S.R.T., Vol 8, pp 1781-1794

Arnold, J.O. & Nicholls, R.W. 1972. J.Q.S.R.T., Vol 12, pp 1435-1452

Arnold, J.O. & Nicholls, R.W. 1973. J.Q.S.R.T., Vol 13, pp 115-133

Arnold, J.O., Whiting, E.E. & Lyle, G.C. 1969. J.Q.S.R.T., Vol 9, pp 775-798

Balfour, W.J. 1970. Astrophys J., Vol 162, pp 1031-1035

Balfour, W.J. 1970. J. Phys B: Atom. Molec. Phys., Vol 3, pp 1749-1756

Balfour, W.J. & Douglas, A.E. 1970. Can. J. Phys., Vol 48, pp 901-914

Barnard, J.A., Lee, R.K.Y., Yates, J.G. 1972. Chem. Ind. (London), Vol 20, pp 810-812

Bates, G.N. & Altick, P.L. 1973. J. Phys. B: Atom. Molec. Phys., Vol 6, pp 653-664

Bates, D.R. & Damgaard, A. 1949. Phil. Trans. Roy. Soc. London A, Vol 242, pp 101-122

Bengtson, R.D., Miller, M.H., Koopman, D.W. & Wilkerson, T.D. 1970. Phys. Fluids, Vol 13, #2, pp 372-377

Bengtsson Knave, E. 1932. Nova Acta Reg. Soc. Sci. Upsal. Ser IV, Vol 8, #4, pp 1-98

Berry, H.G., Bromander, J. & Buchta, R. 1970. Physica Scripta, 1, pp 181-183

Blauer, J., Solomon, W. 1972. J. Chem. Phys., Vol 57, #9, pp 3587-9

Bleakney, W., Weimer, D., Fletcher, C.H. 1949. Rev. Sci. Instr., 20, p 807

Boesgard, Ann Merchant. 1968. Astrophys J., Vol 154, pp 185-190

Boitnott, C.A. & Warder, R.C. 1971. Phys. Fluids, Vol 14, #11, pp 2312-2316

Boldt, G. 1958. Zeits. für Phys., Vol 150, pp 205-214

Boni, A.A. 1968. J.Q.S.R.T., Vol 8, pp 1385-1397

Borrell, P. & Millward, G.E. 1972. J. Chem. Phys., Vol 57, #1, pp 462-469

Boyer, R. 1971. Astron. & Astrophys., pp 464-467

Bozman, W.R., Corliss, C.H., Meggers, W.F. & Trees, R.E. 1953. J. Res. Nat. Bur. Stand., Vol 50, #3, pp 131-132

Branch, David. 1970 Astrophys. J., Vol 159, pp 39-49

Breeze, J.C. & Ferriso, C.C. 1963. J. Chem. Phys., Vol 39, #10, pp 2619-2628

Breshears, W.D. & Bird, P.F. 1972a. J. Chem. Phys., Vol 56, #11, pp 5347-51

Breshears, W.D. & Bird, P.F. 1972b. Los Alamos Scientific Laboratory Report LA-DC-72-369

Byard, P.L. 1967. J.Q.S.R.T., Vol 7, 559-569

Camm, J.C. 1960. Rev. Sci. Instr., Vol 30, #3, pp 278-279

Cann, M.W.P. & Dickermann, P.J. 1968. AFWL-TR-67-76 Molecular f-numbers from High Resolution Spectra

Chan, Arthur C.H. & Davidson, Ernest R. 1968. J. Chem. Phys., Vol 49, #2, pp 727-739

Chan, Arthur C.H. & Davidson, Ernest R. 1970. J. Chem. Phys., Vol 52, #8, pp 4108-4121

Charatis, G. 1961. Ph.D. Thesis. University of Michigan

Charatis, G. & Wilkerson, T.D. 1962. Phys. Fluids, Vol 5, 1661-1662

Ch'en Shang-Yi & Takeo, Makoto 1957. Rev. Mod. Phys., Vol 29, #1, pp 20-73

Ch'en Shang Yi & Henry, Paul K. 1973a J.Q.S.R.T., 13, pp 41-48

Ch'en Shang Yi & Henry, Paul K. 1973b J.Q.S.R.T., 13, pp 385-391

Clouston, J.G., Gaydon, A.G. & Glass, I.I. 1958. Proc. Roy. Soc. A, Vol 248, 429-444

Clouston, J.G., Gaydon, A.G. & Hurle, I.R. 1959. Proc. Roy. Soc. A, Vol 252, 143-155

Cooper, David M. 1972. J.Q.S.R.T., Vol 12, #8, pp 1175-89

Corliss, C.H. & Bozman, W.R. 1962 NBS Monograph #53. "Experimental transition probabilities for spectral lines of 70 elements."

Cunningham, A.J. & Hobson, R.M. 1972a. J. Phys. B: Atom. Molec. Phys., Vol 5, #9, pp 1773-1783

Cunningham, A.J. & Hobson, R.M. 1972b. J. Phys. B: Atom. Molec. Phys., Vol 5, #12, pp 2328-2331

Davidson, N. 1962. Statistical Mechanics. (McGraw-Hill, New York)

Day, R.A. 1969. Phys. Fluids Suppl I, pp 47-49

Demtroder, W. 1962. Zeits. für Phys. Vol 166, pp 42-55

Diebold, G.J., Santoro, R.J. & Goldsmith, G.J. 1974. J. Chem. Phys., Vol 60, #11, pp 4170-4174

Diesen, R.W. & Telmke, W.J. 1963. J. Chem. Phys., Vol 39, #9, pp 2115-2120

Drake, G.W.F. 1966. M.Sc. Thesis. U.W.O., London, Ontario. "The Quantitative Spectroscopy of BeO."

Drake, G.W.F., Tyte, D.C. & Nicholls, R.W. 1967. J.Q.S.R.T., Vol 7, pp 639-659

Earls, L.T. 1935. Phys. Rev., Vol 48, pp 423-424

Eckstrom, D.J. & Bershader, D. 1972. J. Chem. Phys., Vol 57, #2, pp 632-638

Edlen, B. 1953. J. Opt. Soc. Am., Vol 43, #5, pp 339-344

Faddeeva, V.N. & Terentsev, N.M. 1961. Tables of the Probability Integral for Complex Argument. (Pergamon Press, New York)

Faizullov, F.S., Sobolev, N.N. & Kudryavtsev, E.M. 1960. Opt. & Spectr., Vol 8, #5, pp 311-315

Froese Fischer, C. 1975. Can. J. Phys., Vol 53, pp 338-342

Gardiner, W.C. & Kistiakowsky, G.B. 1961. J. Chem. Phys., Vol 35, #5, pp 1765-1770

Garton, W.R.S., Parkinson, W.H. & Reeves, E.M. 1964. Astrophys. J., Vol 140, #3, pp 1269-1279

Garton, W.R.S. & Wilson, M. 1966. Proc. Phys. Soc. A., Vol 87, pp 841-850

Gaydon, A.G. 1968. "Dissociation Energies and Spectra of Diatomic Molecules". 3rd Ed. (Chapman & Hall, London)

Gilbert, A., Sulzmann, K.G.P. & Penner, S.S. 1974. J.Q.S.R.T., Vol 14, pp 455-478

Glass, I.I. 1958. Shock Tubes. Part I: "Theory and Performance of Simple Shock Tubes". UTIA Review #12, Part I. (University of Toronto, Toronto)

Glick, H.S., Klein, J.J. & Squire, W. 1957. J. Chem. Phys., Vol 27, #4, pp 850-857

Grasdalen, G.L., Huber, M. & Parkinson, W.H. 1969. Astrophys. J., Vol 156, pp 1153-1173

Guntsch, A. 1939. Doctoral Dissertation. The University of Stockholm, Sweden

Gutman, D. & Schott, G.L. 1967a. J. Chem. Phys., Vol 46, p 4576-4584

Gutman, D., Hardwidge, E.A., Dougherty, F.A. & Lutz, R.W. 1967b. J. Chem. Phys., Vol 47, p 4400-4407

Gutman, D., Lutz, R.W., Jacobs, N.F., Hardwidge, E.A. & Schott, G.L. 1968. J. Chem. Phys., Vol 48, p 5689-5694

Gutman, D. & Matsuda, Shimpei 1970. J. Chem. Phys., Vol 52, #8, pp 4122-4132

Gutman, D. & Matsuda, Shimpei 1972. Rev. Sci. Instr., Vol 42, #8, pp 1231-1234

Haar, L.& Friedman, A.S. 1955. J. Chem. Phys., Vol 23, #5, p 869-875

Harrington, J.A., Modica, A.P. & Libby, D.R. 1966. J.Q.S.R.T., Vol 6, pp 799-805

Harrington, J.A. 1969. Ph.D. Thesis. York University, Toronto, Ontario. "A Shock Tube Study on the Spectroscopy and Chemical Kinetics of Vanadium Oxide."

Haycock, S.A. 1963. M.Sc. Thesis, U.W.O., London, Ontario. "Line Intensities in Diatomic Electronic Spectra: The Effect of Vibration Rotation Interaction."

Heimel, S., McBride, B.J., Ehlers, J.G. & Gordon, S. 1963. NASA Special Publication 3001. "Thermodynamic Properties to 6000 °K for 210 Substances Involving the First 18 Elements."

Helliwell, T.M. 1964. Phys. Rev. A, Vol 135, pp 325-331

Henneker, W.H. & Popkie, H.E. 1971. J. Chem. Phys., Vol 54, #4, pp 1763-1778

Hidaki, Yoshiaki & Yamamura, Hitoshi 1971. J. Sci. Hiroshima Univ., Ser A-2, Vol 35, #1, pp 53-58

Hill, E.L. & Van Vleck, J.H. 1928. Phys. Rev., Vol 32, pp 250-272

Hooker, W.J. & Millikan, R.C. 1963. J. Chem. Phys. Vol 38, pp 214-220

Hubbell, J.H. 1965. J. Res. Natl. Bur. Stand. U.S., Vol 69C, #2, pp 139-143

Huber, M. & Tobey, F.L. 1968. Astrophys. J., Vol 152, p 609-620

Huber, M.C.E. 1974. Astrophys. J., Vol 190, pp 237-240

Hulpke, E., Paul, E. & Paul, P. 1964. Zeits. für Phys. Vol 177, pp 257-268

Hummer, D.G. 1965. Mem. Roy. Astr. Soc., Vol 70, pp 1-32

Hurle, I.R. 1964. J. Chem. Phys., Vol 41, #12, pp 3911-3920

Hurle, I.R. & Russo, A.L. 1965. J. Chem. Phys., Vol 43, #12, pp 4434-4443

Hurle, I.R. 1967. Proc. 11th Combustion Symposium, pp 827-836 (Butterworths, London)

Jenkins, F.A. & McKellar, A. 1933. Phys. Rev., Vol 42, p 464-486

Just, T. & Stepanek, S. 1970. Prov. VII Inter. Shock Tube Symp., 1969, pp 626-643, I.I. Glass Ed. (University of Toronto, Toronto)

Keck, J.C., Camm, J.C., Kivel, B. & Wentink, T. 1959. Annals of Phys., Vol 7, #1, pp 1-38

Kersten, J.A.H. & Ornstein L.S. 1941. Physica, Vol 8, #10, pp 1124-1136

Khan, M. Aslam 1962. Proc. Phys. Soc., Vol 80, pp 523-524

Kiefer, J.H. & Lutz, R.W. 1966. J. Chem. Phys., Vol 44, pp 668-672

Knave, E. Bengtsson 1932. Nova Acta Reg. Soc. Sci. Upsal. SER IV, Vol 8, #4, pp 1-98

Knight, H.T. & Rink, J.P. 1961. J. Chem. Phys., Vol 35, #1, pp 199-208

Krindach, N.I., Kudryavstev, E.M., Sobolev, N.N., Tunitskii, L.N. & Faizullov, F.S. 1963. Opt. & Spectr., Vol 14, pp 188-193

Laborde, G. 1957. Comptes Rendus de l'Acad., Vol 244, pp 564-566

Laborde, G. 1961. Ann. d'Astrophys., Vol 24, #2, p 89

Lapp, M. 1961. J.Q.S.R.T., Vol 1, #1, pp 30-45

Lapworth, K.C. 1962. Agard Meeting in Brussels, April 1962 on High Temperature Aspects of Hypersonic Flow

Lapworth, K.C. 1969. J. Phys. A: (Gen. Phys.) Ser 2, Vol 2, pp 415-418

Larrabee, R.D. 1959. J. Opt. Soc. Am., Vol 49, #4, pp 619-625

Lawrence, T.R. & Burns, G. 1969. Phys. Fluids Suppl. I, pp 109-112

Levitt, B.P., Parsons, A.B., Colgan, S.J. 1967. "Light Emission From Shock Heated Gases". U.S.C.F.S.T.I. AD-822877

Lippencott, E.R., Steele, D. & Caldwell, P.J. 1961. J. Chem. Phys., Vol 35, #1, pp 123-134

Lundin, L., Engman, B., Hilke, J. & Martinson, L. 1973. Physica Scripta, Vol 8, #6, pp 274-278

Lurio, A. 1964. Phys. Rev. A., Vol 136, #2, pp 376-379

Main, R.P., Carlson, D.J. & Dupuis, R.A. 1967, J.Q.S.R.T., Vol 7, pp 805-811

Mallia, E.A. 1968. Solar Physics, Vol 5, #3, pp 281-301

Margenau, H. & Watson, W.W. 1936. Rev. Mod. Phys., Vol 8, pp 22-53

Marr, G.V. 1966. Proc. Phys. Soc., Vol 87, #2, pp 547-549

Marr, G.V. & Heppinstall, R. 1966. Proc. Phys. Soc., Vol 87, #1, pp 293-298

Martinson, I. 1974. Physica Scripta, Vol 9, #5, pp 281-296

McCallum, J.C., Jarmain, W.R. & Nicholls, R.W. 1970. CRESS Spectroscopic Report Number 1

McCallum, J.C. & Nicholls, R.W. 1971. CRESS Spectroscopic Report Number 2

McGregor, A.T. 1962. M.Sc. Thesis, U.W.O., London, Ontario. "The Shock Excitation of Powdered Ceramics and Sulphides."

Meissner, K.W. 1938. Ann. Phys., Vol 31, p 505-517

Miller, M.H. & Bengtson, R.D. 1969. Astrophys. J., Vol 156, pp393-395

Miyama, H. & Takeyama, T. 1963. J. Chem. Phys., Vol 39, #3, pp 851-2

Miyama, H. & Takeyama, T. 1964. J. Chem. Phys., Vol 40, #7, p 2049-2050

Miyama, H. & Takeyama, T. 1965. Bull. Chem. Soc. Japan, Vol 38, pp 37-44

Modica, A.P. & Hornig, D.F. 1965. J. Chem. Phys., Vol 43, #8, pp 2739-2744

Mulliken, R.S. 1931. Rev. Mod. Phys., Vol 3, pp 89-155

Mundie, L.G. & Meissner, K.W. 1944. Phys. Rev., Vol 65, pp 265-273

Myerson, A.L. & Watt, W.S. 1968. J. Chem. Phys., Vol 49, #1, pp 425-433

Nagamatsu, N.T. Chapter III of Agardograph #41 (cited earlier) Edited by A. Ferri

Nayfeh, Ali Hasan 1966. Phys. Fluids, Vol 9, #12, pp 2351-2356

Newson, G.H. & Shore, B. 1968. J. Phys. B: Atom. Molec. Phys., Ser 2, Vol 1, p 742

Nicholls, R.W. & Jarmain, W.R. 1956. Proc. Phys. Soc. A., Vol 69, #3, pp 253-264

Nicholls, R.W., Parkinson, W.H. & Reeves, E.M. 1963. Applied Optics, Vol 2, #9, pp 919-930

Olsson, E. 1932. Zeit. für Phys., Vol 73, pp 732-746

Ostrovskii, Yu I., Penkin, N.P. & Shabanova, 1958. Sov. Phys. Dokl., Vol 3, p 538

Ostrovskii, Yu I. & Penkin, N.P. 1961. Opt. & Spectr., Vol 11, p. 307-309

Parkinson, W.H. 1957. M.Sc. Thesis U.W.O., London, Ontario. "The Shock Excitation of Powdered Solids."

Parkinson, W.H. 1959. Ph.D. Thesis U.W.O., London, Ontario. "Studies on the Shock Excitation of Powdered Solids."

Parkinson, W.H. & Nicholls, R.W. 1957. J. Chem. Phys., Vol 26, pp 423-424

Parkinson, W.H. & Nicholls, R.W. 1959. Molecular Excitation Group. Contract No. AF 19(604)-4560 Scientific Report No 1. Shock Tube Spectroscopy. I The Shock Excitation of Powdered Solids.

Parkinson, W.H. & Nicholls, R.W. 1960. Can. J. Phys., Vol 38, pp 715-719

Parkinson, W.H. & Reeves, E.M. 1962. Proc. Phys. Soc. A, Vol 86, pp 860-867

Patch, R.W. 1962. J. Chem. Phys., Vol 36, #7, pp 1919-1924

Pekeris, C.L. 1934. Phys. Rev., Vol 45, pp 98-103

Penkin, N.P. & Shabanova, L.N. 1962. Opt. & Spectr., Vol 12, #1, pp 1-5

Plass, G.N. & Fivel, D.I. 1953. Astrophys. J., Vol 117, pp 225-233

Popkie, H.E. 1971. J. Chem. Phys., Vol 54, #11, pp 4597-4605

Posener, D.W. 1959. Austral. J. Phys., Vol 12, pp 184-196

Raff, L.M. & Winter, T.G. 1968. J. Chem. Phys., Vol 48, p 3992

Reeves, E.M. & Parkinson, W.H. 1964. Harvard College Observatory Shock Tube Laboratory. Scientific Report #1 (Cambridge, Mass.)

Rink, J.P. 1962. J. Chem. Phys., Vol 36, #1, 262-265

Risberg, P. 1955, Ark. Fys., Vol 9, #31, pp 483-494

Risberg, G. 1965. Ark. Rys., Vol 28, #32, pp 381-395

Risberg, G. & Swennson, J.W. 1965. Ark. Fys., Vol 31, #16, pp 237-254

Rowlinson, J.S. 1958. Review Article cited by Vardya in Handbuch der Physik, Vol 12, p 1, Ed. S. Flugge (Springer-Verlag, Berlin)

Schadee, A. 1965. Bull. Astron. Soc. Netherlands, Vol 17, #5, pp 311-357

Schadee, A. 1971. Astron. & Astrophys., Vol 14, pp 401-404

Schadee, A. 1967. J.Q.S.R.T., Vol 7, 169-183

Schaefer, A.R. 1971. Astrophys. J., Vol 163, pp 411-416

Seal, K.E. & Gaydon, A.G. 1966. Proc. Phys. Soc., Vol 89, p 459

Sharma, R.D. & Wray, K.L. 1970. Excitation Mechanism for the Schumann-Runge System. U.S.C.F.S.T.I. AD No. 715995

Sidgwick, N.V. 1950. "The Chemical Elements and Their Compounds". Vols 1, 2. (Clarendon Press, Oxford)

Simpson, C.J.S.M. & Simmie, J.M. 1971. Proc. Roy. Soc. A, Vol 325, pp 197-206

Smith, W.W. & Gallagher, A. 1966. Phys. Rev., Vol 145, #1, pp 26-35

Smith, W.H., & Liszt, H.S. 1971. J. Opt. Soc. Am., Vol 61, #7, pp 938-941

Stubbeman, R.F. & Gardiner, W.C. 1964. J. Phys. Chem., Vol 68, #11, pp 3169-3175

Stwalley, W.C. 1970. Chem. Phys. Lett., Vol 7, #6, pp 600-602

Tatum, J.B. 1967. Astrophys. J. Suppl. Vol 14, #124. "The Interpretation of Intensities in Diatomic Molecular Spectra."

Taylor, R.L. & Bitterman, S. 1969. Rev. Mod. Phys., Vol 41, #1, pp 26-47

Texas Instruments, Application Note. 1962. Sc-3323 1262

Treanor, C.E. & Wurster, W.H. 1960. J. Chem. Phys., Vol 32, #3, pp 758-766

Trefftz, E. 1950. Zeit. für Astrophys., Vol 28, pp 67-78

Tyte, D.C. 1964. Nature, Vol 202, #4930, pp 383-384

Tyte, D.C. & Hébert, G.R. 1964. Proc. Phys. Soc., Vol 84, pp 830-832

Tyte, D.C. 1966. J. Appl. Phys., Vol 37, #2, pp 802-806

van de Hulst, H.C. & Reesinck, J.J.M. 1947. Astrophys. J., Vol 106, pp 121-127

Vardya, M.S. 1964. Am. J. Phys., Vol 32, #7, pp 520-525

Von Rosenberg, C.W. & Wray, K.L. 1972. J.Q.S.R.T., Vol 12, #4, pp 531-547

Warner, Brian 1968a. Mon. Not. Roy. Astr. Soc., Vol 139, pp 103-113

1968b. Mon. Not. Roy. Astr. Soc., Vol 140, pp 53-59

Warshay, M. 1972. J. Chem. Phys., Vol 57, #5, pp 2223-2224

Watson, M.D. 1960. M.Sc. Thesis. U.W.O., London, Ontario. "The Interaction of Shock Waves and Powdered Solids."

Watson, R. 1963. J.Q.S.R.T., Vol 3, #3, pp 255-264

Watson, R. 1966. Applied Optics, Vol 5, #2, pp 215-223

Watson, W.W. 1928. Phys. Rev., Vol 32, pp 600-606

Watson, W.W. & Rudnick, P. 1927. Phys. Rev., Vol 29, pp 413-418

Weeks, Dorothy W. & Simpson, Edwin A. 1967. Harvard College Observatory Shock Tube Laboratory Scientific Report No. 19. (Cambridge, Mass.)

Weihs, D. & Manheimer Timnat, Y. 1969. AIAA Journal, Vol 7, #4, pp 764-6

Weiss, A.W. 1967. J. Chem. Phys., Vol 47, #9, pp 3573-3578

White, D.R. 1958. J. Fluid Mech., Vol 4, p 585

White, D.R. 1965. J. Chem. Phys., Vol 42, #2, pp 447-449

Whiting, E.E. 1968. J.Q.S.R.T., Vol 8, pp 1379-1384

Whiting, Ellis E., Arnold, J.O. & Lyle, G.C. 1967. J.Q.S.R.T., Vol 7, pp 725-739

Whiting, E.E., Arnold, J.O. & Lyle, G.C. 1969. NASA Technical Note D-5088

Whiting, E.E. & Nicholls, R.W. 1974. Astrophys. J. Suppl., Vol 27, #235, pp 1-20

Whiting, E.E., Paterson, J.A., Kovacs, I. & Nicholls, R.W. 1973. J. Mol. Spectr., Vol 47, #1, pp 84-98

Wiese, W.L. & Weiss, A.W. 1968. Phys. Rev., Vol 175, #1, pp 50-65

Wiese, W.L., Smith, M.W. & Miles, B.M. 1969. NSRDS-NBS22 "Atomic Transition Probabilities: A critical compilation. Vol II Elements Sodium through Calcium."

Wilkerson, T.D. & Laporte, O. 1961. The Shock Tube as a Spectroscopic Source with Application to Measurement of gf-values for lines of neutral and singly Ionized Chromium. U.S.D.C.O.T.S. AD 262100

Withbroe, G.L. 1968. Solar Physics, Vol 3, pp 146-158

Witliff, C.E., Wilson, M.R. & Hertzberg, A. 1959. J. Aero/Space Sci., Vol 26, pp 219-228

Wolnik, S.J., Berthel, R.O., Larson, G.S., Carnevale, E.H. & Wares, G.W. 1968. Phys. Fluids, Vol 11, #5, pp 1002-1011

Wolnik, S.J., Berthel, R.O., Carnevale, E.H. & Wares, G.W. 1969. Astrophys. J., Vol 157, #2, pp 983-995

Wolnik, S.J., Berthel, R.O. & Wares, G.W. 1971. Astrophys. J., Vol 166, #1 (Part 2), pp L31-L33

Wray, K.L. 1962. J. Chem. Phys., Vol 36, pp 2597-2603

Wray, K.L. & Teare. 1962. J. Chem. Phys., Vol 36, pp 2582-2596

Young, C. 1965. J.Q.S.R.T., Vol 5, pp 545-552

Zare, R.N. 1967. J. Chem. Phys., Vol 47, #9, pp 3561-3572

Zeeman, P.B. & Ritter, G.J. 1954. Can. J. Phys., Vol 32, pp 555-561